



The
University
Of
Sheffield.

**Selective Laser Melting of Nickel Superalloys: solidification,
microstructure and material response**

By:

Neil J Harrison

A thesis submitted in partial fulfilment of the requirements for the degree of
Doctor of Philosophy

The University of Sheffield
Faculty of Engineering
School (or Department) of Mechanical Engineering

Submission Date: 28th of October 2016

Abstract

The Selective Laser Melting (SLM) process generates large thermal gradients during rapid melting, and during solidification certain nickel superalloys suffer from thermally induced micro-cracking which cannot be eliminated by process optimisation.

This investigation sought to investigate and understand the root cause of micro-cracking in nickel superalloys when processed by SLM, with the aim of ultimately being able to predict the crack susceptibility of an alloy from composition alone.

Microstructural analysis as well as implementation of Rapid Solidification Processing (RSP) theory and solute redistribution theory was used to establish SLM as a rapid solidification process. As a consequence, secondary dendrite arm formation and solute redistribution is largely inhibited, resulting in a bulk material which is near to a super saturated solid solution.

The establishment of SLM as an RSP along with morphological and chemical analysis of micro-cracks support Elevated Temperature Solid State (ETSS) cracking as the primary cracking mechanism in SLM processed nickel superalloys.

The crack susceptibility of a nickel superalloy, χ , was defined as the ratio between the solid solution strengthening contribution from alloying elements and apparent thermal stress generated by the process.

Minor increases in the wt% of solid solution strengthening elements in Hastelloy X, a high crack susceptibility alloy, resulted in average reductions of crack density of 65%. Thereby supporting solid solution strength as a key factor in the crack susceptibility of a nickel superalloy. The addition of the apparent thermal stress component, further supported

the crack susceptibility model, with the modified Hastelloy X being predicted to have a lower crack susceptibility.

Additional validation of the crack susceptibility predictor was determined by taking compositions and material properties from published SLM investigations and calculating the crack susceptibility of the respective alloy. The results were found to be in good agreement with the reported observations.

Acknowledgments

I would like to thank everyone who has made success in this project possible. As with anything of this scale, there are countless people involved at various points, all of whom have had an effect on the process and outcome of the work. However, I feel it necessary to thank the following people specifically for their significant contributions and support:

I would like to thank my primary academic supervisor, Dr Kamran Mumtaz, for his support and guidance throughout this project. His encouragement and knowledge of this field ensured a successful conclusion to this project, along with publication of part of this work in a high ranking journal.

I would also like to thank my secondary supervisor, Professor Iain Todd, whose extensive knowledge of metallurgy and enthusiasm for the project was invaluable. I can attribute much of my learning regarding the fundamental aspects of this work to his guidance.

I thank LPW Technology Ltd and EPSRC for their financial support in this project. I also wish to thank my industrial supervisor, Dr Robert Deffley, whose work provided the platform for this project and whose knowledge of the process and nickel alloys

specifically was also invaluable. In addition, I personally thank Dr Phil Carroll (CEO of LPW Technology) for his technical support and helping me integrate with the company.

I would like to thank my colleague Omar Lopez, whose temperature field model featured in this work, in addition to his general support and imparting of knowledge in this area.

Other colleagues without whose assistance I would not have been able to complete this work in its entirety are Dr James Hunt, Dr Fatos Derguti, Ian Woods, Kyle Arnold, Pratik Vora and Dr Cheryl Shaw.

I would also like to thank the Departments of Mechanical Engineering and Materials Science and Engineering at the University of Sheffield for administrative support, use of equipment, and provision of courses and literature for personal development.

The guys in D14 Garden Street also deserve significant praise for breaking up the long days with occasional games of office golf and various internet based games, but punctuated with actual work. Without them, I doubt I would have had the drive required to put in a full day every day. So thank you Tom, Ryan, Ste and Luke.

Perhaps the greatest thanks goes to my family, without the support, encouragement and love from them, I would have struggled to get through the difficult periods of the last 4 years. Mum, Dad, Mark, Sue, Alastair, Grandma, I love you and thank you.

Finally my beautiful wife, Catherine, thank yous will never be enough to balance the love, support and encouragement you have given me. Without you I would never have considered this avenue in my career, and therefore I would have never have found myself in the position that I am in now. From long before this project began, throughout its duration and every day after, you have been my constant, my rock, and my best friend. I could not have done this without you. I love you more than anything.

Table of Contents

Abstract	1
Acknowledgments.....	2
Table of Contents.....	4
Publications	8
List of Tables.....	8
List of Figures.....	9
List of Abbreviations.....	15
Nomenclature.....	17
1 Introduction.....	21
1.1 Problem statement.....	21
1.2 Aims and Objectives of Research.....	22
1.3 Thesis structure	22
2 Background and Literature review	25
2.1 Selective Laser Melting: An Additive Manufacturing technique.....	25
2.1.1 The process	25
2.1.2 Applications	27
2.2 Problem characteristics in SLM.....	29
2.2.1 High thermal and residual stresses.....	29
2.2.2 Porosity.....	37
2.2.3 Surface roughness	39
2.2.4 Process induced cracking.....	42
2.3 Failure by fracture and critical crack length.....	44
2.4 Solidification and microstructure theory.....	47
2.4.1 Solidification fundamentals.....	47
2.4.2 Rapid solidification	55
2.4.3 In SLM.....	64
2.5 Superalloys – History and Development	67
2.5.1 High temperature superalloys: the emergence of Nickel as the material of choice 68	
2.5.2 Nickel as a solvent.....	68
2.5.3 Conventional Manufacturing	70
2.6 Superalloys - Metallurgy	76
2.6.1 Phases and microstructure.....	76

2.6.2	Alloying elements and their effects (nickel and nickel-iron)	79
2.6.3	Strengthening	80
2.7	Cracking in welding of Ni-base alloys and superalloys	87
2.7.1	Solidification cracking	87
2.7.2	Heat affected zone (HAZ) Liquation cracking	89
2.7.3	Ductility dip cracking and ductility minimum	90
2.7.4	Elevated temperature solid state cracking	92
2.7.5	Elements associated with cracking mechanisms	93
2.8	SLM processing: Nickel alloys, thermal stress and crack formation	98
2.8.1	Nickel superalloys: microstructure, mechanical properties and defects	98
2.8.2	Reduction of thermal stress build up	103
2.8.3	Post process crack and defect elimination	105
2.8.4	Anisotropic mechanical properties and crystal orientation	107
2.8.5	Investigations in micro-cracking	108
2.9	Improvement of processability through alloy composition	114
2.9.1	Weldability, crack susceptibility and SLM	114
2.9.2	Beneficial minor element additions	116
2.9.3	Low thermal expansion alloy systems	116
2.10	Chapter summary	118
3	Principle experimental methodology and preliminary investigations	120
3.1	Renishaw SLM125	120
3.1.1	Controllable parameters	121
3.1.2	Beam measurements	123
3.1.3	DOE – Process parameter considerations	128
3.2	Analysis techniques	131
3.2.1	Sample preparation	131
3.2.2	Microscopes	132
3.2.3	Porosity analysis	132
3.2.4	Micro-crack analysis	133
3.3	Hastelloy X	134
3.3.1	Hastelloy X Powder	135
3.3.2	Parameter optimisation	139
3.4	Chapter summary	153
4	Establishment of Rapid Solidification	155
4.1	Rapid solidification conditions applied to SLM	155

4.1.1	Interface velocities and microstructure.....	155
4.1.2	Solute trapping.....	165
4.2	Experimental verification.....	167
4.2.1	Microstructure analysis.....	167
4.2.2	Microsegregation of minor elements.....	173
4.3	Sub-micron precipitate analysis.....	174
4.4	Chapter summary.....	182
5	Cracking mechanism and crack susceptibility defined.....	184
5.1	Mechanism for process induced micro-cracking in SLM.....	184
5.2	Crack susceptibility defined.....	187
5.3	Chapter summary.....	191
6	Tensile strength contribution.....	192
6.1	Development of tensile strength model.....	192
6.2	Application to reduce crack susceptibility.....	195
6.2.1	Hastelloy X composition alteration.....	196
6.2.2	Modified Hastelloy X: material response and property comparison.....	199
6.3	Cracking with geometry, power and energy density.....	208
6.3.1	Initial findings.....	208
6.3.2	DOE.....	210
6.3.3	General results.....	211
6.3.4	Laser power relationship.....	214
6.3.5	Energy density relationship.....	216
6.3.6	Sample size relationship.....	216
6.3.7	Applicability to crack susceptibility theory.....	218
6.4	Chapter Summary.....	219
7	Thermal stress modelling.....	220
7.1	Stress simulation discussion.....	221
7.2	Temperature field simulation.....	226
7.3	Thermo-Calc: method for obtaining thermal dependent properties.....	229
7.4	Calculation methodology.....	232
7.4.1	Thermo-Calc simulation of thermal dependent material properties.....	233
7.4.2	ΔT calculations using Lopez model.....	236
7.4.3	'Apparent' thermal stress calculations.....	245
7.5	Chapter Summary.....	246
8	Crack susceptibility model: coupling of solid solution strengthening and thermal stress.....	248

8.1	Crack susceptibility predictor: Method.....	248
8.1.1	OHX and MHX crack susceptibility comparison.....	249
8.2	Validation experiment: Inconel 713 LC.....	250
8.2.1	Model predictions.....	251
8.2.2	Experimental and results	251
8.3	Validation experiment: Novel alloys	256
8.3.1	Fabrication: Arc melted casting and ball milling.....	257
8.3.2	Model predictions.....	264
8.3.3	SLM processing methodology.....	264
8.3.4	Results and discussion	266
8.3.5	Conclusions	269
8.4	Crack susceptibility predictor: Discussion and Summary.....	270
8.4.1	Additional alloys and validation comparison	270
8.4.2	Discussion of model effectiveness.....	276
8.5	Low crack design model.....	280
8.5.1	Model plan	280
8.5.2	Input and additional model considerations	281
8.6	Chapter Summary	282
9	Further considerations, summary and conclusions	284
9.1	Recent publications and further considerations.....	284
9.1.1	Recent publications	284
9.1.2	Further considerations.....	290
9.2	Summary of chapters.....	292
9.2.1	Review of literature	292
9.2.2	Experimental methodology and preliminary investigations.....	293
9.2.3	Establishment of rapid solidification and microstructure	294
9.2.4	Micro-cracking mechanism	296
9.2.5	Tensile strength contribution.....	296
9.2.6	Thermal stress simulation	298
9.2.7	Crack susceptibility predictor	300
9.3	Conclusions.....	301
10	References.....	304

Publications

It is noted that there has already been one publication from this work, relating to the work discussed in Chapters 4-6, details of which are below. This statement therefore acts as reference to said publication for this work.

Harrison, N. J., et al. (2015). "Reduction of micro-cracking in nickel superalloys processed by Selective Laser Melting: A fundamental alloy design approach." *Acta Materialia* **94**(0): 59-68.

List of Tables

Table 2.1 - Mechanical properties for range of alloys and metals. Values of yield strength, Ultimate Tensile Strength (UTS), elongation and K1c are all maximums in the range, taken from CES Edupack 2014, c_{crit} values are calculated.....	46
Table 2.2 - Key material properties of nickel.....	69
Table 2.3 - Nominal compositions of IN713C and IN713LC, values in wt% (Donachie and Donachie 2002).	94
Table 2.4 - Tensile data for room and elevated temperature of IN713C and IN713LC (Donachie and Donachie 2002).	95
Table 2.5 - Tensile properties of nickel base superalloys for conventional (Con.), SLM as processed (SLM) and SLM as processed plus heat treatment (+ht).....	101
Table 3.1 - Beam diameter and intensity readings. Pk% of 0.0mm is what percentage of the peak at 0.0mm focus offset the given peak is.....	126
Table 3.2 - Composition in wt% of LPW Hastelloy X with nominal specification range as given by LPW Technology Ltd.....	135
Table 4.1 - Glossary of terms - adapted from (Bass 2012)	156
Table 6.1 - Strengthening constants for alloying elements of nickel	194
Table 6.2- Composition of OHX and MHX with concentrations, elemental strengthening coefficients (k) and resulting σ_{ss} values. Values for k taken from Mishima et al.[32].....	198
Table 6.3 - Mean coefficient of thermal expansion for OHX and MHX alloys over full and partial temperature ranges.	207
Table 6.4 - DOE values for crack density with volume, power and energy density trial	210
Table 7.1 - Nominal composition of Hastelloy X to be used for validation calculations ...	232

Table 7.2 - Example thermophysical property values calculated using Thermo-Calc simulation	234
Table 7.3 - Thermophysical properties from Mills (2002)	236
Table 7.4 - Input process parameters for Lopez model	237
Table 8.1 - Crack susceptibility predictions for OHX and MHX	249
Table 8.2 - Elevated temperature mechanical properties of Inconel 713 LC taken from (Donachie and Donachie 2002)	250
Table 8.3 - Composition used for crack susceptibility predictions of Inconel 713 LC	251
Table 8.4 - Tensile testing data for as processed IN713LC – tensile specimens built in x-y orientation.....	253
Table 8.5 - Designed alloy compositions with predicted solid solution contribution	256
Table 8.6 – Designed and actual composition of the two low SSS and high SSS alloys fabricated by arc melting-ball milling.....	261
Table 8.7 - Key crack susceptibility calculation components of High and Low SS alloys	264
Table 8.8 - Crack density (per mm ²) for the three alloys for both 0.06 and 0.09 μm hatch spacings	267
Table 8.9 - Hardness values for novel alloys and MHX.....	269
Table 8.10 – Solid solution contribution, apparent thermal stress and crack susceptibility values for alloys with SLM as processed and conventional process ‘book’ properties. With observations from experimental investigations on micro-cracking severity	273

List of Figures

Figure 2.1 - Schematic of the SLM build process for Renishaw SLM 125.....	26
Figure 2.2 – Representation of TGM, with thermal strain ϵ_{th} , plastic strain ϵ_{pl} , tensile stress σ_{tens} and compressive stress σ_{comp} – direct from (Mercelis and Kruth 2006)	31
Figure 2.3 - Residual stress in the part and base plate, interface is at 20 mm height – direct from Mercelis and Kruth (2006).	32
Figure 2.4- Modelled stress profile of part after removal from baseplate– direct from Mercelis and Kruth (2006).....	33
Figure 2.5 - Modelled progression of residual stress profiles of part attached to substrate (left) and removed (right) with increasing number of layers– direct from Mercelis and Kruth (2006)	34
Figure 2.6 - Measured residual stress profile for as processed part attached to base plate in strong agreement with Mercelis and Kruth (2006) model (left), with conversely weak relationship between scan speed and maximum residual stress (right)– directly from Shiomi, Osakada et al. (2004)	36
Figure 2.7 - a) High porosity caused by lack of fusion and b) low porosity achieved through parameter optimisation– adapted from Rickenbacher (2013).....	38
Figure 2.8- a) the wetting of a liquid on a solid substrate, b) transition from half cylinder to sphere, depending on dimensions of the molten laser pool (Kruth, Froyen et al. 2004).	40
Figure 2.9 - Process windows for a) continuous wave and b) pulsed laser systems (Kruth, Froyen et al. 2004).....	41

Figure 2.10 - Micro-cracking in as processed austenitic steel. Note that crack '1' appears to have initiated at a pore. Both cracks have formed along grain boundaries also- adapted from Yu, Rombouts et al. (2013).....	43
Figure 2.11 - Top surface crack observed in SLM fabricated Waspaloy, again the crack is observed to lie along the grain boundary- direct from Mumtaz, Erasenthiran et al. (2008).....	43
Figure 2.12- Lines of force in a cracked body under load, taken from (Ashby, Shercliff et al. 2007)	44
Figure 2.13 - Solidification in conventional casting- direct from (Kurz and Fisher 1998)	49
Figure 2.14 - Microstructural formation in casting - direct from (Kurz and Fisher 1998).....	50
Figure 2.15 - Solid-liquid interface morphology and temperature distribution, s = solid phase, l = liquid, q = heat flux- direct from (Kurz and Fisher 1998)	50
Figure 2.16- Dendrite root and tip for columnar growth at same point in solidification but separated by distance $\gg \lambda_1$. Note how λ_2 evolves, beginning small at the tip and eventually growing to the point of dissolution of the tertiary arms at the root- direct from (Kurz and Fisher 1998)	52
Figure 2.17 - Crystal morphologies of Al-2Cu alloy with increasing V along the top of the image - from left to right: Plane front, cellular, cellular-dendritic, dendritic, dendritic with secondary arms, fine cellular and plane front. V_c is the limit of constitutional- direct from (Kurz and Fisher 1998)	53
Figure 2.18 - Dendritic structure of DS MarM246. White regions are dendrite crystals with black interdendritic regions visible due to differences in chemical concentrations being highlighted by chemical etching- direct from (McLean 1983)	54
Figure 2.19 - Predicted arsenic ($k_e = 0.3$) segregation in silicon with Aziz's continuous growth model (b) and stepwise growth model (a), and Baker model (Baker and Gahn 1969)(c). (d) is data from Baeri, Foti et al. (1981). Here $u = V$. Direct from (Aziz 1982).	58
Figure 2.20 - Melt pool formation for laser surface processing at high beam velocities. Where V_s (max) $\equiv V_b$. - adapted from (Gremaud, Carrard et al. 1990)	61
Figure 2.21 - Interface response function for microstructure forms, plane front T_p , cellular-dendritic T_D with undercooling-velocity T_U . Microstructures are denoted as plane front P, cellular C, dendrite D and banded B - Adapted from (Kurz and Trivedi 1994).....	63
Figure 2.22 - Microstructure selection map in G-V coordinates. Columnar dendrites are indicated by D_s , banded structure B and planar structure P- adapted from (Kurz and Trivedi 1994).	64
Figure 2.23 - Micrographs from several studies of SLM processing of different alloys and processing parameters. a) IN625 processed on an EOS M270 SLM system with a power of 200 W and scan velocity of 1000 mm/s (Amato 2012), b) Nimonic 263 processed on a Trumpf SLM machine with laser power of 200W and scan velocity of 100 mm/s (Vilaro, Colin et al. 2012), c) Ti-6Al-4V processed on a customised laser machine with a power of 42 W and scan velocity of 200 mm/s (Thijs, Verhaeghe et al. 2010), d) Ti-6Al-7Nb on a SLM Realiser II (MCP-HEK) machine with power of 100W and scan velocity of 150 mm/s (Chlebus, Kuźnicka et al. 2011). 65	
Figure 2.24 - Inverse pole figure EBSD maps direct from a) Bauer, Dawson et al. (2013) and b) Divya, Muñoz-Moreno et al. (2016)	66
Figure 2.25 - Inverse pole figure EBSD maps for energy densities of a) 116 J/mm ³ and b)66 J/mm ³ - direct from Bauer, Dawson et al. (2013)	67
Figure 2.26 - Crystal structures of the transition metals and their position on the periodic table - taken from (Reed 2006)	70

Figure 2.27 - Diagram detailing the stages of investment casting– direct from (Donachie and Donachie 2002)	71
Figure 2.28 - Three common forms of wrought working – adapted from (Donachie and Donachie 2002)	73
Figure 2.29 - Process steps for forging vs HIP and Direct Hip– direct from (Donachie and Donachie 2002)	76
Figure 2.30 - Schematic of edge and screw dislocations– adapted from (Tilley 2013).....	81
Figure 2.31 - a) representation of substitutional solute atom (green) in lattice, b) propagation of edge dislocation through lattice being prevented by solute atom. Stress fields (purple rings) of substitutional atom and dislocation repel each other, inhibiting further propagation– adapted from (Gedeon 2010).....	82
Figure 2.32 - a) Representation of interstitial solute atom (red) in lattice, b) as with Figure 2.31- adapted from (Gedeon 2010).....	83
Figure 2.33 – $M_{23}C_6$ carbides precipitated along the grain boundary of an experimental superalloy during creep testing at 950°C and 290 MPa – direct from (Reed 2006)	86
Figure 2.34 - Solidification cracking in a) Alloy 625 and b) Alloy 230W. Light area highlighted by arrows in a) is Nb rich eutectic which has healed the crack. In Alloy 230W the liquid film has a lower volume fraction and the cracks remain– adapted from (Böllinghaus, Herold et al. 2008).88	
Figure 2.35 - Pictorial description of PIC cracking. A) partially coherent sub-micron sized $(Cr,Fe)_{23}C_6$ form on grain boundary in reheated weld metal creating significant mismatch. B) precipitation creates stresses between carbides, promoting crack nucleation. C) macroscopic thermal and solidification stresses link the intercarbide cracks resulting in DDC along the grain boundary (Young, Capobianco et al. 2008).....	91
Figure 2.36 - XRD spectra peaks for pre-alloyed Inconel 718 powder compared to as processed SLM processed Inconel 718 (left). Supporting TEM image apparently showing nano precipitates of Ni ₃ Nb in as processed SLM processed Inconel 718 (right) – adapted from (Amato, Gaytan et al. 2012).....	99
Figure 2.37 - Proposed TiC carbides highlighted by arrows, in Nimonic 263 processed by SLM – adapted from (Vilaro, Colin et al. 2012).....	100
Figure 2.38 - SEM micrographs of as processed IN738. Crack is approximately 80µm in length, and contrary to original author of investigation, look to be as a result of solid state rupturing – adapted from (Rickenbacher 2013).	103
Figure 2.39 - (a) SLM as processed microstructure, (b) SLM + HIP'd microstructure. Note different magnifications. Adapted from (Amato 2012).....	106
Figure 2.40 – Grain structure created by island scanning strategy – direct from (Carter, Martin et al. 2014).....	110
Figure 2.41 - Micrographs from Tomus, Jarvis et al. (2013) apparently showing a reduction in cracking for b) 'low' Si + Mn over a) 'high' Si + Mn content.....	112
Figure 3.1 - Representation of how point distance, exposure time and hatch spacing apply to scanning and melt pool geometry.	122
Figure 3.2 – Gaussian and Doughnut profiles – direct from (Swartz 2016)	124
Figure 3.3 - Effect of changing focus offset on position of laser focal point and incident spot size on substrate	125
Figure 3.4 – Laser power: 200 W, with focus offsets of a) 0.0 mm, b) 2.0 mm, c)4.0 mm and d)6.0 mm. White circle is the guide area, inner green circle represents beam diameter at 13.5% of peak intensity, yellow circle represents limit of differentiable beam (from background).....	126
Figure 3.5 – Focus offset vs beam diameter and peak intensity for a laser powder of 200W.....	127

Figure 3.6 - Schematic showing geometry of cross section of melt tracks with controllable parameters LT and HS highlighted in bold. Hatched area represents potential unmelted or consolidated region.	129
Figure 3.7 - Representation of how OM micrograph is turned into a binary image	133
Figure 3.8 - Schematic demonstrating geometry of sections and micrograph positions	134
Figure 3.9 - Particle size distribution of LPW Hastelloy X powder, as volume density.....	136
Figure 3.10 - SEM micrograph of Hastelloy X powder in Secondary Electron (SE) imaging mode. Note that this is sample was taken from powder which had been through a processing run, and although sieved, some remelted particles have remained.....	137
Figure 3.11 - Particle size distribution of LPW Hastelloy X powder as number frequency.	138
Figure 3.12 - Contour plot of CCD model, contours are porosity as labels, red dots are the 9 parameter pairs. Note that maximum mathematical porosity is 100%, but model generated unrealistic contours >100 as no limit was input.	140
Figure 3.13 - Plot of apparent velocity against porosity for fixed parameters of LP: 195W, LT: 53µm, HS: 0.09 mm and FO: 0 mm. Marked on the plot is porosities of <1%, in green, and regions of high porosity (>5%) in red with blue representing porosities between 1% and 5%.	141
Figure 3.14 - The three distinct types of porosity identified in the first experimental trial: a) Large empty pores indicative of vapourisation, b) medium to large size spherical pores indicative of insufficient overlap and c) severe lack of fusion porosity as indicated by whole powder particles.....	142
Figure 3.15 - Schematic presenting parameters chosen for screening trial. Four processing parameters were varied using minimum and maximum values. ET and PD values combined to give four values for apparent velocity.	143
Figure 3.16 - Plot of porosity against apparent velocity, for the four sets of samples.....	144
Figure 3.17 - Porosity with varying hatch spacing and focus offset.....	144
Figure 3.18 - Relationship between beam diameter and weld track width and beam expander setting for EOS M280 with fixed power and laser scan speed of 195 W and 800 mm/s respectively. Beam expander is a non-continuous parameter with a maximum value of 10. Direct from (Deffley 2012).....	145
Figure 3.19 - Cross section of weld tracks with decreasing power from left to right for Inconel 718. Note the depth of the tracks remains the same as the Marangoni convection carries heat to the top edges. Adapted from (Deffley 2012).....	146
Figure 3.20- Plot of crack density against apparent velocity, for the four sets of samples. Both samples built at LT 53 µm and 714 mm/s crack free but very porous.....	148
Figure 3.21- a) FO 4, LT 20, Ap. Vel 477, one of the lowest porosities achieved yet there is extensive cracking through the centre of this sample with 36 ± 3.6 cracks per mm ² . b) FO 0, LT 20, Ap. Vel 477, the same processing conditions as a) except the FO, note the absence of large spherical pores in a) compared with b). c) FO 4, LT 20, Ap Vel 714, low crack density but significant levels of lack of fusion porosity. d) FO 4, LT 53, Ap. Vel 596, extensive large lack of fusion pores resulting from insufficient energy penetration.....	149
Figure 3.22 -Crack density with focus offset and hatch spacing.....	150
Figure 3.23 - Ap. Vel vs Laser Power for low porosity samples.....	151
Figure 3.24 - Crack density vs Apparent velocity for laser powers of 150-195 W.....	151
Figure 3.25 - Porosity (grey) and crack density (black) with 1D energy density in sets of laser power.....	153
Figure 4.1 - Temperature for a given depth with time.....	159

Figure 4.2 - Thermal gradient with melt depth.....	160
Figure 4.3 - Cooling rate with melt depth.....	160
Figure 4.4 - Solidification rate with melt depth.....	161
Figure 4.5 - Solidification rate at base of melt pool.....	161
Figure 4.6 - Reproduction of Figure 2.21 for easy reference.....	163
Figure 4.7 - Grain growth for melt pool in first layer (left) and then epitaxial growth in subsequent layer.....	164
Figure 4.8 - Optical micrograph of etched vertical section of Hastelloy X fabricated with LP of 195W, PD of 53 μm and ET of 115 μs . Sample has a crack density of 34 ± 3.5 cracks per mm^2 . Note the absence of visible boundaries between grains, this is as a result of no segregation of solute to the edges of the grain and thus etching only reveals dendritic structure.....	169
Figure 4.9 - a) Vertical section shows dark interdendritic regions between light coloured dendrites, with micro-crack running between grains regions of different orientated dendrites (grains). b) Horizontal section, orientations which vary from perpendicular to incident line of sight are highlighted by polarisation and appear lighter in colour and deviate from the circular cross section of the cell-dendrites.....	169
Figure 4.10 - SE mode SEM micrographs. Primary grain boundaries are visible running up the centre of the melt trace, a second less visible boundary is magnified in the secondary image. Note that the visible apexes on the crystals are not a physical feature and are in fact a result of the crystal orientation intersecting the observational plane.....	171
Figure 4.11 - High magnification SE mode SEM micrograph showing dendrite wall features which may be interpreted as secondary arm nubs - magnified in white circle. Light edging implies minor solute diffusion to interdendritic region.....	172
Figure 4.12 - Two EDS line scans of a crack at medium (left) and high (right) magnification....	174
Figure 4.13 - Ultra high magnification SE mode SEM micrograph showing potential secondary phases. Globular particles are of the order of 50-100 nm in size.....	176
Figure 4.14 - High magnification SE mode SEM micrograph showing dendrite edge features..	177
Figure 4.15 - Electron back scatter SEM micrograph showing cell-dendrite primary trunks with precipitates (brighter contrast) in interdendritic regions.....	177
Figure 4.16 - Electron back scattered micrograph of cross sectioned microstructure - indicating positions of EDS point scans (red crosses).....	179
Figure 4.17 - EDS point spectra for precipitate and dendrite in cross section.....	179
Figure 4.18 - Back scattered micrograph of vertical sectioned microstructure - indicating positions of EDS point scans (red crosses) and base of melt pool trace.....	180
Figure 4.19 - EDS point spectra for precipitate and dendrite in vertical section.....	180
Figure 5.1 - Crack observed with SEM for a range of process parameters, axis in (c) applies to all images. a) is from the initial density trial, a large crack is observed with significant solid state fracturing clear in the centre. b) an etched sample from the LP vs Ap Vel trial, majority of microcracks follow this appearance, still appears to be fracture driven rather than separation - likewise with (c). d) less jagged in appearance, although feature central to length of the crack is fracture-like.....	185
Figure 5.2 - Higher magnification micrograph of sample in Figure 4.#. Cracks lie exclusively along grain boundaries and are all of a similar morphology. None are observed to propagate along melt traces.....	186
Figure 5.3 - High magnification SEM mode SEM micrographs of microcracks. Fabric of the dendrites is observed to have been disturbed and ruptured, rather than merely separating....	186

Figure 6.1 - Crack densities of OHX (filled) and MHX (unfilled) measured in vertical (V) build orientation, bottom plot, and horizontal (H) build orientation, top plot.	200
Figure 6.2 – OHX vs MHX. Horizontal sections of OHX and MHX for two sets of processing parameters, demonstrating the reduce micro-cracking in MHX.	201
Figure 6.3- Tensile properties comparison for OHX and MHX: RT = Room Temperature, HT = High temperature (1033 K).....	202
Figure 6.4 – Fracture surface of high temperature tensile bar for OHX, carbides are highlighted by white circles and arrows. Taken in SE mode.	205
Figure 6.5 - Fracture surface of high temperature tensile bar for MHX white circles highlight precipitated carbides. Both alloys display small carbides which have formed as a consequence of the elevated temperature plastic deformation. Taken in SE mode.....	206
Figure 6.6 - Thermal expansion data for OHX (solid grey line) and MHX (dashed line) plotted as a function of temperature.	207
Figure 6.7 - Crack densities of OHX with 1D energy density, separated into series of laser power.	209
Figure 6.8 - Crack densities of MHX with 1D energy density, separated into series of laser power.	210
Figure 6.9 - Averaged crack density with density for samples with laser power.....	213
Figure 6.10 - Averaged crack density with density for samples with 1D line energy density.....	213
Figure 6.11- Averaged crack density and density with sample volume.....	214
Figure 6.12 - Comparison between crack sizes in 5x5x5mm and 10x10x10mm samples of LP 200W, ED 0.4 J/mm.	215
Figure 6.13 - Crack susceptibility with laser power for samples sizes 2.5-10 mm cubes.....	215
Figure 6.14 - Averaged crack density and density values for set exposure times.....	216
Figure 6.15 - Crack density with sample size and laser power.....	217
Figure 7.1 - Flowchart representing thought process for determining composition dependent thermal stress.....	223
Figure 7.2 - Flowchart representing process steps and inputs for determining composition dependent thermal stress.....	226
Figure 7.3 - 2D temperature field over time. Spot number indicated in top left corner of each image.....	238
Figure 7.4 - Continuation from Figure 7.3.....	238
Figure 7.5 - Continuation from Figure 7.4.....	239
Figure 7.6 - Representation of exposure points (spots), which time after each traverse hatch.....	240
Figure 7.7 - Temperature over time for 18 nodes in layer 1.....	240
Figure 7.8 - Node 7 for layer 1.....	242
Figure 7.9 - Temperature over time for 18 nodes in layer 2.....	243
Figure 7.10 - Temperature over time for 18 nodes in layer 3.....	243
Figure 8.1 - Crack susceptibility scale, numerical value of χ scales inversely with crack susceptibility.	249
Figure 8.2 - Crack density with 1D line energy density for Inconel 713 LC.....	252
Figure 8.3 Optical micrograph of as processed Inconel 713 vertical (left) and cross (right) section.....	253
Figure 8.4 – SE mode SEM micrograph of fracture surface of Inconel 713LC as processed tensile specimen tested at room temperature. Micro-cracks are labelled and/or highlighted by white rings.	254

Figure 8.5 – SE mode SEM micrograph of fracture surface of Inconel 713LC as processed tensile specimen tested at 760°C. As expected the fracture surfaces support a brittle fracture, but there is also evidence of pitting implying some amount of deformation had occurred before failure.255

Figure 8.6 - Schematic of melt spinner259

Figure 8.7 – SE mode SEM micrographs of alloys after ball milling. a) Low SS alloy and b) High SS alloy263

Figure 8.8 - Diagram of modified substrate for novel alloy fabrication.....265

Figure 8.9 - Full cross sections of SLM processed ball milled powders and MHX powder267

Figure 8.10 - Comparison of micro-cracking between high and low SSS.....268

Figure 8.11 - Crack susceptibility of alloys based on SLM as processed properties.....271

Figure 8.12 - Crack susceptibility of alloys based on conventionally processed properties272

Figure 8.13 - Crack susceptibility of alloys based on SLM as processed properties at elevated temperatures.....275

Figure 8.14 – Transformation diagram for γ' and γ'' phases in Inconel 718 – direct from (Davis 1997)278

Figure 8.15 - Basic design model flow chart281

Figure 9.1 - Liquid fraction simulation of Inconel 738LC – modified from (Cloots, Uggowitzner et al. 2016). Red dotted line indicates solids temperature simulated by Thermo-Calc 2015.285

Figure 9.2 - Mass fraction of liquid with temperature for Inconel 738LC as simulated by Thermo-Calc 2015 using Schiel solidification model.286

Figure 9.3 - Composition of liquid phase with temperature of Inconel 738LC as simulated by Thermo-Calc 2015 using Schiel solidification model.287

Figure 9.4 - Mass percent of Zr in liquid phase of Inconel 738LC as simulated by Thermo-Calc 2015 using Schiel solidification model.....288

List of Abbreviations

AM	- Additive Manufacturing
SLM	- Selective Laser Melting
CAD	- Computer Aided Design
DMLS	- Direct Metal Laser Sintering
SLS	- Selective Laser Sintering
DLD	- Direct Laser Deposition
DLMD	- Direct Laser Metal Deposition
EBM	- Electron Beam Melting
TGM	-Thermal Gradient Mechanism

UTS - Ultimate Tensile Strength
XRD - X-Ray Diffraction
EDM - Electrical Discharge Machining
DS - Directional Solidification
RS - Rapid Solidification
RSP - Rapid Solidification Processing
SSS - Solid Solution Strengthening
SSSS - Substitutional Solid Solution Strengthening
ISSS - Interstitial Solid Solution Strengthening
HIP - Hot Isostatic Press
FCC - Face Centre Cubic, written as fcc
BCC - Body Centre Cubic, written as bcc
HCP - Hexagonal Close Packed, written as hcp
PMG - Platinum Metal Group
P/M - Powder Metallurgy
SCTR - Solidification Cracking Temperature Range
HAZ - Heat Affected Zone
PMZ - Partially Melted Zone
DDC - Ductility Dip Cracking
MGB - Migrated Grain Boundaries
PIC - Precipitation Induced Cracking
ETSS - Elevated Temperature Solid State (cracking)
EDS - Energy Dispersive Spectroscopy
PPM - Parts per million
PD - Point Distance
ET - Exposure time
LT - Layer Thickness
FO - Focus Offset

HS - Hatch Spacing
LP - Laser Power
DOE - Design of Experiments
TEM - Traverse Electromagnetic Mode
BD - Beam Diameter
OM - Optical Microscope/microscopy
SEM - Scanning Electron Microscope/microscopy
LSD - Laser Size Diffraction
SE - Secondary Electron (imaging mode)
Ap Vel. - Apparent Velocity
CCD - Central Composite Design
TEM - Transmission Electron Microscope/microscopy
TSR - Thermal Shock Resistance
OHX - Original unmodified Hastelloy X
MHX - Modified Hastelloy X
FEM - Finite Element Model
CFD - Computational Fluid Dynamics
LC - Low Carbon
ICP-OES- Inductively Coupled Plasma Optical Emission Spectroscopy
APT - Atomic Probe Topography

Nomenclature

E - Young's modulus or elastic modulus
 θ_γ - angle of intersect between solid surface and liquid surface
 σ_{SV} - surface energy (surface)
 σ_{SL} - surface energy (liquid)
 σ_{LV} - surface energy (vapour)

K_I	- stress intensity factor
K_{Ic}	- fracture toughness
c_l	- crack length
σ^*	- stress at propagation
σ_y	- yield strength
c_{crit}	- minimum crack length for crack propagation
q_e	- internal heat flux
H	- enthalpy
T	- temperature
c	- specific heat per unit volume
H_f	- latent heat of fusion
h_f	- latent heat of fusion per unit volume
t	- time
\dot{T}	- cooling rate
f_s	- volume fraction
A'	- surface area
v	- volume
G	- temperature gradient (dT/dr)
V	- growth rate of solid, or solidification rate – also V_s
λ_1	- primary dendrite arm spacing
λ_2	- secondary dendrite arm spacing
D	- solute diffusion co-efficient
D_s	- solute diffusion coefficient in solid
D_l	- solute diffusion coefficient in liquid
D_i	- solute diffusion coefficient in solid-liquid interface
λ	- eutectic spacing
R	- dendrite tip radius
J	- steady state flux

$J(z)$ - solute diffusivity flux
 $C(z)$ - net solute concentration
 ν_s - attempt frequency
 $\Delta\mu_B^{0*}$ - molar free energy of activation
 γ_s - activity coefficient
 f - fraction of sites in solid s, liquid l
 γ_s - activity coefficient of the solute in solid s, liquid l
 β - dimensionless velocity
 $k(V)$ - partition coefficient
 k_e - partition coefficient at equilibrium
 δ - interface thickness
 V_{crit} - solute trapping transition velocity
 V_b - beam velocity
 τ - stress required to move dislocation
 σ_{th} - thermal stress
 α_{CTE} - mean coefficient of thermal expansion
 m - mass of material
 L_f - Latent heat of fusion
 E_m - energy to melt mass of material
 P - laser power
 t_{exp} - exposure time
 x_{PD} - point distance
 Q - energy
 L - line length
 $erfc$ - complimentary error function
 κ - thermal conductivity
 q_0 - absorbed power density
 T_0 - initial temperature

x	- depth beneath surface
α	- diffusivity = $k / (\rho \times C_p)$
γ	- $t - \tau$
τ	- heat time (duration of laser power)
T_m	- melting temperature/point
V_{comp}	- velocity for complete solute trapping
V_{onset}	- velocity for onset of solute trapping
T_{diff}	- diffusion temperature
$\delta_{precipitate}$	- steady state diffusion distance for precipitation
σ_{UTS}	- ultimate tensile strength
ν	- Poisson ratio
σ_{YS}	- yield strength
σ_0	- lattice stress
k_d	- locking parameter
d	- average grain size
σ_{ss}	- solid solution contribution
σ_P	- Peierls stress
k_i	- strengthening parameter for solute i
c_i	- concentration of solute i
Z	- atomic mass
T_{amb}	- ambient temperature
T_{vap}	- evaporation temperature
t_{idle}	- time between exposure points
ρ	- density
T_{freeze}	- freezing temperature
σ_{app-th}	- apparent thermal stress

1 Introduction

1.1 Problem statement

Additive Manufacturing (AM) is a method of manufacturing by means of successive layering of processed material to achieve a 3-dimensional part. The extended design freedom and low material waste it allows has resulted it in being one of the fastest growing industries in the world.

Although polymer based systems lead the consumer market, metal based technologies are the focus of engineering and functional industries such as aerospace, automotive and medical.

A key target for the aerospace industry is the processing of high temperature performance alloys, for use in next generation turbine engines. These difficult to work with alloys are costly to process and design freedom is limited by conventional techniques.

AM, specifically laser powder bed fusion techniques such as Selective Laser Melting (SLM), offer a new avenue of development and the potential step change required for the aerospace industry's next generation technology.

The alloys of focus for this investigation are nickel-base superalloys. These are the obvious choice for aerospace users, as they operate in the hottest part of the engine and must also withstand tens of thousands of hours of operation without failure.

Despite many of the alloys being easily 'weldable', recent investigations have revealed that many of the nickel-base superalloys suffer from micro-cracking during processing.

Seemingly process optimisation is not sufficient to eliminate the problem, and a fundamental design approach is required to optimise these alloys for the SLM process.

1.2 Aims and Objectives of Research

- To develop an understanding of the SLM process, specifically relating to the influence of process parameters on material response and resultant microstructures and behaviour of as processed material
- To investigate and understand the root cause of micro-cracking in nickel superalloys when processed by SLM
- To develop a method for identifying if an alloy will be susceptible to micro-cracking based on composition and fundamental material properties

1.3 Thesis structure

Chapter 2 will feature an extensive literature review of the following:

- Nickel superalloys – history, applications, metallurgy
- Fundamentals of solidification
- Selective laser melting – process, current literature, characteristics of the process
- Nickel superalloys processed by SLM
- Cracking mechanisms in nickel superalloys processed by conventional techniques

In Chapter 3 the experimental methodology for the project and preliminary investigations will be discussed. Although much of the specific methodology will be discussed in the relevant chapters, the operation of the SLM system, methods for sample

analysis and equipment details are discussed here. The preliminary investigations focus on verification of micro-cracking as a problem in a known crack-susceptible nickel superalloy, Hastelloy® X, as well as establishment of relationships between density and cracking and process parameters.

Chapter 4 discusses the establishment of SLM as rapid solidification process, and the implications this has on the microstructure, material properties and therefore material response of nickel superalloys. As well as discussing the unique microstructure of SLM, and how it evolves during processing. This understanding is key to the further development of a hypothesis for root cause of micro-cracking in SLM processed nickel superalloys.

Chapter 5 uses conclusions of Chapter 4 to discuss a hypothesis for the root cause of micro-cracking in SLM processed nickel superalloys. It also establishes *crack susceptibility* as a material property, referring to the likelihood an alloy will experience process induced micro-cracking with SLM. It is defined as the balance between the tensile strength of the material and thermal stress imposed on the material by the process.

Chapter 6 develops the crack susceptibility theory further, focussing on a method for modelling/predicting the strengthening contribution of the alloying elements. The theory is then tested by means of a direct comparison between the Hastelloy® X from Chapter 3 and a modified version with increased material strength. The two alloy powders are processed with SLM, and the processed material is subjected to microstructural and material property analysis, specifically looking at crack density and tensile performance.

Chapter 7 develops the process induced stress contribution for crack susceptibility. Specifically looking at a method for simulating a stress component from composition and

fundamental material properties alone. Various methods are discussed and tested for suitability, before one is ultimately chosen.

In Chapter 8, the complete solution for prediction of crack susceptibility is validated. This includes the design and manufacture of novel alloy powder as well as processing of additional alloys. Finally, data from published investigations on processing nickel superalloys by SLM is used to complete validation by means of comparison of crack susceptibility prediction and reported/observed behaviour. Also discussed are publications which may have impact on the work in this investigation, which have been published after, or close to the end of completion.

Chapter 9 summarises the work conducted throughout the investigation as well containing conclusions and final remarks.

2 Background and Literature review

2.1 Selective Laser Melting: An Additive Manufacturing technique

2.1.1 The process

Selective laser melting (SLM) is one of a number of processes which come under the umbrella of Additive Manufacturing (AM). A process is defined as being additive if it uses layering or epitaxial growth to construct a three dimensional object. The most common types of material processed are plastics (polymers) and metals (or metallic), followed by organic material and ceramics (Gibson, Rosen et al. 2010); SLM is a metallic process.

SLM (and other AM technologies) has seen a sharp increase in interest in both research and commercial industry in recent years, and is looking set to be a part of future manufacturing (Gibson, Rosen et al. 2010). This is largely down to the following reasons: building a part by layering allows for geometries that are simply not possible with conventional techniques, such as internal lattice structures or complex cooling channels. The precision of the processes allows for fine details which are either impossible or extremely difficult/wasteful/expensive to achieve with casting or machining. Components with moving parts can be fabricated in a single build, although this is more difficult to achieve in the metallic processes. Finally, any material (powder) which is not fused can be recycled thus providing huge feedstock waste reductions compared to machining.

Due to branding and commercial competition a number of different names exist for the SLM process; Renishaw, Realizer and SLM Solutions all use SLM, Concept Laser call it LaserCUSING® and EOS use Direct Metal Laser Sintering (DMLS). It may also be referred

to in literature as selective laser sintering (SLS) and direct laser (metal) deposition (DLD or DLMD), although strictly these are separate processes.

In SLM, metallic powder is selectively melted and fused by a high powered laser. Cross sections of a part are fused in layers, which are built up successively to create the complete 3D object – see Figure 2.1. It is this fabrication of solid parts through consecutive layers which classes it as an AM process.

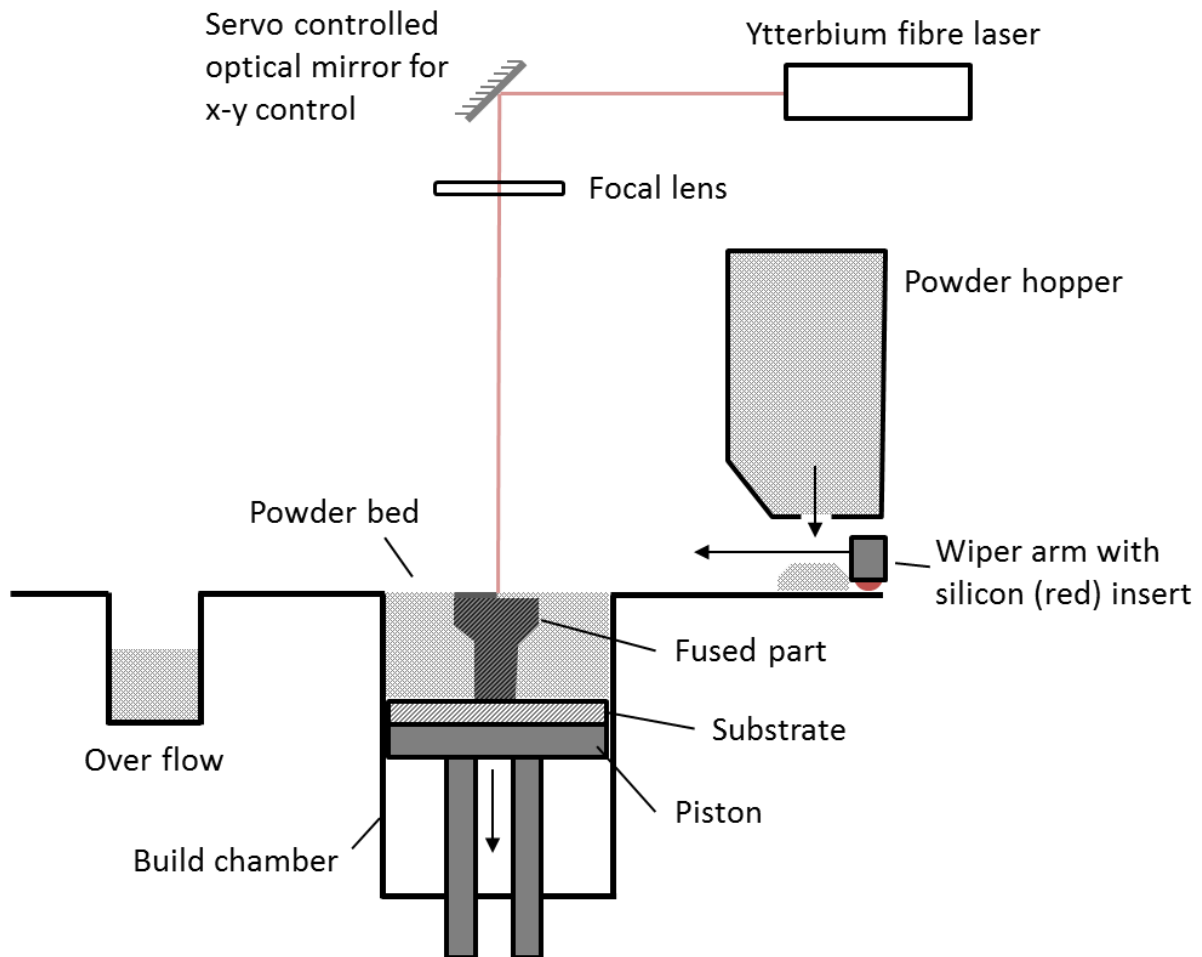


Figure 2.1 - Schematic of the SLM build process for Renishaw SLM 125

A similar process to SLM is Electron Beam Melting (EBM), in which the same process is used but, as the name suggests, it uses an electron beam rather than a laser.

Of SLM and EBM, neither is greatly superior to the other and both have advantages over the other for various applications. SLM can build components to a higher degree of precision than EBM, the advantage of which is twofold: finer geometries (resolution of $\approx 200\mu\text{m}$ (Vilaro, Colin et al. 2012)) and better surface finish. Surface finish is of desirability if one wishes to keep the component as 'one process', having to extensively machine the part after build would diminish the process' advantage.

EBM is preferable for rapid building as it has both a larger spot size and a higher limiting power, but as a consequence is not able to deliver the same level of precision. Both are able to produce fully dense parts (Wang, Hong et al. 2009, Parthasarathy, Starly et al. 2010, Wang 2011, Wang, Wu et al. 2011, Wang, Guan et al. 2012).

2.1.2 Applications

SLM is a developing technology, therefore the number of applications it is compatible with is ever increasing as the limiting factors are overcome. However, like any technology, there are certain applications which it is more suited to.

Due to the large start-up costs (machines typically cost in excess of £250,000), running costs of the machines and relatively low production volume, the technology is more suited to high value markets such as dentistry, medical, jewellery and aerospace.

AM is perfect for customisable components, as no moulds or separate tooling have to be created and subtle differences in shape and size can be easily processed in CAD software. It therefore lends itself well to the production of patient-specific implants for the dental and medical industries, of which there have been a number of reported successes; Vandenbroucke and Kruth (2007) being one example. A specific example of one such application already being implemented is joint replacements. The artificial socket is

constructed with the intention of creating an interface which encourages bone and tissue to grow into/assimilate the socket and thus reduce chances of infection or foreign body rejection. This is achieved by building a fine complex mesh structure as the outer layers, with the socket itself being machined and polished (Parthasarathy, Starly et al. 2010). The meshwork is of too finer detail to be created using a cast, and would be highly time consuming and wasteful if one were to try and machine it.

A large sector which is investing heavily in AM technology is the aerospace industry. The aerospace industry demands the highest level of component integrity and performance. All new materials and processes are subject to extensive testing and standardisation before they can be approved for production use. High performance alloys, such as titanium alloys and nickel/cobalt superalloys, are the material of choice for many of the components, especially those operating at elevated temperatures (Reed 2006). Unfortunately, the high performance properties of these alloys make them difficult to form using conventional techniques. Building aerospace components with SLM offers huge potential cost reductions for the industry, if the technology can be optimised; and there has already been some success in the industry. The Rolls Royce Trent XWB-97 engine boasts the world's largest additive manufactured aero-engine component assembly; a ring of compression vanes with a 1.5 m diameter, which had been manufactured out of Ti6Al4V on an Arcam EBM machine (Howie 2014).

However, there has been less success with the higher temperature performance nickel base superalloys – see Section 2.8. These alloys are primarily used in the hottest part of the jet turbine engines and are often exposed to temperatures well in excess of 540 °C whilst under heavy loading (Donachie and Donachie 2002). Material responses combined with SLM process characteristics have led to difficulties achieving the level of part

integrity required for aerospace components. Problem characteristics of the SLM process will be discussed in the following section - Nickel base superalloys will be discussed in further detail in Sections 2.5 and 2.6.

2.2 Problem characteristics in SLM

As with any processing technique, SLM has a number of process characteristics which can cause problems with material processing if not understood and/or controlled. The nature, impact and controllability of these characteristics will now be discussed.

2.2.1 High thermal and residual stresses

Residual stress can be simply defined as internal stresses which exist within a part without any applied force or constraint. They are strongly associated with processing, and it has been said that 'every production process will introduce some amount of residual stress' (P. J. Withers 2001). As their presence is deemed inevitable, it is therefore the management and manipulation of residual stress which has become the focus of many investigations. Purely, they are the stress which results from elastic strains caused by elastic misfits between regions. The nature of these misfits is varied, and can be anything from lattice dislocations to thermally-induced strains (Moat 2009).

If of sufficient magnitude, residual stress can lead to part deformation, micro-cracks and limitations on load resistance/tensile performance (Merzelis and Kruth 2006).

There are three types of residual stresses, which vary over increasingly smaller length scales. Type I stresses are continuous across grain boundaries and vary over length scales comparable to the size of a part, as such they are described as macro stresses. Type II

stresses vary over a length scale comparable to that of grain size, and are generated by misfit strains. Type III stresses are inhomogeneous across the grain and are caused by lattice defects such as dislocations and interstitial solutes (Moat 2009). Both Type II and III are micro stresses. Due to the length scales over which they vary, Type I stresses have the most influence on material strength. They are also generated by the thermal elastic strains associated with changes in material temperature – no more extreme than in fusion processes. As such, Type I stresses are the primary focus of investigations of thermal and residual stresses in AM processes.

Note: From this point we are only concerned with the mechanisms which create residual stress, namely the in situ thermal stresses. However, thermal stresses are difficult to measure in situ and it far easier to measure the resulting residual stress of a part once processed. Ultimately relationships between process parameters and residual stress infer the same for the thermal stresses from which the residual stress arose.

Mercelis and Kruth (Mercelis and Kruth 2006) described the residual stress found in SLM and SLS parts as arising from two mechanisms; thermal gradient mechanism (TGM) and the cool-down phase of molten top layers. TGM results from the steep thermal gradients generated by the laser interaction with the material. The rapid heating of the top surface, combined with the relatively slow heat conduction of the material creates a steep temperature gradient. When the top layer expands, it is restricted by the significantly cooler lower layer, inducing elastic compressive strain. However, at an increased temperature the yield strength of the top layer is reduced, allowing it to be plastically compressed. Cooling of the now plastically compressed top layer, causes it to shrink, inducing a bending angle towards the laser. This introduces a tensile stress in the build

direction. It is important to note that this mechanism occurs in the solid phase (does not require the material to be molten). Figure 2.2 demonstrates TGM for a laser incident on solid material.

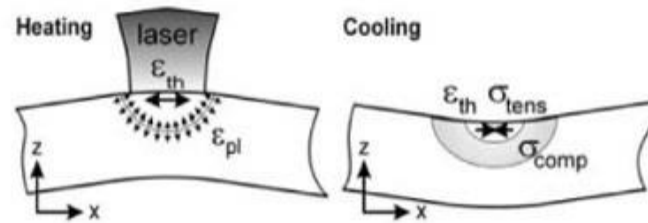


Figure 2.2 – Representation of TGM, with thermal strain ϵ_{th} , plastic strain ϵ_{pl} , tensile stress σ_{tens} and compressive stress σ_{comp} – direct from (Merzelis and Kruth 2006)

The cooling of the molten top layer induces stress in a similar way to TGM. When the material cools and solidifies it shrinks due to thermal contraction. This shrinkage is again restricted by the cooler underlying material, causing tensile stress in the top layer and compressive stress in the underlying layer.

There have been several studies both observing and aiming to understand residual stress build up the SLM process, through both modelling and experimental analysis.

Merzelis and Kruth performed an extensive study into residual stresses in SLS and SLM (Merzelis and Kruth 2006). The study aimed to model the thermal stresses induced by the process and then compared the predicted stress profiles with experimentally measured values. They used a simple model which assumed: room temperature build, beam theory is valid, no external forces to part-base plate combination, stress in x direction is independent of y co-ordinate, the upper layer induces stress as a result of shrinkage and that the tensile strength is equal to the material's yield strength.

The model uses a baseplate of height of 20mm, with a part built in 50 layers of thickness of 50 μm . The Young's modulus, E , of the baseplate and part are 210 GPa and 110 GPa respectively, and the yield strength of the material is 300 MPa. Figure 2.3 shows the result given the initial parameter values.

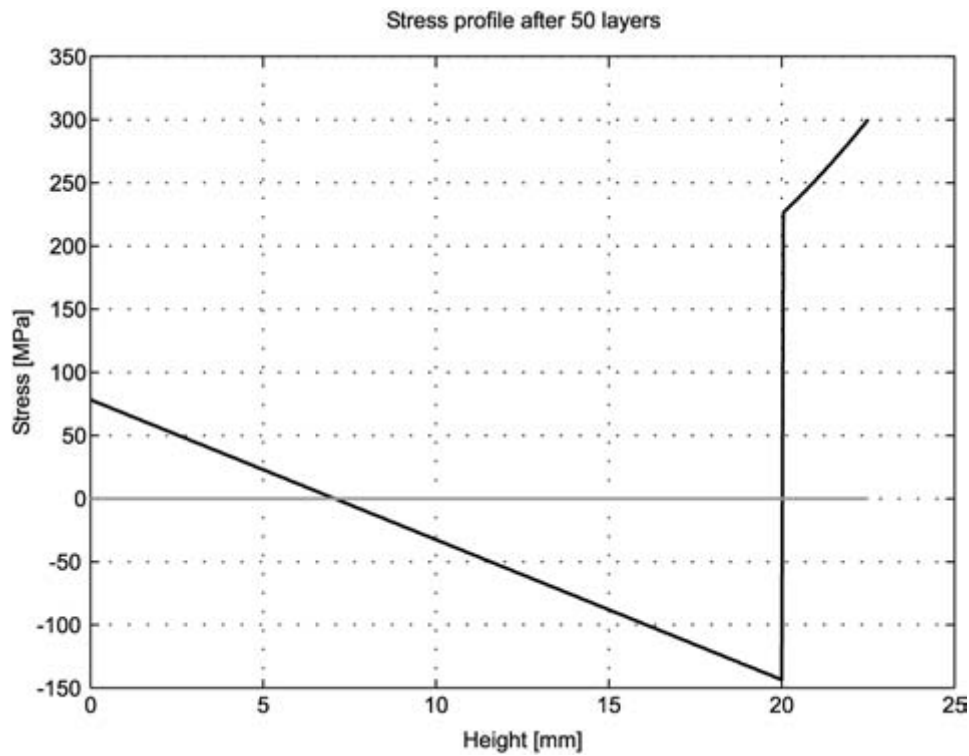


Figure 2.3 - Residual stress in the part and base plate, interface is at 20 mm height – direct from Mercelis and Kruth (2006).

The addition of a layer to the baseplate induced a compressive stress in the upper region and a tensile stress in the lower. The addition of further layers added to the stress profile of the base plate but also to the underlying layers, thereby reducing the tensile stress present from previous layering.

Figure 2.4 gives the stress profile after the part has been removed. Both the part and the baseplate undergo relaxation, in the case of the part this occurs through uniform shrinkage (constant part of the relaxation stress) and bending deformation (linear part

of the relaxation stress). After removal the part's stress profile consists of tensile stress on the upper and lower surfaces with compressive stress in the central zone.

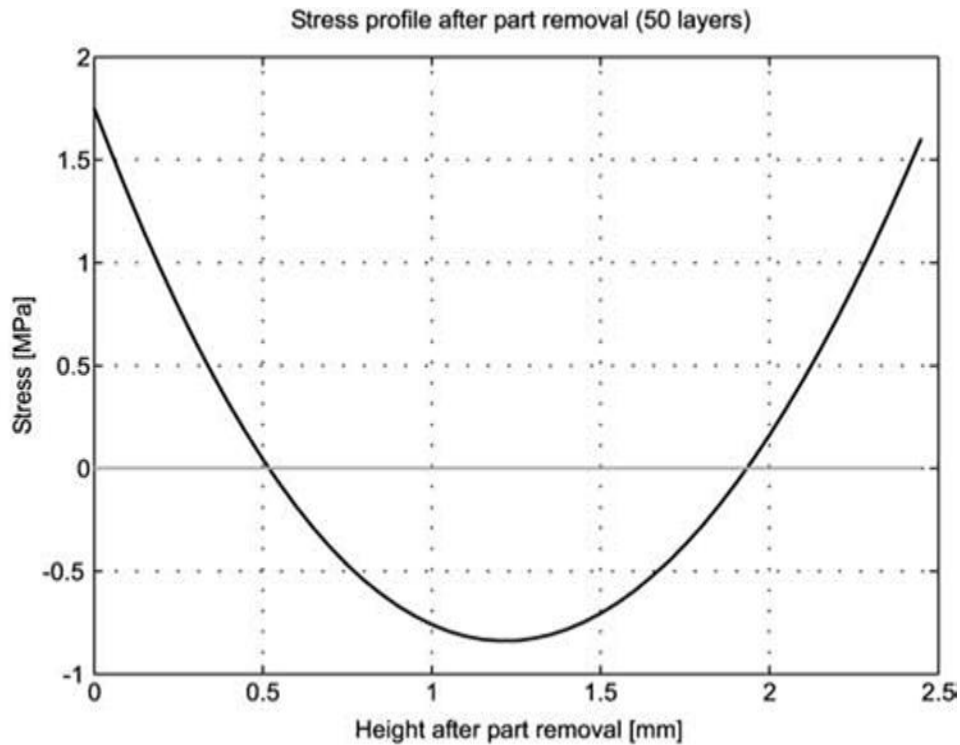


Figure 2.4- Modelled stress profile of part after removal from baseplate- direct from Mercelis and Kruth (2006).

The effects of number of layers, baseplate thickness and material yield strength on the stress profile were also modelled. An increase in layers results in a higher final residual stress, with a reduction in the x-axis shrinkage as the number of layers increases, see Figure 2.5. This is an important result as it confirms that larger parts, as a consequence of increased exposures, will build up greater residual stress.

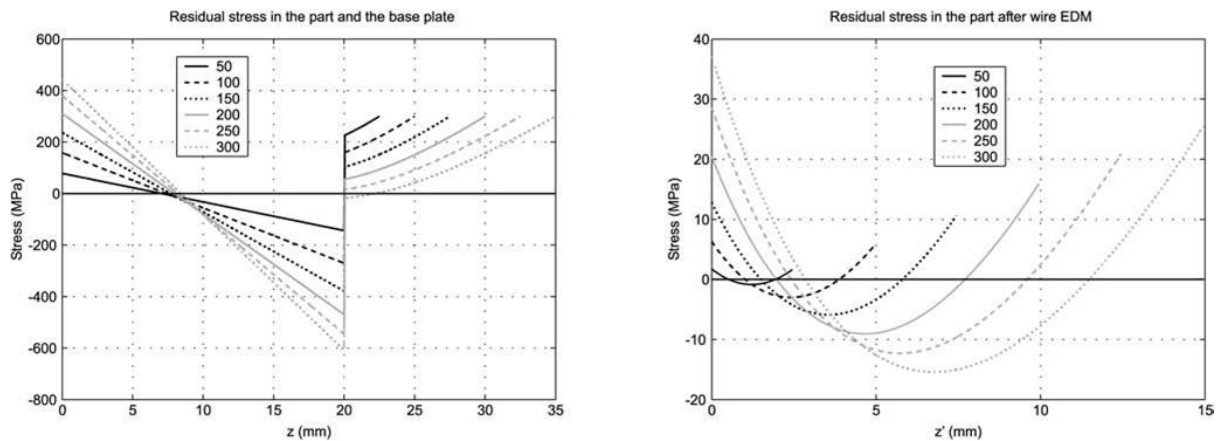


Figure 2.5 - Modelled progression of residual stress profiles of part attached to substrate (left) and removed (right) with increasing number of layers- direct from Mercelis and Kruth (2006)

As baseplate thickness increases the final residual stress decreases, and bending deformation of the part is also decreased with increasing plate thickness. Increasing the yield strength of the material increases the residual stresses – although not necessarily a surprising result, this is of particular importance when considering the high strength superalloys.

The model had good qualitative agreement with the XRD tests but a quantitative comparison was ‘not easy’. This was primarily because the model did not include the effects of TGM, only those of solidification shrinkage. It also did not account for the porosity that occurred in the XRD samples. Porosity reduces the stress values as the stress around each porosity boarder equals zero. Also worth mentioning is that the part is built straight onto the baseplate without the use of supports. This means in reality the part has to be removed by wire cutting or EDM, which itself can induce large tensile stresses. This method also requires additional work to recycle the base plates. The use of supports makes the part easier to remove and also helps with the fabrication of more complex geometries. When a part is built on supports, the stress profile will not be the same as that of the ‘as processed’ parts in the Mercelis and Kruth investigation. Although

the supports may have some effect, the part is more likely to have the stress profile of the 'removed and relaxed' parts.

Shiomi, Osakada et al. (2004) measured the distribution of residual stress within an as processed steel part fabricated by SLM. The material was a mixture of chrome molybdenum steel with copper phosphate and nickel powder - which potentially responds differently to fully prealloyed powder, but a similarity will be assumed for this example. A cuboid of dimensions 6×5×45 mm height×width×length respectively was built onto a substrate of 8×9×49 mm. Given a layer thickness of 100 μm, the built part consisted of 600 layers. Residual stress was measured as a maximum of 500 MPa tensile on the top surface down to 50-100 MPa of compressive stress 2 mm from the base plate, returning to tensile stress along the interface between the base plate and the part. The measured stress profile, see Figure 2.6, is in agreement with the stress profile predicted by the Mercelis and Kruth model (Mercelis and Kruth 2006), although the return to tensile stress before the interface is not consistent with that predicted for when the component is still attached to the base plate. Instead the measured profile is closer to the inverse quench predicted for a removed part, implying that in the experimental case there may not be perfect cohesion between the part and the base plate.

Shiomi and Osakada also investigated the relationship between the top layer (maximum) residual stress and laser scan speed, see Figure 2.6. Although a weak parabolic relationship for mean values is recorded, the large error variations lead to a conclusion that the maximum stress is not greatly affected by the scan speed.

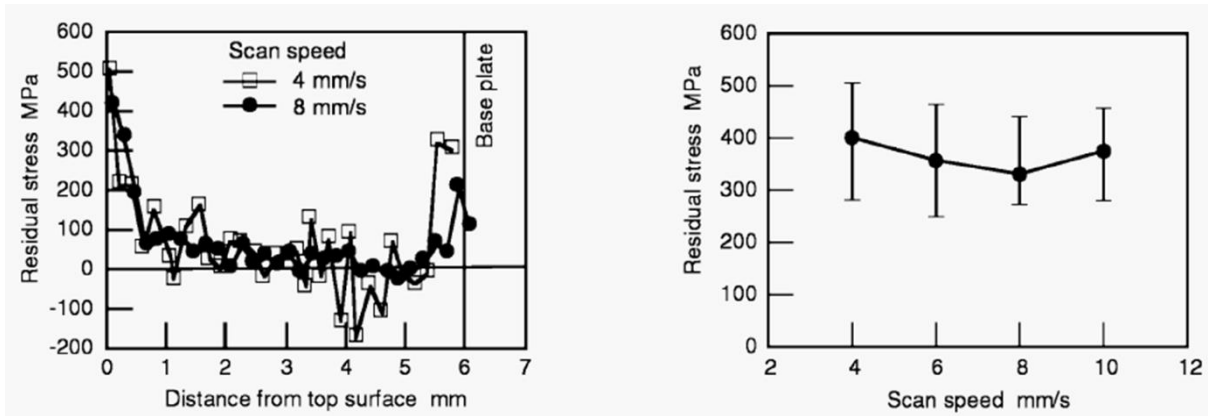


Figure 2.6 - Measured residual stress profile for as processed part attached to base plate in strong agreement with Mercelis and Kruth (2006) model (left), with conversely weak relationship between scan speed and maximum residual stress (right)- directly from Shiomi, Osakada et al. (2004)

Moat, Pinkerton et al. (2011) studied the effects of laser pulse length and duty cycle on the residual stress of SLM fabricated Waspaloy and Inconel 718. Although they built thin walls rather than cuboidal structures, the stress profiles measured agreed well with the findings of Mercelis and Kruth (2006). Stresses parallel to the free surfaces were tensile, with those in the interior being compressive. It was found the stress profiles had a weak dependence on the pulse length, but pulse length had little effect on the maximum stresses. Increasing the duty cycle increased the stress gradient and size of the region of maximum stress for x-direction tensile stresses.

Longitudinal tensile stresses near the top surface were attributed to part shrinkage, under the mechanism of *top layer cool down*. Longer pulses were found to increase the proportion of high residual stress compared to short pulses. The increased exposure time results in higher temperatures around the laser point, leading to higher cooling rates. This is similarly explained by TGM.

The featured literature focussed on relationships between process parameters and residual stress. However, because the residual stress can be said to derive entirely from thermal stress induced by the fusion process, it is actually the relationships between process parameters and thermal stress that were revealed. Residual stress can be relieved by simple post process heat treatments; therefore, as standalone problem it can be easily remedied. It is the other, less reversible effects of thermal stress - defects which occur as a material response to the stress, such as deformation or fracturing/rupture - that pose a greater challenge.

2.2.2 Porosity

Porosity refers to a pore, or number of pores present within a volume, and is usually quoted as a % volume or area. However, the more common case is to quote a samples density (% or kgm^{-3}); this is because porosity refers to the characteristic, rather than a physical property. Pores are considered detrimental because they are potential crack initiation sites, ultimately influencing the mechanical performance of the material. As such the achievement of full density with a material is usually sought before conducting mechanical investigations. Many of early or initial investigations into processing of alloys with SLM focus largely or only on densification of the material (Morgan, Sutcliffe et al. 2004, Kruth, Levy et al. 2007, Mumtaz, Erasenthiran et al. 2008, Gu, Hagedorn et al. 2012, Savitha, Gokhale et al. 2012, Kamath, El-dasher et al. 2014). From these investigations it is gleaned that porosity in SLM occurs due to five reasons: insufficient melt overlap, insufficient melting/fusion depth, trapped gas, balling and vapourisation. Balling and vapourisation are also linked to poor surface finish, and will be discussed further in Section 2.2.3. Examples of porosity reported in SLM processed IN738LC (Rickenbacher 2013) are given in Figure 2.7.

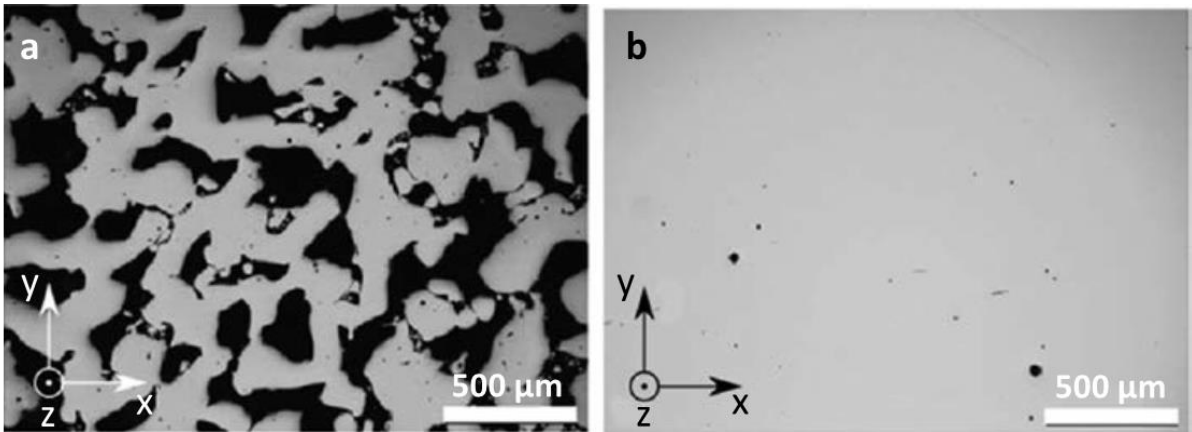


Figure 2.7 - a) High porosity caused by lack of fusion and b) low porosity achieved through parameter optimisation- adapted from Rickenbacher (2013)

The porosity observed in Figure 2.7a has occurred due to lack of fusion, this is evident because whole powder particles are still present within the voids. This is an extreme case, at 53% porosity, and is a result of insufficient energy absorption. In Figure 2.7b the process parameters have been optimised leading to a porosity of only 0.2%. There are a few pores still present, two large spherical and a number of significantly smaller spherical pores. All spherical pores are caused by the trapping of gas within the melt. The gas expands uniformly upon heating, creating a spherical void. The larger spherical pores are approximately 50 μm in diameter, too large to be porosity present within the powder itself; those are the cause of the much smaller micro-pores. The large pores are actually the result of insufficient overlap, where all of the available powder has been melted but hydrostatic forces have led to the creation of a void, in which gas can be trapped. An indicator to this mechanism is the alignment of pores to a pattern or direction, as it implies they have formed along a hatch line. This mechanism will be discussed further in the design of experiments in Chapter 3.

With the exception of trapped gas, which can originate from the powder particles, all porosity is controllable with laser scan and machine parameters. Eliminating or minimising porosity is therefore a matter of parameter optimisation specific to a given material.

2.2.3 Surface roughness

Balling is a phenomenon in which molten liquid solidifies as beads on the surface, rather than hemi-spheroidal drops. It occurs when the molten material does not (sufficiently) wet the underlying material due to surface tension, causing the liquid to spheroidise (Kruth, Froyen et al. 2004). The beads create a rough surface, which if built on result in high porosity and a high surface roughness of the part. Kruth, Froyen et al. (2004) investigated the physical mechanism and came up with a strategy to avoid the phenomenon based on laser scan parameters.

Figure 2.8 depicts a flat, smooth and chemically homogenous surface (S), in contact with non-reactive liquid (L) in the presence of a vapour phase (V). If the liquid does not fully cover the surface, the liquid surface will intersect the solid surface at an angle θ . θ corresponds to a minimum of the total free energy of the system. Due to the very short interaction time of the laser melting, θ can be said to obey the classical equation of Young (1804):

$$\cos \theta_Y = \frac{\sigma_{SV} - \sigma_{SL}}{\sigma_{LV}}$$

Equation 2.1

where σ_{SV} , σ_{SL} and σ_{LV} are the surface energies of the system, and θ_Y is the intersection angle. If the melt pool created by a laser is approximated as a half cylinder, balling is said to occur when the total surface of the molten pool becomes larger than that of a sphere

with the same volume. Thus, in order to avoid balling, one must ensure that the length to diameter ratio of the melt pool is less than 2.1.

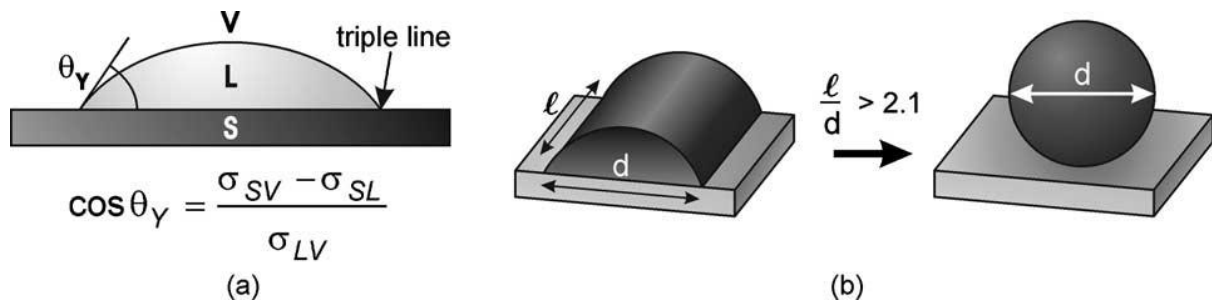


Figure 2.8- a) the wetting of a liquid on a solid substrate, b) transition from half cylinder to sphere, depending on dimensions of the molten laser pool (Kruth, Froyen et al. 2004).

This is achieved through optimisation of the laser scan parameters. Kruth and Froyen created parameter windows for a continuous and pulsed laser system, see Figure 2.9, based on laser power against laser scan speed. They found that high scan speeds combined with high power resulted in reduced balling. The high speeds reduce the length of the melt track, satisfying the above ratio, whilst the high power ensures full melting of the powder. In contrast, other studies (Gu, Hagedorn et al. 2012) found that low power with low speeds also reduced balling. This is attributed the low scan speeds allowing for an increase in the width of the melt track through heat conduction. Again, the increased width means that $l:d$ is kept below 2.1.

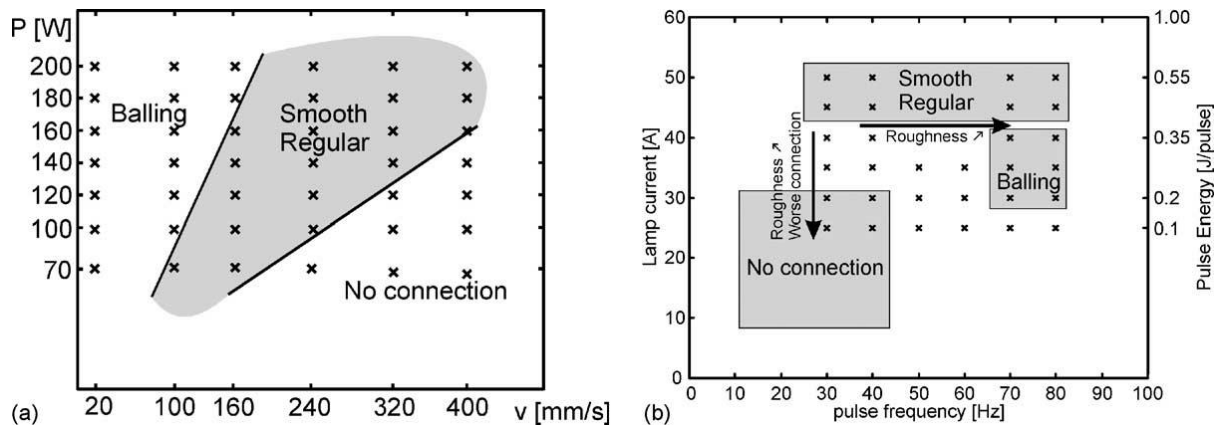


Figure 2.9 - Process windows for a) continuous wave and b) pulsed laser systems (Kruth, Froyen et al. 2004)

In Figure 2.9, we can see that balling occurs at high powers with low speeds, however there is a further effect which can occur with this parameter set. The slow speed and high power results in a high energy density, allowing the laser melting temperature to meet and exceed the evaporation temperature of the material. The evaporation causes a rapid expansion of the particles, creating a recoil pressure on the molten pool. The vapour can then sometimes interact with laser radiation (if the incident intensity is high enough) causing it to become ionised, forming a plasma (Kruth, Froyen et al. 2004). A low 'plasma recoil' pressure can result in the flattening of the melt surface, thereby reducing any balling effects and improving surface roughness. High pressures, however, result in the expulsion of melt material and even nearby powder particles from the layer. Much like balling, it creates irregular voids through the layer, which obstruct a smooth layer deposition resulting in high porosity in the part and puckered or uneven top surfaces.

2.2.4 Process induced cracking

Process induced cracking refers to the macro or micro-cracks which form as a direct result of the process. They can either form during processing or once processing has finished – although they would have to occur without external influence to still be considered process induced.

Unfortunately, a large number of investigations in this field are carried out by commercial bodies, and therefore often the results are not made public. Although there are a few publicly available studies which report micro-cracking in SLM as processed material, it is believed the number of affected alloys far exceeds those reported. If we include reports for all laser deposition techniques, crack susceptible alloys reported in the public domain are as follows: Hastelloy X (Wang 2011, Tomus, Jarvis et al. 2013), Inconel 738 (Zhong, Sun et al. 2005, Rickenbacher 2013), Waspaloy (Mumtaz, Erasenthiran et al. 2008), CM247-LC (Carter, Martin et al. 2014), Aluminium 6061 (Fulcher, Leigh et al. 2014) and austenitic stainless steel (Yu, Rombouts et al. 2013).

Figure 2.10 and Figure 2.11 display cracks observed in laser deposited austenitic steel and SLM processed Waspaloy respectively. A key observation is that the cracks in both cases initiate from a pore/defect and propagate along the grain boundary, and they are both jagged in morphology implying fracture of solid state material.

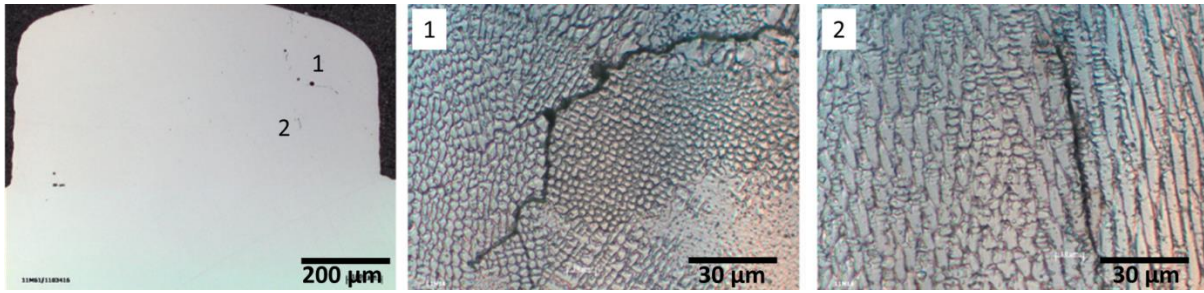


Figure 2.10 - Micro-cracking in as processed austenitic steel. Note that crack '1' appears to have initiated at a pore. Both cracks have formed along grain boundaries also- adapted from Yu, Rombouts et al. (2013)

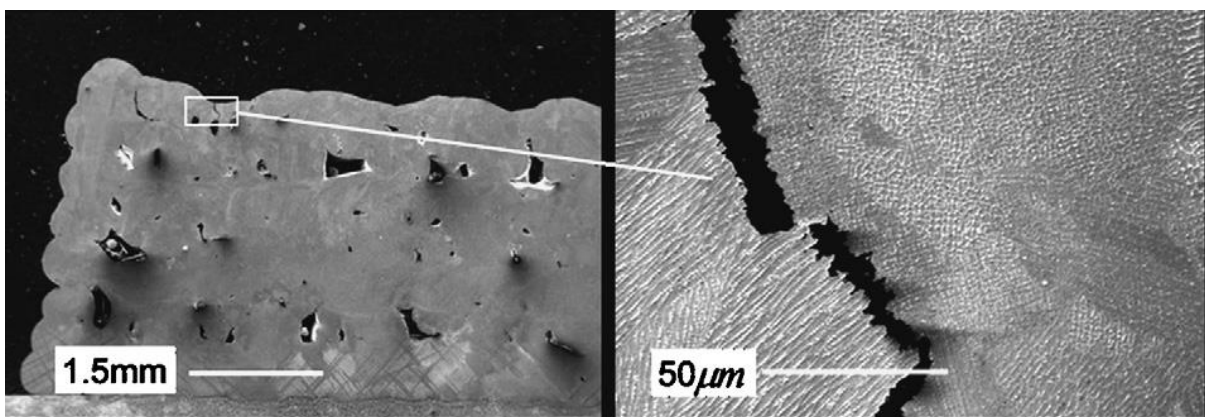


Figure 2.11 - Top surface crack observed in SLM fabricated Waspaloy, again the crack is observed to lie along the grain boundary- direct from Mumtaz, Erasenthiran et al. (2008)

From those materials reported, the majority of crack susceptible alloys are nickel-base superalloys. The key point raised from these investigations is that although parameter optimisation can reduce micro-cracking, it has not been sufficient to eliminate it (Rickenbacher 2013, Tomus, Jarvis et al. 2013). Clearly micro-cracking affects a range of alloys, however, as will be discussed in a Section 1.7 and 1.8, the specific mechanisms behind cracking may not be same for each alloy.

2.3 Failure by fracture and critical crack length

Micro-cracks, along with other internal defects, act as crack initiation sites, that is, points from which a *macro* crack will propagate leading to component failure. It is therefore paramount for industries such as aerospace, where the overriding design criteria is safe operation, that components are as close to defect free as possible. A crack will propagate once the *stress intensity factor*, K_I , exceeds the *fracture toughness*, K_{Ic} , of the material (Ashby, Shercliff et al. 2007). If we consider a crack of length c_l , as depicted by Figure 2.12, with applied remote stress σ , then K_I and K_{Ic} are described by Equation 2.2 and Equation 2.3 respectively.

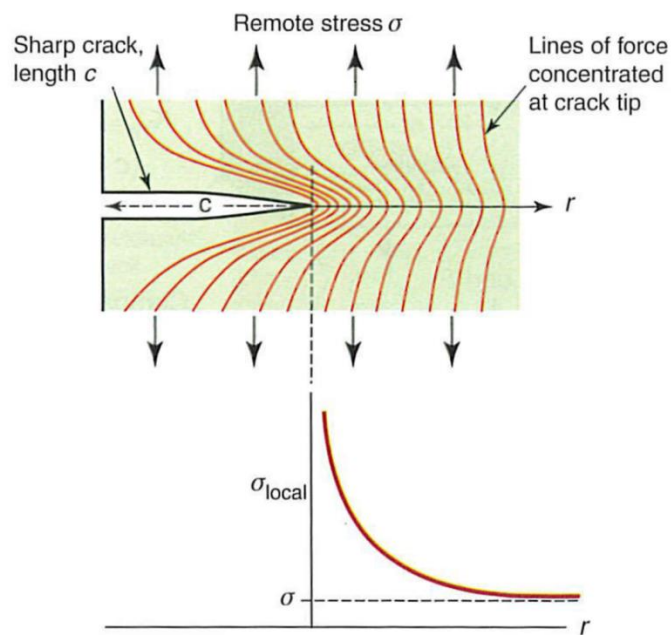


Figure 2.12- Lines of force in a cracked body under load, taken from (Ashby, Shercliff et al. 2007)

$$K_I = Y\sigma\sqrt{\pi c_l}$$

Equation 2.2

$$K_{1c} = Y\sigma^*\sqrt{\pi c_l} \approx \sigma^*\sqrt{\pi c_l}$$

Equation 2.3

where σ^* is stress at propagation and Y is 1 providing $c_l \ll$ width of component. K_{1c} is a material property (independent of measurement technique) and is often known for established metals and alloys. If a crack is small, the material may yield before fracture, in which case σ^* is equal to the yield strength σ_y . The minimum crack length required for crack propagation, c_{crit} , in a material can therefore be defined as

$$c_{crit} = \frac{K_{1c}^2}{\pi\sigma_y^2}$$

Equation 2.4

or

$$c_{crit} = \frac{K_{1c}^2}{2\pi\sigma_y^2}$$

Equation 2.5

For an enclosed crack, where crack length is defined as $2c_l$.

Using Equation 2.4, c_{crit} has been calculated for a number of common alloys and metals, see Table 2.1.

Material	Yield (MPa)	UTS (MPa)	Elongation (%)	K _{1c} (MPa.m ^{1/2})	c _{crit} (mm)
Nickel					
Inconel 718	800	914	3.49	98	2.4
Inconel 718 aged	1110	1320	15	130	2.2
Inconel 625	434	900	34.9	358	108.3
Hastelloy X	724	777	40	400	48.6
Iron	210	432	36	80	23.1
316l wrought	310	620	50	72	8.6
Titanium	570	690	25	50	1.2
Ti6Al4V aged	1080	1270	13	100	1.4
Al6061 T651	266	605	10	29.2	1.9
Al 7075	110	236	16.1	39	20.0

Table 2.1 - Mechanical properties for range of alloys and metals. Values of yield strength, Ultimate Tensile Strength (UTS), elongation and K_{1c} are all maximums in the range, taken from CES Edupack 2014, c_{crit} values are calculated.

From initial observation, it appears that the majority of materials will only fracture if an internal crack is of the order of a millimetre or greater. The implication then being that a micro-crack (of the order of 10-100 µm) is not considered an integral problem, as the material will yield before it would fracture. This would be the case if there was only one micro-crack within the component. However, if there were multiple micro-cracks, and particularly if cracks were aligned providing potential link up, then it is the *total crack length* that may be considered. At this point, component size becomes an important consideration. If a material has a crack density, number of cracks per unit area or volume, smaller components are less at risk as *c_{crit}* is an absolute value. Conversely, larger components are more at risk of failure by fracture as they will contain more micro-cracks and have a greater total crack length.

If a component of cross sectional area 40 mm² is made of material which has a crack density of 10 cracks per mm², with each crack ~ 50 µm in length, total crack length is 2 mm. This value is comparable to the critical crack length of aged Inconel 718, one of the most commonly used nickel superalloys, meaning it is unlikely to be acceptable for service in a high loading environment.

If an alloy is susceptible to process induced micro-cracking, this places uncertainty on whether it will be suitable for service as potential total crack length could exceed c_{crit} depending on component size. Far better is to use a material with ultra-low or zero crack susceptibility, that way mitigating the risk of exceeding c_{crit} .

Given their reported high crack susceptibility it is therefore likely that, in their current state, many nickel superalloys processed by SLM will not be accepted by aerospace industry regulators.

2.4 Solidification and microstructure theory

2.4.1 Solidification fundamentals

Although this research concerns additive manufacturing only, solidification is a subject of such intricacies that it is necessary to first cover solidification fundamentals, before moving on to the specific cases of laser processing and additive manufacturing

In order for a melt to solidify, heat must be extracted. This is achieved by the application of cooling to the melt leading to the creation of an external heat flux, q_e . Heat extraction affects the energy of the solid and liquid states by decreasing the enthalpy due to cooling (of liquid and solid), $\Delta H = \int c dT$, and due to transformation (from liquid to solid) which is the same as the latent heat of fusion, ΔH_f . The resultant cooling rate, dT/dt or \dot{T} is related to the external heat flux by Equation 2.6, using the latent heat per unit volume $\Delta h_f = \Delta H_f/v_m$ (Kurz and Fisher 1998).

$$q_e \left(\frac{A'}{v} \right) = -c \left(\frac{dT}{dt} \right) + \Delta h_f \left(\frac{df_s}{dt} \right)$$

Equation 2.6

where c is specific heat per unit volume, df_s/dt is change in volume fraction over time and (A'/v) accounts for the effect of casting geometry, with the ratio of surface area, A' , to volume, v . The control of heat extraction allows for the control of cooling rate which for a given location and time is given as

$$\dot{T} = \frac{dT}{dt} = \frac{dT}{dr} \cdot \frac{dr}{dt} = G$$

Equation 2.7

where dT/dr is the temperature gradient G and dr/dt is the growth rate of the solid, or solidification rate, V (or V_s). In the case of simple casting, heat is extracted through via a chill through the walls of the mould, see Figure 2.13. Here, the solidification front moves in a direction parallel and opposite to the heat flux, moving from the mould wall forming a columnar zone. As the solid front advances, the heat flux decreases (McLean 1983) and therefore so do G and V . There are three distinguishable regions during the growth of the columnar zone regions: liquid, liquid + solid (mushy) and solid. The mushy zone is where microstructural characteristics, such as grain size, porosity, precipitates are established. But the morphology of the microstructure depends upon G and V and on the alloy composition (Kurz and Fisher 1998).

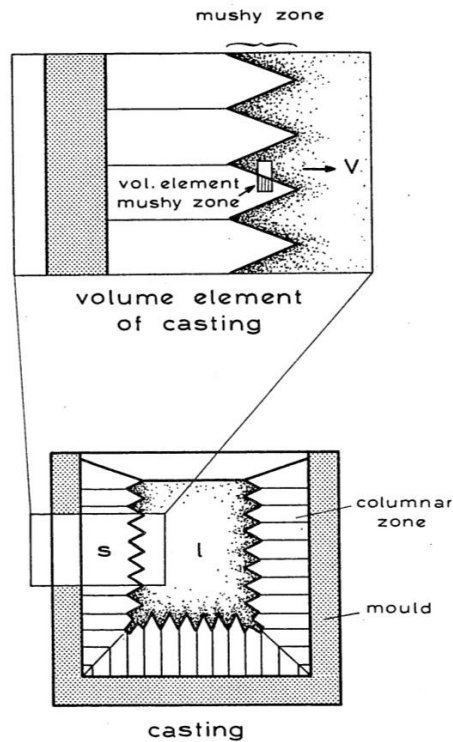


Figure 2.13 - Solidification in conventional casting- direct from (Kurz and Fisher 1998)

The microstructural formation of a casting is shown in Figure 2.14. Initially, the relatively low temperatures of the mould wall induce a high cooling rate resulting in the nucleation of small randomly orientated equiaxed grains. The grains rapidly become dendritic and grow arms in preferential crystallographic directions ([001] for cubic). Those grains which can grow anti parallel to the heat flux eliminate others through competitive growth, resulting in the columnar (directional) grain morphology, Figure 2.14a. Directional growth is characterised by a positive thermal gradient, G . In the centre, dendrite branches which have detached from the columnar arms are allowed to grow independently. Their latent heat is extracted radially through the undercooled melt resulting in an equiaxed grain formation, Figure 2.14b (Kurz and Fisher 1998). This is similarly explained by Figure 2.15.

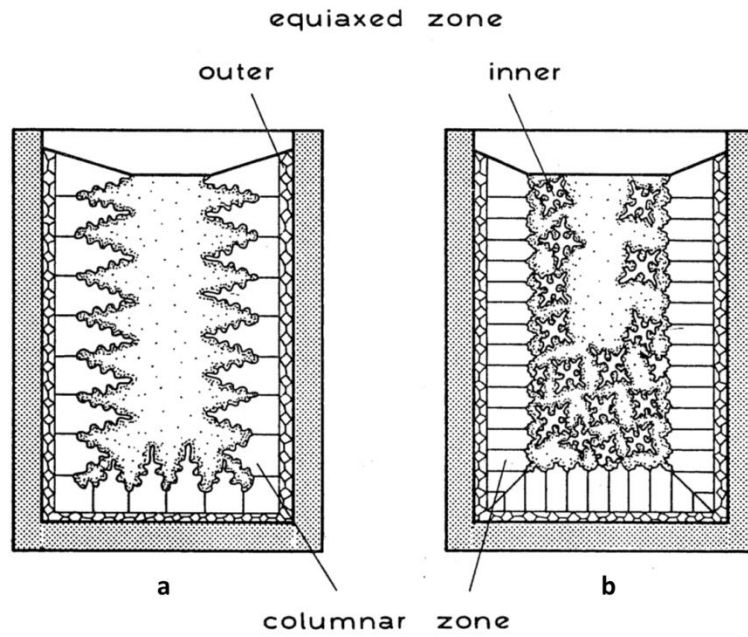


Figure 2.14 - Microstructural formation in casting - direct from (Kurz and Fisher 1998)

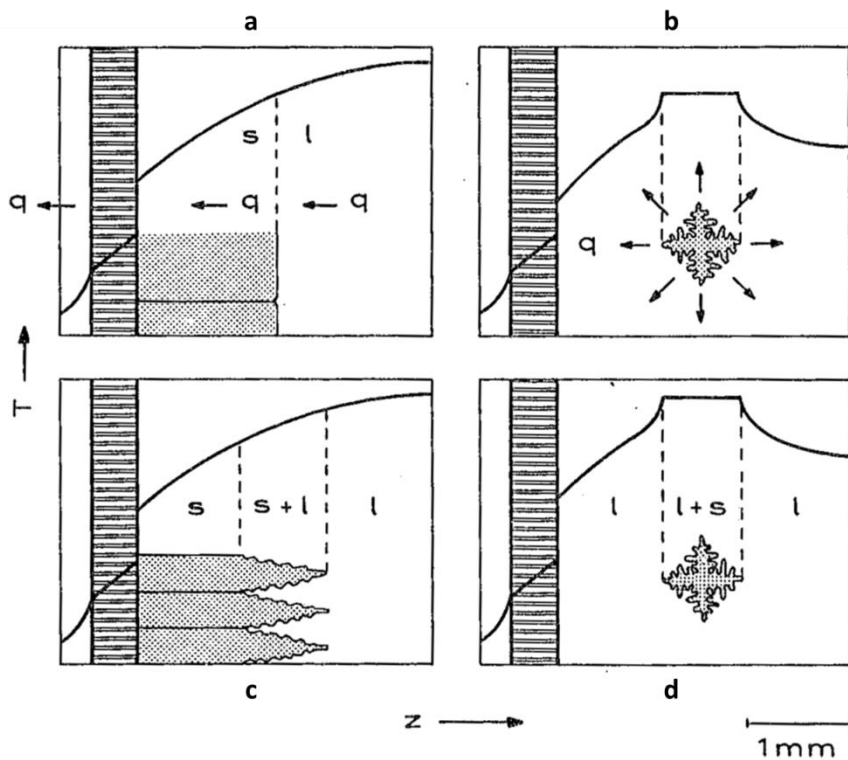


Figure 2.15 - Solid-liquid interface morphology and temperature distribution, s = solid phase, l = liquid, q = heat flux - direct from (Kurz and Fisher 1998)

In Directional Solidification (DS), solidification is controlled through control of heat flux. The most basic form uses a chill at the base of a mould, with insulating walls. This results in a unidirectional heat flux down through the base of the mould, and therefore the formation of columnar grains perpendicular to the base, with equiaxed at the top of the mould.

In a pure metal, Figure 2.15a, the columnar grains have a planar interface and grow antiparallel to the heat flux. In alloys, or if impurities are present, the columnar crystals are dendritic. For the central equiaxed region, crystals grow the same in both cases, which is radially with heat flux direction. However, size may vary as in an alloy the growth is controlled mainly by solute diffusion rather than just heat flux as for pure metals. If one looks at the temperature profile it is observed that in columnar growth the liquid is the hottest part of the system, $G > 0$, however in equiaxed it is the crystal which is hottest, $G < 0$. This implies that the liquid must be undercooled for equiaxed crystals to form (Kurz and Fisher 1998).

In the solidification of an *alloy*, solutes are rejected by the advancing solid front, causing variation of the local equilibrium melting point along the solid-liquid interface, due to varying local concentrations. This creates instability in the initially planar interface, which materialises as perturbations. The tips of the perturbations grow faster as they can reject solutes radially, and ultimately the planar front breaks down, forming cells. Cells are crystals and will only grow during the directional growth of alloys; they always grow antiparallel to the heat flux direction, whereas dendrites grow along the preferred crystallographic direction closest to parallel with the heat flux. As V increases, conditions become more favourable to dendrite formation and dendrites form quickly from the cells. However, at high V cells can form as conditions approach absolute stability, see Figure

2.17. The distance between the centre of adjacent cells or dendrite trunks is the primary (dendrite arm) spacing, λ_1 , and this remains the same throughout solidification through to full freezing. If conditions allow, secondary dendrites arms can form perpendicular to primary trunk, these can then also have tertiary arms, see Figure 2.16. Secondary arm spacing, λ_2 , is also a characteristic value for dendrites. Both λ_1 and λ_2 depend on, and can be used to calculate, the cooling rate (Davies, Shohoji et al. 1980).

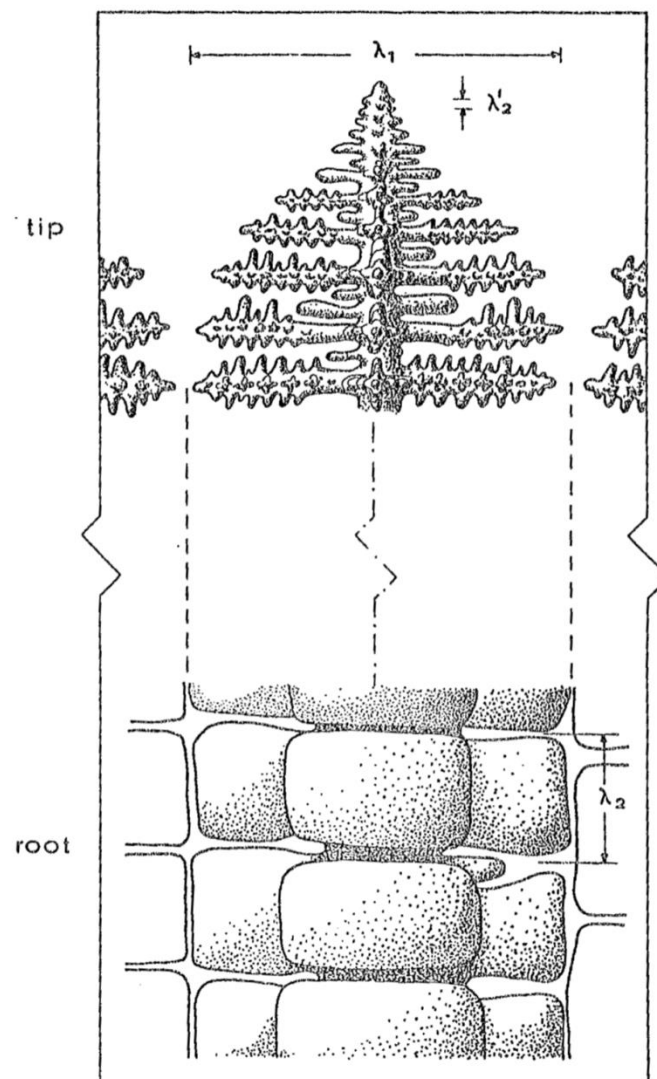


Figure 2.16- Dendrite root and tip for columnar growth at same point in solidification but separated by distance $\gg \lambda_1$. Note how λ_2 evolves, beginning small at the tip and eventually growing to the point of dissolution of the tertiary arms at the root- direct from (Kurz and Fisher 1998)

Figure 2.17 displays the change of crystal morphology with increasing V , and also the tip radius R and λ_1 . High velocity, or rapid, solidification will be discussed in more detail in Section 2.4.

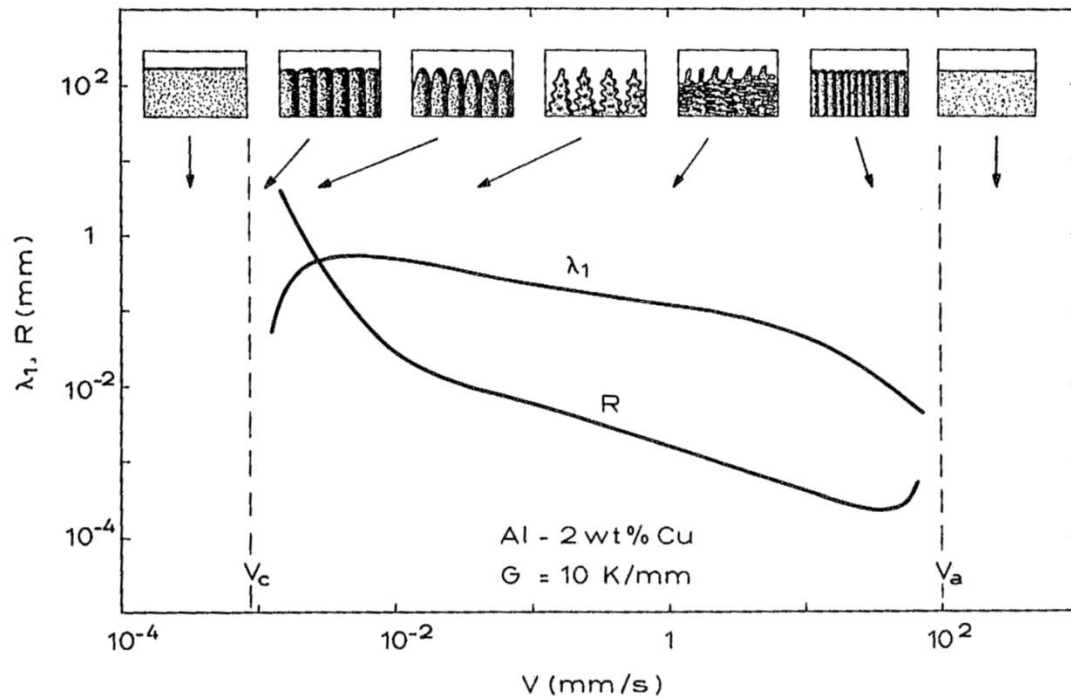


Figure 2.17 - Crystal morphologies of Al-2Cu alloy with increasing V along the top of the image - from left to right: Plane front, cellular, cellular-dendritic, dendritic, dendritic with secondary arms, fine cellular and plane front. V_c is the limit of constitutional- direct from (Kurz and Fisher 1998)

The rejection of solutes from the dendrite tips results in increased concentrations of solute within the liquid. As this is pushed out radially it can become trapped between the dendrite trunks and solidifies resulting in interdendritic regions with different solute concentrations to the primary dendrite trunk. The mechanism is called segregation, or on this scale, microsegregation. To what extent a solute will segregate depends on its diffusion in the solid and liquid and the shape and size of the dendrite (Kurz and Fisher 1998) – which in turn depends on V and \dot{T} . Every element has a solute diffusion coefficient

D specific to solution, which also varies for solid D_s , liquid D_l and solid-liquid interface D_i . Each has to be experimentally determined and thus only common solute-solution values are available in literature.

If we take the simplest form of alloy, a binary system, it is theoretically possible to achieve uniform concentrations of solute by means of diffusion between the solid and liquid phases (McLean 1983). However this requires unrealistically fast diffusion rates, or, impractically slow solidification velocities (0.5×10^{-14} m/s for substitutional, and 0.5×10^{-11} m/s for interstitial solutes (McLean 1983)) and thus in *conventional* solidification one will always observe some microsegregation. Figure 2.18 demonstrates microsegregation occurring in dendrite formation. This is often observed experimentally, where higher concentrations of solute are found in the interdendritic regions and are darker in contrast. As will be discussed in the next section, it is possible to have segregation free structures, with very high solidification rates.

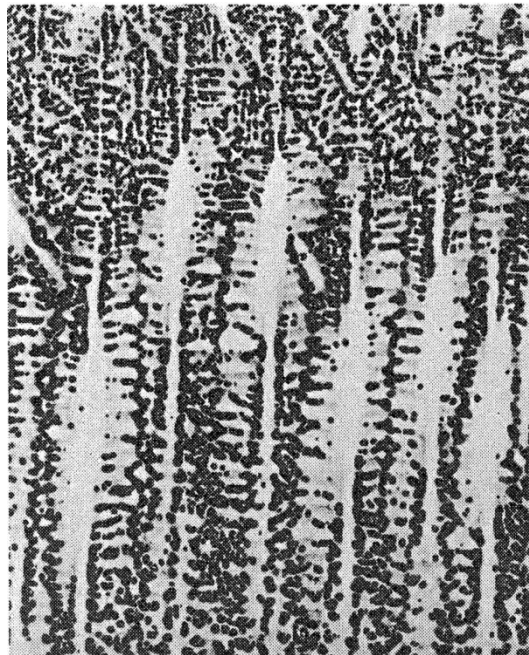


Figure 2.18 - Dendritic structure of DS MarM246. White regions are dendrite crystals with black interdendritic regions visible due to differences in chemical concentrations being highlighted by chemical etching- direct from (McLean 1983)

2.4.2 Rapid solidification

2.4.2.1 Solute diffusion and solute trapping

Rapid Solidification (RS) will occur either due to high undercooling of the melt e.g. rapid quenching, or with rapidly moving temperature fields e.g. surface processing with high power density sources such as lasers (Kurz and Fisher 1998). Although the name suggests a dependence on solidification velocity, the characteristic phenomenon of RS depends on the relationship between solidification velocity and diffusion. In low V conditions, microstructure evolves according to the relationship $R^2V = \text{const}$ where R is dendrite tip radius (or $\lambda^2V = \text{const}$ for eutectic spacing λ). Diffusion distance $d = 2D_L/V$, where D_L is the solute diffusion coefficient in the liquid adjacent to the solid-liquid interface. If $2D_L/V < R$, the diffusion field becomes localised with respect to microstructure, limiting solute segregation. This point is deemed as the onset of RS, and occurs at critical $V \sim 10^{-2}$ m/s (Kurz and Trivedi 1994).

As V increases, it eventually becomes comparable to, and then greater than, the diffusion rate at the solid-liquid interface D_L/λ ; where D_L is the solute diffusion coefficient in liquid and λ is the inter atomic spacing (Aziz 1982). The solute atoms are then trapped by the advancing solid-liquid interface and incorporated into the solid. Concurrently, the crystal no longer has time to change its composition so as to reach the same chemical potential of the melt and therefore the solid-liquid interface is no longer in equilibrium (Kurz and Fisher 1998). The two mechanisms are known as solute trapping and departure from local equilibrium, respectively.

Michael Aziz formulated a model for the redistribution of solutes during rapid solidification (Aziz 1982). In which he proposed two mechanisms of growth: stepwise and continuous. In stepwise, the growth occurs in lateral steps of height λ , where λ is the

interatomic spacing. The average time between each step is $\tau = \lambda/V$. If the solute atom does not diffuse back into the liquid before τ expires, then it is trapped within that monolayer as the interface advances. In continuous growth, the solute atom is being 'dragged' towards its lattice site over time τ , whilst at the same time trying to diffuse out. Rather than being in fixed steps, the potential surrounding of the solute is continuously changing, making accurate solutions more difficult to write. However, ultimately continuous growth was proved to be in better (and very good) agreement with experimental results than stepwise growth, by Aziz himself and other authors (Aziz, Tsao et al. 1986, Aziz 1988, Ahmad, Wheeler et al. 1998). As such it will be discussed in more detail.

Consider solute atoms jumping across the interface between solid and liquid. For continuous growth it is assumed that this occurs with a steady state flux, J . It is also assumed each jump requires an activation energy, which must be greater than that for crystallisation. For solute transition the jump is equal to λ , for crystallisation the jump is $< \lambda$. In the reference frame of the moving interface (moving at V), the steady state requirement of the net solute diffusivity flux $J(z)$ and net solute concentration $C(z)$ is

$$\frac{\partial}{\partial z}(J - VC) = 0$$

Equation 2.8

This then becomes

$$J_{s \rightarrow l} - J_{l \rightarrow s} = V(C_{li} - C_{si})$$

Equation 2.9

where $J_{s \rightarrow l}$ is flux from solid to liquid and $J_{l \rightarrow s}$ is flux from liquid to solid, both are described by Equation 2.10 and Equation 2.11. C_{si} is the solute concentration in the newly formed solid and C_{li} is solute concentration in the liquid.

$$J_{s \rightarrow l}(t) = f_s v_s \lambda \gamma_s C_{si}(t) \exp\left(\frac{-\Delta\mu_B^{0*}}{RT_i}\right)$$

Equation 2.10

$$J_{l \rightarrow s}(t) = f_l v_l \lambda \gamma_l C_{li}(t) \exp\left(\frac{-\Delta\mu_B^{0*} - \Delta\mu_B^0}{RT_i}\right)$$

Equation 2.11

For Equation 2.10, f_s is the fraction of sites in the solute from which an atomic jump can occur, v_s is the attempt frequency in the solid, $\Delta\mu_B^{0*}$ is the molar free energy of activation to the transition state, γ_s is the activity coefficient of the solute in the solid, R is the molar gas constant and T_i is the temperature at the interface. For Equation 2.11 f_l , v_l and γ_l are the same but for in liquid and $\Delta\mu_B^0$ is the change in standard molar free energy upon recrystallization.

An interface diffusivity D_i (which is smaller than D_l) and equilibrium segregation coefficient $k_e(T_i)$ are then defined as $D_i \equiv \lambda^2 f_l v_l \gamma_s \exp\left(\frac{-\Delta\mu_B^{0*}}{RT_i}\right)$ and $k_e(T_i) \equiv \frac{\gamma_l}{\gamma_s} \exp\left(\frac{-\Delta\mu_B^0}{RT_i}\right)$, feeding these into Equation 2.11 and defining a dimensionless velocity $\beta \equiv \frac{v\lambda}{D_i}$ this simplifies to

$$\beta(C_{li} - C_{si}) = C_{si} - k_e C_{li}$$

Equation 2.12

Or, if diffusion in the solid is taken to be negligible, so that $C_s = C_{si}$ we get

$$k(V) = \frac{C_s}{C_{li}} = \frac{\beta + k_e}{\beta + 1}$$

Equation 2.13

From this expression we see that as $V \rightarrow 0$, the partition coefficient $k(V)$ approaches k_e , and if $V \gg \frac{D_i}{\lambda}$ then $k(V)$ approaches 1. Therefore giving a transition range beginning at equilibrium segregation at low V , up to complete solute trapping when $V \gg \frac{D_i}{\lambda}$. The interface velocity range over which this transition occurs is predicted as a few orders of magnitude of V ; which for the case used in Aziz (1982), is 0.1-100 m/s, see Figure 2.19. It is noted that this relationship was initially only for dilute solutions, and it was assumed that $D_i/\lambda = D_l/\lambda = 10$ m/s with D_i is taken as $\sim 10^{-9}$ m²/s and $T_i = T_m$.

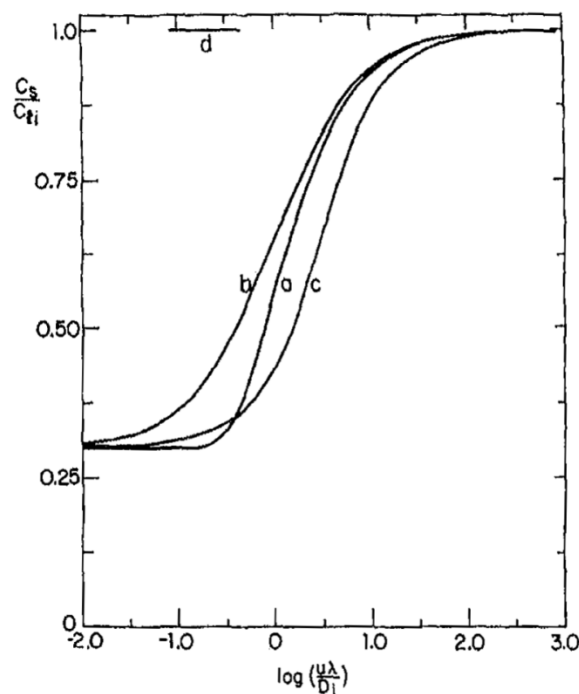


Figure 2.19 - Predicted arsenic ($k_e = 0.3$) segregation in silicon with Aziz's continuous growth model (b) and stepwise growth model (a), and Baker model (Baker and Gahn 1969)(c). (d) is data from Baeri, Foti et al. (1981). Here $u = V$. Direct from (Aziz 1982).

The prediction of whether solute trapping will occur for a specific system is dependent on the values of V , D_i and λ . However, the values chosen for D_i and λ carry the most significance as they determine what the transition velocity range V_{crit} will be.

λ (replaced with the interface thickness δ_i in later works (Kurz and Trivedi 1994)), is usually taken as 10^{-9} m (Kurz and Fisher 1998), but can be replaced by a specific distance if using for larger length calculations. Although Aziz initially assumed $D_i \sim D_l$ it is now believed that $D_i < D_l$, evidence of which was actually reported in Aziz (1982) when data from Baeri, Foti et al. (1981) suggested complete solute trapping of arsenic in silicon at 0.1 m/s. Boettinger, Coriell et al. (1984) proposed the calculation of D_i at interface temperature T_0 for various compositions. For the case of Silver, $T_0 = 943$ K, and based on an activation energy of 40 kJ mol^{-1} , D_i was calculated to be $6 \times 10^{-10} \text{ m}^2/\text{s}$. This implied a $V_{crit} \sim 0.01\text{-}10 \text{ m/s}$. Again this is for a dilute solution, calculations for concentrated solutions such as superalloys have not been conducted. Arnold and Aziz later adapted the Aziz model to include the atomic diffusive speed, which is the growth rate at which $k(V)$ is in mid transition between k_e and unity (Arnold, Aziz et al. 1999), Equation 2.14.

$$k(V) = \frac{k_e + \frac{V}{V_D}}{1 + \frac{V}{V_D}}$$

Equation 2.14

This model was previously verified experimentally for planar interfaces using pulsed laser processing, but using V_D as a free parameter to help fit dendrite-undercooling data. In Arnold, Aziz et al. (1999), V_D was measured independently in a dilute Ni-Zr alloy and found to be 26 m/s. This implies a lower limit of $V = 26 \text{ m/s}$ to achieve full solute trapping than the initially predict 100 m/s. Unfortunately, what is very difficult to predict is the

onset of solute trapping, all of the calculated or measured values only concern full solute trapping, or microsegregation free structures i.e. planar. In more complex alloy systems, each solute atom will possess a different diffusion rate, and solute-solute interactions will also affect V_{crit} .

2.4.2.2 Microstructures in RSPs and laser surface treatment

Selective laser melting, as the name suggests, is a laser melting process and employs a moving power source thereby creating moving temperature fields. In absence of established theory for SLM, it is therefore reasonable to discuss the solidification and microstructure formation theory of laser surface processing, as established in the late 1980s and early 1990s.

The characteristic solidification conditions for laser surface processing are outlined by Kurz and Trivedi (Kurz and Trivedi 1994) in their work on Rapid Solidification Processing (RSP). In RSP, microstructure selection is driven by the interface velocity V_s and cooling rate \dot{T} , and temperature gradient at the interface G is less significant.

Lasers transfer heat into a material through the reverse Bremsstrahlung effect – the Bremsstrahlung effect is the process of photon emission by an excited electron – that is an electron being excited by the interaction with an incident photon. In the case of laser processing it is the interactions between photons from the laser with free or bound electrons in the material (Bass 2012). In a metal, the electrons are free - separate to the atom – and sit in an electron cloud allowing for higher conductance through electron-electron interactions. Interactions between the excited electrons and lattice phonons result in phonon vibrations. It is the vibrations that are detected as heat. If the metal absorbs sufficient energy, the vibrations are enough to stretch the lattice bonds to the extent they lose their mechanical strength and the metal melts (Deffley 2012).

Figure 2.20 is a schematic showing the melt pool morphology and solidification conditions that occur with a moving laser source. Solidification velocity V_s increases rapidly from zero at the base of the melt pool to $\sim V_b$ (beam velocity) at the surface via the relationship $V_s = V_b \cdot \cos\theta$, where θ is the angle between the velocities (Gremaud, Carrard et al. 1990).

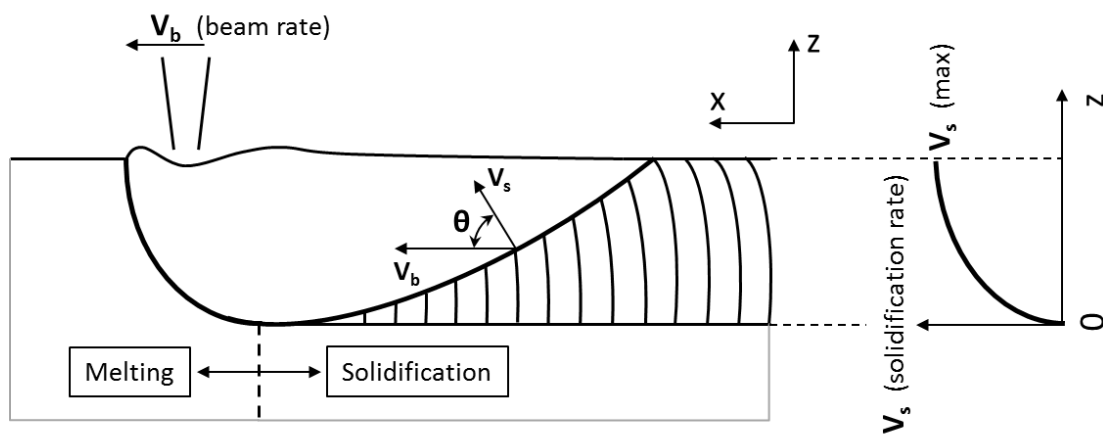


Figure 2.20 - Melt pool formation for laser surface processing at high beam velocities. Where V_s (max) $\equiv V_b$. - adapted from (Gremaud, Carrard et al. 1990)

Therefore, a beam velocity of 1 m/s results in a peak V_s of 1 m/s at the top of the trace. However, the acceleration from zero at the base of the trace to such a maximum over the relatively short distance of the trace depth, potentially results in a departure from steady state theory. This would make it difficult to interpret microstructural observations as established phase transformation models, such as those discussed in Section 2.4.1, which were developed for steady-state conditions. Zimmermann, Carrard et al. (1989) demonstrated that a quasi-steady state condition would be satisfied providing that the change in V_s , through a distance of D/V_s , was significantly less than V_s - where D is the diffusion coefficient of the solute in liquid - see Equation 2.15.

$$\frac{D}{V_s} \frac{\partial V_s}{\partial x} \ll 1$$

Equation 2.15

Taking the maximum value for $(\Delta V_s/\Delta x)$ as 10^3 - 10^4 s⁻¹ (Zimmermann, Carrard et al. 1989) and taking D to be of the order 10^{-9} m²/s (Kurz and Fisher 1998), the LHS of Equation 2.15 has values of 10^{-6} - 10^{-3} when applied to typical laser surface treatment solidification rates. The quasi-steady state condition is therefore satisfied, and steady state growth theory can be applied.

Along with additional works (Gremaud, Carrard et al. 1990, Carrard, Gremaud et al. 1992), Kurz and Trivedi (1994) determine that solidification conditions for laser surface treatment will, in most cases, lead to columnar (directional) growth of dendrites. However Zimmermann, Carrard et al. (1989) discovered that in the laser remelting of Al-Cu eutectics, a new phase formed in between cellular and planar forms at high solidification velocities. Beyond $V_s = 0.5$ m/s, they observed a banded structure which when analysed was comprised of supersaturated α -Al solid solution and wavy eutectic α -Al/ θ -Al₂Cu.

Figure 2.21 shows the interface response functions (T - V curve) for the various microstructures observed. Ordinarily beyond limit of absolute stability, plane front morphology is the most stable. However, between the velocity range of V_a and the V_{Tmax} - maximum of T_p - steady state plane front growth is unstable in time resulting in oscillatory instabilities and an alternative growth of cell-dendrites and plane front morphology. This materialises as submicron spaced bands which are parallel to the solidification front (Kurz and Trivedi 1994).

Plane front morphologies represent microsegregation free structures, where complete solute trapping has occurred during solidification. Figure 2.22 shows a microstructure selection map, in G - V coordinates. It is observed that laser surface treatments will either form cell-dendrites at lower V or banded structures when pushing towards 1 m/s or higher. With regards to solute trapping, in order to form dendrites there must be small amount of diffusion, complete solute trapping will always result in a plane front morphology, but the banded structure clearly represents a transition between the two.

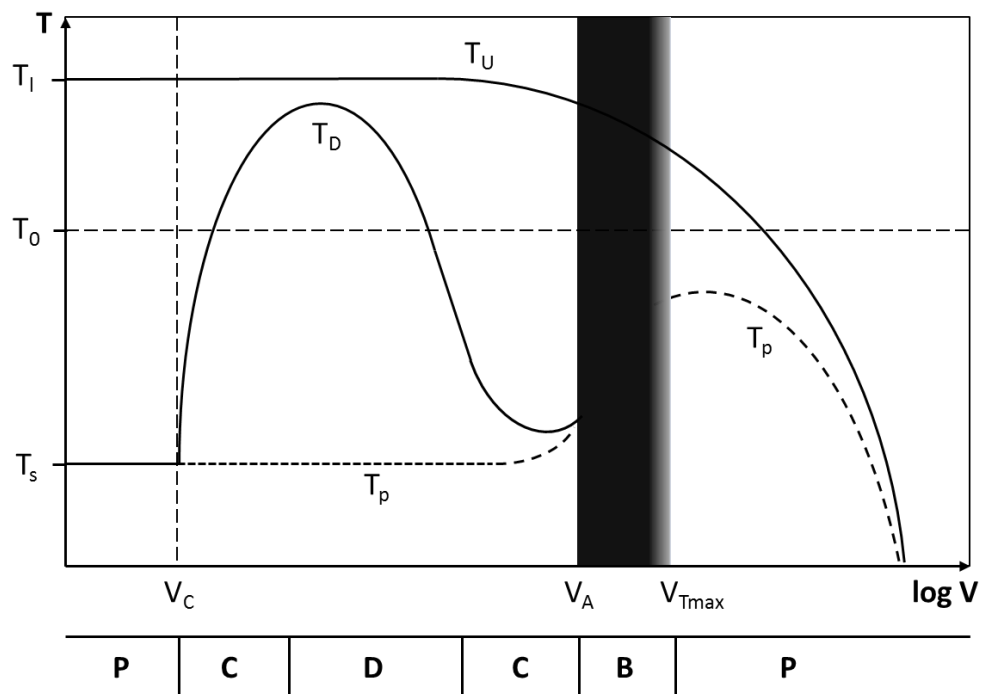


Figure 2.21 - Interface response function for microstructure forms, plane front T_p , cellular-dendritic T_D with undercooling-velocity T_U . Microstructures are denoted as plane front P, cellular C, dendrite D and banded B - Adapted from (Kurz and Trivedi 1994)

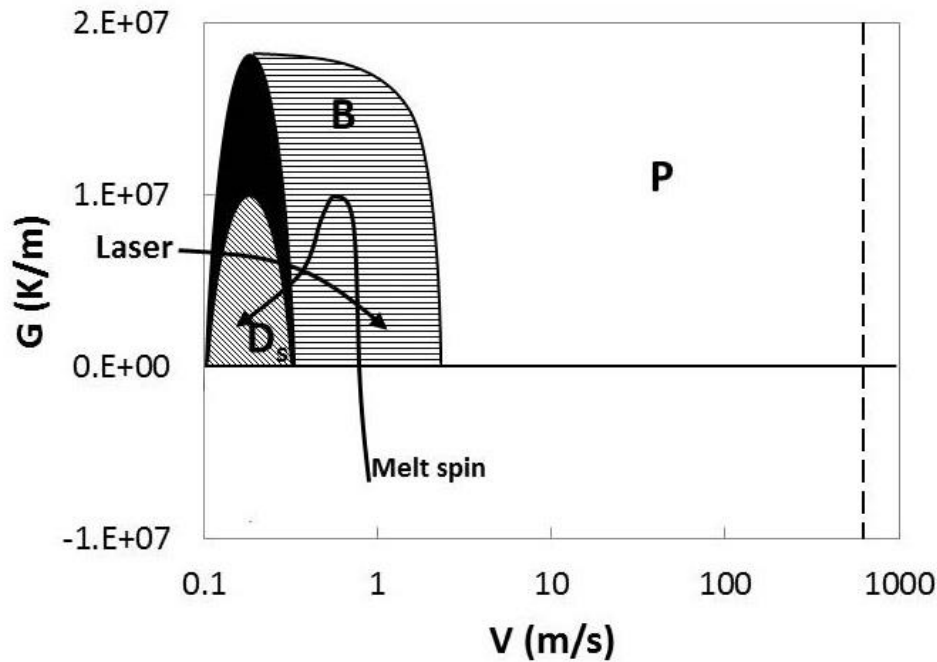


Figure 2.22 - Microstructure selection map in G-V coordinates. Columnar dendrites are indicated by D_s , banded structure B and planar structure P- adapted from (Kurz and Trivedi 1994).

2.4.3 In SLM

The application of a concentrated heat source makes additive manufacturing more like welding than casting or wrought manufacturing. Although there have been a number of investigations on the modelling and simulation of the heat transfer process in SLM (Matsumoto, Shiomi et al. 2002, Gusarov, Yadroitsev et al. 2007, Gusarov and Smurov 2009, Gusarov, Yadroitsev et al. 2009, Roberts, Wang et al. 2009, Hussein, Hao et al. 2013), many of these only model single layers or in 2 dimensions. There are few or no investigations on the full modelling of microstructure formation for multi-layered SLM processing.

The majority of research concerning SLM microstructure is observational (Gu and Meiners 2010, Thijs, Verhaeghe et al. 2010, Kempen, Yasa et al. 2011, Amato 2012, Amato, Gaytan et al. 2012, Vilaro, Colin et al. 2012, Wang, Guan et al. 2012). A key observation to

come out of these reports is that the grain structure of SLM as processed material appears to be relatively invariable. In that, regardless of material, machine or process parameters, the basic structure is the same. That is, large high aspect ratio columnar grains, with low angle grain boundaries, which have a preferred orientation of growth parallel to the build direction – see Figure 2.23. The grains themselves are made up fine of columnar dendrites, with only primary arms visible. Also visible is evidence of the melt pools/tracks and the layering process.

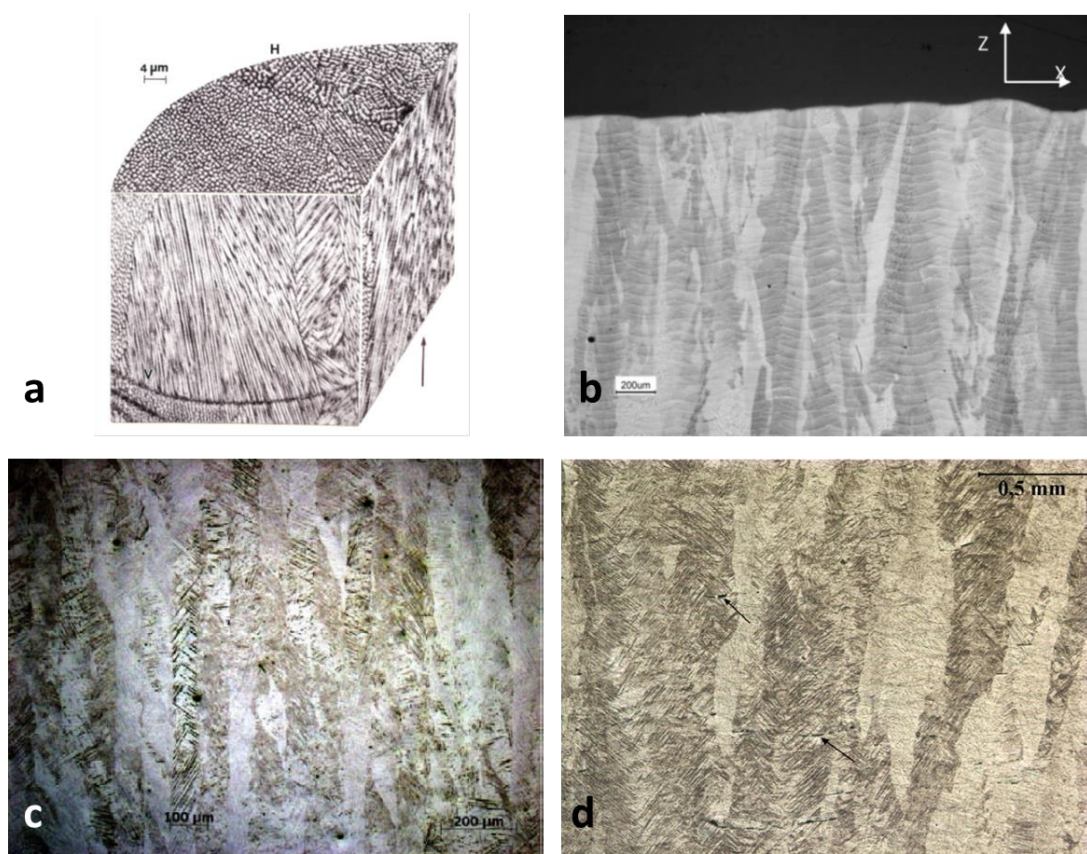


Figure 2.23 - Micrographs from several studies of SLM processing of different alloys and processing parameters. a) IN625 processed on an EOS M270 SLM system with a power of 200 W and scan velocity of 1000 mm/s (Amato 2012), b) Nimonic 263 processed on a Trumpf SLM machine with laser power of 200W and scan velocity of 100 mm/s (Vilaro, Colin et al. 2012), c) Ti-6Al-4V processed on a customised laser machine with a power of 42 W and scan velocity of 200 mm/s (Thijs, Verhaeghe et al. 2010), d) Ti-6Al-7Nb on a SLM Realiser II (MCP-HEK) machine with power of 100W and scan velocity of 150 mm/s (Chlebus, Kuźnicka et al. 2011).

In addition to SEM analysis of microstructures, some investigations have used Electron Back Scatter Diffraction (EBSD) to analyse the crystallographic texture of SLM processed material (Bauer, Dawson et al. 2013, Etter, Kunze et al. 2015, Divya, Muñoz-Moreno et al. 2016). From these investigations it is noted that solidification fibre texture tends to a preferred orientation of $\langle 001 \rangle$ which is parallel to the direction of growth, see Figure 2.24. Additionally, Bauer, Dawson et al. (2013) reports that reduced energy densities, specifically higher scan rates, resulted in a more chaotic microstructure, whereby the epitaxial growth was disrupted and the texture became less distinct – see Figure 2.25.

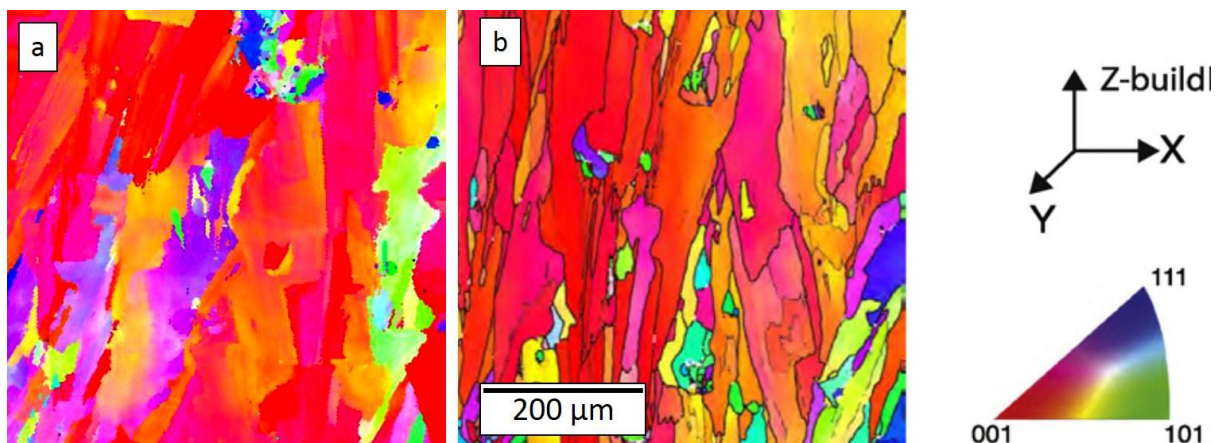


Figure 2.24 – Inverse pole figure EBSD maps direct from a) Bauer, Dawson et al. (2013) and b) Divya, Muñoz-Moreno et al. (2016)

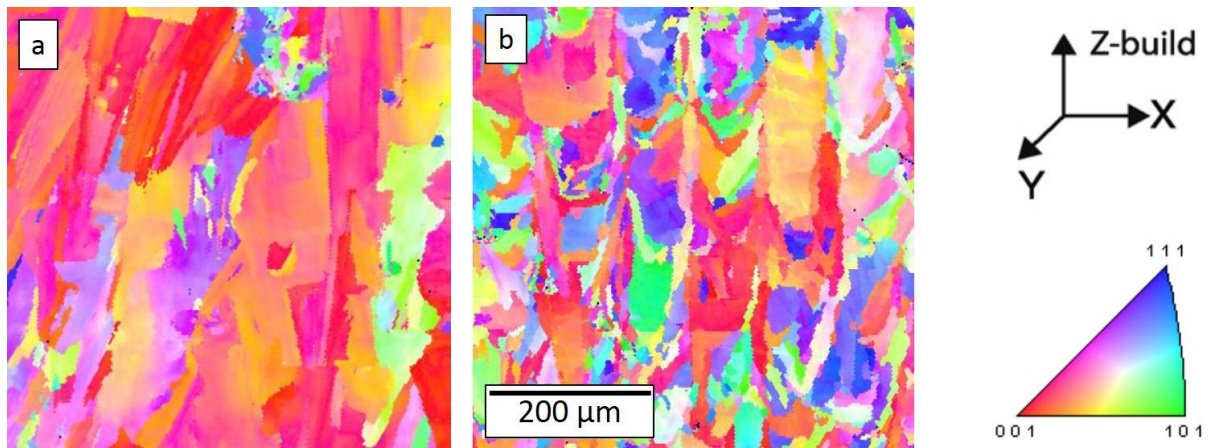


Figure 2.25 – Inverse pole figure EBSD maps for energy densities of a) 116 J/mm³ and b) 66 J/mm³ – direct from Bauer, Dawson et al. (2013)

Although it appears that the SLM process places relatively tight constraints on microstructure, further investigative analysis is required before conclusions can be made with regards the particular solidification conditions and microstructure formation in SLM. This will be carried out as part of the investigations of this work, details of which are found in Chapter 4.

2.5 Superalloys – History and Development

The term ‘Superalloy’ refers to a group of high temperature performing alloys which can operate at temperatures in excess of 540°C, and have base metals of nickel, iron-nickel and cobalt. This study focusses on nickel- and iron-nickel-base superalloys, as collectively they form by far the largest group and by contrast have had relatively little attention in the field of additive manufacturing research.

In this section we will discuss how and why nickel-base alloys were developed and what properties and attributes they have which make them the material of choice for high temperature applications.

2.5.1 High temperature superalloys: the emergence of Nickel as the material of choice

In the early decades of the 20th century, it became apparent that current metals were not adequate for the technologies of the day and stronger, more corrosive resistant, high temperature materials had to be developed. The stainless steels provided some respite, but their strength limitations were soon highlighted and they became merely a stepping stone to what be eventually be required.

With the beginning of World War II came the dawn of the gas turbine, these machines required materials which could withstand high loads at temperatures well in excess of 540°C, and the alloys and steels of the time simply could not perform. As the technology was developed, designers were pushing for components with greater and greater properties, not just in high temperature strength but also in corrosion resistance and operational lifetime. The first true superalloys were derived from alloys used in quite different applications to that of aerospace. The first cobalt superalloy was derived from Vitallium, an alloy used in dentistry, whilst nickel-chromium alloys (Inconel and Nimonic) were said to have been adapted from the material used in toaster wire, Nichrome (Donachie and Donachie 2002).

2.5.2 Nickel as a solvent

As mentioned above, superalloys are not exclusively based on nickel, but nickel- and iron-nickel-base superalloys have become the material of choice for high temperature applications. This section summarises the properties and chemistry of nickel and shines a light on the reason why its alloys dominate the aerospace industry.

Atomic number	Atomic weight	Isotopes	Melting point (°C)	Density (kgm ⁻³)	Crystal structure
28	58.71	58,60,61,62,64	1445	8907	FCC

Table 2.2 – Key material properties of nickel

Despite an obvious success as a base metal for high temperature superalloys, if one looks at the material properties of nickel it is not obviously clear as to why. It has a mid-range melting temperature, less than half that of Carbon or Tungsten, and quite a high density - twice that of titanium (4508 kgm⁻³). However, the key property of nickel is its crystal structure. If one views the transition metals, they are seen to be split into three structure groups. Body Centred Cubic (bcc) largely to the left, Hexagonal Close Packed (hcp) in the centre, and Face Centred Cubic (fcc) concentrated to the right. BCC metals tend to be brittle and there is also a ductile/brittle transition which results in toughness decreasing significantly with decreasing temperature. FCC metals on the other hand are both tough and ductile and are thus preferred for high temperature applications. Nickel's fcc structure is stable from room temperature up to its melting point. As a consequence, nickel does not experience any phase changes as it is heated up to this point, minimising thermally induced expansion or contraction. This is as a result of the significantly strong cohesive energy provided by the outer d-shell electrons; the same effect responsible for nickel's high density (Reed 2006).

FCC metals also have low diffusion rates, giving them considerable *microstructure stability* at elevated temperatures. Low diffusion rates are also synonymous with low rates of thermally activated creep, making fcc metals ideal for high temperature applications (Reed 2006).

However, as can be seen from Figure 2.26, the choice of viable candidates is quite limited. The Platinum group metals (PGMs) are very dense and very costly, as are gold and silver,

and mercury is liquid at room temperature. HCP are metals can be used, but out of them only cobalt provides a viable candidate (Os has a poisonous oxide, Tc is radioactive and Re and Ru are PGMs). Cobalt-base superalloys are in fact used; however they are more expensive than nickel-base and nickel-iron base, thus making them less commercially attractive (Reed 2006).

IIIB	IVB	VB	VIB	VIIIB	VIIIB	VIIB	IB	IIB	
21 Sc 44.956	22 Ti 47.90	23 V 50.942	24 Cr 51.996	25 Mn 54.9380	26 Fe 55.847	27 Co 58.9332	28 Ni 58.71	29 Cu 63.54	30 Zn 65.37
39 Y 88.905	40 Zr 91.22	41 Nb 92.906	42 Mo 95.94	43 Tc [99]	44 Ru 101.07	45 Rh 102.905	46 Pd 106.4	47 Ag 107.870	48 Cd 112.40
* 57 La 138.91	72 Hf 178.49	73 Ta 180.948	74 W 183.85	75 Re 186.2	76 Os 190.2	77 Ir 192.2	78 Pt 195.09	79 Au 196.967	80 Hg 200.59

BCC
← VIIIB →
HCP
FCC
Liquid

Figure 2.26 - Crystal structures of the transition metals and their position on the periodic table - taken from (Reed 2006)

Commercial viability is a large driver behind alloy development; alloy development is driven by component design, which is driven by commercial demand. Thus it is no surprise that alloys based on nickel, the fifth most abundant element on earth, have become the industry favourite.

2.5.3 Conventional Manufacturing

Conventional manufacturing refers to any established manufacturing process of which there are industry standards in place. In the case of superalloys it specifically relates to casting, wrought (forging/working) and powder metallurgy. Welding of superalloys will be covered in detail in a later section, as it is a joining process rather than manufacturing.

2.5.3.1 Investment casting

Investment casting, like any other casting, involves the solidification of molten material by means of heat extraction through the walls of a shaped mould. Disposable (generally wax) models of the component are covered in ceramic slurry, this then hardens and the wax is disposed of (usually with steam) leaving a moulded cavity. Molten material is then poured into the ceramic mould and allowed to cool and solidify. The mould is then destroyed to allow the removal of the components – hence ‘investment’ casting (Donachie and Donachie 2002), see Figure 2.27.

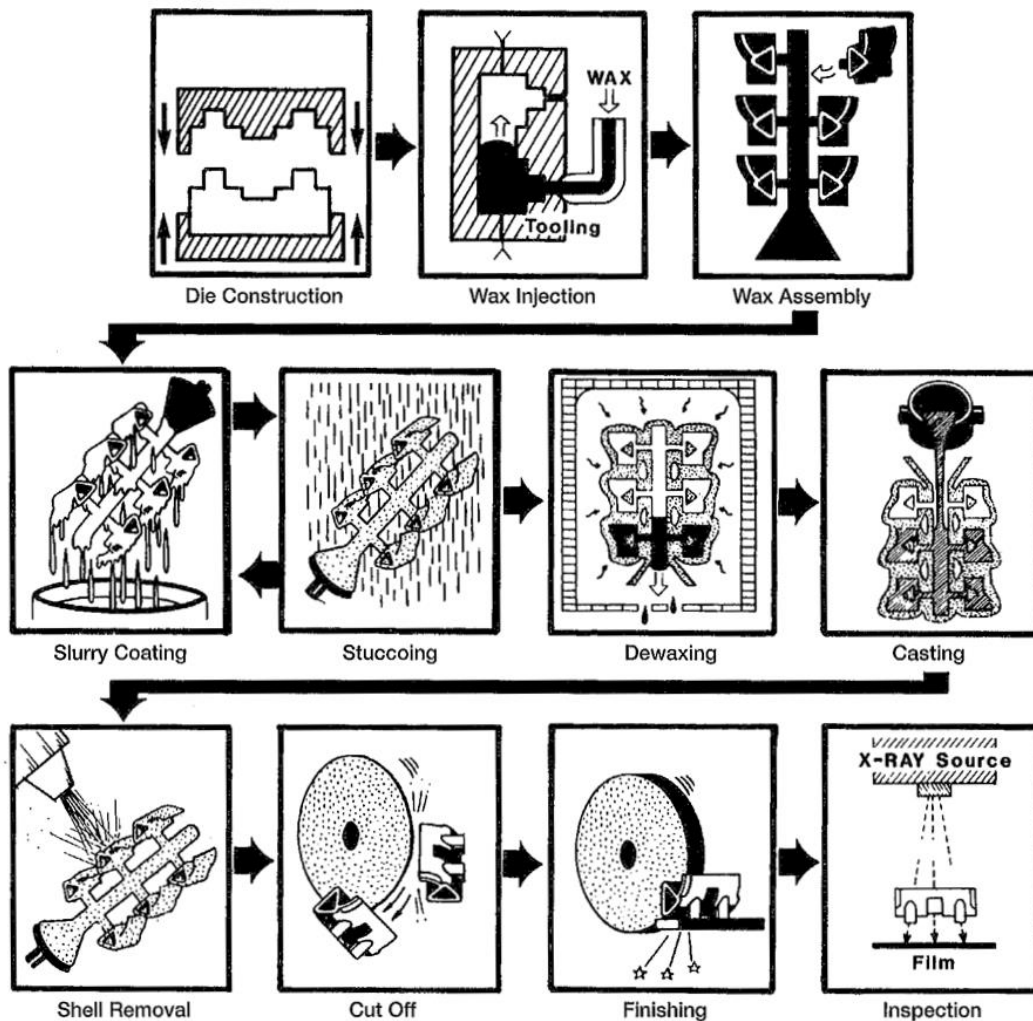


Figure 2.27 - Diagram detailing the stages of investment casting- direct from (Donachie and Donachie 2002)

Investment casting has been used heavily over the last 60 years in the manufacture of superalloy components, and specifically turbine blades or aircraft jet engines. In the 1950s nickel-base turbine blades were solid and forged from castings. However as the operating temperatures increased, internal cooling channels were required and investment cast blades took over (Donachie and Donachie 2002)

The grain structure which results from casting depends on strength and direction of heat extraction. Investment casting began with standard (uninfluenced) casting which resulted in a coarse poly crystalline structure similar to that described in Section 2.4.1. Directional solidification was then implemented to create a columnar grain structure, and then further to that single crystal structures. The coarse polycrystalline structure is stronger than the finer structure of forged components at elevated temperatures, and is also more resistant to creep due to reduced grain boundaries (Reed 2006). The columnar grain structure resulted in a substantial improvement in properties and allowed for the use of nickel superalloys which had previously abandoned due to low ductility. The first alloy to be commercially fabricated with DS was MAR-M-200, known as PWA 664 for DS, which as cast had a high tensile strength but average ductility. Processing with DS casting increased its ductility whilst maintaining the high tensile strength. Unfortunately, PWA 664 suffered from columnar grain separation at traverse grain boundaries. Addition of hafnium solved the issue, and the new alloy was named PWA 1422.

Single crystals are the ultimate in creep resistance due to the absence of grain boundaries, and allow for more freedom with composition variations leading to more exotic, higher performance alloys. Again, MAR-M-200 was the first single crystal alloy, but arguably the first commercial application was with PWA 1480 (Donachie and Donachie 2002).

As the requirement for greater cooling increased, blades with more complex internal designs were needed. The disposable models were becoming increasingly difficult to fabricate, bringing about one of the first applications of AM. Techniques such as stereolithography and selective laser sintering are used to generate 3D patterns in either wax or polymer, leading to the early adopted name 'Rapid Prototyping'. Interestingly in Donachie and Donachie (2002) direct fabrication of the turbine blades themselves by AM is already being considered.

2.5.3.2 Wrought and forging

Wrought alloys begin as cast ingots, but are then reheated and/or deformed numerous times until a desired property or microstructure is reached. The deforming process breaks up the coarse grains from casting into finer grain structure. Wrought alloys tend to be more homogenous than cast, as the segregation present in cast microstructures is dissolved and dispersed by the reheating and reforming. All of this means wrought alloys are typically more ductile than cast, lending themselves to the forming of large components such as turbine disks (Donachie and Donachie 2002). Any process which is forging or forming is considered wrought, for example: die forging, extrusion and rolling, see Figure 2.28.

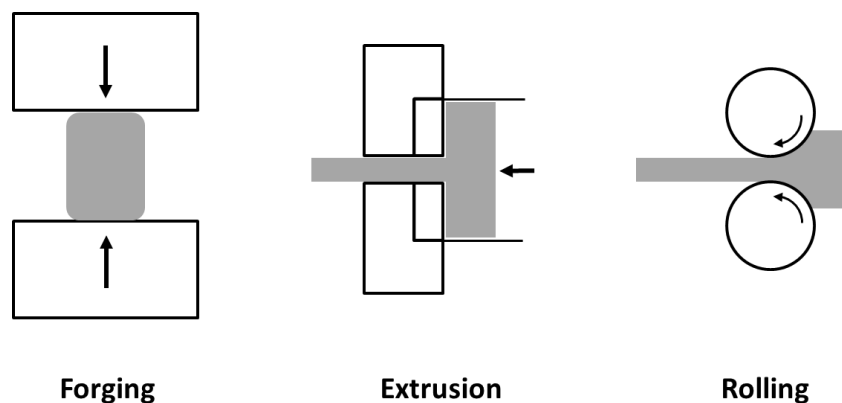


Figure 2.28 - Three common forms of wrought working - adapted from (Donachie and Donachie 2002)

The advantage of forging is the ability to impart designed material properties through the introduction of work energy by management and control of temperature and deformation. As such a range of properties can be obtained from a single alloy composition. However certain alloys are more forgeable than others. An alloy is principally forgeable if it can be deformed to a specific shape without creating surface ruptures or internal defects. The rating increases in multiples of 1 (easily forgeable) with increasing difficulty of forming i.e. more blows and more operations.

The design requirements for stronger and higher temperature performance nickel superalloys lead to a range of alloys which were increasingly less forgeable. High temperature steels such as A-286 have a forgeability rating of 1. However, Hastelloy X, which is not even used in high loading applications, has a rating of 3. Astroloy, designed for application in turbine disks, has a rating of 5 (Donachie and Donachie 2002).

A high rating does not mean the alloy is not forgeable; more that the energy and work required to form and shape it is significantly increased. However, for the ultra-high strength alloys such as Astroloy and Rene 95, forging was too impractical and costly.

2.5.3.3 Powder Metallurgy processing

Powder Metallurgy (P/M) processing is used exclusively for nickel superalloy production, and primarily for the high forgeability rated alloys designed for gas and jet turbine disks.

Principally, P/M uses high pressure and heat to consolidate powder into a net shape 'preform', which then requires machining and finishing to create the end product – much like forging. Its introduction stemmed from difficulties and cost of forging Astroloy as well as its tendency to suffer from scattering – chemical segregation. The solution was to employ the rapid solidification conditions of atomisation. Prealloyed feedstock (cast

ingot) was atomised into powder, with fine grain structure and minimal segregation, which was then consolidated – but not remelted – to fully density by P/M processes. (Donachie and Donachie 2002). The primary P/M technique is Hot Isostatic Pressing, or HIP(ing). Powder is poured into stainless steel containers which are either simple shapes for billets or, in the case of a preform, more complex moulds. The container is then placed with an autoclave and heated and pressurised isostatically using an inert gas, usually argon. Typical temperature and pressure values for nickel superalloys are 1100-1200 °C with 100 MPa (Donachie and Donachie 2002).

P/M requires fewer steps and reduced material input weight than forging (see Figure 2.29), meaning it can achieve the same level of microstructural refinement at a reduced machine cost. However, increased cost of prealloyed powder feed stock combined with high running costs of the machines mean P/M is only used when the alloy has a high forgeability rating or there is a property advantage (Donachie and Donachie 2002).

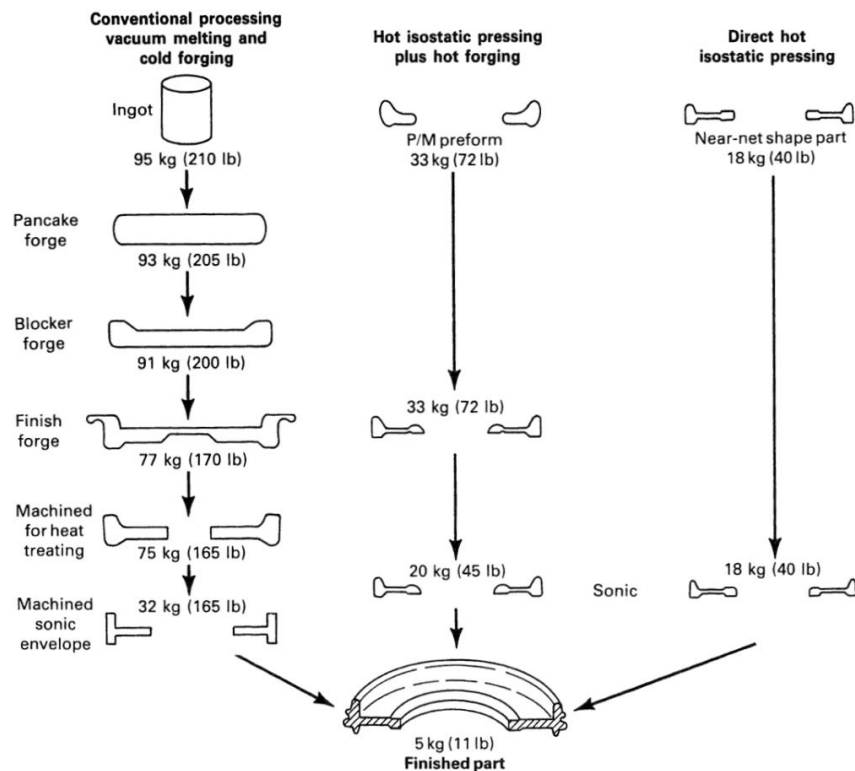


Figure 2.29 - Process steps for forging vs HIP and Direct Hip- direct from (Donachie and Donachie 2002)

The powder feedstock used for P/M is the same as that used for metal AM (if perhaps a different size range), however in the majority of AM processes, the powder is fully melted leading to new grain structures. The existence of P/M processing meant that there was no gap in supply of prealloyed powder feedstock for the new AM processes, and much of the relevant knowledge and understanding of powders already exists.

2.6 Superalloys - Metallurgy

2.6.1 Phases and microstructure

Phases of an alloy form as a result of differing melting points of solutes within solution. As the solution cools, the various phases will separate by means of differing solidification temperatures. The first phase to form, in which the majority of the solvent element will

reside, is known as the primary γ phase. All other phases are collectively known as secondary phases and include the γ' phase and carbides. This section details the all of the observed phases (beneficial and detrimental) in superalloys, including their microstructural contributions and the chemical forms which they take. The following list adapted from Donachie and Donachie (2002) and Gessinger (1984).

Phase	Crystal structure	Chemical form	Comments
γ	fcc structure	Solid Solution	This is <u>the</u> primary phase, it exhibits an fcc structure and nearly always forms a continuous matrix in which other secondary phases often reside
γ'	fcc	$\text{Ni}_3\text{Al}/\text{Ni}_3(\text{Al}_x\text{Ti}_y)$, with x and y varying between 0.5-1 and 0-0.5 respectively, depending on relative wt% of Al and Ti	This is the principal strengthening phase in the majority of nickel- and nickel-iron base superalloys. It exhibits an fcc structure, which varies in lattice size by only 0 – 0.5% from that of the γ matrix, and thus is often coherent with it. It forms as precipitates within the γ matrix, whose shape varies from spherical to cuboidal and whose size varies with temperature and cooling rates. In most modern superalloys, the precipitates are cuboidal.
γ''	bct (ordered D_{022})	Ni_3Nb	The second most important strengthening phase, occurs in nickel and nickel-iron base superalloys which have relatively high Niobium (Nb) contents. It precipitates within the matrix as coherent discs aligned in the {100} plane that have an average diameter of 600Å and thickness 50-90 Å. It is the principle strengthener in Inconel 718.

Carbides come in 4 forms, M represents metal element, C is carbon. Principle effect is improvement of creep-rupture strength by reduction of grain boundary sliding, full details of effects are described in subsequent section:

MC	Cubic	TiC, NbC and HfC, HfC most stable	Cubic structure – ‘M’ elements can be Ti, Nb, Hf, Ta, Thorium and Zr. Active in and at grain boundaries of the matrix and appears as globular, irregularly shaped particles
M₂₃C₆	fcc	Cr₂₃C₆ (Fe,W,Mo) ₂₃ C ₆	Form from the breakdown of MC’s at lower temperatures. It can precipitate as films,

			globules, platelets, lamellae and cells and mostly forms <u>at</u> grain boundaries. As films it is brittle having an adverse effect on ductility, however in globules it provides grain boundary strengthening.
M₆C	fcc	Fe₃Mo₃C Fe ₃ W ₃ C- Fe ₄ W ₂ C Fe ₃ Nb ₃ C Nb ₃ Co ₃ C Ta ₃ Co ₃ C	Randomly distributed carbides, usually pinkish in colour. Similar effects to mechanical properties as M ₂₃ C ₆ , however are more stable at higher temperatures. M elements are usually Mo or W.
M₇C₃	Hexagonal	Cr ₇ C ₃	Usually observed as blocky intergranular precipitate. In more complex alloys is unstable and transforms into M ₂₃ C ₆ .
M₃B₂	Tetragonal	Ta ₃ B ₂ V ₃ B ₂ Nb ₃ B ₂ (Mo,Ti,Cr,Ni,Fe) ₃ B ₂ Mo ₂ FeB ₂	Borides: Observe in Ni and Fe-Ni-base superalloys with a %wt of >0.03 Boron. Act in similar ways to carbides, also reside in grain boundaries. No preference of 'M' elements.
MN	Cubic	TiN (Ti,Nb,Zr)N (Ti,Nb,Zr)(C,N) ZrN NbN	Nitrides: Observed in alloys containing Ti, Nb Zr. Not insoluble in temperatures below the melting point. Have square rectangular shape.

The topologically close packed phases or tcp phases are regarded as highly undesirable.

They include the below phases and are detrimental to rupture strength and ductility.

They are more likely to form with greater segregation.

η	hcp (D0 ₂₄)	Ni₃Ti	This is an undesirable hcp phase which can be found in all superalloys with high Ti:Al ratios after extended exposure.
δ	Orthorhombic	Ni₃Nb	Observed in overaged Inconel 718. Forms between 815-980°C by cellular reaction.
μ	Rhombohedral	Co ₂ W ₆ (Fe,Co) ₇ (Mo,W) ₆	Usually observed in alloys with higher concentrations of Mo or W. Form as coarse irregular Widmanstätten platelets at high temperatures.

Laves	Hexagonal	Fe ₂ Nb Fe ₂ Ti Fe ₂ Mo Co ₂ Ta Co ₂ Ti	More common in the iron-base and cobalt base superalloys, usually appearing as elongated globules or platelets. Precipitate after long term high temperature exposure.
σ	Tetragonal	FeCr FeCrMo CrFeMoNi CrCo CrNiMo	Most common in iron-nickel- and cobalt-base superalloys. Similar in morphology to laves, but form after extended periods of exposure between 540°C and 980°C

2.6.2 Alloying elements and their effects (nickel and nickel-iron)

This short section details the various alloying elements specific to nickel-base superalloys. This gives a more general overview as to the choice of alloying elements. The below table has been created with information from Gessinger (1984) and Donachie and Donachie (2002).

Group	Elements	Effect
Matrix (γ) class	Co, Fe, Cr, Mo, W, V, Ti, Al, C*	Solid solution strengthening. *All are substitutional except for carbon, which is interstitial
γ'/γ''	Al, Ti, Nb, Ta	Precipitation strengthening
Carbide forming	Cr, Mo, W, V, Nb, Ta, Ti, Hf	Reduction of grain boundary sliding. Increasing creep-rupture strength
Boride forming	Mo, Ta, Nb, Ni, Fe, V	Similar to carbides
Nitride forming	Ti, Zr, Nb, C
Grain boundary active	Zr, B	Enhance creep strength and rupture ductility
Additional	Co	Raises solvus temperature of γ'
	Al, Cr, Y, La, Ce	Oxidation resistance
	La, Th	Improve hot corrosion resistance

Cr, Co, Si	Sulfidation resistance
B, Ta	Improves creep properties**
B, C, Zr, Hf	Grain-boundary refiners**
Re	Retards γ' coarsening

** By means of the formation of borides and carbides

2.6.3 Strengthening

If one wants to control the mechanical properties of a superalloy, then one needs to be able to affect the microstructure. This is achieved by control of the processing conditions or the chemical composition (Reed 2006). A good example of strengthening by processing is wrought; where the microstructure of a cast alloy is physically altered by forming. However, in the majority of cases, an alloy's strength is controlled by both process conditions and chemical composition.

As has already been discussed in Section 2.6.2, an alloy's chemical strength comes from the addition of alloying elements and the formation of phases. Depending on which phase is active, the strengthening effects fall into three main categories: Solid Solution Strengthening (SSS), precipitation strengthening and grain boundary strengthening.

Ultimately, the strength of metals is dependent on the propagation of dislocations through the crystal structure. Dislocations occur in all real life materials, and the type and magnitude of these dislocations strongly affect a material's properties. Dislocations come in 3 forms: edge, screw and mixed, where mixed is a part way between the other two. In real life materials it is generally mixed (Tilley 2013).

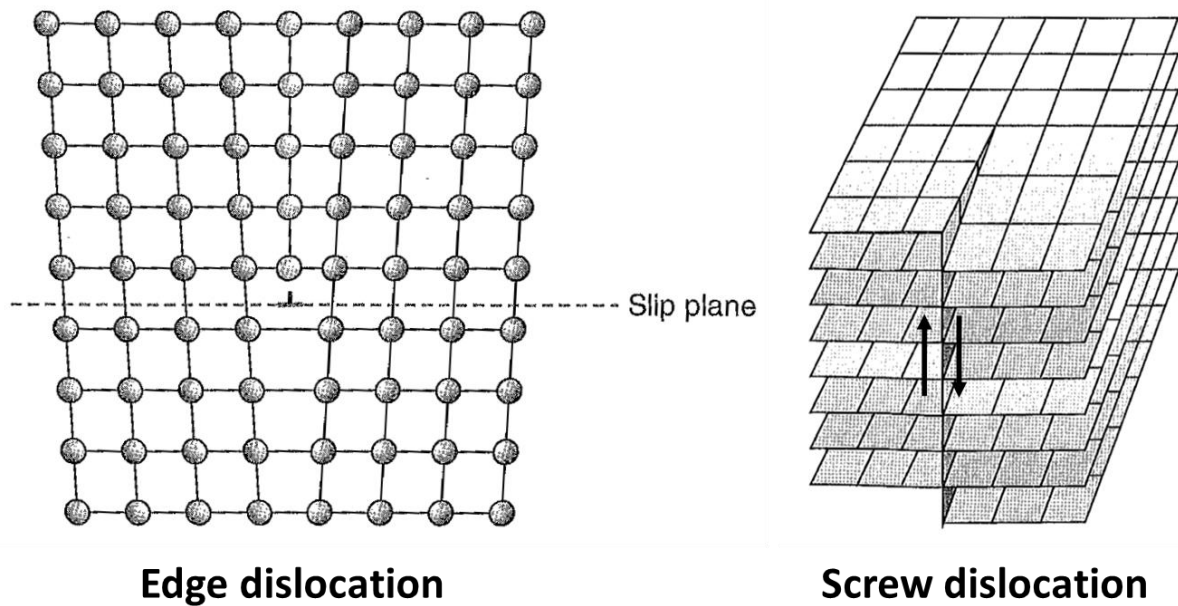


Figure 2.30 - Schematic of edge and screw dislocations– adapted from (Tilley 2013)

Dislocations form stress fields around them, which are specific to the type of dislocation. When stress is applied to the material, the dislocation propagates causing local deformation. In a brittle material, the energy required to propagate a crack is less than that required to propagate a dislocation, in a ductile material the opposite is the case (Newey and Weaver 2013).

2.6.3.1 Solid-solution strengthening

When solvent atoms are placed within a solute lattice, local stress fields are formed as a result of both lattice distortions (differing atomic size and lattice parameters) and differing atomic moduli. A difference in lattice parameter results in a high stress field around the solute atom, which will interact with those of the dislocation and inhibit its propagation (Tilley 2013). A difference in modulus changes the local energy around the dislocation, increasing the magnitude of the energy well and hence increasing the force required to move past it. Both of these effects result in an increase of the yield stress of the lattice (lattice stress), and therefore an increase the *yield strength* of a material.

Depending on the relative size of the solute atoms, they will cause different types of lattice distortion. If the solute atoms size differs by less than 15% of that of the solvent atoms, then it can replace a solvent atom in the lattice forming a substitutional solid solution (Tilley 2013). If this results in increased lattice stress then it is referred to as *Substitutional Solid Solution Strengthening (SSSS)*– see Figure 2.31. Substitutional solute atoms generate spherical stress fields, which have no shear stress component. This means they cannot interact with screw dislocations, as they possess shear stress fields.

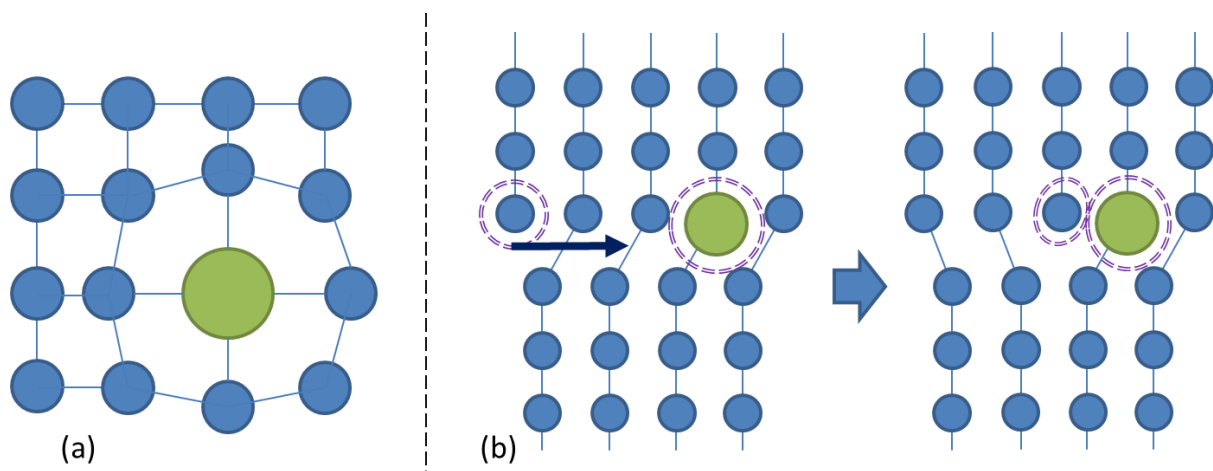


Figure 2.31 - a) representation of substitutional solute atom (green) in lattice, b) propagation of edge dislocation through lattice being prevented by solute atom. Stress fields (purple rings) of substitutional atom and dislocation repel each other, inhibiting further propagation– adapted from (Gedeon 2010)

If the solute atom is similar in size or smaller than the solvent atoms, it can occupy the interstices of the lattice. This is known as *Interstitial Solid Solution Strengthening (ISSS)*. Interstitial atoms create tetragonal distortion, which *can* interact with sheer stress fields and hence edge, screw and mixed dislocations – see Figure 2.32. As a consequence small interstitial solute atoms such as carbon, tend to be the more effective solid solution strengtheners, per unit space (Donachie and Donachie 2002). One of the most common examples of ISSS is in carbon solute in iron, otherwise known as steel. In this system, the

carbon atoms are distributed randomly throughout the fcc structure of the iron, forming austenite (Tilley 2013).

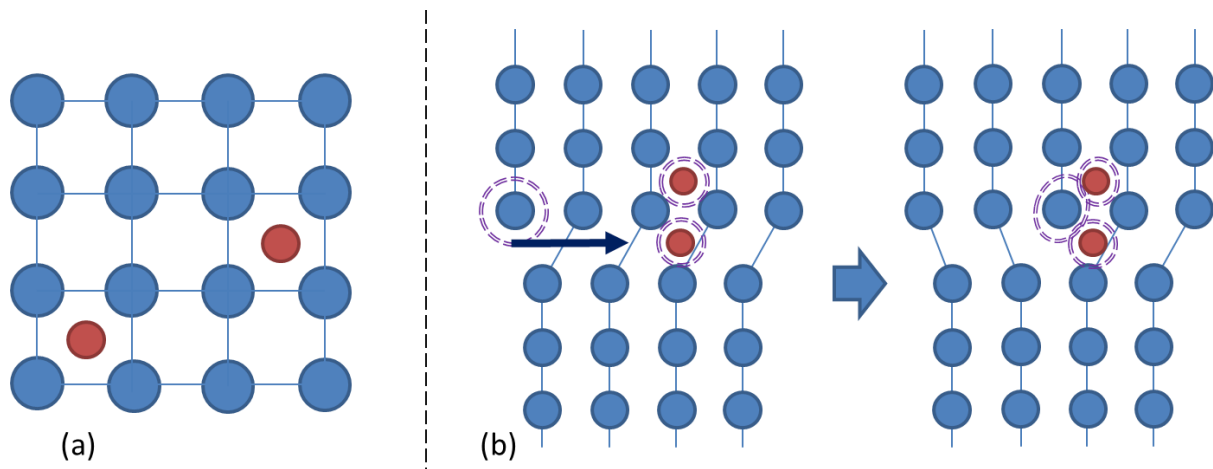


Figure 2.32 - a) Representation of interstitial solute atom (red) in lattice, b) as with Figure 2.31- adapted from (Gedeon 2010)

If we now consider the stress required to move the dislocation, τ :

$$\Delta\tau = Gb\epsilon^2\sqrt{c}$$

Equation 2.16

Where G is the shear modulus, b is the magnitude of the Burger's vector, ϵ is the lattice strain caused by the solute and c is the concentration of the solute atoms. It can be seen from Equation 2.16 that an increase in the concentration of solute atoms, will lead to an increase in τ and thus an increase in the material's yield strength. However, this is not a limitless solution as each solvent has a solubility limit for any given solute. It is also only applicable for a single solute in solution. In multiple element alloys, compositions must be carefully balanced so as to maintain a full solution and the prediction of resulting lattice stress is far more complex.

2.6.3.2 Precipitation strengthening

In Section 2.6.1, the various elements involved in precipitation strengthening were highlighted. The term encompasses the strengthening effects of any precipitate (secondary) phase, however it is usually only in reference to the γ' and γ'' phases. As in solid solution strengthening, it is the impediment of dislocations by the precipitates which acts to strengthen the alloy. The effectiveness of the precipitation strengthening depends on a number of factors: precipitate-matrix crystal coherence, crystal order and precipitate size.

The most effective strengthening is typically achieved when the precipitates crystal structure is coherent with that of the matrix, however semi-coherent and incoherent matches can still provide strengthening. In the optimal situation, the two would have the same crystal structure and a similar crystal lattice size. The greater the coherence, the more precipitate one can pack into the matrix lattice. Thereby increasing the density of blocking 'elements' and increasing dislocation impediment. In real world nickel-base superalloys coherence achieved is approximately 99- 100% (Donachie and Donachie 2002).

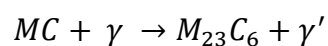
Precipitates such as γ' and γ'' have ordered crystal structures i.e. atomic position preference. Ordered states have greater energies than disordered, thus the introduction of an ordered precipitate into a comparatively disordered matrix creates an energy 'wall'. The higher energies increase the force required for dislocations to propagate (Reed 2006).

The size of precipitates probably has the greatest effect on the mechanical properties of the alloy. Optimal size is dependant of the desired property; if the precipitates are too small they will not block any dislocations effectively, too large and the dislocation will

bow and strength will be lowered (Donachie and Donachie 2002). Creep-rupture strength benefits from smaller precipitates, whereas larger precipitates promote yield strength. In reality, this results in compromises or the sacrifice of one property for the gain in another.

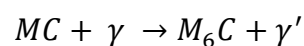
2.6.3.3 Carbides and grain boundary strengthening

Principally, carbides are used to strengthen grain boundaries, increase creep-rupture strength, prevent grain-boundary sliding and permit stress relaxation. They can also act as substitutional solid solution strengtheners if they form fine precipitates within the matrix structure. A tertiary effect is that the carbides often tie up potential detrimental elements, which may otherwise cause phase instabilities during service. The several types of carbide usually co-exist, but they do not all form at the same time. MC are generally (depending on the M element) high temperature forming, and thus tend to form in the molten state. M_6C is intermediate (816-982°C), and $M_{23}C_6$ and M_7C_3 are low temperature (790-816°C) (Donachie and Donachie 2002); these are generally formed by breakdown reactions of the MC, as seen in the below equations.



Equation 2.17

and



Equation 2.18

MC carbides are fcc in structure and are distributed heterogeneously through the alloy. They can be found in both intergranular and transgranular locations, often in the interdendritic regions. As well as forming in the melt they can also form in the

precipitation from supersaturated solid solutions at high temperatures (>1038°C). In order of decreasing stability, the preferred natural order of MC carbides is HfC, TaC, NbC and TiC. These are not mutually exclusive compounds and the metallic elements can readily substitute each other e.g. (Ti,Nb)C and even certain less reactive elements such as Mo can be substituted e.g. (Ti,Mo)C (Donachie and Donachie 2002).

$M_{23}C_6$ is the primary grain boundary carbide and if formed correctly, occurs as irregular, blocky and *discontinuous* particles, as in Figure 2.33. In some cases, the MC particles can be coated in a layer of γ' precipitate; this addition increases the ductility of the grain-boundary layer (Gessinger 1984). The M_6C carbide can also precipitate as a blocky particle in the grain boundaries, as well as sometimes forming in a Widmanstätten intragranular morphology. Unlike MC carbides, M_6C have a complex cubic structure and can only form if the molybdenum and/or tungsten content is more than 6 at.% (Donachie and Donachie 2002).

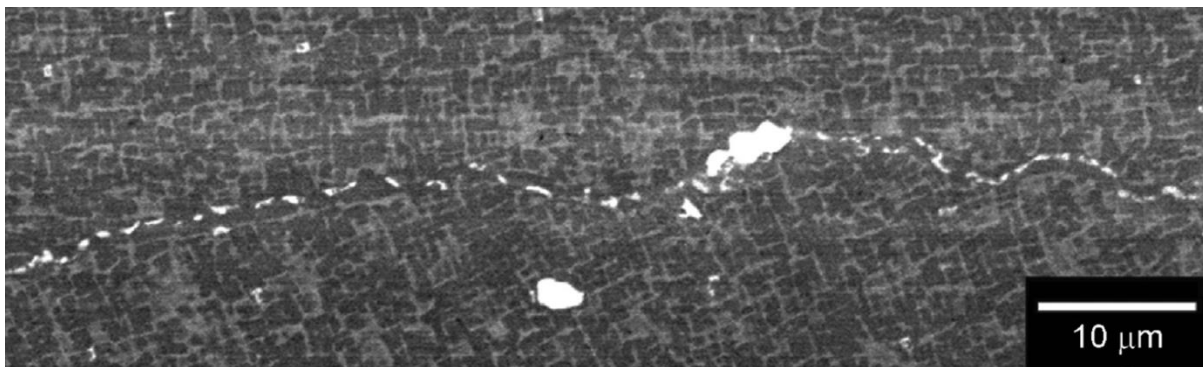


Figure 2.33 – $M_{23}C_6$ carbides precipitated along the grain boundary of an experimental superalloy during creep testing at 950°C and 290 MPa – direct from (Reed 2006)

Similar to carbon, boron has been found to improve the elevated temperature creep properties of superalloys. The small size of the atom allows it to diffuse relatively easily through the matrix and as with carbon it tends to concentrate and precipitate at the grain boundaries of the γ matrix (Reed 2006).

2.7 Cracking in welding of Ni-base alloys and superalloys

In this section, established mechanisms for welding induced cracking in nickel alloys and superalloys are discussed and considered. In the absence of research on cracking mechanisms for AM or SLM, welding is the closest process with regards to solidification conditions. It must be stressed that the applicability of these mechanisms to the SLM process is not to be assumed at this stage, but that they are kept in mind for the chapters and sections which follow.

2.7.1 Solidification cracking

The use of solidification cracking as a general term must be done so with care, as it refers to a specific cracking mechanism. Solidification cracking occurs in the final phase of solidification, where a thin film of liquid phase remains at the grain boundary, and sometimes interdendritic regions, at the point in time when the solid phase is beginning to shrink. The liquid film offers no resistance to the strains generated by the shrinking grains and a crack opens up along the grain boundary (Lippold, Kiser et al. 2011). The 'terminal solidification films' are eutectic type compositions, the formation of which is permitted by solute diffusion. The fraction of liquid film which forms can vary with alloy composition and is dependent on the solidification temperature range of the alloy, as well as solidification conditions (Lippold, Kiser et al. 2011). Solute diffusion is therefore an important factor in solidification cracking, as it affects both the solidification temperature range at the solid-liquid interface and the formation of the eutectic type phase. The existence of a solidification temperature range results in formation of a solid+liquid zone, called the mushy zone. It is within the mushy zone that the terminal liquid film forms and a solidification crack propagates. The longer the mushy zone exists, the greater the window for solidification cracking is. Higher solidification rates should therefore inhibit

the solidification cracking mechanism, but this is highly dependent on the diffusion rates of the alloy elements.

Figure 2.34 shows solidification cracking in Alloy 625 and Alloy 230W. In Alloy 625 it was observed that terminal eutectic liquid phase fraction was high enough to heal the crack that had formed (Lippold, Kiser et al. 2011). However, in Alloy 230W, the film is so thin that it is not observable and only the crack can be seen. The morphology of the cracks is relatively unique as it follows the path of grain boundaries only, and because there has not been any rupturing or fracturing of solid phase material, the crack edges are relatively smooth.

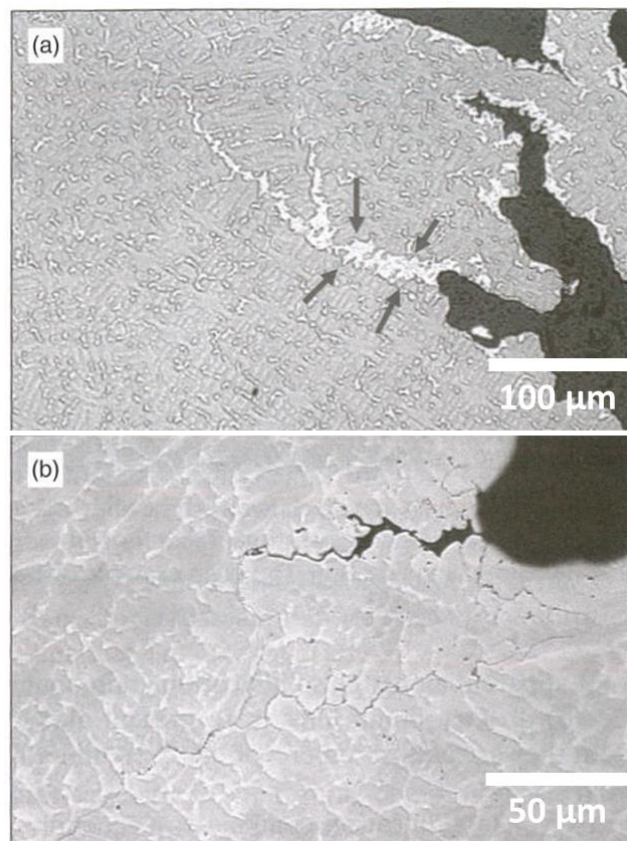


Figure 2.34 - Solidification cracking in a) Alloy 625 and b) Alloy 230W. Light area highlighted by arrows in a) is Nb rich eutectic which has healed the crack. In Alloy 230W the liquid film has a lower volume fraction and the cracks remain- adapted from (Böllinghaus, Herold et al. 2008).

The susceptibility to solidification cracking has been quantified for some alloys by means of determining the Solidification Cracking Temperature Range (SCTR), which is smaller or equal to the solidification temperature range of the alloy. Alloys which are particularly susceptible to solidification cracking are Alloy 625 with an SCTR = 210 K, Hastelloy X with SCTR = 190 K and Hastelloy W with SCTR = 145 K (Lippold, Kiser et al. 2011). As a general indication, the larger the solidification temperature range of a nickel superalloy the more susceptible it is to solidification cracking.

2.7.2 Heat affected zone (HAZ) Liquation cracking

HAZ liquation cracking occurs when solid material adjacent to fusion zone is exposed to a range of peak temperatures resulting in partial melting of the microstructure, or Partially Melted Zone (PMZ). Similar to solidification cracking, the partially melted material cannot withstand the thermally induced strains and forms a crack. There are two mechanisms established as causing HAZ liquation cracking, solute segregation and melt penetration (Lippold, Kiser et al. 2011).

Segregation of solutes or impurities to the grain boundary depresses the melting temperature in the local region. In the PMZ, the material is now more likely to form a liquid film along the grain boundary as the low melting composition is already present. This is different to solidification cracking as the segregation has already occurred and it is subsequent heating that is driving the mechanism.

In penetration, local melting in the microstructure is intersected by a mobile grain boundary. The liquid then penetrates, and moves along, the grain boundary and a crack forms as above (Lippold, Kiser et al. 2011).

2.7.3 Ductility dip cracking and ductility minimum

2.7.3.1 Elevated temperature ductility minimum

The elevated temperature ductility minimum is a phenomenon that occurs when nickel superalloys are plastically deformed at elevated temperatures. The critical temperature at which this occurs, is approximately 760°C or 1400 °F – an often chosen temperature for elevated temperature tensile testing (Arkoosh and Fiore 1972).

The precise mechanism is detailed in Arkoosh and Fiore (Arkoosh and Fiore 1972) but simply: the plastic deformation initiates the rapid formation of MC carbides, the higher the temperature, the more carbides form. At first the carbides act against dislocation slip and deformation, affectively reducing the ductility of the material. This occurs to up a point – the ductility minimum – beyond which the depletion of solid solution strengthening elements in the matrix becomes more significant and normal ductility resumes.

2.7.3.2 Ductility Dip Cracking (DDC)

DDC may be perceived as a more general term as it is often used incorrectly or inconsistently in literature. However specifically it refers to the cracking of an alloy as result of a sudden dip in ductility over a temperature range (Lippold, Kiser et al. 2011). This can occur as a result of the mechanism detailed in Section 2.7.3.1, but also due to segregation of minor elements and formation of secondary phases such as carbides. In nickel base weld metals, cracks are always observed along a migrated grain boundary (Lippold, Kiser et al. 2011). Migrated Grain Boundaries (MGBs) form from the primary solidification grain boundaries and are a separation of the crystallographic component from the compositional component. MGBs carry the same high angle misorientation as the parent solidification grain boundary; they form as result of straightening of the

crystallographic boundary to a lower energy state and pull away from the solidification grain boundary. The formation of an MGB is more likely in multiple pass welds, due to reheating.

There have been a number of theories over the years as to the mechanisms behind DDC, most recent of which was proposed by Young, Capobianco et al. (2008) who investigated the effect of chromium content in DDC of welded Ni-Cr alloys.

Full microstructural, chemical, tensile analysis and finite element modelling all indicated that the DDC was caused by a combination of macro, thermal and solidification stresses induced by the welding, and local grain boundary stresses generated during precipitation of partially coherent $(Cr,Fe)_{23}C_6$ carbides at the grain boundaries, see Figure 2.35.

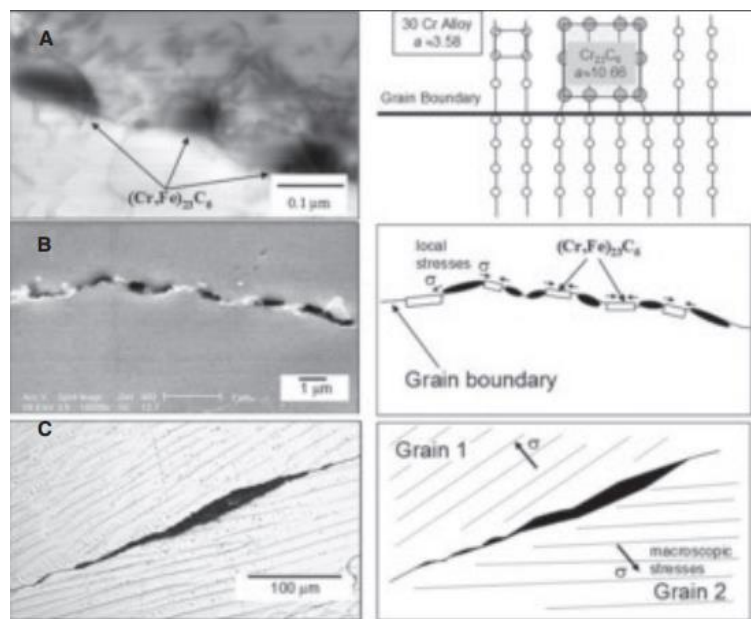


Figure 2.35 - Pictorial description of PIC cracking. A) partially coherent sub-micron sized $(Cr,Fe)_{23}C_6$ form on grain boundary in reheated weld metal creating significant mismatch. B) precipitation creates stresses between carbides, promoting crack nucleation. C) macroscopic thermal and solidification stresses link the intercarbide cracks resulting in DDC along the grain boundary (Young, Capobianco et al. 2008).

This mechanism of Precipitation-Induced Cracking (PIC) can be mitigated by alloying to minimise the formation of the problem carbides (Cr and Fe), through Nb or Ti additions which form NbC and TiC instead. These simple carbides promote the formation of tortuous grain boundaries which more resistant to DDC (Lippold, Kiser et al. 2011). It is noted that chromium content is the primary factor in DDC of welded nickel alloys, and as such alloys with low chromium content are not as susceptible to DDC.

2.7.4 Elevated temperature solid state cracking

Elevated Temperature Solid State (ETSS) cracking is crucially different to solidification or liquation cracking because it occurs once the material is in solid phase. In the case of ETSS, the material has fractured (or ruptured if ductile) in response to high thermal stresses induced by the process. It is different to DDC in mechanism in that it is not caused by a sudden drop in ductility or exhaustion of ductility (Lippold, Kiser et al. 2011). Quite simply it occurs when the local stress exceeds the UTS of the material in its current state.

ETSS cracks are visually very similar to DDC cracks and identifiable by the exposed crystal structure within their interiors and a distinctly jagged profile. They are most likely to form along the solidification grain boundaries as they are typically the path of least resistance. High magnification electron microscopy and EDS can be used to check for the presence of carbides or segregated solutes, which are indicative of DDC. If there is no presence of secondary phases or concentrated solutes it is then assumed that the fracture has occurred purely as a stress relaxation mechanism.

2.7.5 Elements associated with cracking mechanisms

The majority of the cracking mechanisms detailed in the previous sections are influenced by the concentration of solute elements (including impurities), however which elements and in what concentrations varies depending on the alloy. To date, there is insufficient data in the public domain to draw any conclusions regarding the effects of certain solute elements on the 'processability' of an alloy for SLM. In section 2.7.3, carbon and other solute elements were implicated as having influence on DDC of nickel alloys and superalloys. However, many of these elements serve a specific purpose once the alloy is in operational state and therefore it is important to identify which elements, and at what concentrations, are detrimental to weldability.

2.7.5.1 Carbon

From Section 2.6, it is known that the primary purpose for carbon in superalloys is to form carbides. Carbides, when present in optimum size and numbers, are central for grain boundary strengthening and creep resistance. It is also used as an interstitial solid solution strengthener.

Due to their small size, carbon atoms sit interstitially within the lattice. This allows them to move relatively freely through the lattice as they jump from interstice to interstice. This high mobility allows carbon to segregate to regions of high energy (or stress) such as grain boundaries, even in rapid solidification conditions. The segregation increases the likelihood of carbide formation, which generates localised stress fields and can lead to DDC (Section 2.7.3). This is a particularly prevalent problem in welding of nickel base alloys, resulting in the creation of low carbon (LC) versions of cast or wrought alloys.

Work by Collins and Lippold (Collins and Lippold 2003) reviewed the reported effects of carbon (and other minor element) content on weldability and micro-cracking of nickel based filler materials.

In concentrations of <0.1 wt%, it is shown to have only minor effect on micro-cracking. However, for concentrations >0.1 wt% it can have an effect on solidification path which can influence micro-cracking behaviour. The reason for this is that the increased volume fraction of carbides at the grain boundary ensures a liquid film is retained to lower temperatures. This allows for increased risk of solidification cracking, but importantly does affect DDC.

Although the formation of carbides has been linked to DDC (Young, Capobianco et al. 2008), carbide formation requires both carbon and the M element in sufficient concentrations (Donachie and Donachie 2002) and in Young, Capobianco et al. it was excessive M element concentration that was highlighted as being the problem.

In consideration of ETSS cracking, an increase in yield strength is often associated with a reduction in ductility or increase in stiffness. It must therefore be considered that carbon content could have an effect on the ETSS by reducing the ductility of the superalloy. As a case study, a comparison between the chemical composition and tensile performance of IN713C and IN713LC, high and low carbon versions of the same alloy base, is detailed in Table 2.3 and Table 2.4 respectively.

Alloy/Element	Ni	Cr	C	Mo	Al	B	Ti	Ta	Zr	Other
IN713C	74	12.5	0.12	4.2	6	0.012	0.8	1.75	0.1	0.9 Nb
IN713LC	75	12	0.05	4.5	6	0.01	0.6	4	0.1	-

Table 2.3 - Nominal compositions of IN713C and IN713LC, values in wt% (Donachie and Donachie 2002).

Alloy/Temp	UTS (MPa)		Yield strength (MPa)		Elongation (%)	
	21°C	538°C	21°C	538°C	21°C	538°C
IN713C	850	860	740	705	8	10
IN713LC	895	895	750	760	15	11

Table 2.4 - Tensile data for room and elevated temperature of IN713C and IN713LC (Donachie and Donachie 2002).

It is observed that, with the exception of a few elements, the compositions of the two alloys are near identical. The carbon content of IN713LC is significantly reduced, but there is also a large increase in the concentration of tantalum, which forms secondary phases and is used for precipitation strengthening. This could be the reason that IN713LC outperforms IN713C for tensile strength across the temperature range, whilst still having an increased (if only marginally) ductility. The tensile properties certainly place doubt on the proposal of carbon reducing ductility as a compromise for increased tensile strength, however the addition of tantalum and the fact that the tensile tests have been carried out on solution treated and aged samples muddies the comparison. Interestingly the nominal carbon content of IN713C is above the 0.1 wt% limit for excessive carbide formation leading to increased chance of solidification cracking, as highlighted by Collins and Lippold. This, combined with tensile properties, all but confirms that the reduction of carbon in nickel alloys to increase weldability is to reduce the chance of solidification cracking and not to increase the ductility and prevent ETSS cracking.

2.7.5.2 Other minor elements

Minor elements are elements within an alloy which are of ~2 %wt or less. They can be purposeful additions, such as carbon in steel (typically <1 %wt) or impurities, such as sulphur, which are inherent with the addition of certain alloying elements.

From Collins and Lippold (Collins and Lippold 2003), varying concentrations of C, Si and S in Inconel 718 between 0.007-0.05%, 0.05-0.25 and 0.0006-0.0027 wt% respectively, had no effect on micro-cracking under welding. However, combinations of S, P and B can yield better or poorer weldability depending on the ratios, making it difficult to pin point any one particular element. The general conclusions were as follows:

- Sulphur should be kept as low as possible as it is a tramp element and imparts no particular benefit to the alloy or its weldability. Sulphide formers such as Mg, Ti, Zr and Mn can be used to combine with sulphur and reduce its effects.
- Phosphorus – high P values can be used to improve creep properties, but generally it is to be considered in a similar vein as sulphur.
- Boron should be kept as low as possible, but not so low as creep properties are affected
- Synergistic or competitive relationships between B, C and P relative to weldability have been observed, but cannot be quantified.

Savage and Krantz investigated 'Hot cracking in Hastelloy X' (Savage and Krantz 1966) and 'Microsegregation in autogenous Hastelloy X welds' (Savage and Krantz 1971). Although not specifically named, the cracking mechanism implied is DDC rather than 'hot cracking', which is now associated with solidification or liquation cracking (Lippold, Kiser et al. 2011). In the 1966 study, the relationship between micro cracking and solute segregation was investigated, with particular focus on S, Si and Mn. Optical microscopy showed that micro-cracking had occurred exclusively in regions exhibiting segregation, and it was also confirmed that the microsegregation in the fusion zone had occurred as a result of the solidification process.

Savage and Krantz (1971) sought to identify all of the solute elements which had segregated, and establish which species (secondary phases) they had formed as a result. Solute segregation at the grain and sub-grain boundaries was confirmed by specimen-current imaging. These regions were found to have high concentrations of Mo, S and Si, moderate concentrations of Cr and Mn and were depleted in Ni, Fe and Co. Powder analysis revealed the presence of six sulphides, three carbides, two nitrides and 2 'miscellaneous' species. It was deemed, by argument of known physical properties and metallurgical behaviour, that only the sulphides (Co_2S_4 , Cr_5S_6 , Cr_7S_8 , $\text{Fe}_{x-1}\text{S}_x$, MnS and MoS_2) and carbides (M_6C , M_{23}C_6 , $(\text{Cr,Fe})_7\text{C}_3$) were detrimental to crack behaviour. The carbides were observed to assist liquation cracking by providing 'easy' nucleation sites, whilst the sulphides are believed to reduce crack resistance and are responsible for the poor cracking behaviour in a 'high sulphur' version of Hastelloy X.

Interestingly, although silicon is revealed to be very mobile, it is not deemed to have a direct influence on the cracking resistance of the alloy – contrary to more recent publications (Tomus, Jarvis et al. 2013, Yu, Rombouts et al. 2013).

2.7.5.3 Possible effects of hydrogen inclusion

Hydrogen has been shown to have a pronounced negative effect on the DDC of Ni-base welding filler metals (Collins and Lippold 2003). Cracking was found to be quite significant at temperatures between 850 – 1000°C with 1% applied strain. Rather than creating a new mechanism, it increased the number of susceptible grain boundaries. It must be stressed that hydrogen was added to melt using 95Ar-5H₂ shielding gas, rather than being present in the metal before welding; also that samples were heated and loaded, and cracks which formed as consequence of welding alone were not considered.

Ordinarily hydrogen cracking is not a concern in fully austenitic (fcc) structures because hydrogen has a high solubility and low diffusivity (in austenitic structures). However, *atomic* hydrogen is an extremely mobile interstitial addition and may increase DDC cracking if it occurs in sufficient concentration. Through optical microscopy, it was found that cracking was predominant at triple point intersections, supporting the hypothesis that hydrogen diffuses to regions of the crystal lattice where tensile stress concentrations are present, decreasing grain boundary cohesion and ultimately increasing DDC susceptibility.

2.8 SLM processing: Nickel alloys, thermal stress and crack formation

2.8.1 Nickel superalloys: microstructure, mechanical properties and defects

There have been a number of studies on nickel superalloys processed by SLM, the majority of which have investigated effect of process parameters on densification and microstructure. To date, nickel superalloys reported to have been processed with full density are Inconel 718 (Amato, Gaytan et al. 2012, Wang, Guan et al. 2012), Inconel 625 (Amato 2012, Savitha, Gokhale et al. 2012), Nimonic 263 (Vilaro, Colin et al. 2012), Inconel 939 (Kanagarajah, Brenne et al. 2013), Inconel 738 LC (Rickenbacher 2013) and Hastelloy X (Wang 2011). The range of alloys in this list should not be surprising, as the stability of the nickel base fcc structure means the alloy does not experience phase changes before melting making it easy to melt and fuse.

The microstructure conforms to that observed in other materials. Wang, Guan et al. (2012) highlights the absence of γ'' Ni₃Nb precipitates in as processed Inconel 718, and attributes this to inhibition of precipitate formation due to high solidification rates. Conversely Amato, Gaytan et al. (2012) argue the presence of γ'' precipitates through XRD

and TEM analysis. In the XRD, although γ'' -bct Ni_3Nb peaks are detected, both the (200) and (220) texture coincide with those for the γ -fcc matrix peak and it is conceded that additional evidence is required. TEM appears to show 'lenticular-like/oblate ellipsoidal' γ'' precipitates coherent with [100] planes, orthogonal to the build direction, as well as some coincident to the [010] plane (parallel to build direction) – see Figure 2.36.

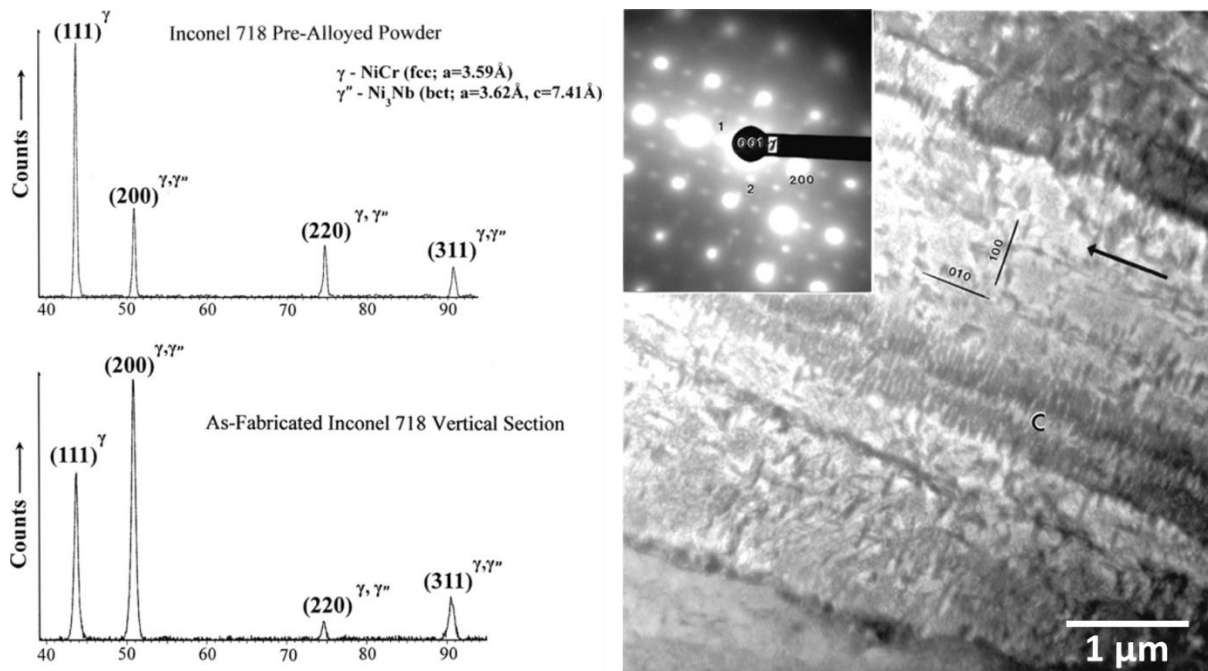


Figure 2.36 - XRD spectra peaks for pre-alloyed Inconel 718 powder compared to as processed SLM processed Inconel 718 (left). Supporting TEM image apparently showing nano precipitates of Ni_3Nb in as processed SLM processed Inconel 718 (right) – adapted from (Amato, Gaytan et al. 2012)

Vilaro, Colin et al. (2012) observed no γ'/γ'' precipitates in SLM processed Nimonic 263, stating that solidification rates were high enough to inhibit their precipitation. However, high magnification SEM imaging appears to show the presence of sub-micron sized carbides surrounding interdendritic regions. Vilaro states that the segregation of Ti solute to the interdendritic region is sufficient to allow the precipitation of TiC carbides. The microstructural features to which Vilaro refers, are actually seen to be distributed throughout the crystal structure, some even within the centre of a dendrite, which

conflicts with the statement, see Figure 2.37. Unfortunately, there is no additional data to confirm the chemical composition of the features.

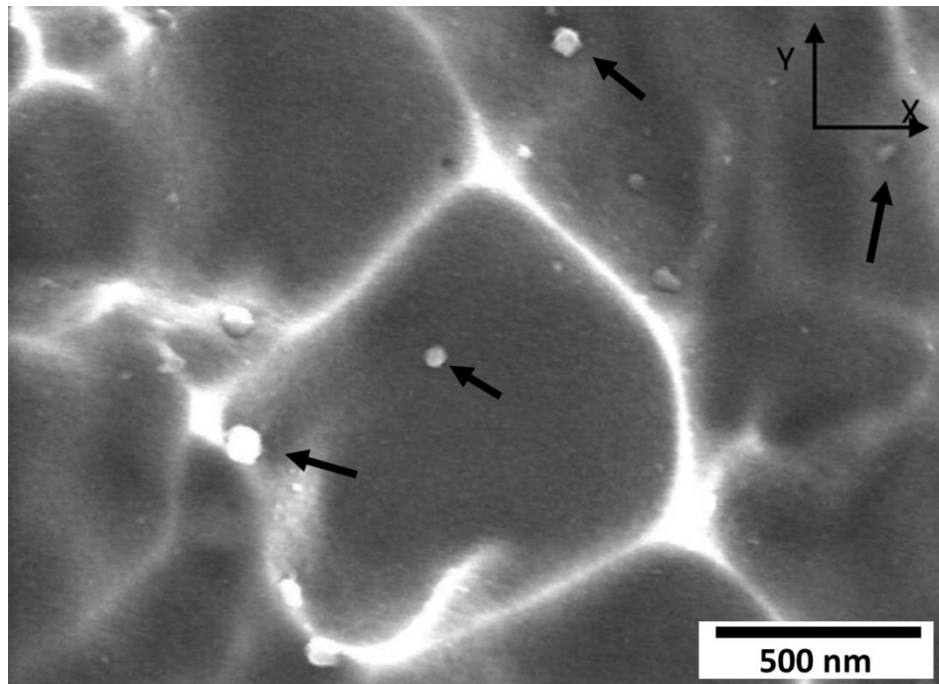


Figure 2.37 - Proposed TiC carbides highlighted by arrows, in Nimonic 263 processed by SLM – adapted from (Vilaro, Colin et al. 2012)

Precipitation strengthened alloys, such as Inconel 718, therefore still require solution treatment and aging if the designed properties are to be achieved. Indeed, in the as processed state, the room temperature yield strength of Inconel 718 was reported to be 889-907 MPa, compared to 1030-1167 MPa of wrought and aged. However once the SLM processed Inconel 718 was heat treated, yield strength increased to 1137-1161 MPa. UTS, Young's modulus and elongation were also all equivalent once heat treated (Wang, Guan et al. 2012). Amato, Gaytan et al. (2012) reported similar results, but reported that the SLM and heat treated Inconel 718 had slightly superior tensile strength to the equivalent wrought. In fact for the majority cases, once heat treated and/or aged, precipitation strengthened alloys have comparable or superior tensile properties when processed by

SLM compared to wrought (Vilaro, Colin et al. 2012, Kanagarajah, Brenne et al. 2013, Rickenbacher 2013).

The same is true for solution strengthened alloys such as Hastelloy X. Wang (2011) reports room temperature yield strength, UTS and elongation values of between 812- 816 MPa, 923-937 MPa and 34-36 % respectively for the as processed state. Compared to max yield strength 385 MPa and UTS of 775 MPa and elongation 45 % of for heat treated sheet Hastelloy X (Inc. 1997), this represents a significant increase in tensile strength whilst still maintaining good ductility. Table 2.5 gives a comparison between SLM and conventionally processed nickel superalloys.

	$\sigma_{y0.2}$ (MPa)			σ_{UTS} (MPa)			E (GPa)			δ (%)		
	Con.	SLM	+ht	Con.	SLM	+ht	Con.	SLM	+ht	Con.	SLM	+ht
Hastelloy X^a	360	816	-	785	937	-	205		-	43	35	-
Inconel 718^b	1185	907	1161	1435	1148	1358	208	204	201	21	26	22
Nimonic 263^c	580	818	843	970	1085	1268	-	163	206	39	24	53

^a values for Con. (Donachie and Donachie 2002), SLM (Wang 2011)

^b values for Con. (Donachie and Donachie 2002), SLM and +ht (Wang, Guan et al. 2012)

^c values for Con. (Donachie and Donachie 2002), SLM and +ht (Vilaro, Colin et al. 2012)

Table 2.5 - Tensile properties of nickel base superalloys for conventional (Con.), SLM as processed (SLM) and SLM as processed plus heat treatment (+ht).

The increase in tensile strength for the SLM as processed states is attributed to the fine grain structure, due to the Hall-Petch relation for grain size and yield strength, whilst the columnar structure allows for maintained (or sometimes increased) ductility (Vilaro, Colin et al. 2012, Wang, Guan et al. 2012, Kanagarajah, Brenne et al. 2013).

Amato, Gaytan et al. (2012) and Kanagarajah, Brenne et al. (2013) also investigated the consequence of the columnar microstructure on the directionality of tensile properties. Amato reported that Inconel 718 samples built parallel to build direction had slightly increased yield strength and UTS and elongation then those built perpendicular to the

build direction. Interestingly Kanagarajah, Brenne et al. (2013) reported tensile strength was similar between test orientations, but that elongation was greater by a factor of two for samples built parallel to the build direction. It was proposed that a difference in grain aspect ratio with respect to the loading axis induces different mean free paths of dislocation.

Although not as frequently reported as by commercial users, there are reports of micro-cracking in as processed nickel superalloys in the public domain. Mumtaz, Erasenthiran et al. (2008) mention issues of micro-cracking in processing Waspoly. Cracking was reduced through the optimisation of scan parameters, is implied to not have been eliminated. Similarly Wang (2011) reports micro-cracking in fully dense components of Hastelloy X, typically thought of as a 'weldable' alloy. Cracking is reported to be more severe towards the edges of the parts, implying a relationship between cracking and the thermal stress as described by (Merzelis and Kruth 2006), where tensile stress builds up along the free surfaces. Unfortunately, neither Mumtaz nor Wang provide observational evidence for either the initial micro-cracking or efforts to improve it.

Rickenbacher (2013) however, does provide observation evidence of micro-cracking in SLM processed Inconel 738LC. SEM micrographs, see Figure 2.38, reveal that cracks are of the order of 50 μm in length and are predominantly intergranular. Based on the surface morphology of the cracks i.e. exposed dendrites and intergranular, then cracks are considered (by Rickenbacher) to most likely be caused by solidification or liquation cracking. DDC is not considered a likely cause, although no further investigation into this is conducted.

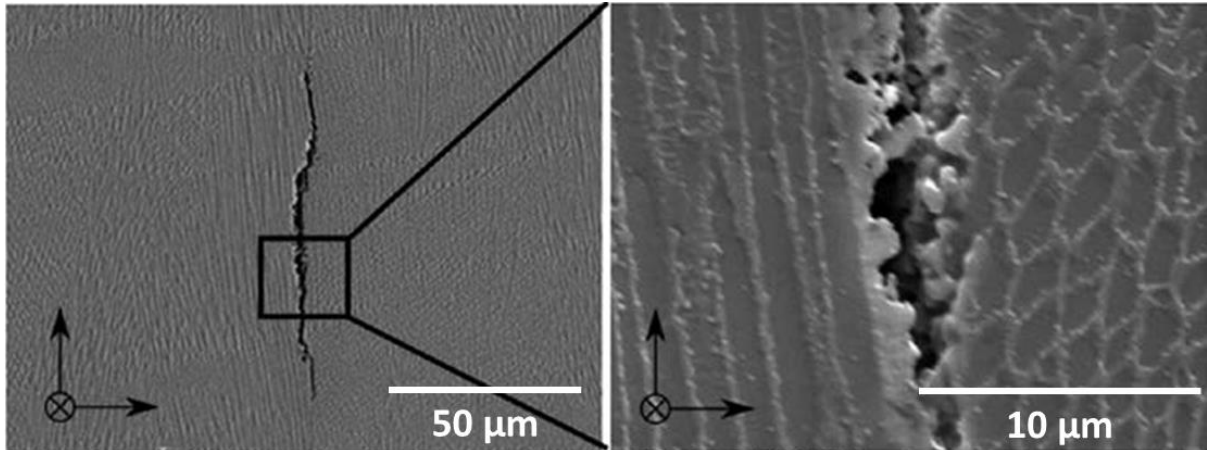


Figure 2.38 - SEM micrographs of as processed IN738. Crack is approximately 80 μ m in length, and contrary to original author of investigation, look to be as a result of solid state rupturing - adapted from (Rickenbacher 2013).

2.8.2 Reduction of thermal stress build up

In Section 2.2, high thermal stress and part residual stress was highlighted as a characteristic problem for SLM processing. In response there have been a number of studies which investigated the optimisation of laser scan parameters, in particular scan strategy, to control and reduce thermal and residual stress (Shiomi, Osakada et al. 2004, Mercelis and Kruth 2006, Moat 2009, Yilbas, Karatas et al. 2011).

In the second half of their investigation into thermal and residual stresses in SLM and SLS, Mercelis and Kruth (2006) found that a sectioned (chequerboard) scan pattern reduced the maximum tensile stress compared to a simple raster pattern. In chequerboard, the area is split up into a number of squares in which a raster pattern is scanned. Subsequent squares are then selected at random, until the entire area is complete. The raster pattern in each square is perpendicular in orientation with respect to its neighbour. By sectioning, randomising and alternating the scan orientation, it ensures patterns of stress

do not build up over the course of multiple layers. The scan strategy has been adopted by machine manufacturers, EOS and Concept Laser.

Shiomi, Osakada et al. (2004) conducted a similar investigation into modelling and reduction of residual stress in chrome molybdenum steel. The modelling results are previously discussed in Section 2.2. Initially they found that heat treatment of as processed parts - held at 600-700°C for one hour, without a controlling atmosphere - resulted in a 70% reduction in the residual stress. This is not a surprising result as heat treatment is often employed to relieve residual stress after conventional processing. Layer rescanning - rescanning of the layer with the same or different laser scan parameters - was also investigated. The hypothesis being that the secondary scanning would reheat the solid layers below, effectively annealing them and relieving some of the built up stress. Again, this is similar to a conventional technique known as laser annealing, which a laser surface treatment is used to relief stress along the surface of a part. In Shiomi, Osakada et al. (2004), the secondary scan had the same parameters as the primary. The result was a 55% reduction in residual stress compared to a part built without rescanning.

Both Shiomi and Mercelis also investigated the effects of a heated powder bed on the residual stress of a part. In principle, heating of the powder bed reduces the thermal gradient by reducing the temperature difference between the laser incident surface and the powder/under lying material. Reduction of the thermal gradient reduces stress generated by TGM, and therefore the overall residual stress is reduced. The investigation found that increasing the powder bed temperature to 160°C by means of a heated substrate, resulted in a 40% reduction in final part residual stress. This agreed with the qualitative findings of Mercelis and Kruth (2006).

2.8.3 Post process crack and defect elimination

One solution to the problem of defects and cracking of SLM processed material is post process treatments. Wang (2011) describes how internal defects in SLM processed Hastelloy X, such as cracks, pores and unmelted powder particles can be consolidated through HIPing.

HIPing has traditionally been used as both a powder metallurgy process and for changing/improving the properties of already formed material. The high temperature and applied pressure induce plastic deformation, creep and diffusion. The isostatic application of pressure means that defects which are linked to the surface are not closed, and only truly internal defects can be consolidated. Wang (2011) offers a remedy to this, of simply machining off areas in which cracks remain; however, this is not ideal for a number of reasons. Primarily, the loss of material would have to be accounted for in the component design phase and would be difficult to predict. Secondly the application of destructive machining, as opposed to surface finishing, would add to the total process cost and time.

Wang (2011) compared the tensile properties of SLM as processed and SLM + HIP'd Hastelloy X. Although still superior to hot forged properties, the SLM + HIP'd samples displayed significantly lower yield strength, UTS and elongation. The reason for this is understood from an investigation carried out by Amdt (2012) for IN625. Comparisons of the microstructure between SLM as processed samples and samples which were HIP'd post SLM processing can be seen in Figure 2.39.

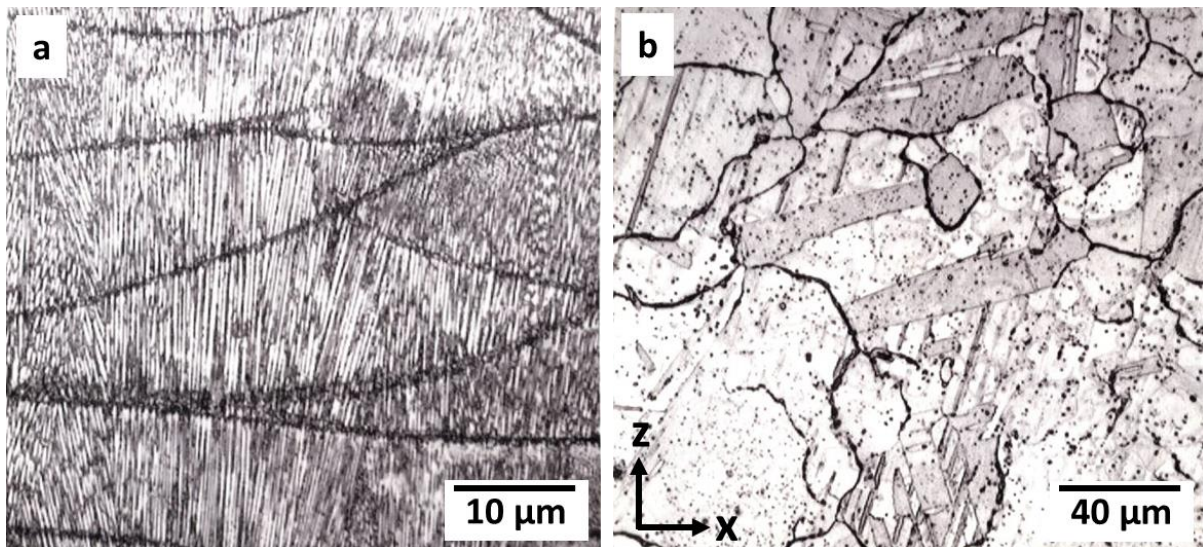


Figure 2.39 - (a) SLM as processed microstructure, (b) SLM + HIP'd microstructure. Note different magnifications. Adapted from (Amato 2012).

As can be seen, the fine columnar grain structure of the as processed sample has been dissolved and a coarser random orientation equiaxed structure has formed. The increase in grain size results in a reduction of the tensile strength of the material, thus explaining the findings of Wang (2011). In the case of the investigation of Amato (2012) however, the SLM samples were not fully dense resulting in poor tensile performance, and therefore a fair comparison cannot be made.

Amato (2012) also compared as processed and HIP'd + annealed components of Inconel 718 for microstructural and mechanical properties. Again the same transformation of microstructure is observed, however the addition of annealing allows for the correct precipitation of γ'' Ni_3Nb and therefore the HIP'd + annealed components had marginally higher yield strength and UTS than the as processed components.

Although annealing and heat treatments are used to precipitate out desired phases, they can achieve this whilst maintaining the grain structure. HIPing on the other hand will always result in a markedly different grain structure, which may not be desirable.

2.8.4 Anisotropic mechanical properties and crystal orientation

Of the investigations carried out into the mechanical properties of SLM processed nickel superalloys, several report marked differences between test pieces built in the x-y (horizontal) orientation and z (vertical) orientation (Vilaro, Colin et al. 2012, Bauer, Dawson et al. 2013, Kanagarajah, Brenne et al. 2013, Rickenbacher 2013). Specifically, it is the elastic (or Young's) modulus which varies most significantly, with x-y orientated pieces displaying higher values than those built in the z orientation. The anisotropy is attributed to the high aspect ratio of the grain structure; however, it can be explained further.

Etter, Kunze et al. (2015) investigated the phenomenon in SLM processed Hastelloy X and sought to reduce the anisotropy through heat treatment. It is reported that the elastic tensor single crystal of Hastelloy X at room temperature is $c_{11} = 230.40$ GPa, $c_{12} = 156.12$ GPa, $c_{44} = 121.77$ GPa. This results in a minimum of Young's modulus of 104 GPa parallel to $\langle 100 \rangle$ and maximum of 294 GPa parallel to $\langle 111 \rangle$. As with the other investigations, specimens tested in the x-y orientation displayed a significantly higher Young's modulus than those tested in the z direction, typically 170 GPa versus 150 GPa respectively. As with the investigations discussed in Section 2.4.3, the fibre texture of the as built material was observed to be $\langle 001 \rangle$ parallel to the build direction, however this results in a nearly transverse isotropic elastic tensor, with respect to the build direction. Heat treatment of the specimens resulted significant grain coarsening and equiaxed grain formation, therefore creating additional texture components and reducing the anisotropy.

There is one other interesting point is to be considered from the above observations. Although a strong fibre texture is present for the overall bulk material, not every grain is mutually aligned. Therefore, when stress is applied across multiple grains – as would be

the case for Type 1 stresses generated by TGM - each grain may possess a different elastic modulus in that given stress plane. This variation could plausibly result in stress formation along the grain boundaries, creating weak points and possible crack initiation sites within the material – similar to grain boundary carbide formation and DDC. This may therefore be considered as possible explanation for why nickel superalloys display a high susceptibility to micro-cracking during SLM processing.

2.8.5 Investigations in micro-cracking

Several studies on laser metal deposition and SLM have investigated micro-cracking of alloys during laser powered fabrication (Li, Hu et al. 2005, Zhong, Sun et al. 2005, Tomus, Jarvis et al. 2013, Yu, Rombouts et al. 2013, Carter, Martin et al. 2014, Carter, Essa et al. 2015), with Tomus, Jarvis et al. (2013), Carter, Martin et al. (2014) and Carter, Essa et al. (2015) relating to the specific topic of this work - nickel base superalloys processed with SLM.

Zhong, Sun et al. (2005) investigated boundary liquation and interface cracking of laser deposited Inconel 738LC onto a directionally solidified Ni-base superalloy substrate. They identified that there were five separate cracking situations:

1. Liquation cracking in substrate and liquation penetration into IN738 layer
2. Liquation cracking in substrate and cracking in IN738 layer, but without signs of liquation
3. Cracking from substrate into deposition layer without signs of liquation
4. Cracking in substrate but no penetration into deposition layer
5. Cracking in deposition layer originating from interface but no crack in substrate

Despite the high cooling rates of laser metal deposition eutectic liquation at the grain boundaries still occurred. One key point to highlight is that the liquation cracking initiated in the substrate, and only penetrated into the deposition layer. This implies that the lower cooling rates experienced by the substrate, as a result of thermal conductance, allowed the eutectics to form and thus the liquation to occur. Penetration liquation cracking may occur if the 'local composition/structure conditions are favourable'.

Indeed, the high temperature gradients and solidification rates associated with AM techniques are expected to inhibit liquation at grain boundaries, due to the formation of fine directional columnar structures and low segregation. Zhong and Sun thus attribute the cracking to "the comprehensive effects of various beneficial and detrimental factors which are dependent on the processing parameters and local composition/structure conditions"(Zhong, Sun et al. 2005).

Li and Hu (Li, Hu et al. 2005) investigated the effect of carbon content on the microstructure and cracking of laser clad Fe-based alloys. It was found that both the microstructure and cracking susceptibility were very sensitive to the carbon content. Three powders were trialled of identical chemical compositions (Fe95.5-Ni1.5-Cr1-Mn1-Si1 wt.%) bar the carbon content, which was 0.2, 0.3 and 0.4 wt.%. The alloys were clad onto a medium carbon steel substrate using 3.5 kW CO₂ laser with a diameter of 4mm. Cracks were not observed the powders of 0.2 and 0.3 wt.%, but were observed in the powder of 0.4 wt.%.

The powder with the lowest carbon content demonstrated good cracking resistance, this was attributed to a higher plasticity as a result of the lower carbon wt.%. Also believed to be of importance was the nature of the solidification. The powder in question displayed a peritectic reaction (as opposed to eutectic), which exhausts all the liquid and δ

simultaneously, thereby removing the detrimental effects of remaining liquid films between the grain boundaries.

Carter (2014) investigated the influence of laser scanning strategy on the microstructure and cracking behaviour of nickel superalloy CM247-LC. It was reported that the 'island' scan strategy (similar to a chequerboard with alternating hatch orientation) had a significant influence on the microstructure of the material, by creating a bimodal grain structure – see Figure 2.40. Larger elongated grains were present in the centre of the islands, preferentially orientated to [001], but these were surrounded by a highly misorientated fine grain structure.

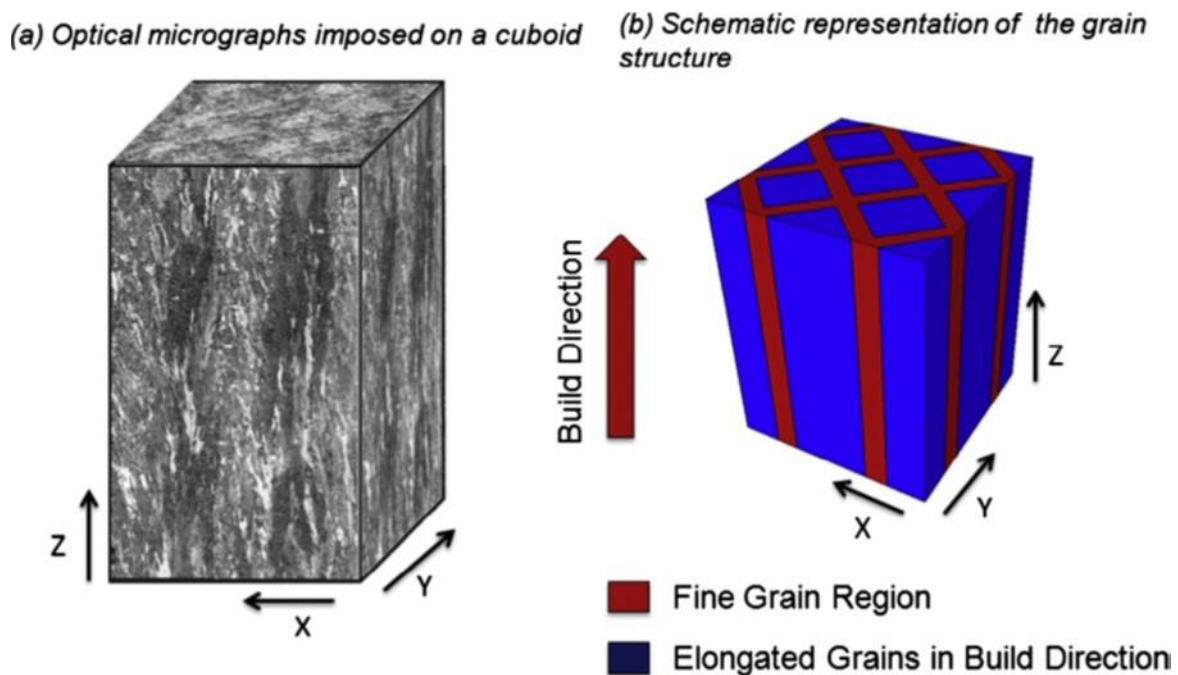


Figure 2.40 – Grain structure created by island scanning strategy – direct from (Carter, Martin et al. 2014)

It was also reported that micro-cracks were more concentrated in the fine grain region, and proposed that the misorientated grain boundaries acted as weak points within the material. Carter proposes that the mechanism for micro-cracking is that of DDC, however the description presented aligns it more with that of ETSS cracking. It is also possible that

misorientation is creating increased stress along grain boundaries due to differences in elastic moduli for a given stress plane – as discussed in Section 2.8.4

In addition to the work on CM247-LC, Carter, Essa et al. (2015) investigated the influence of laser scanning parameters on the microstructure and cracking behaviour of single crystal nickel superalloy CMSX486. A statistical design of experiments, employing surface response methodology was used to determine the key influencing parameters relating to densification and micro-crack formation. It was found that laser power and laser scan speed (and the interactions between the two) had the greatest influence of micro-crack formation. However, no clear relationship could be defined for the input nominal energy density. Low power (125W) and high scan speed (2000 mm/s) were calculated to be optimum pairing for minimum micro-cracking, however this was contrary to the optimum parameters for maximum density (high power and lower scan speed). Micro-cracking was reduced to 2.24 mm/mm² with optimum parameters of 128W laser power, 1007 mm/s laser scan speed, and 63µm hatch spacing, whilst also achieving ~100% density. However, it was concluded that there would always be a compromise between achieving maximum density and minimum cracking.

Tomus, Jarvis et al. (2013) investigated the effects of minor elements on the crack susceptibility of Hastelloy X as processed by SLM. This was conducted by comparing samples of a 'low' and 'high' Mn + Si content alloy built under a controlled set of processing conditions. This is a reapplication of the work carried out by Savage and Krantz (1971), although the choice of Mn and Si as controlling elements runs slightly contrary to the conclusions of the earlier papers. As a secondary point of investigation, the effect of scan speed on crack formation was also studied. Crack susceptibility was measured by crack density, which was determined by visual comparison.

It was reported that the samples built with the 'low' Mn + Si content powder had lower crack densities, and the addition of a low scan speed yielded a 'crack free' sample – although this is difficult to confirm visually in the literature due to insufficient image resolution, see Figure 2.41. Focused ion beam micrographs of the cracked samples showed that the cracks lay along the grain boundaries and are jagged in morphology; implying cracks are ETSS or DDC cracks, but higher magnification images would be required to confirm.

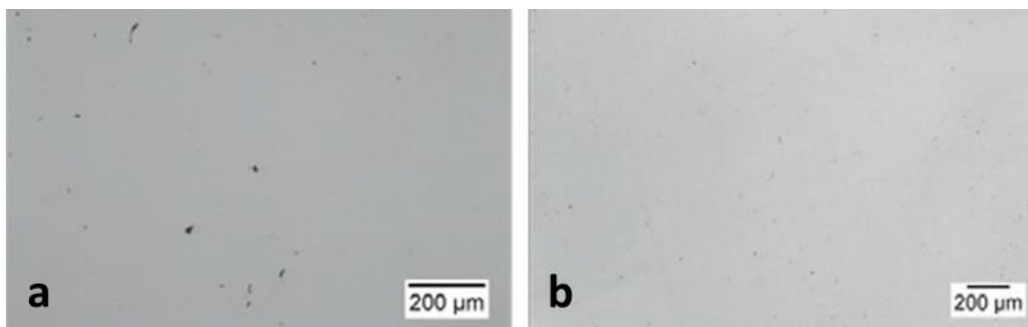


Figure 2.41 - Micrographs from Tomus, Jarvis et al. (2013) apparently showing a reduction in cracking for b) 'low' Si + Mn over a) 'high' Si + Mn content.

Thermodynamic simulations were also conducted on the effect on melting temperature as a function of fraction of solid. This showed a decrease in melting temperature range with increased Mn and Si content. This is an expected result as alloying element/impurity content is well known to effect melting ranges.

The effect of minor element content on cracking is attributed to an increase in microsegregation to the grain boundaries. This in turn increases risk of crack initiation at grain boundaries due to 'unavoidable' shrinkage strains associated with SLM.

Although this is not the only paper to imply microsegregation as a key factor in micro-cracking with SLM processing, it is the first to conclude it. Unfortunately, however, there

are a number of reasons as to why this work is not fully conclusive. Primarily, there is no analytical proof provided to back up the conclusion. Micrographs of the samples do show cracks along the grain boundaries, however in a fully dense material grain boundaries offer the path of least resistance for a crack to propagate. In addition, unlike with Yu, Rombouts et al. (2013), Tomus did not perform any type of chemical analysis on the cracked regions of the samples. Therefore, there is no evidence that Mn and Si were in proportionately higher concentrations in the crack regions, and hence that their segregation to the grain boundaries was driving the crack susceptibility.

There is no doubt that the 'high' Si + Mn concentration samples had a higher crack density, but the reasons behind this have not been fully explored. As the exact wt% chemical composition of the 'high' and 'low' samples is not reported, there can be no comprehension as to the relative influence compared to the standard Hastelloy X specification. Furthermore, there is nothing to deny that the increase in Mn and Si concentrations is not having additional or alternative effects, e.g. affecting material properties associated with thermal stress, such as Young's modulus or the thermal expansion co-efficient.

Despite the inconclusive nature of this paper, evidence from separate investigations (Yu, Rombouts et al. 2013) does imply microsegregation of minor elements as a factor in micro-cracking. What the paper fails in doing, is clarifying whether this effect is significant in the standard composition of Hastelloy X, or any other nickel-base superalloy.

2.9 Improvement of processability through alloy composition

As was discussed in Section 2.7.5, certain elements have been identified as influencing cracking in *welded* nickel alloys, leading to the creation of versions of alloys specific for welding. This section discusses elements which have been identified as potentially detrimental in SLM processing, but also alloy performance in general. In addition, potentially beneficial alloying elements and systems will also be discussed.

2.9.1 Weldability, crack susceptibility and SLM

In section 1.7.5.2, sulphur and phosphorus were highlighted as offering no benefit to an alloy and being detrimental to weldability (Collins and Lippold 2003). Indeed, the presence of impurities is rarely seen as beneficial and ‘cleaner’ alloys will always be preferred. However, there is now evidence to suggest that certain intentional ‘minor’ elements may be affecting the crack susceptibility of superalloys in SLM.

Tomus et al. (2013) provides the first report of specific changes to alloy composition affecting crack susceptibility of a nickel superalloy alloy processed by SLM. Although not conclusive or quantified, Si and Mn content appeared to affect the crack susceptibility of the alloy. This was reported to be the case for autogenous welding of Hastelloy, also, in work by Savage and Krantz (1966, 1971) and was attributed to segregation of said elements to the grain boundaries.

A review by Jena and Chaturvedi (1984) looked at the roles of alloying elements in the design of nickel-base superalloys. In this work, manganese is reported to be useful for sulphidation resistance, and excess manganese (>1%) improves oxidation resistance and weldability. However, the excess can lead to loss of ductility and therefore manganese is restricted to 0.2-1 wt%. Silicon also improves oxidation resistance but is again kept to

between 0.2 and 1 wt% due to embrittlement effects and influence on promotion of M_6C carbides and Laves phases. The detrimental effects occur when Mn and Si segregate to the grain boundaries; this becomes more likely with higher concentrations. This raises a conflict of reasoning. In Tomus' work (Tomus, Jarvis et al. 2013) the high Si + Mn content resulted in more micro-cracking, but a high Mn content should improve processability – assuming similar solidification conditions in SLM to welding. Silicon was therefore perhaps the more influential of the two, and likely in concentrations greater than the specification limits of Hastelloy X.

Other elements that should be kept to a minimum are those which are insoluble in nickel such as bismuth, lead, thallium and tellurium. These have the propensity to segregate to the grain boundaries resulting in weakening and cracking, even when present in trace amounts (Jena and Chaturvedi 1984, Donachie and Donachie 2002).

Oxygen, nitrogen and hydrogen (ONH), like carbon, are small enough to sit in interstices of the lattice and have high diffusion rates. Therefore, even in conditions of rapid solidification, they may still be able to segregate to grain boundaries and areas of high stress.

Ultimately the detrimental effect of many alloying elements depends on whether they are allowed to segregate to grain boundaries or into sufficient concentrations to form precipitates. From knowledge of rapid solidification, it is proposed that segregation of solute elements will be limited (Section 2.4.2). This is supported by the reported microstructures of SLM processed alloys, which do not show evidence of significant secondary phase formation/precipitation (Section 2.4.3). The precise nature of solidification and phase formation in SLM must therefore be established as a priority before considerations of solute elements and their effects can be made.

2.9.2 Beneficial minor element additions

In contrast there are also a number of possible minor element *additions* which can be made to help reduce crack susceptibility and improve alloy response

Magnesium will improve the stress rupture life of an alloy by reacting with interstitial impurities such as oxygen, nitrogen and hydrogen. It also reduces grain boundary embrittlement caused by sulphur. Zirconium also reacts with sulphur, as well as carbon, tying up both in carbides and carbo-sulphides, again improving ductility. Hafnium and rare earth elements will also react with sulphur and eliminate its effects (Jena and Chaturvedi 1984).

2.9.3 Low thermal expansion alloy systems

The majority of the problem characteristics in SLM stem from the high thermal stresses. Equation 2.19, demonstrates that thermal stress σ_{th} it is influenced by both the process and material, where α_{CTE} is mean coefficient of thermal expansion, E is Young's modulus and ΔT is change in temperature.

$$\sigma_{th} = E\alpha_{CTE}\Delta T$$

Equation 2.19

If one wanted to keep the tensile properties of an alloy the same, or similar, then the most appropriate solution is to attempt to reduce the thermal expansion.

Rather than attempting to reduce the thermal expansion co-efficient of a solid solution, EOS GmbH focussed on the phase change between liquid and solid, specifically solidification shrinkage. They developed a bronze-based multicomponent alloy called DM20. DM20 contains components which expand 'during the build process', these

counter the shrinkage of the bulk material resulting in an overall reduced shrinkage. The macro effect, is a component with superior dimensional accuracy and importantly, reduced residual stresses. Unfortunately, as this is a commercial product, the chemical composition data of DM20 is not publicly available and as such the exact characteristics of the expanding components is unknown.

One such metal which could be implemented in a material such as DM20 is Bismuth. Like water, Bismuth expands in volume upon solidification (by $\sim 3.32\%$). It has a history of being used in 'low expansion' alloys, where it (again) compensates for the solidification shrinkage of the bulk components (Norman 1998). The difficulty with using it for selective laser melting is the effective application of the expansion. In order to be effective, Bismuth has to be in crystal form, rather than an alloy. Bismuth also has a comparatively low melting temperature of 271°C , compared to the average melting temperature of a superalloy of $\sim 1300^\circ\text{C}$. As a consequence, it is possible that it may be isolated as a eutectic phase and precipitate either inter- intra- or transgranularly, much like MC carbides.

Another material of interest for thermal expansion properties, is INVAR. INVAR is an iron-nickel alloy which has a thermal expansion coefficient of approximately $1.2 \times 10^{-6} \text{ K}^{-1}$ between $20\text{-}100^\circ\text{C}$, compared to that of steel ($\sim 11\text{-}15 \times 10^{-6} \text{ K}^{-1}$). INVAR is classically $64\text{Fe-}36\text{Ni}$, although other variants exist such as Invoco ($\text{Fe-}33\text{Ni-}4.5\text{Co}$, has an α_{TE} of $0.55 \times 10^{-6} \text{ K}^{-1}$ from $20\text{-}100^\circ\text{C}$) which have an even lower thermal expansion coefficient.

The low thermal expansion of INVAR makes it perfect for use in high precision instruments, where a high dimensional stability is required. INVAR owes its low expansion properties to a ferromagnetic phenomenon, known as the Invar effect, which depends on the energetic state of the nearest neighbour Fe-Fe bonds. Rancourt and Dang

(1996) found that up to one in five magnetic exchange bonds in Invar were energetically unsatisfied, and as such it was a heavily frustrated system. Calculations of the ground state magnetovolume properties revealed that the unsatisfied bonds display the opposite magnetovolume action to satisfied bonds. The effect is large enough to near fully restrain the normal thermal expansion of the alloy from 0 -150 °C. Up until this point, the kT energy is anomalously used up changing the domain alignment patterns from ferro- to paramagnetic, rather than increasing the vibrational energy of the atom. After this point, the effect begins to diminish until reaching the Curie temperature (279°C), at which point the material becomes completely paramagnetic and normal Fe-Ni alloy expansion resumes (Roy, Agrawal et al. 1989). This of course means that only regions of the material which are at temperatures lower than 200°C will experience reduced thermal stress. Unfortunately in SLM, upon laser exposure temperatures fluctuate between ~2500°C and 30°C over a period of only milliseconds (Roberts, Wang et al. 2009). So although the bottom 200°C will occur with low expansion, the rest will be no different to a mild steel and therefore thermal stress is unlikely to be significantly lower.

As a final note on the subject, the ferromagnetic-magnetovolume phenomenon is sensitive to alloy composition. Fe content has to be > 45 wt.%, with the effect only being substantial between 60 and 70 wt.%. This means it is effectively impossible to mimic the phenomenon in an established superalloy, and very unlikely that INVAR can be modified to meet the same standards without eliminating phenomenon.

2.10 Chapter summary

The relatively low number of publications specific to this investigation made it necessary to seek theory and understanding from areas outside of this field of research. This

allowed for a more holistic consideration of the potential mechanisms which influence the material behaviours of nickel superalloys during SLM processing. Review of rapid solidification theory was vital in aiding the hypothesis and ultimate validation of establishment of SLM as a rapid solidification process. Together with a review of cracking mechanisms of nickel superalloys in laser welding, and more recent publications on mechanisms driving thermal stress in SLM processing, this helped form a full hypothesis for the potential root cause of process induced micro-cracking of nickel base superalloys. Finally, recent publications on SLM processing of nickel superalloys were reviewed, with specific focus on the few which detailed micro-cracking and methods to improve or eliminate it. Although there was some success in reduce micro-cracking reported, none of the works achieved complete elimination, and chemical alteration to the alloys, rather than processing parameter optimisation, showed the most promise.

3 Principle experimental methodology and preliminary investigations

3.1 Renishaw SLM125

All samples were fabricated on a Renishaw SLM 125 machine with all metallic powder feedstock being supplied by LPW Technology unless stated otherwise. The Renishaw SLM 125 uses a modulated 200W Ytterbium fibre laser to process deposited powder feedstock within a 125x125x125 mm build volume. The modulated laser scans in a point-to-point regime, rather than a continuous scan seen on other systems such as those by EOS or Concept Laser.

To avoid oxidation during melting, the process is conducted within an argon atmosphere. This is done by both holding an argon atmosphere and running a flow of argon across the powder bed, which also helps to remove oxidised or partially sintered particles.

Before melting commences, the chamber is put under vacuum to remove air from the chamber. Once under pressure reaches 945 mBar, the chamber is then flooded with argon gas until a specified oxygen content is reached. The chamber has oxygen detectors at the top and bottom of the build chamber. Oxygen limit readings are taken from the bottom detector. All of the experiments were built with an oxygen limit of <1000 ppm, although the oxygen content continues to drop throughout the build as more argon is introduced into the system to maintain chamber pressure.

The argon flow is filtered to remove fine powder and burnt particles picked from the powder bed, before being recirculated back across the powder bed. The gas circulation is

only initiated whilst the laser is melting, as the argon atmosphere is sufficient to prevent any further oxidation whilst new layer is deposited.

3.1.1 Controllable parameters

There are seven controllable processing parameters on the Renishaw SLM 125; Point Distance (PD), Exposure Time (ET), Layer Thickness (LT), Focus Offset (FO), Hatch Spacing (HS), Laser Power (LP) and scan strategy. Layer thickness is simply the thickness of powder deposited for each layer, the implications of a thinner or thicker layer will be discussed in Section 3.1.3 (DOE). Laser power is the input power of the laser and has a range of 0-200 W. The effect of power on material response will be discussed in the DOE section.

In the point to point regime, rather than having a continuous scan of the laser along track length. A scan length is made up of a series of exposure points of set *exposure time*, separated by a set *point distance*, which is defined as distance between the centres of successive exposure points– see Figure 3.1. After each exposure the laser turns off, moves by the point distance and then turns back on for the next exposure. Hatch spacing is the distance between the centres of two adjacent melt tracks.

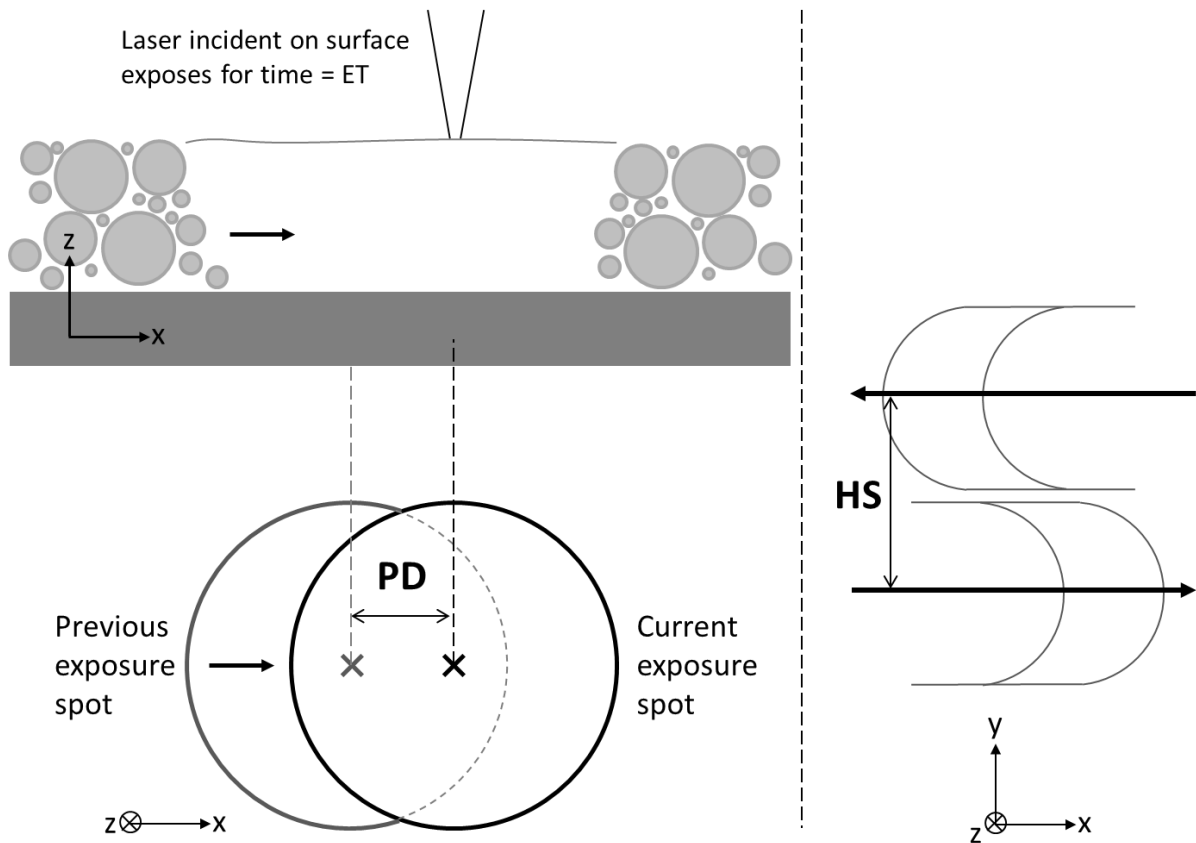


Figure 3.1 - Representation of how point distance, exposure time and hatch spacing apply to scanning and melt pool geometry.

Focus offset is used to alter the position of the focal point of the laser (in the z axis). This is used to alter the focus of the laser and thereby the incident beam width and peak intensity. If a laser has a particularly sharp profile, focus offset may be used to gain a better distribution of energy and/or reduce the peak intensity for more control over melting. The effect of varying focus offset on beam profile characteristics are covered the next section (3.1.2).

The scan strategy, or hatch pattern, is the pattern the laser will follow for the melting of a two dimensional shape. The simplest form would be a repetition of parallel straight lines across the width of an area. If the scan alternates in a parallel direction i.e. back and forth, this is known as a raster pattern. Many strategies exist, each with a specific purpose,

whether it be to reduce residual stress or reduce build time. The Renishaw SLM 125 has a number of preloaded strategies, but for the purposes of consistency the same strategy was used throughout all experiments in this work. The strategy used was a 'meander' scan strategy, which is a raster pattern with a 67° rotation for each layer and is optimised to minimise residual stress.

3.1.2 Beam measurements

Before material investigations were carried out, it was necessary to observe the energy density profile of the laser beam for the Renishaw SLM 125 to assess whether it had any anomalies or features that may affect melting. As well as merely observing the profile, the peak intensity and beam diameter were also measured. In addition, the influence of focus offset on the beam diameter and peak intensity was also investigated.

Understanding the profile of a laser beam is important as the distribution of energy incident on the surface of a material has great effect on how the material responds. The Transverse Electromagnetic Mode (TEM) of a laser describes the radial variation in beam intensity, by means of two subscripts, p and l : p represents the node along the radius of the beam intensity cross-section, and l represents the node along the circumference (Deffley 2012). A common TEM for welding and cutting lasers is TEM_{00} , which is cylindrical in cross section and has a single peak Gaussian profile, see Figure 3.2. The concentration of energy towards the centre of the beam allows for greater precision and high energy densities (Mumtaz 2008).

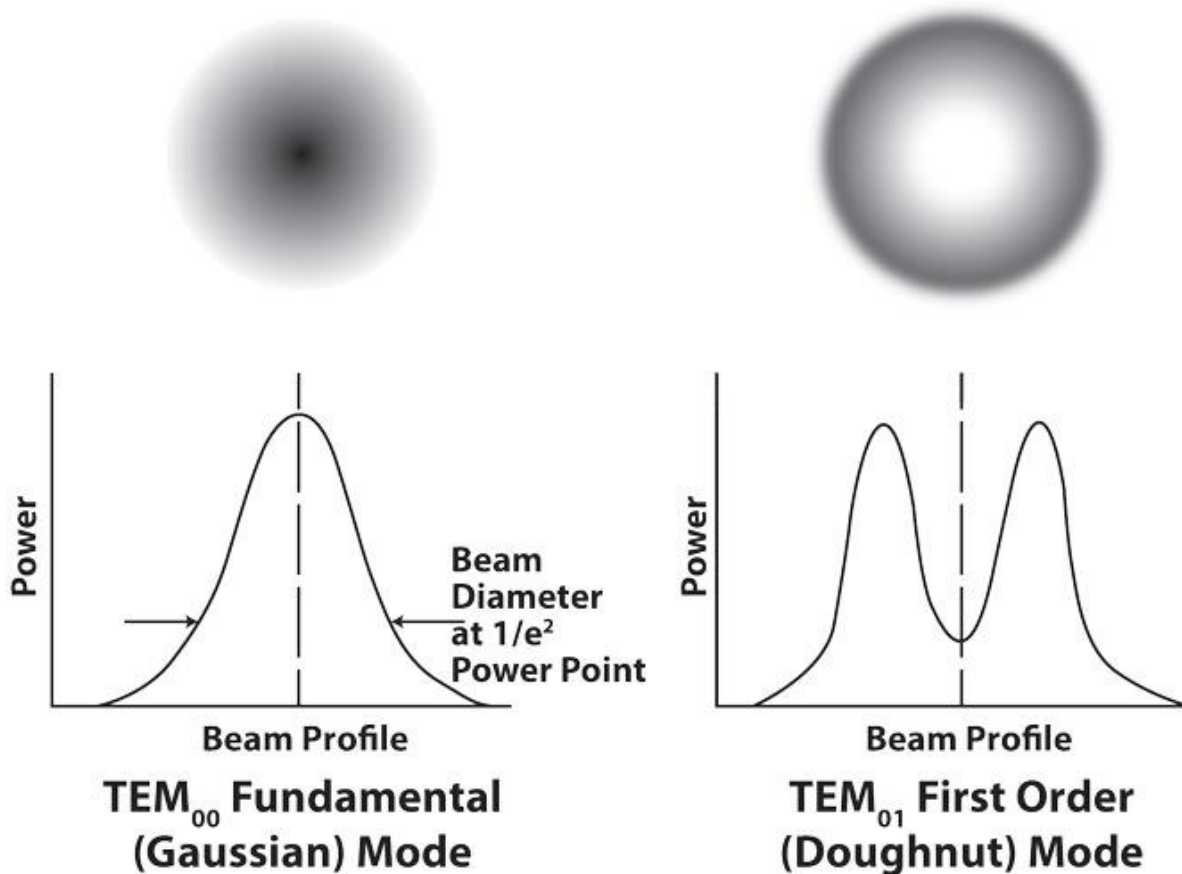


Figure 3.2 – Gaussian and Doughnut profiles – direct from (Swartz 2016)

Beam profiling was carried out using an Ophir-Spiricon® BeamGage® and BeamMic™ analysis software. The laser beam can be measured at operational powers by passing it through a series of splitters and filters, to reduce the incident energy, onto a CCD which measures the light intensity as counts per pixel. The profile is recorded, and analysis can be performed on the still, including calculations of peak intensity and beam diameter.

3.1.2.1 Profiling and beam diameter results and discussion

The physical effect of changing the focus offset is detailed in Figure 3.3. A positive increase in FO results in negative shift in the z axis of the focus point of the laser. This has the effect of increasing the spot size of the laser, i.e. the cross section of the beam incident on the substrate.

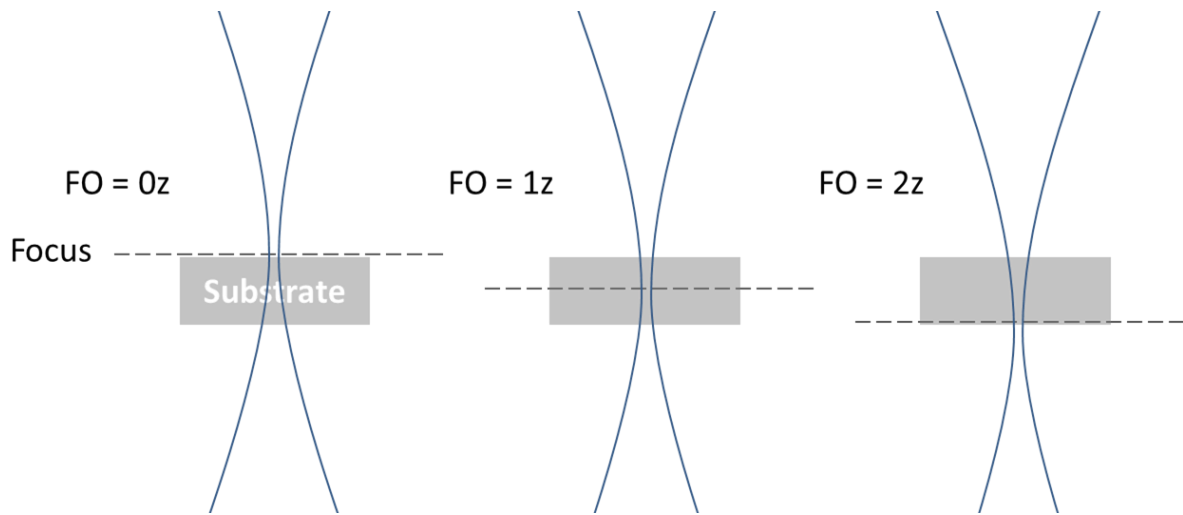


Figure 3.3 - Effect of changing focus offset on position of laser focal point and incident spot size on substrate.

Before investigating the effect of FO on spot size and beam diameter, the profile of the focussed beam (FO set as 0 mm) was observed, Figure 3.4a. As can be seen it is a sharp Gaussian-type with a mild elliptical base profile (yellow circle), but appears to be without any secondary peak features. Focus offset was then increased in 2 mm intervals up to 6 mm, each time observing and measuring the resulting beam profile. Figure 3.4 shows the x and y profiles for the beam set at 200W with an FO of 0, 2, 4, and 6 mm for a)-d) respectively.

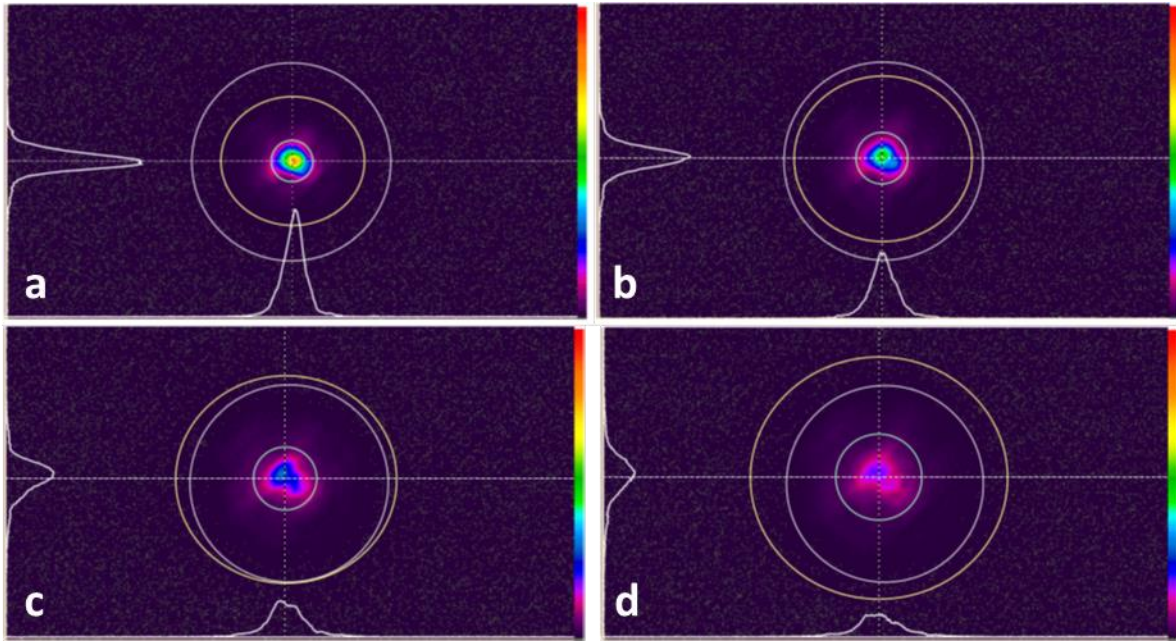


Figure 3.4 – Laser power: 200 W, with focus offsets of a) 0.0 mm, b) 2.0 mm, c)4.0 mm and d)6.0 mm. White circle is the guide area, inner green circle represents beam diameter at 13.5% of peak intensity, yellow circle represents limit of differentiable beam (from background).

As expected, the increase in FO results in an increase of beam diameter and reduction of intensity. The beam diameter is highlighted by the inner most circle (green) and is taken as the $1/e^2$ of peak intensity, or 13.5% of the peak intensity. This method was used as the background noise levels were too high to enable clear distinction between the background and the edge of the beam. Table 3.1 lists the measured values of x, y and combined $1/e^2$ diameter values as well as the peak intensity for the four FO's

FO (mm)	D%Pk (μm)	D%PkX (μm)	D%PkY (μm)	Peak (cnts)	Pk % of 0.0 mm (%)
0	114	127	101	3299	100.0
2	144	158	123	2137	64.8
4	194	194	158	1221	37.0
6	257	264	224	757	22.9

Table 3.1 – Beam diameter and intensity readings. Pk% of 0.0mm is what percentage of the peak at 0.0mm focus offset the given peak is.

It is observed that an FO increased to 6mm results in a doubling of the beam diameter and a quartering of the peak intensity. It must be stressed that the laser power, and therefore the total energy incident on the surface, remains the same however the distribution of that energy is spread across a greater area. Qualitatively the increase in FO results in a more even distribution and takes on a more classical Gaussian distribution at FO's of 4 and 6 mm. For the application of SLM, an FO of 4 or 6 mm may be preferable as it will result in a more even distribution energy compared to the focussed beam. The effect of FO on material response will be investigated Section 3.1.2.

The relationship between FO and Beam Diameter (BD) and Peak intensity has been plotted below in Figure 3.5, and data for the beam profiles is displayed in Table 3.1. Both BD and Peak intensity have a linear relationship with FO.

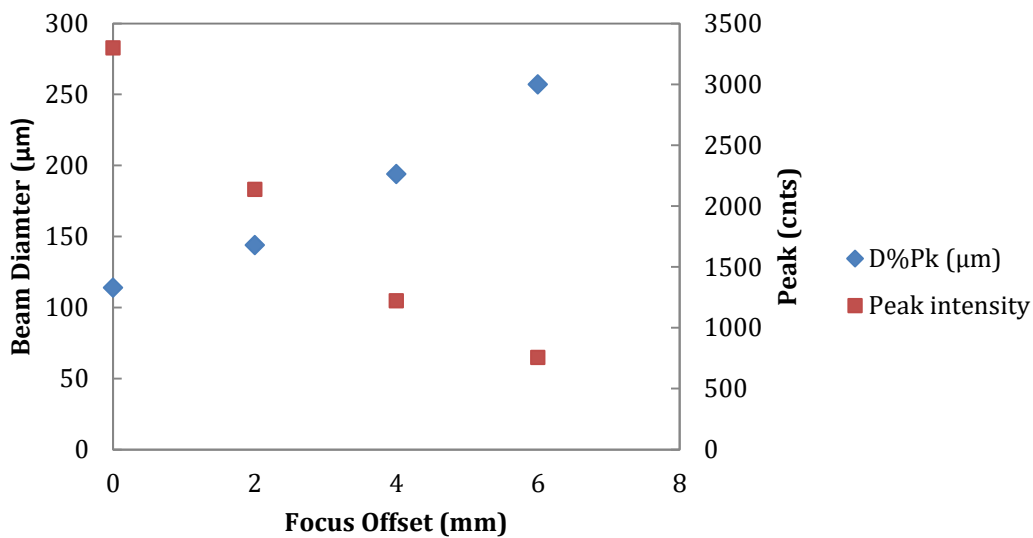


Figure 3.5 – Focus offset vs beam diameter and peak intensity for a laser powder of 200W.

Unfortunately, the method of beam measurement employed by the BeamGage™ relies on filters to reduce the energy of the beam incident on the CCD. It was observed, at lower powers, that changing to a lower grade filter resulted in a small increase of the measured

beam diameter. For reference the quoted value for 'spot size' – defined as effective fusion spot by Renishaw plc – is 50 μ m. Therefore, the measured beam diameters will not be taken as absolutely representative of those during processing, but the relationship between FO and BD and peak intensities still stand.

3.1.3 DOE – Process parameter considerations

In this section, the thought process behind the designing of experiments will be detailed, with primary focus on aiming to achieve full density. There are many approaches to Design Of Experiment (DOE) from heavily statistical to purely empirical, and everything in between. Statistical methods such as those employed by DOE software, attempt to minimise the number of samples or experiments by creating mathematical solutions from an initial test experiment. The accuracy of these solutions depends on the scatter and consistency of the initial results; as such they may not be ideal for new or less well understood processes.

For less well understood processes, wide field screening trials followed by a series of narrowing field trials give the user a more complete picture of the material response; enabling the identification of a global feature (minimum or maximum) and then increasing the resolution to establish local features. The advantage to the screening trials is that a greater number of controllable parameters can be investigated in the same initial experiment; subsequent narrower field trials are then used to investigate the effects of individual parameters. Although the number of experiments is greater in a screening trial method, statistical design can still be employed in the latter stages to minimise sample number.

In the case of SLM, to achieve full density one must consider the melt pool and track geometries with regards to controllable parameters. Figure 3.6 represents the cross section of two adjacent melt tracks in an SLM process.

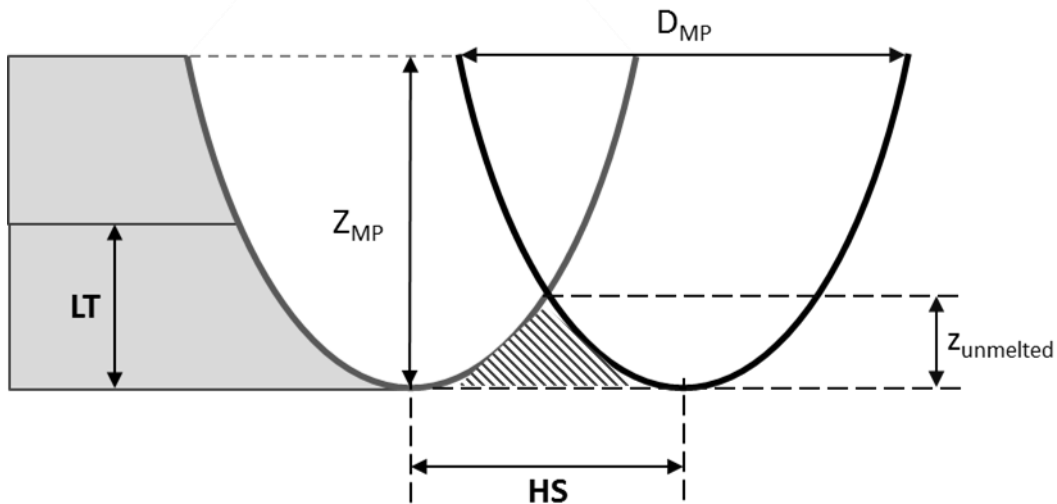


Figure 3.6 - Schematic showing geometry of cross section of melt tracks with controllable parameters LT and HS highlighted in bold. Hatched area represents potential unmelted or consolidated region.

The diameter of the melt track D_{MP} and depth of the melt track Z_{MP} are both controlled by the energy absorbed by the material, which in the case of the Renishaw SLM 125 is controlled by LP, ET and PD. The occurrence and subsequent size of the potential unmelted region depends on whether the choice of LT and HS is correct for melt track dimensions which result from the chosen LP, ET and PD.

In the absence of literature to use as a starting point, the energy required to melt a mass of material, E_m , can be calculated with the following equation

$$E_m = mc\Delta T + mL_f$$

Equation 3.1

where m is the mass of the material, c is the specific heat capacity, ΔT is the change in temperature from ambient to melting point of the material and L_f is the latent heat of fusion. For the case of laser fusion, the value is then divided by the absorptivity α of the material for the given laser wavelength.

$$E_m = \frac{mc\Delta T + mL_f}{\alpha}$$

Equation 3.2

If the material is in powder form however, the absorptivity is not the same as that for the bulk. Unfortunately, there is limited data on the relationship between powder and absorptivity, and usually a reduction of 50% is employed. The mass of powder can be worked out by assuming a volume comprised of the $LT \times HS \times PD$, and dividing by the apparent density of the powder (this can be measured by weighing un-agitated powder in a known volume). However, if one wanted to include overlap of melt pools appropriate increases to LT , HS and PD would have to be made e.g. for 50% overlap multiply each dimension by 1.5.

From the calculated required energy, one can then use measured beam diameter to work out an energy density, and from this extrapolate an LP and ET . The obvious problem with this method is that it requires predetermined values for LT , HS and PD . Ultimately it will only ever serve as an approximation which can be used as a starting point for a full scale DOE or to aid development of a DOE.

3.2 Analysis techniques

3.2.1 Sample preparation

For initial experiments, samples were vertically sectioned using a Buehler IsoMet® 5000 linear precision saw before being mounted in Bakelite using a Buehler SimpliMet® 100. However in later experiments, smaller sample size meant the initial sectioning stage was not required and instead twin samples were mounted orthogonally to each other and thus once mounted giving a vertical and horizontal section – Figure 3.8 in Section 3.2.4.

All mounted samples were ground and polished on an EcoMet® 250 Grinder-Polisher. Grinding and polishing stages were as follows: silicon carbide pads of 800, 1200 and 2500, followed by Diamet diamond suspension of 3 and 1 µm and a final stage of 0.05 silica suspension. Often additional polishing with 0.05 silica was required to reveal cracks in samples as the initial grind process can result in the covering of cracks in ductile materials.

If the samples were to be analysed with electron microscopy, they were mounted in Buehler Konductomet, which is a graphite and mineral (SiO₂) filled phenolic thermoset. The addition of graphite allows for conduction of electrons through the mounting, negating the application of conductive paints or ribbon to the sample. Given that secondary SEM analysis was always a possibility; samples were usually mounted in Konductomet.

Etching was also performed on samples for microstructural analysis, however as etchants and the associated procedures are material specific, these will be detailed in the appropriate sections.

3.2.2 Microscopes

Microstructural analysis was performed on a Nikon Eclipse LV150 optical microscope (OM) and Camscan S2 scanning electron microscope (SEM). Energy Dispersive Spectroscopy (EDS) line scans were conducted on a FEI Inspect F field emission microscope.

3.2.3 Porosity analysis

Porosity values were determined through area percentage measurements from optical micrographs of prepared samples. Although Archimedes analysis is more precise, it would not have been able to provide details of the porosity (size and morphology - gaseous or lack of fusion etc), nor would it give a comparable value. Although literature values for the density of many commercial alloys are available, these may be different to that of the composition provided a given supplier, and thus any numerical value for density would be meaningless. Porosity percentage combined with visual evidence is far more applicable.

Low magnification (x50) micrographs were chosen for porosity analysis so as to have the biggest focal area thereby minimising the bias caused by local variations. At this magnification the captured sample area was 2×2.5 mm. The number of micrographs taken depended on sample size, the aim being not to overlap images or include edge boundaries between the mounting medium and the sample. 5×5 mm samples can accommodate four micrographs, for example. Mean values and standard errors were then calculated from the micrograph measurements.

ImageJ software was used to process the images into a binary (black and white in this case) image. The software then calculated the percentage of the area/features that have been converted to distinctive dark regions. A visual example is displayed in Figure 3.7

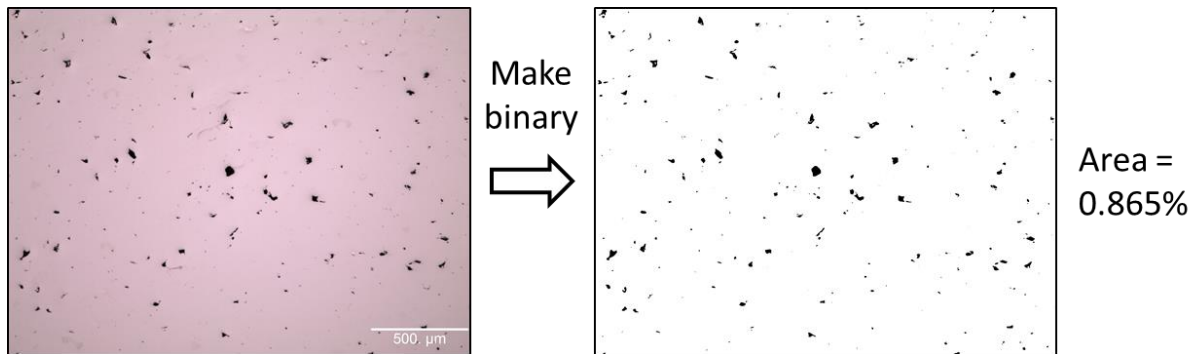


Figure 3.7 - Representation of how OM micrograph is turned into a binary image

3.2.4 Micro-crack analysis

Crack density was determined by counts per unit area. Using an area of 0.25 mm^2 ($500 \times 500 \mu\text{m}$) square, 20 measurements were taken from each sample, enabling a statistically safe determination of an average per mm^2 with 95% confidence level error. The 20 measurements were split across multiple micrographs depending on how many were taken per sample; for the case of a $5 \times 5 \times 5 \text{ mm}$ cube this would be 5 measurements per micrograph, 4 micrographs per sample. In addition, micrographs were taken across specific regions of the sample – central, edge, top corner and bottom corner - again to remove local bias, see Figure 3.8.

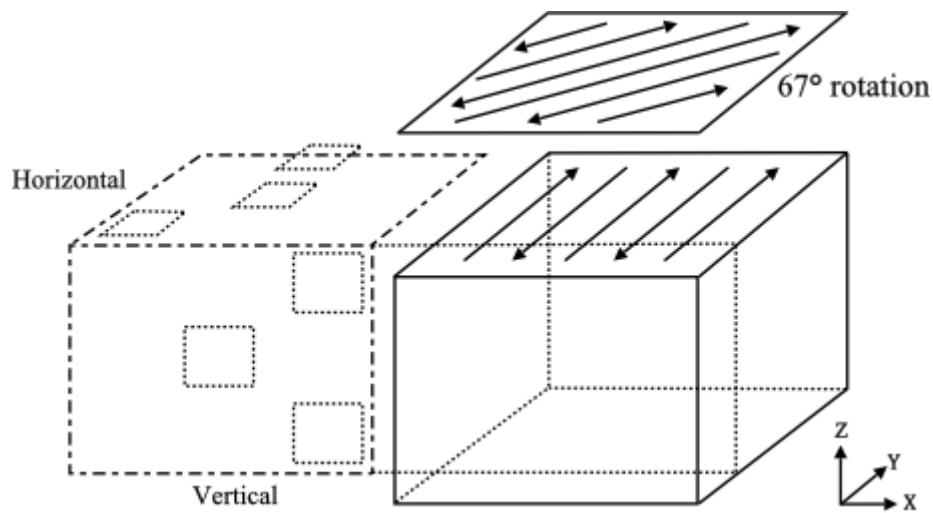


Figure 3.8 - Schematic demonstrating geometry of sections and micrograph positions

Another technique which can be used to quantify micro-cracking is measurement of total crack length for a given area/micrograph. Total crack length can be measured using ImageJ software.

Both techniques have advantages. The total crack length method relies less on human measurements (i.e. counting), but crack density is more scalable. Also the reliance on the software to differentiate between a crack and an irregular pore may result in bias.

3.3 Hastelloy X

This section details the DOE conducted to optimise process parameters for maximum density, and subsequently minimum micro cracking, for nickel base superalloy Hastelloy X. A high density (>99.5%), or rather low porosity (<0.5%), had to be achieved before concentrating on cracking, as any large pores or defects would be considered equally as detrimental.

Hastelloy X was chosen as the focus alloy for the investigation because it had been established as high crack susceptibility alloy (when processed by SLM) in both literature (Wang 2011) and by commercial users.

3.3.1 Hastelloy X Powder

The power used in this phase of the investigation was gas atomised Hastelloy X supplied by LPW Technology Ltd and was sized at 20-53 μm . The composition of the powder was independently analysed by LSM International and is detailed in Table 3.2 along with the specification ranges for each alloying element.

Element	Nominal Specification (wt%)	LPW Hastelloy X (wt%)
Ni	bal	bal
Cr	20.5-23.0	21.3 \pm 0.19
Fe	17.0-20.0	19.5 \pm 0.17
Mo	8.0-10.0	9.0 \pm 0.12
Co	1.5-2.5	1.04 \pm 0.04
Mn	0.2-1.0	0.48 \pm 0.03
Si	max 1.0	0.32 \pm 0.02
W	0.6-1.0	0.56 \pm 0.03
C	0.05-0.15	0.057 \pm 0.01

Table 3.2 – Composition in wt% of LPW Hastelloy X with nominal specification range as given by LPW Technology Ltd

Particle size analysis was carried out on the LPW Hastelloy X powder to confirm the particle size range and also obtain information regarding the particle size distribution. In addition, SEM imaging was used to analyse the morphology of the powder.

Particle size distribution was measured by Laser Size Diffraction (LSD) and was carried out on a Malvern® Mastersizer® 3000. The particle shape was assumed to be spherical and a Fraunhofer scatter model was used. Powder delivery was by dry dispersion; this has an advantage over wet dispersion as it avoids conglomeration of smaller particles which can be detected as one large particle – although dry agglomeration may still occur. A total of 3 cycles were performed, although data presented is for the mean average, see Figure 3.9. The Dv (%) values, that is size of which a given percentage of the particles were less than, were as follows: Dv (90) 56.8µm, Dv (50) 37.7 µm and Dv (10) 24.8 µm.

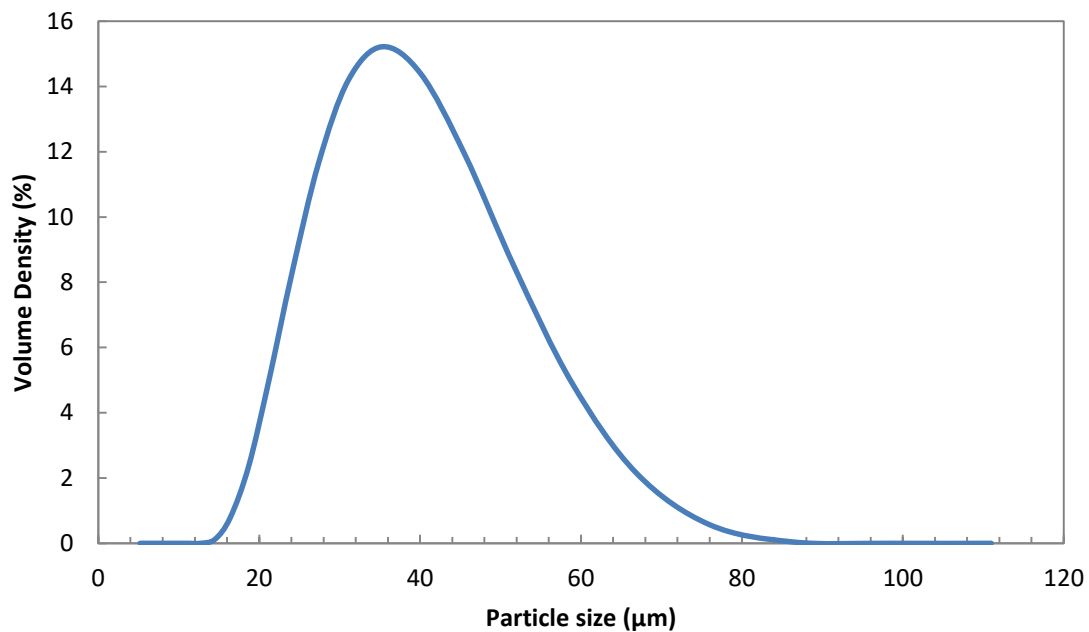


Figure 3.9 - Particle size distribution of LPW Hastelloy X powder, as volume density.

Although the powder was sized to a 20-53 µm range, approximately 15% of the powder *volume* consists of particles which are >53µm in size and 3.5% are <20µm; with 0.6% being >75 µm. It is noted that the Mastersizer 3000 (a similar systems) exaggerates volumes for particles >45 µm as the algorithm breaks down over a certain diffraction angle. When the powder is observed under SEM, see Figure 3.10, it is observed that very

few of the particles are $>53 \mu\text{m}$ in diameter. For a quantitative understanding of the number distribution, the volume % data is converted by dividing through by the average radius for each size bin. Figure 3.11 gives the particle *number* distribution. As can be seen, there is a significant shift of the peak towards the left (finer particles), with the peak 16.8% of the particles being $\sim 25 \mu\text{m}$ in size.

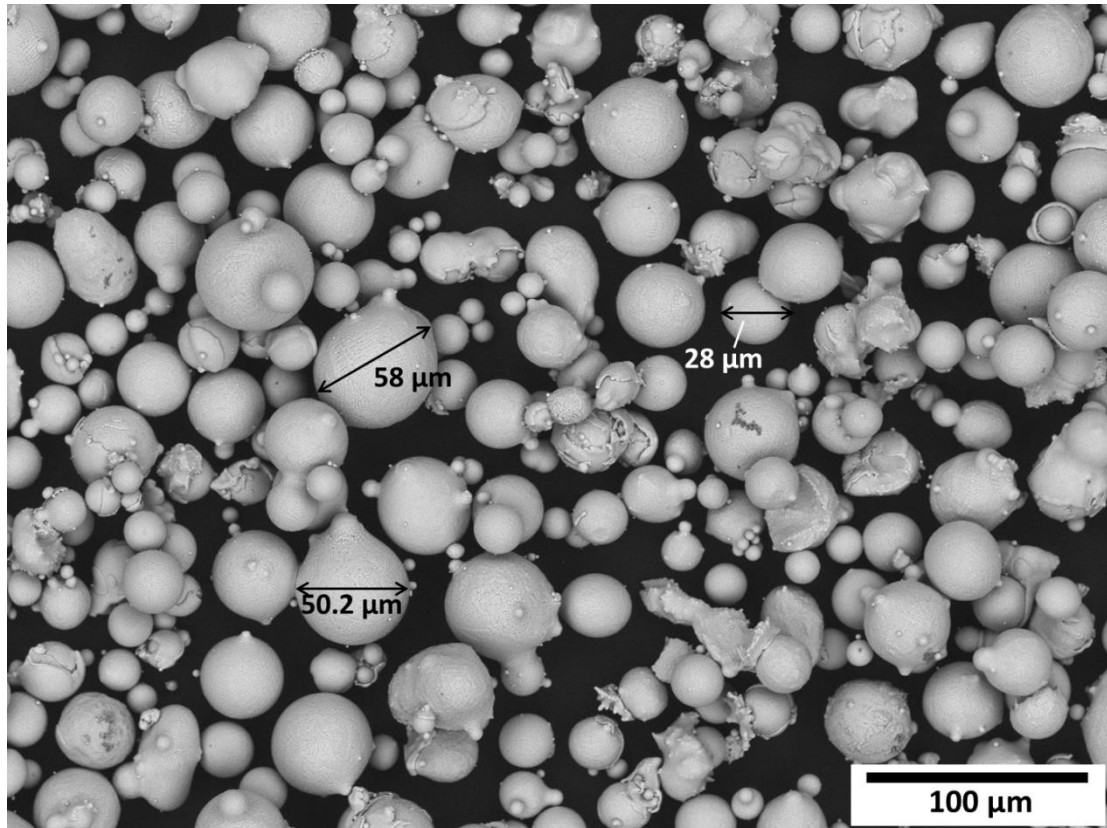


Figure 3.10 - SEM micrograph of Hastelloy X powder in Secondary Electron (SE) imaging mode. Note that this sample was taken from powder which had been through a processing run, and although sieved, some remelted particles have remained.

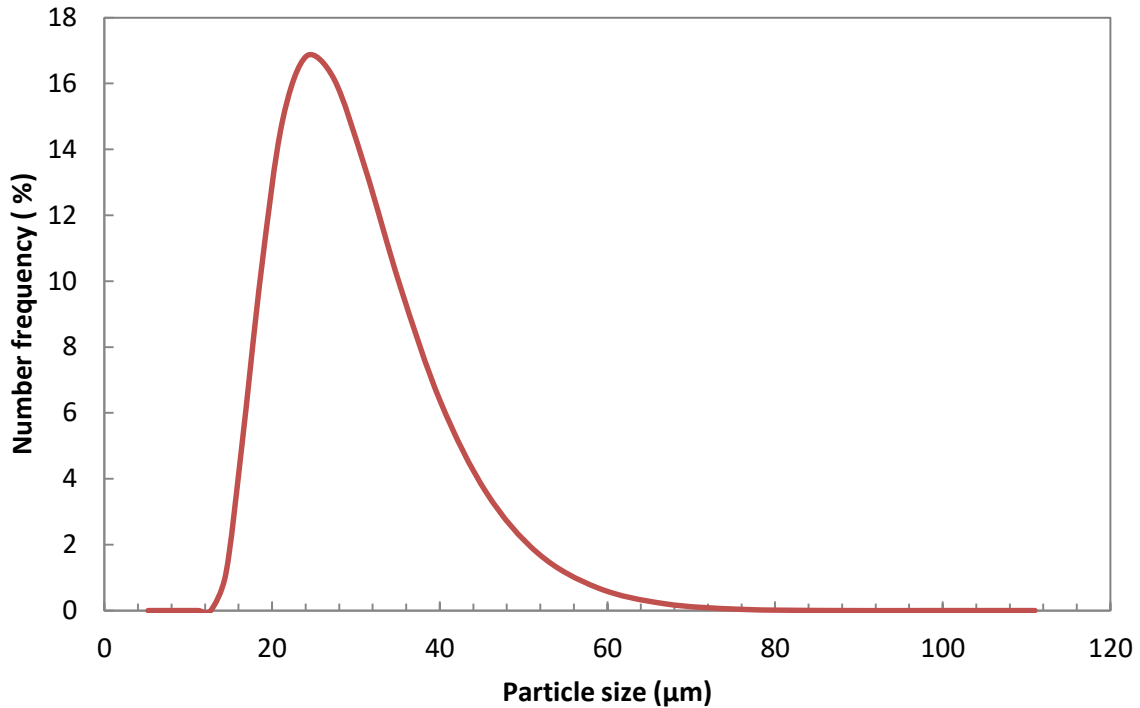


Figure 3.11 - Particle size distribution of LPW Hastelloy X powder as number frequency.

In Figure 3.10 there do not appear to be any particles greater than 60 µm in size, thus the observational data does not fully agree with the LSD data. This could be for a few of reasons. Firstly, one may note the number of conjoined particles, which have partially recombined in the atomisation process. The conjoined particles can be detected by LSD as significantly larger particles, if the diameter is measured along their long axis. In addition, although dry dispersion was used, there is still the possibility of having agglomerates. Agglomerates are groupings of smaller particles which are bound by friction or moisture; again these may be detected as a single large particle. Finally, the number distribution implies only ~1% of the particles are >60 µm in size, and therefore may have just been outside of the field of view of the SEM micrograph.

For the purposes of processing, volume distribution is actually more applicable as the user wants to know what percentage of deposited powder layer is taken up by particles

larger, or smaller, than a chosen layer thickness. SEM micrographs are useful for assessing the quality of the powder; there are also a number of techniques for measuring powder flow, which is an important factor in the processability of a powder.

3.3.2 Parameter optimisation

3.3.2.1 Densification

Due to the number of controllable parameters, a series of trials had to be conducted to assess the effect of each one on porosity and cracking.

Wang, Wu et al. (2011) processed Hastelloy X powder using a continuous laser SLM system, and achieved full density (>99.5%) parts. The process parameters reported were thus used as a guide for the initial wide field trial in this investigation. In order to compare the scan speed of a continuous laser to the PD and ET of a modulated laser, an apparent velocity, or Ap Vel. can be calculated from PD, ET and the known time between exposures – see Equation 3.3

$$Ap. Vel = \frac{1}{\frac{t_{exp}}{x_{PD}} + \frac{1}{v_{idle}}}$$

Equation 3.3

where x_{PD} is point distance, t_{exp} is exposure time and v_{idle} is the velocity at which the laser travels between exposure spots.

The first trial looked to find a global minimum in porosity for Ap. Vel (PD and ET). This was achieved by Central Composite Design (CCD) consisting of 13 experimental parameter pairs of ET and PD (8 plus 1 central point repeated 5 times) generated using DOE software Design X. Samples were built using the 13 parameter pairs built and then

analysed for porosity. The porosity values were then input back into the software, which generated a 4-part solution for achieving <1% porosity. Alternative solutions taken from the generated model were also built alongside the four initial ones. Samples were built as 10x10x10 mm cubes. Figure 3.12 is a contour plot of the resulting model. The fixed parameters in this trial were LP: 195 W, LT: 53 μ m, HS: 0.09 mm and FO: 0 mm, as taken from Wang, Wu et al. (2011).

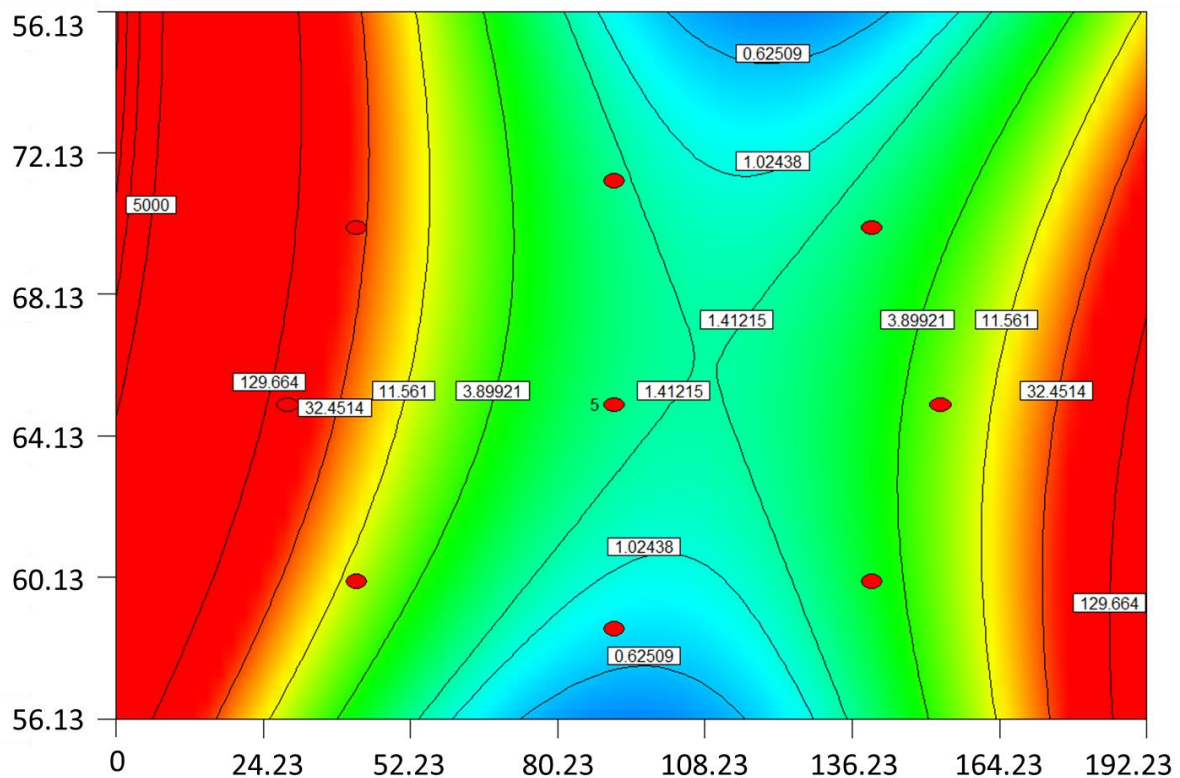


Figure 3.12 - Contour plot of CCD model, contours are porosity as labels, red dots are the 9 parameter pairs. Note that maximum mathematical porosity is 100%, but model generated unrealistic contours >100 as no limit was input.

The full set of values are plotted below in Figure 3.13, in which a clear global minimum is observed between 400-600 mm/s. Another notable observation is the apparent inconsistency of results, with the repeated samples (556 mm/s) varying between 1.13 and 2.10 % porosity; giving a standard deviation of 36.3%. In addition, none of the four

solution values achieved values of <1%. This is perhaps not surprising given the variation of the repeated values.

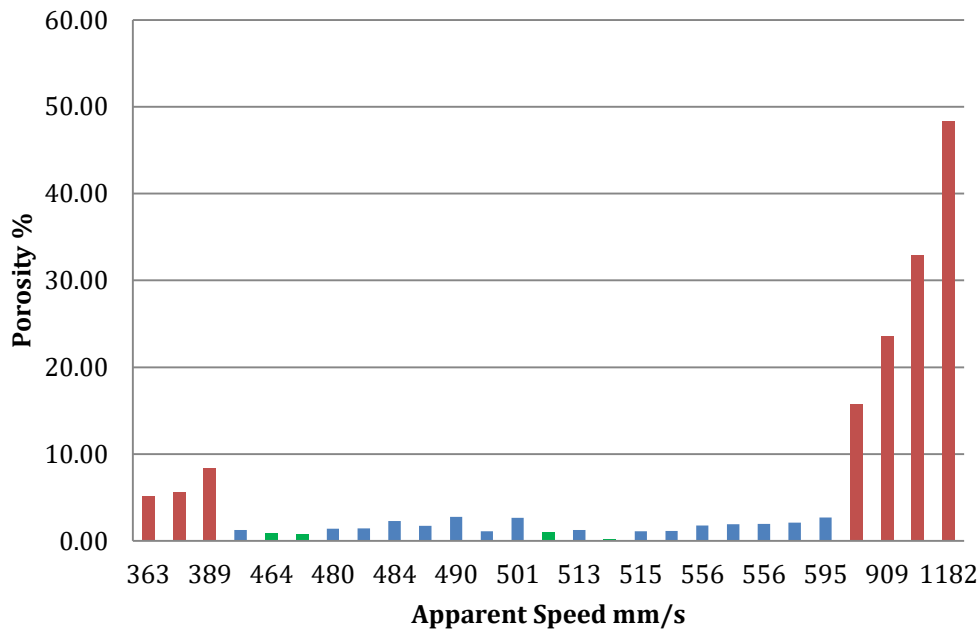


Figure 3.13 – Plot of apparent velocity against porosity for fixed parameters of LP: 195W, LT: 53 μ m, HS: 0.09 mm and FO: 0 mm. Marked on the plot is porosities of <1%, in green, and regions of high porosity (>5%) in red with blue representing porosities between 1% and 5%.

Samples with porosity > 5% were classed according to the type of porosity that was observed. Those at Ap. Vel <400 mm/s had very large irregular pores, void of powder, which are believed to be caused by plasma recoiling as described in Section 2.2.3, see Figure 3.14a. At velocities >700 mm/s, the point energy density was not sufficient to fully penetrate the layer, causing lack of fusion pores throughout the sample, some of which were very extensive, see Figure 3.14c.

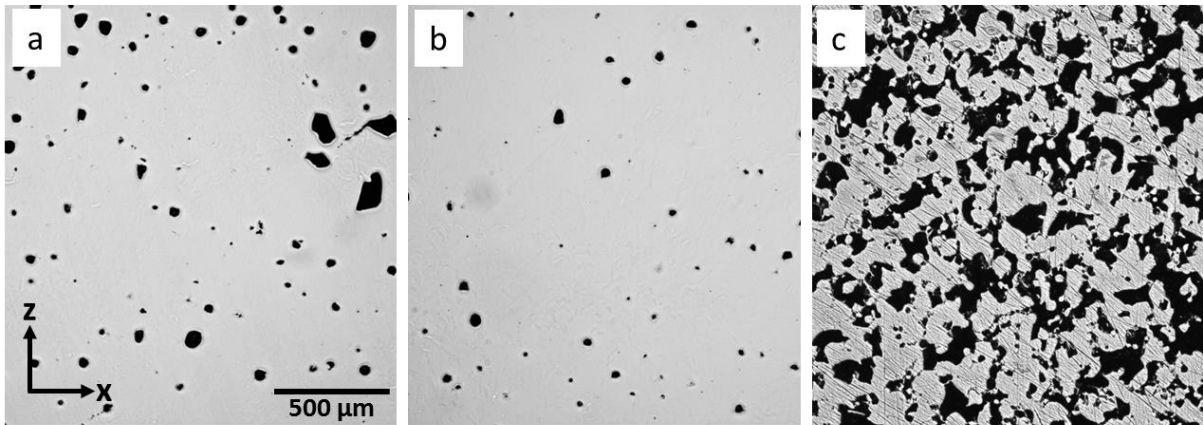


Figure 3.14 - The three distinct types of porosity identified in the first experimental trial: a) Large empty pores indicative of vapourisation, b) medium to large size spherical pores indicative of insufficient overlap and c) severe lack of fusion porosity as indicated by whole powder particles.

The inconsistency in samples between 400-600 mm/s was attributed to the type of porosity seen within them. Although the samples were of 2% or less porosity, the majority of the pores were spherical (gaseous) and large ($>50\ \mu\text{m}$); too large to be caused by porosity within the powder. The implication was that these were caused by insufficient overlap, however no discernible pattern was observed – see Figure 3.14b.

It was therefore evident that the parameters reported in Wang, Wu et al. (2011) were not applicable for the Renishaw SLM 125 system, and as such a screening trial was designed to begin the DOE process from a base level.

The screening trial took minimum and maximum values of PD, ET, LT and FO. The minimum LT the machine can process is $20\ \mu\text{m}$ and the maximum value was taken as the upper particle size limit of the powder, $53\ \mu\text{m}$. Focus offset was applied to investigate the effect of broadening the laser beam to aid melt track overlap, and reducing the peak intensity to avoid vapourisation. The FO limits were set as 0 mm – in focus - and 4 mm. FO of 4 mm was chosen as the maximum as it was felt that the reduction in peak intensity for and FO of 6 mm was too great and would have likely led to extensive lack of fusion.

Set parameters were LP at 195 W and HS at 0.09 mm. Figure 3.15 shows a schematic representing the DOE for the screening experiment.

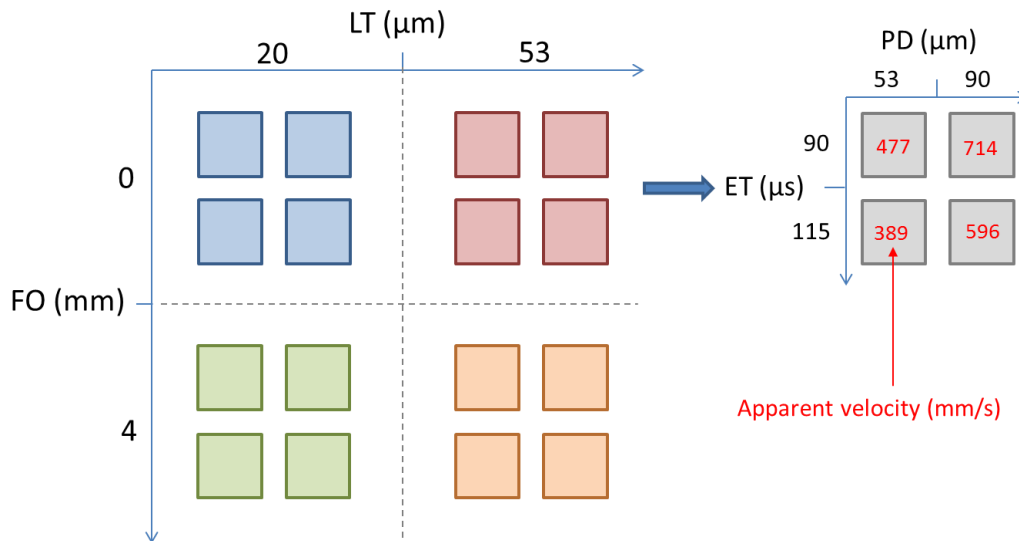


Figure 3.15 - Schematic presenting parameters chosen for screening trial. Four processing parameters were varied using minimum and maximum values. ET and PD values combined to give four values for apparent velocity.

The results of this trial for porosity are displayed in Figure 3.16. From the porosity plot we see that LT of 20 μm yielded the lowest porosities, of which, samples built with a FO of 4 mm had the lowest. Porosities of <0.1 % were achieved, and there was higher a consistency between the 20 μm layer samples compared to the 53 μm . In the LT 20, FO 4 samples, the large spherical porosity was not present; this was not mirrored in the 53 μm layer samples as the reduced beam intensity resulted in minor lack of fusion.

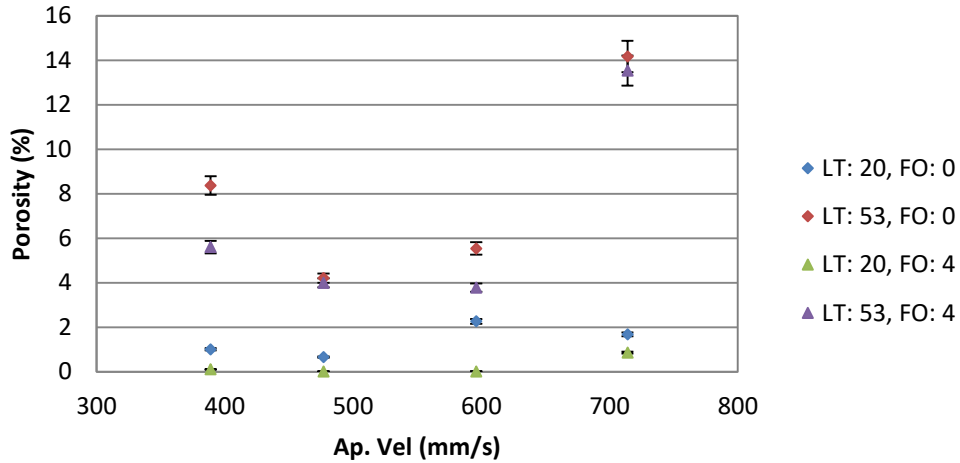


Figure 3.16 – Plot of porosity against apparent velocity, for the four sets of samples

It was thus concluded that the large pores were as a result of insufficient melt track overlapping, and that as varying (reducing) hatch spacing may also have the same effect a HS vs FO trial needed to be conducted.

For the HS vs FO trial, all samples were built with LP = 195 W, Ap. PD = 90 μm , ET = 115 μs and LT = 20 μm – these were the optimum parameters taken from the screening trial. The results porosity results for the HS vs FO trial are detailed in Figure 3.17.

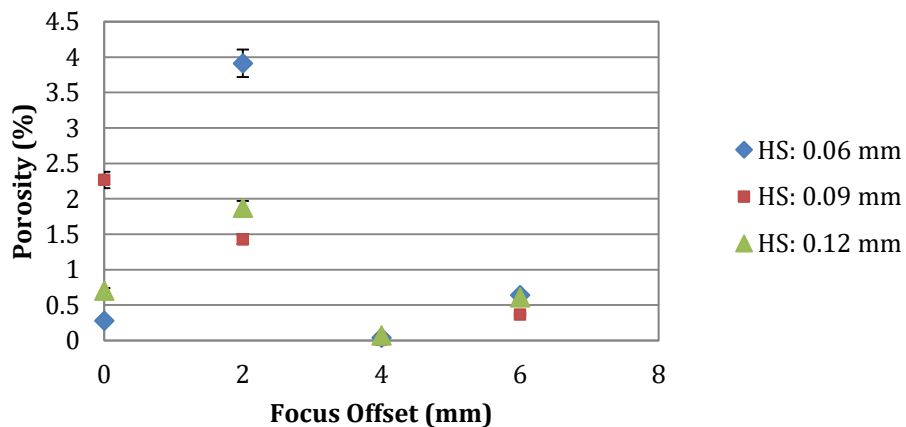


Figure 3.17 – Porosity with varying hatch spacing and focus offset

Porosity appears to peak at a FO of 2 mm, finds a minimum at 4 mm before rising again at 6 mm. These observations agree with the findings of Deffley (2012) who investigated

the effects of beam diameter and laser power on weld track widths for Inconel 718. It was reported that an increase in beam diameter increases the width of the weld track until the incident energy density is reduced to the point where the width begins to decrease – see Figure 3.18.

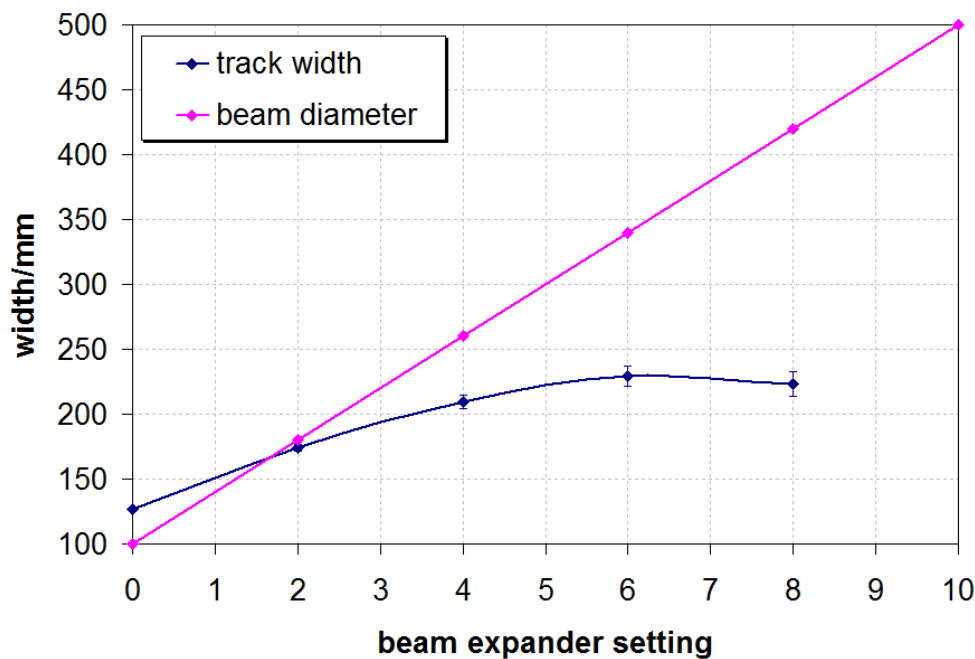


Figure 3.18 - Relationship between beam diameter and weld track width and beam expander setting for EOS M280 with fixed power and laser scan speed of 195 W and 800 mm/s respectively. Beam expander is a non-continuous parameter with a maximum value of 10. Direct from (Deffley 2012)

Additionally, when power was increased for the fully focussed beam, weld track width increased. Analysis of the cross section of the weld track revealed the presence of ‘wings’ (extended width) at the top surface of weld tracks for the higher power samples. These features are attributed to the increased significance of Marangoni convection over heat conduction within the melt pool. Initially, increased energy density allows for the formation of a melt pool larger than the diameter of the beam, however as the melt pool widens the top surface temperature at the edge of the pool decreases which increases the surface tension compared to the centre. The differential in surface tension induces a flow

of fluid from the centre to the edge, and then from the edge down back towards the centre (Limmaneevichitr and Kou 2000), see Figure 3.18. The increase in Marangoni convection transfers heat from the centre to the edge resulting in an expansion of the melt into the solid material at the top surface, hence creating the ‘wings’.

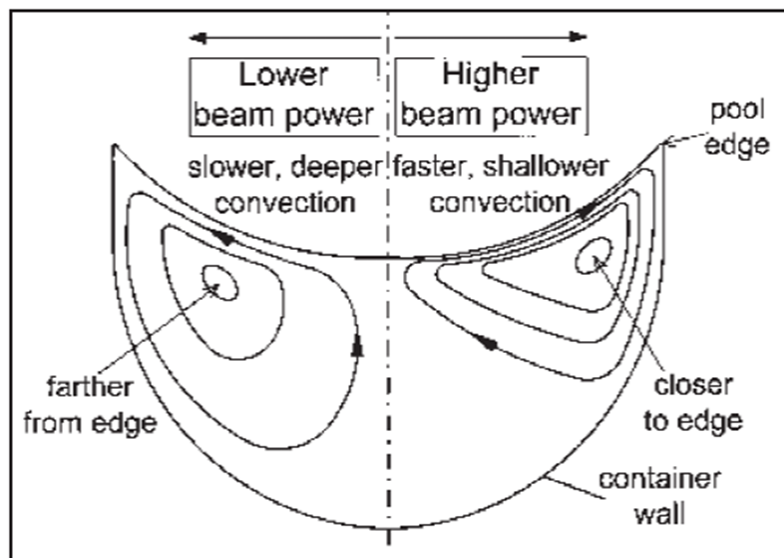


Figure 3.18 - The effect of laser power on the flow pattern in Marangoni convection - direct from (Limmaneevichitr and Kou 2000)

Figure 3.19 displays the cross sections of three of the samples from the Deffley experiment, and demonstrates the effect of a reduction in energy density on the cross sectional shape of the weld track.

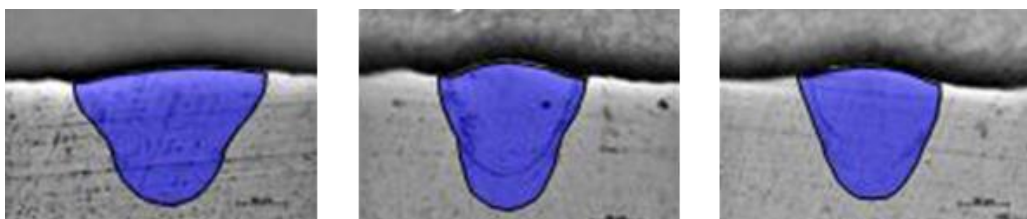


Figure 3.19 - Cross section of weld tracks with decreasing power from left to right for Inconel 718. Note the depth of the tracks remains the same as the Marangoni convection carries heat to the top edges. Adapted from (Deffley 2012).

The above can now be used to explain the relationship observed in Figure 3.17. At FO = 0 mm, although the beam is comparatively narrow, the incident energy density is high enough to generate a melt pool which expands beyond the beam width develops 'wings' due to Marangoni convections. At FO = 2 mm, the beam diameter has increased peak energy density has reduces and the situation is now akin to the far right image in Figure 3.19 and the effect of Marangoni convection has reduced. In the absence of the wings, the melt pool width is insufficient for the required overlap resulting in porosity formation. At FO = 4 mm the beam diameter has increased further resulting in an increase in melt track width and providing sufficient overlap. For FO = 6 mm, micrographs show the presence of lack of fusion porosity, indicating that the peak energy density was not sufficient to fully melt through the layer. The work from Deffley (2012) is applicable to this experiment as Inconel 718 is very similar to Hastelloy X in composition and the work was performed on an commercial SLM machine.

Clearly, the beam diameter and energy density resultant from FO = 4 mm yields more consistent and stable melting. As such, FO = 4 mm was fixed for the remaining experiments.

3.3.2.2 Reduction of crack density

Once full density (99.5%) had been achieved with the screening trial, the samples from that trial were analysed for crack density. This involved additional polishing to reveal the cracks, as described in section 3.2.4. Figure 3.20 shows the results for crack density with apparent velocity.

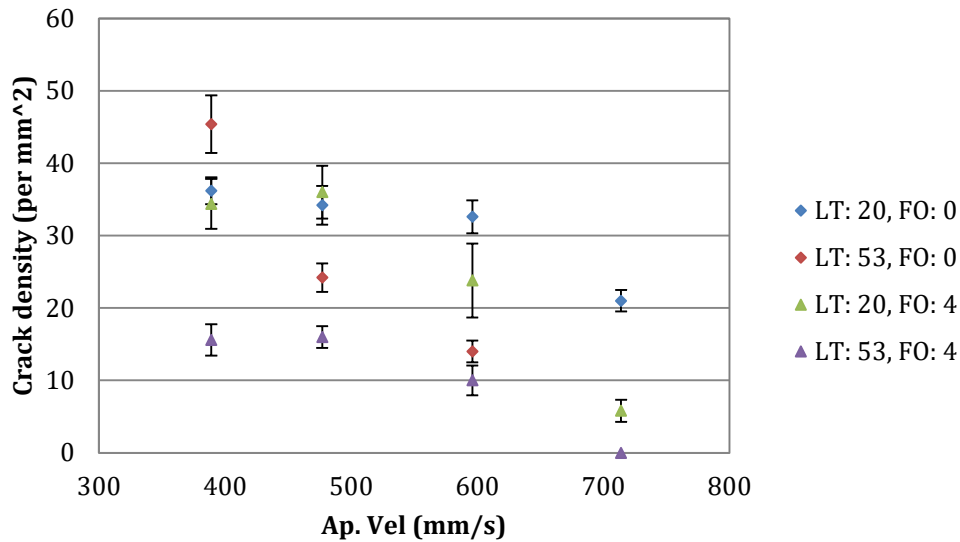


Figure 3.20– Plot of crack density against apparent velocity, for the four sets of samples. Both samples built at LT 53 μm and 714 mm/s crack free but very porous.

The crack density held to a general trend of reduction with increasing apparent velocity. When this observation is compared with the porosity results, it is also noted that samples with higher porosities tend to have lower crack density values. Examples of the extensive cracking seen in samples and also of the ‘higher porosity-lower cracking’ samples are displayed in Figure 3.21. Within Figure 3.21a, a secondary image magnifies the cracks within that sample and also represents the crack counting method – although it is stressed that the box is only representative and dimensions are smaller than that used in the actual analysis.

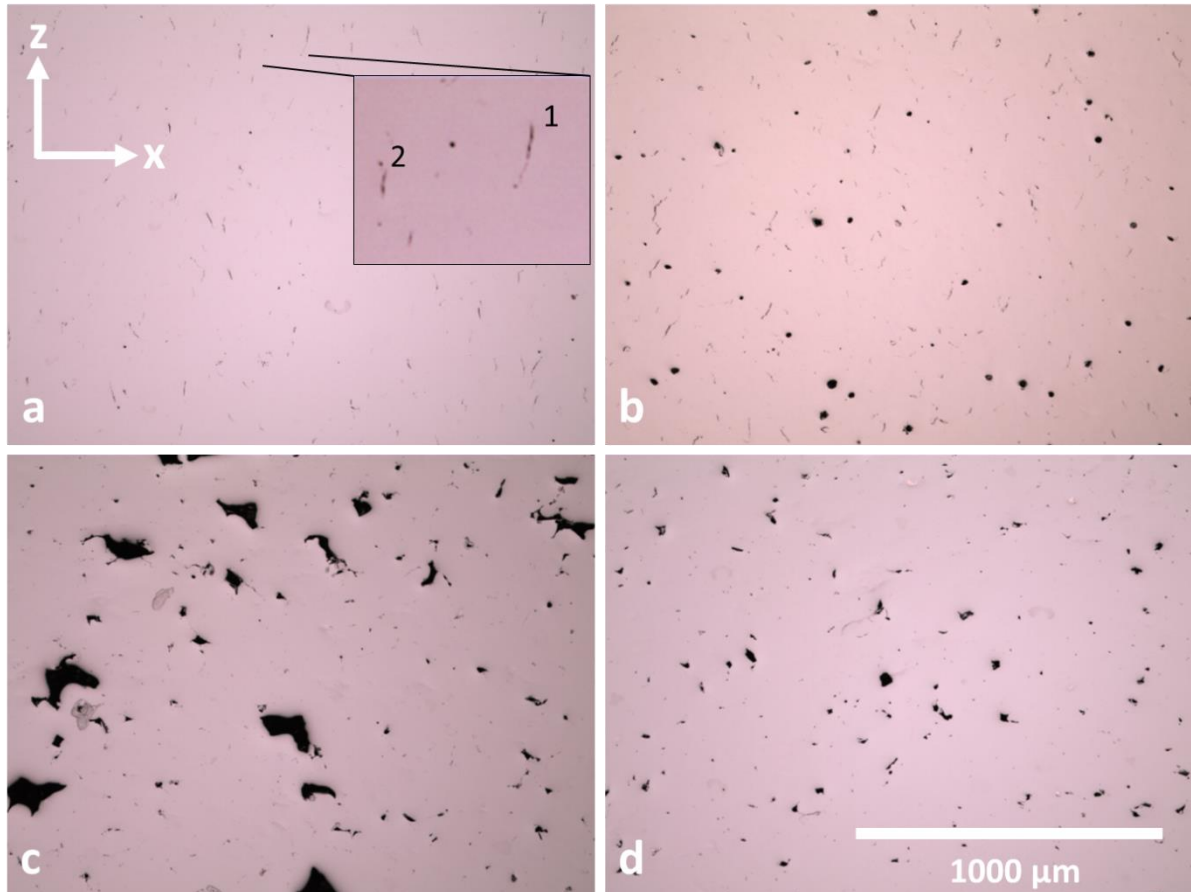


Figure 3.21- a) FO 4, LT 20, Ap. Vel 477, one of the lowest porosities achieved yet there is extensive cracking through the centre of this sample with 36 ± 3.6 cracks per mm^2 . b) FO 0, LT 20, Ap. Vel 477, the same processing conditions as a) except the FO, note the absence of large spherical pores in a) compared with b). c) FO 4, LT 20, Ap Vel 714, low crack density but significant levels of lack of fusion porosity. d) FO 4, LT 53, Ap. Vel 596, extensive large lack of fusion pores resulting from insufficient energy penetration.

As with the screening trial, crack density analysis was also performed on the samples from the FO vs HS trial; Figure 3.22 displays the results.

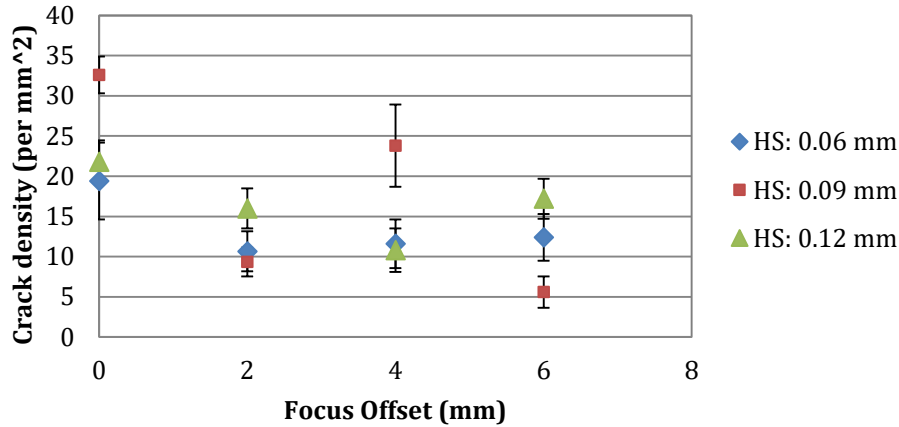


Figure 3.22 –Crack density with focus offset and hatch spacing

If the results in Figure 3.22 are compared to porosity results (Figure 3.17) it is observed that the trend of low porosity with higher crack density – as observed in the screening trial also – is present. Beyond this, there is no strong pattern from which to make a confident conclusion.

A final trial looked at whether crack density could be reduced by using a lower power, whilst still maintaining 99.9% density. It was expected that there would be a strong trend for low porosity of ‘high power high speed’ or ‘low power low speed’, as reported in other work (Deffley 2012). A range of 100-195 W and ~ 300-600 mm/s was chosen for LP and Ap. Vel respectively. Fixed parameters were FO = 4mm, HS = 0.09 mm and LT = 20 μm. All parts built at less than 150 W and one built at 150 W failed due to insufficient melting, which resulted from the low energy densities. Of the successful parts, those with porosities <0.5% are plotted in Figure 3.23.

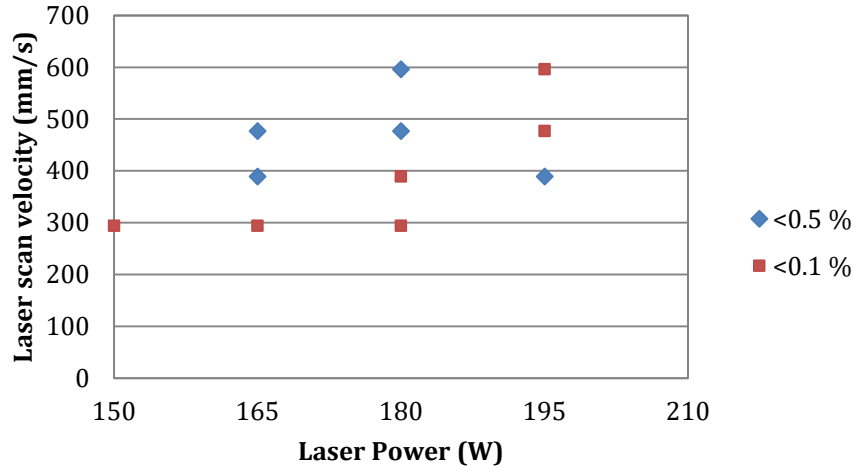


Figure 3.23 – Ap. Vel vs Laser Power for low porosity samples.

Figure 3.24 displays the corresponding crack density results, from which it is difficult to argue any particular trend, although 477 – 596 mm/s results in a drop in crack density for all powers.

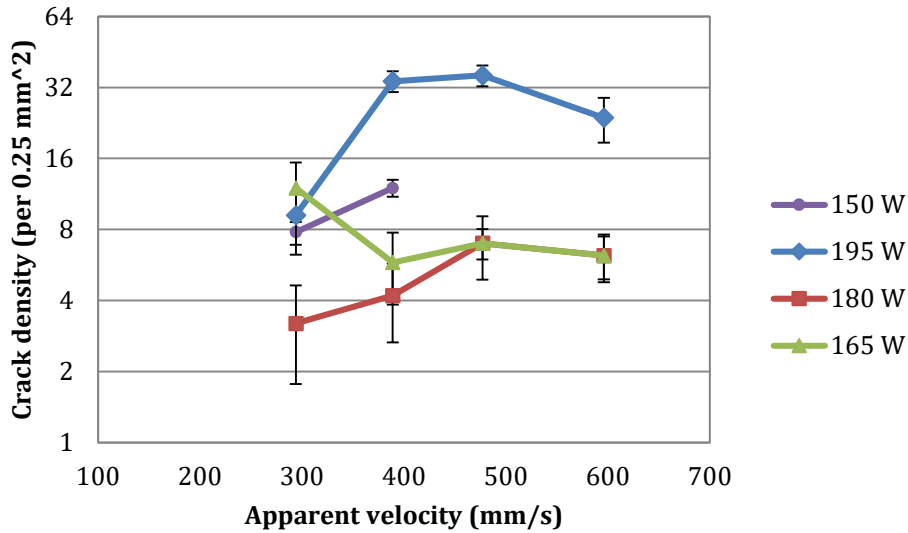


Figure 3.24 – Crack density vs Apparent velocity for laser powers of 150-195 W.

At this point it was decided that the use of apparent velocity was not the most appropriate method of combining PD and ET. Power, exposure time and point distance are all

controlling variables of laser energy, either per unit time or unit length. Plotting density against one or two of the three is nonsensical as it neglects the influence of the other two. As such, LP, ET and PD have been dimensionally reduced into a single parameter of 1D line energy density. This is an appropriate use of energy density since layer thickness and hatch spacing are fixed, thus any variation in density is purely as a consequence of the absorbed energy. If the energy density is considered over a set length it can be described as *Energy per point × Points per unit length* or $P \times ET \times 1/PD$, this becomes:

$$\frac{Pt_{exp}}{x_{PD}} \equiv \frac{Q}{l}$$

Equation 3.4

where P is power of the source, t_{exp} is the exposure time, x_{PD} is the distance between points of exposure, Q is energy and l is line length.

Figure 3.25 displays the LP vs Ap Vel results as 1D energy densities. It is observed that sample porosity has a strong relationship with energy density, whereas crack density is more dependent on laser power. This is understood if the Rosenthal model for a moving laser source is considered, in which the temperature profile has a significantly higher dependence on laser power than beam velocity (Rosenthal 1946). Higher temperature profiles result in steeper thermal gradients, and therefore an increase in the magnitude of thermal stress (Merzelis and Kruth 2006) which in turn increases the susceptibility of micro-cracking.

The minimum crack density achieved was 3.2 ± 1.4 cracks per mm^2 , for parameter set LP 180 W, PD 50 μm , ET 150 μs , LT 20 μm , FO 4 mm and HS 0.09 mm – this had a 1D energy density of 0.54 J/mm. The relatively large errors on crack density are a consequence of

the analysis method. As cracks are counted as integers, once low numbers are reached the deviation between measurements become respectively larger.

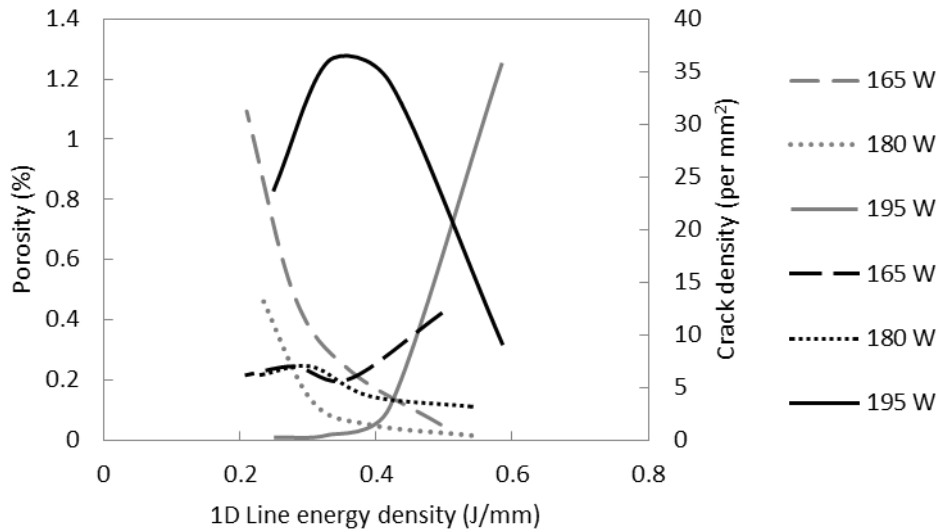


Figure 3.25 - Porosity (grey) and crack density (black) with 1D energy density in sets of laser power.

After all controllable parameters have been tested and optimised it can be said with confidence that it is not possible to process this composition of Hastelloy X without micro-cracks – as detectable through optical or electron microscopy, when processed on a Renishaw SLM 125 system; proving the need for an alternative solution to parameter optimisation.

3.4 Chapter summary

In this chapter, a number of preliminary but key experiments were performed. The purpose of these experiments was to gain understanding in operation of the SLM system and the influence of process parameters on material response, as well as establishing a benchmark for micro-cracking of a ‘crack susceptible’ alloy for later experiments.

A DOE approach was used to optimise process parameters for maximum density and minimum porosity. Crack density was reduced to a minimum of 3.2 cracks per mm², but

critically, cracks could not be eliminated, providing justification for an alloy design approach.

It was found that there was a relatively large process window in which >99.5% density could be achieved, however crack density was much more sensitive, and clear relationships between process parameters and crack density could not be defined.

4 Establishment of Rapid Solidification

The theory of microstructure development for laser surface processing was discussed in Section 2.4. SLM is regarded as a laser surface process, however up until this point SLM has not been fully established as a Rapid Solidification Process (RSP).

Before considerations for adapting material response can be made to improve alloy processability, the microstructure of the processed material must first be established, and to an extent predicted. This chapter looks to establish whether SLM is indeed an RSP and what the implications will be on the microstructure and properties of SLM processed material.

4.1 Rapid solidification conditions applied to SLM

4.1.1 Interface velocities and microstructure

From Section 2.4.3, observations in literature imply relatively strict solidification conditions which result in similar microstructures for different materials and process parameters – although the limit to this relationship is unknown.

In order to establish whether SLM lies in the realm of RSP, the relationships discussed in Section 2.4.2.2 are applied to known SLM quantities. Firstly, for the solidification interface velocity resultant from a moving laser beam (Gremaud, Carrard et al. 1990), we calculate $V_s \leq 1$ m/s given typical beam velocities of 0.1-1 m/s. This places the solidification interface velocity firmly in the region of RS. However, the scenario is more complicated when considering the specific Renishaw SLM125 system, as the beam does not have velocity. Instead we consider the solidification for an individual melt pool.

Kear and Breinan (Bass 2012) described the heat transfer relationship for a single laser spot for thermal gradient and cooling rate. First though, the solutions of the transient temperature field during heat and cooling are described.

Term	Description	Units	Value (material Hastelloy X)
erfc	complimentary error function		
κ	thermal conductivity	W/cmK	@RT = 9.1
q_0	absorbed power density	W/cm ²	750,000
t	time	s	
T	temperature	K	
T_0	initial temperature	K	293
x	depth beneath surface	cm	
α	diffusivity = $\kappa / (\rho \times C_p)$	cm ² /s	@RT = 0.023
γ	$t - \tau$	s	
τ	heat time (duration of laser power)	s	100×10^{-6}

Table 4.1 - Glossary of terms - adapted from (Bass 2012)

During heating:

$$T(x, t) = \frac{q_0}{\kappa} \left[\left(\frac{4\alpha t}{\pi} \right)^{\frac{1}{2}} e^{-[x/(4\alpha t)^{1/2}]^2} - x \operatorname{erfc} \left(\frac{x}{(4\alpha t)^{1/2}} \right) \right] + T_0$$

Equation 4.1

During cooling:

$$T(x, t) = \frac{q_0}{\kappa} \left\{ \left(\frac{4\alpha t}{\pi} \right)^{\frac{1}{2}} e^{-[x/(4\alpha t)^{1/2}]^2} - \left(\frac{4\alpha \gamma}{\pi} \right)^{\frac{1}{2}} e^{-[x/(4\alpha \gamma)^{1/2}]^2} - x \left[\operatorname{erfc} \left(\frac{x}{(4\alpha t)^{1/2}} \right) - \operatorname{erfc} \left(\frac{x}{(4\alpha \gamma)^{1/2}} \right) \right] \right\} + T_0$$

Equation 4.2

The thermal gradient $G(x,t)$ and cooling rate $T(x,t)$ can then be written by partially differentiating Equation 4.2 with respect to x and t respectively.

$$G(x, t) = \frac{\partial T}{\partial x} = -\frac{q_0}{\kappa} \left[\operatorname{erfc} \left(\frac{x}{(4\alpha t)^{1/2}} \right) - \operatorname{erfc} \left(\frac{x}{(4\alpha \gamma)^{1/2}} \right) \right]$$

Equation 4.3

$$\dot{T}(x, t) = \frac{\partial T}{\partial t} = \frac{q_0}{\kappa} \left[\left(\frac{\alpha}{\pi t} \right)^{1/2} e^{-[x/(4\alpha t)^{1/2}]^2} - \left(\frac{\alpha}{\pi \gamma} \right)^{1/2} e^{-[x/(4\alpha \gamma)^{1/2}]^2} \right]$$

Equation 4.4

Solidification rate $V = \dot{T}/G$ or $\dot{T} = GV$.

Equation 4.5

Equation 4.3 and Equation 4.4 can then be used to predict the solidification velocity range, through Equation 4.5, for a given material and laser exposure parameters. It is important to note at this point that this model does not consider latent heat of melting.

In order to calculate values from Equations 4.3-4.5 it is necessary to first consider the initial conditions.

The maximum power output of the Renishaw SLM125 is 200 W, therefore given a beam diameter $\sim 100\mu\text{m}$, the *incident* power density is $\cong 2.5 \times 10^6 \text{ W/cm}^2$. However, for the wavelength of the Ytterbium fibre laser, 1060 nm, the absorptivity of nickel is 0.6 (60%), in addition we assume a further 90% reduction as a result of material being in powder form, giving a $q_0 \cong 150,000 \text{ W/cm}^2$. This large reduction was determined by comparison of predicted melt pool depths and those from experimental trials. Although it seems

unnaturally low, the use of higher absorptivity values results in unrealistic maximum temperatures, this phenomenon is reported in other works (Roberts, Wang et al. 2009).

For a nickel base alloy, 200W laser power combined with exposure times of $\sim 100 \mu\text{s}$ result in melt pool depths of $\sim 150 \mu\text{m}$ – with a powder depth of $20 \mu\text{m}$. $150 \mu\text{m}$ is then set as the melt pool depth, d for the chosen q_0 .

The condition of full melting implies that the temperature at the base of the melt pool, where $x = d$, will be that of the melting point of the alloy, T_m . Equation 4.1 can then be solved iteratively, setting it equal to T_m (for nickel superalloys 1500 K) to calculate the time taken for $T=T_m$ at $x=d$; this is referred to as the heat time τ .

Given that the alloy is being surface heated, the temperature at the surface continues to rise over time until it reaches its maximum, T_{max} , at time τ . T_{max} can therefore be calculated by solving Equation 4.1 for $x = 0$ and $t = \tau$.

Once the material has been melted to a depth d , after time τ , energy input is ceased and the melt begins to cool, and then solidify. As the material solidifies, the depth at which the temperature is equal to T_{melt} moves towards the surface. Solidification is complete once the surface temperature is equal to the T_{melt} . The time $t = \tau'$ at which solidification is complete is established by solving Equation 4.2 iteratively for depth, between the limits of $0 < x < d$. This is represented graphically in Figure 4.1.

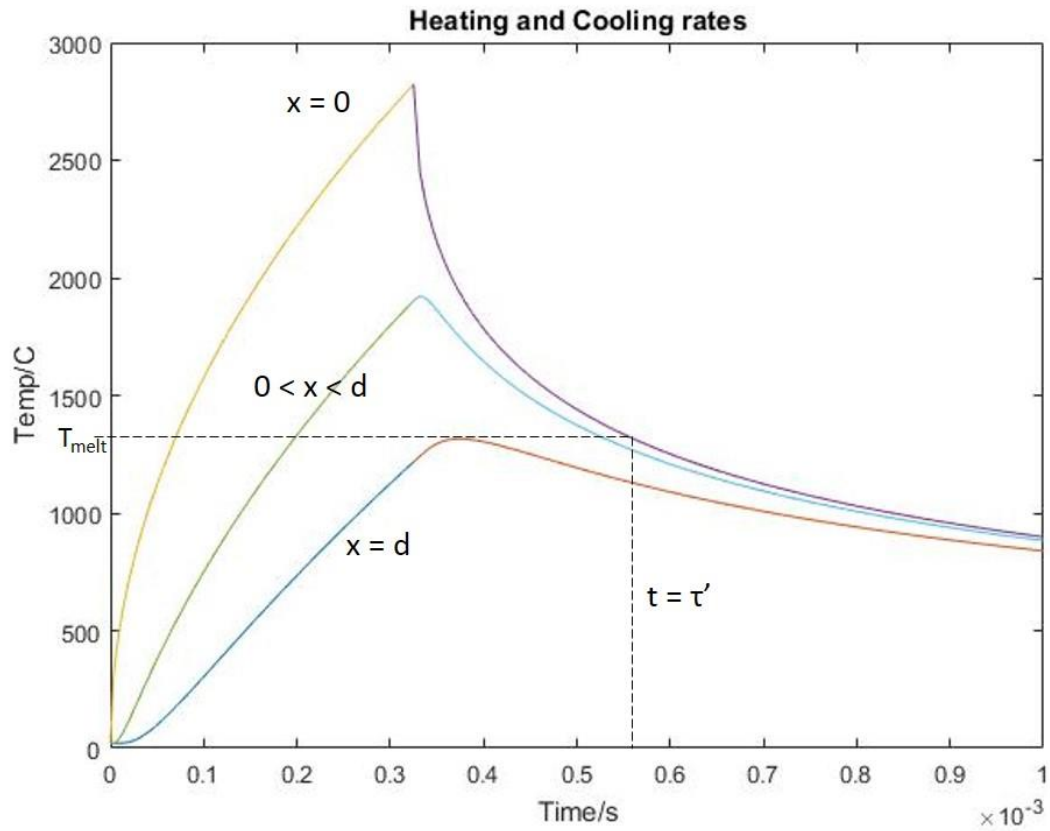


Figure 4.1 - Temperature for a given depth with time.

Once τ' had been calculated, a limiting value for γ was determined and Equation 4.3 and Equation 4.5 could be solved. The resulting plots are given in Figure 4.2 to Figure 4.5

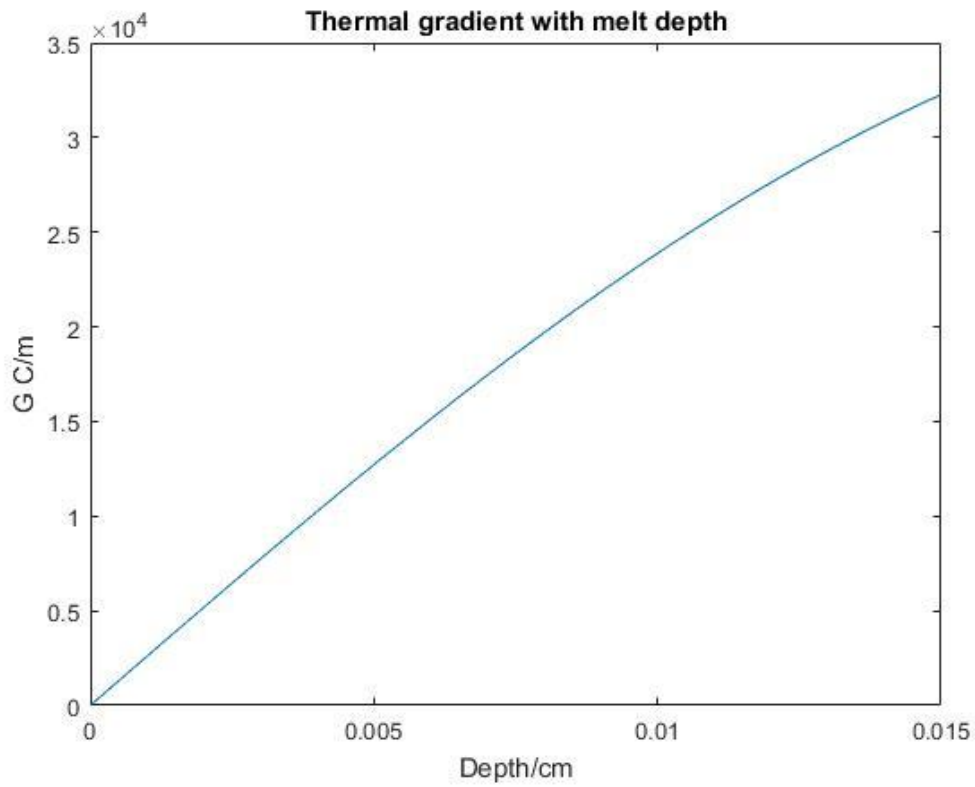


Figure 4.2 - Thermal gradient with melt depth

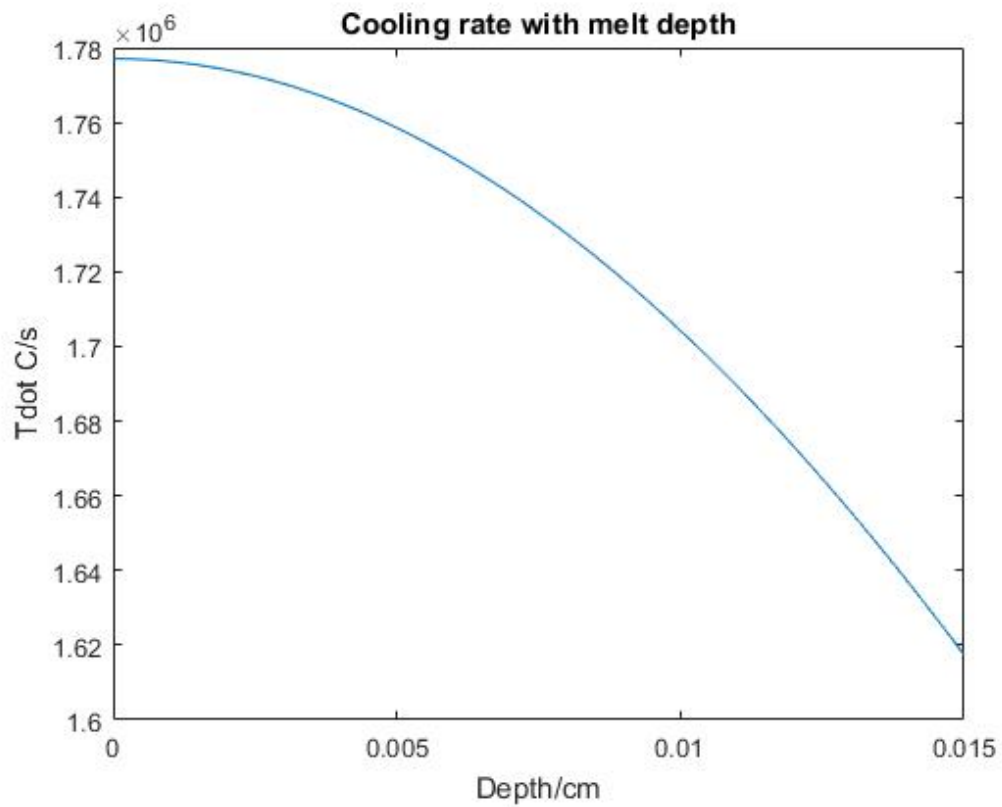


Figure 4.3 - Cooling rate with melt depth

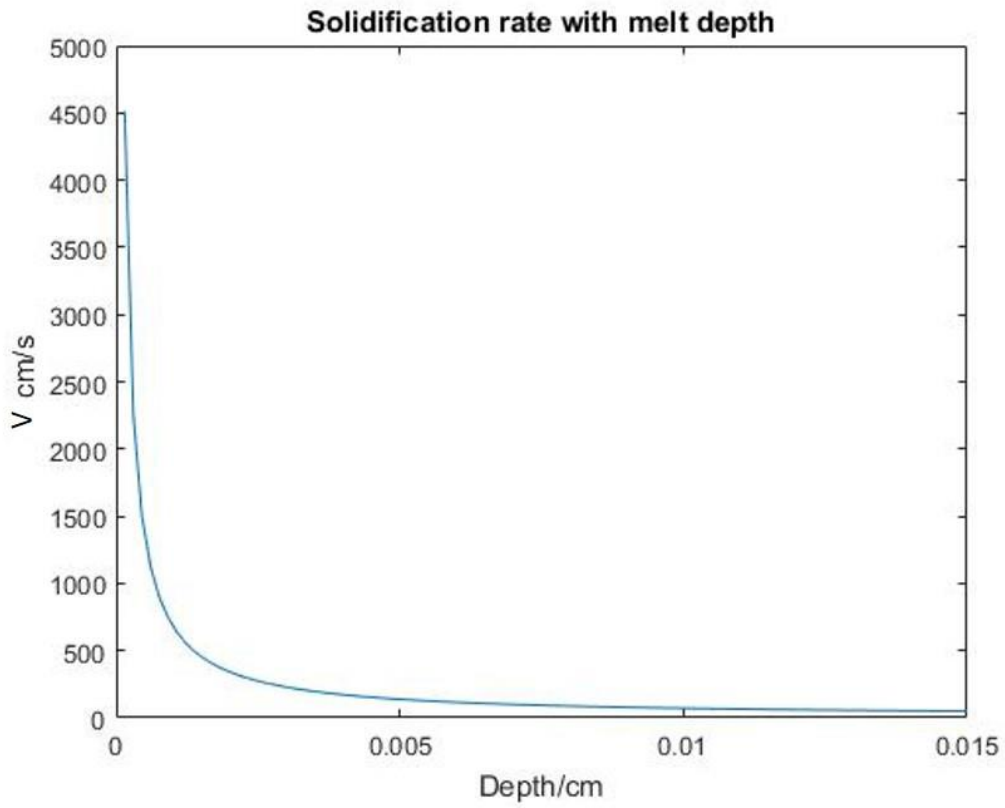


Figure 4.4 - Solidification rate with melt depth

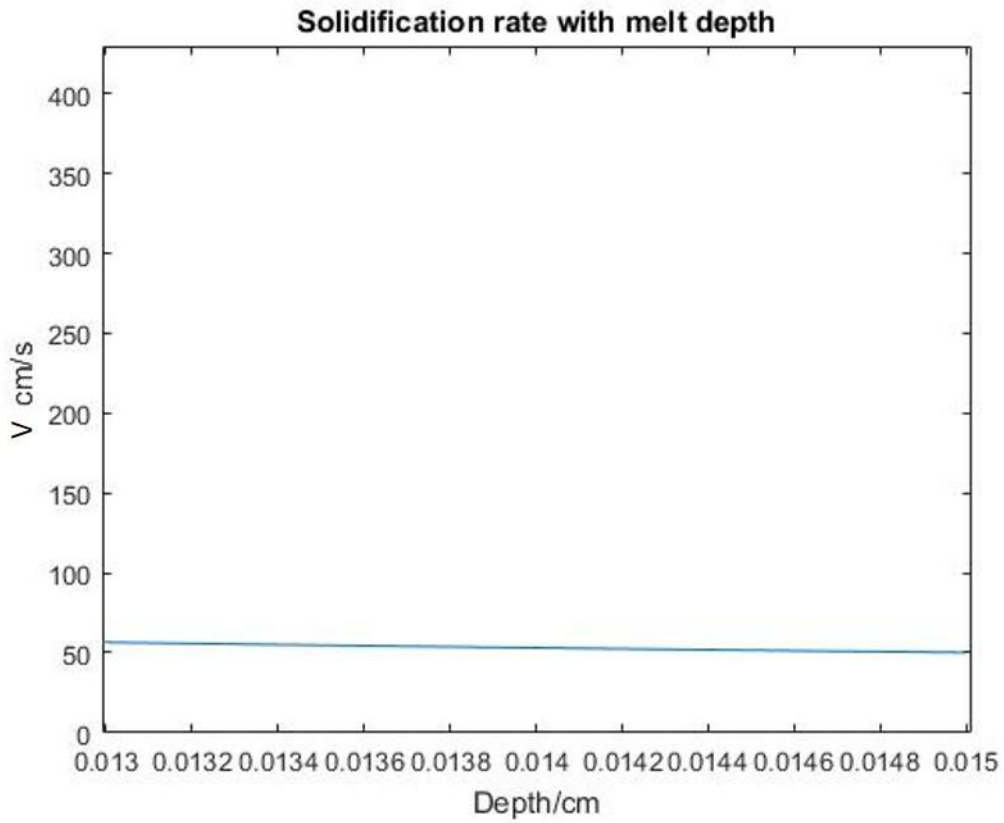


Figure 4.5 - Solidification rate at base of melt pool

From Figure 4.4 and Figure 4.5 we can see that the solidification rate V is 0.5 m/s at the base of the melt pool, accelerating to a point of infinity at the surface. The behaviour of thermal gradient G and cooling rate $|\dot{T}|$ agrees with that described by Kurz and Trivedi (1994) for solidification with a moving laser source. However, the solidification rate shows a different form. This is not unexpected as the case described in this section is for a single laser spot with stationary source, and it does agree with the example for pure nickel, given in (Bass 2012). It is expected for the case of SLM, the subsequent fusion spots would influence the final stages of solidification, as heat is conducted from the neighbouring fusion point. The solidification rate would be slowed as the spot was partially remelted – given that the point distance is typically less than the length of the melt pool.

Although this model is relatively simple, as it does not include latent heat of fusion in its calculations, the minimum solidification rate of 0.5 m/s serves as supporting evidence that SLM on a Renishaw style point to point system will still result in rapid solidification conditions.

With regard to predicted microstructure, it is again first established whether solidification will occur in steady state conditions. Using the relationship from Zimmermann, Carrard et al. (1989) and the predicted V_s range, it is predicted that $\frac{D \partial V_s}{V_s \partial x} < 10^{-4}$ and steady state growth theory can still be applied. Therefore, as with laser welding, the microstructure is predicted to be columnar dendritic/cellular, depending on beam velocity and chemical composition. This statement can be justified by consulting the microstructure selection map in Figure 4.6. Given a $\Delta T \sim 2500$ K (based on an ambient $T = 300$ K and a max surface $T = 2800$ K – as predicted by the single spot model), and

distance of $\sim 150 \mu\text{m}$ (depth of a melt pool), a $G \sim 10^6 \text{ K/m}$ is calculated. Using 0.1 m/s as the lower interface velocity limit, microstructure falls into the columnar dendrite range.

The packing of the dendrites can be predicted by first predicting the primary DAS λ_1 . Davies *et al.* (Davies, Shohoji *et al.* 1980) determined a relationship between λ_1 and cooling rate, given as $\left(\frac{\partial T}{\partial t}\right)$, as shown in Equation 4.6.

$$\lambda_1 = 97 \pm 5 \left(\frac{\partial T}{\partial t}\right)^{-0.36 \pm 0.01}$$

Equation 4.6

Using the relationship for directional growth of $|\dot{T}| = GV$, and the G and V used for microstructure selection, a $|\dot{T}| \sim 10^5 \text{ K/s}$ is predicted for SLM processing. This gives a $\lambda_1 = 1.5 \pm 0.1 \mu\text{m}$, implying fine and/or close packed dendrites. It is not expected that banded or planar structures will be achieved simply because the interface velocities are not sufficient, see Figure 4.6, nor have they been reported in SLM processing to date.

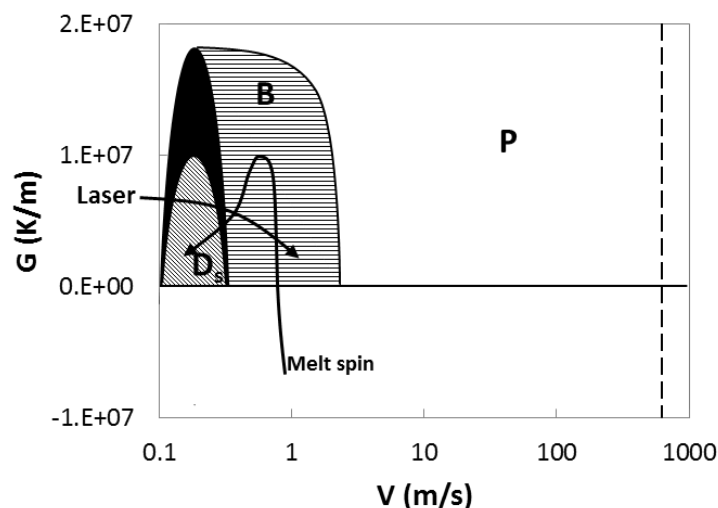


Figure 4.6 - Reproduction of Figure 2.21 for easy reference

From crystal growth theory discussed in Section 2.4.1 it is predicted that the dendrites will grow along the preferred crystallographic orientation, closest to the direction which

is anti-parallel to the heat flux, with grains prevailing through competitive growth. A melt pool contained within a solid material is comparable to a melt contained with a mould. The heat flux is therefore perpendicular to the melt pool trace (interface between melt and solid material) and is approximately radial, therefore resulting in radially orientated grains, see Figure 4.7.

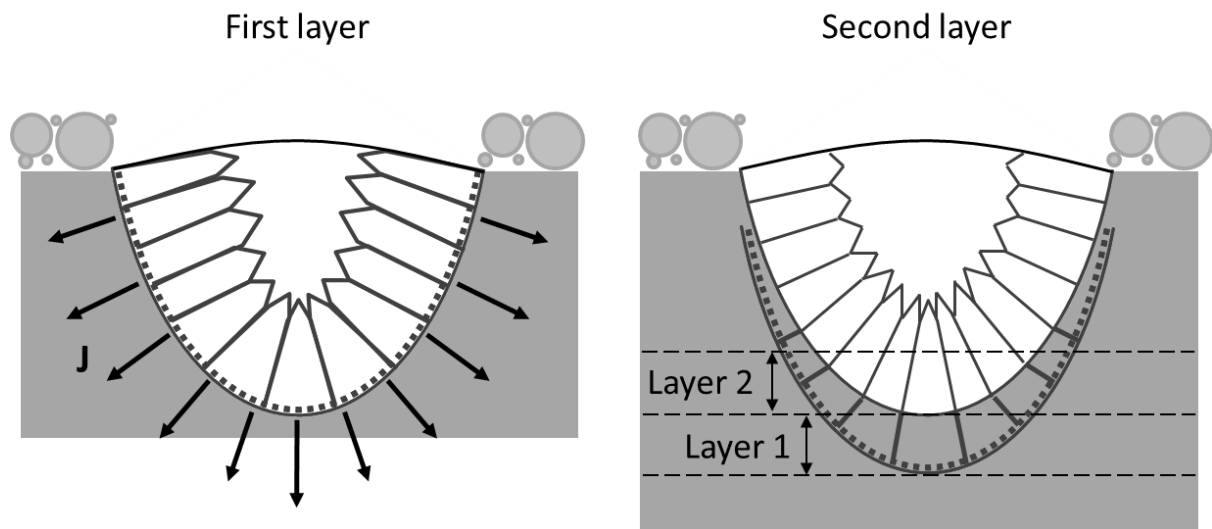


Figure 4.7 - Grain growth for melt pool in first layer (left) and then epitaxial growth in subsequent layer.

In the successive layer, rather than nucleation at the edge of the melt trace and competitive growth of grains, crystal growth is continued from the previous layer and the dendrites advance epitaxially transcending multiple layers. As each successive layer remelts the majority of the previous one, only the grains at the base of the trace remain each time, Figure 4.7 right-hand image. The orientation of the dendrites is maintained by the presence of a large heat sink (substrate) which creates a strong heat flux anti-parallel to the build direction. All this culminates in high aspect ratio columnar grains oriented in the build (z) direction (Deffley 2012); this microstructure has been well documented in SLM investigations (Amato 2012, Vilaro, Colin et al. 2012, Wang, Guan et al. 2012, Rickenbacher 2013).

4.1.2 Solute trapping

The prediction/observation of dendrite-cells (Amato, Gaytan et al. 2012, Vilaro, Colin et al. 2012, Wang, Guan et al. 2012, Rickenbacher 2013) in AM microstructures means that segregation free microstructures are not in general to be expected, however the magnitude of segregation and over what length scale it occurs has significant effects on material response and processed material properties.

From Section 2.4.2.1 it is evident that the predicted critical velocity for complete solute trapping ranges from ~ 0.1 m/s for arsenic in silicon (Baeri, Foti et al. 1981) up to 26 m/s for zirconia in nickel (Arnold, Aziz et al. 1999), however as we do not expect complete solute trapping it is instead the onset velocity, and transition velocity range, that are critical to the discussion of microstructural evolution here. In order to predict this the following approach is taken:

From Figure 2.19 complete solute trapping occurs when $\log\left(\frac{V\lambda}{D_i}\right) = 2$ and onset at $\log\left(\frac{V\lambda}{D_i}\right) = -1$. Therefore the interface velocity for complete solute trapping V_{comp} and onset of solute trapping V_{onset} are given in Equation 4.7 and Equation 4.8.

$$V_{comp} = 100 \times \frac{D_i}{\lambda}$$

Equation 4.7

$$V_{onset} = 0.1 \times \frac{D_i}{\lambda}$$

Equation 4.8

It is now assumed that the nickel-zirconia system, although dilute, is the closest representation of a nickel superalloy in literature for this problem. Therefore, using a $\lambda = 10^{-9}$ m and replacing the upper limit of 100 m/s with 26 m/s

$$V_{comp} = 26 = 100 \times \frac{D_{i[Ni-Zr]}}{10^{-9}}$$

Equation 4.9

Therefore $D_{i[Ni-Zr]} = 0.26 \times 10^{-9} = 2.6 \times 10^{-10} \text{ m}^2/\text{s}$. Putting this value into Equation 4.8, we get a calculated $V_{onset} = 0.026$ m/s which serves as the lower limit for solute trapping. In order to determine when significant solute trapping will occur, we determine the critical velocity for significant solute trapping V_{crit} by assuming $\log\left(\frac{V\lambda}{D_i}\right) \geq 0$, and hence

$$V_{crit} = \frac{D_{i[Ni-Zr]}}{\lambda}$$

Equation 4.10

Giving a $V_{crit} = 0.26$ m/s.

This analysis implies that, for the example of the Ni-Zr system, SLM processing should indeed result significant solute trapping, but that is unlikely to result in segregation free structures – if considering Figure 4.6. The calculated D_i is also of the same order of magnitude as that calculated via the alternative analysis of Boettinger et al. (Boettinger, Coriell et al. 1984) and implies that for the majority of cases $V_{onset} \sim 10^{-2}$ m/s and $V_{crit} \sim 10^{-1} - 1$ m/s.

It is therefore accepted that under SLM solidification conditions, highly mobile solutes may achieve very short distance diffusion, but V_s is high enough to inhibit intergranular

segregation, and there is no direct evidence either from the literature to date or from the present work to suggest otherwise. This therefore places doubt on the conclusions drawn on scant evidence by Tomus *et al.* regarding the segregation of minor elements towards grain boundaries and the formation of brittle/weak phases as a key factor in the generation of micro-cracking in nickel alloys. However, the result of increasing the Si and Mn content should not be ignored as it still affects the crack susceptibility, regardless of mechanism.

4.2 Experimental verification

It has been proposed in Section 4.1 that SLM processing conditions will result in the formation of dendrite-cells with segregation limited to interdendritic regions or near completely inhibited. Observational evidence from literature serves as part validation, but further experimentation and analysis is required to make confident conclusions.

4.2.1 Microstructure analysis

Samples from the parameter optimisation trial were etched to reveal microstructures and observed by both optical and electron microscopy.

As seen in Figure 4.8, the grain structure is as predicted and consists of large columnar grains which cross multiple layers. The larger grains are of the order of 500 μm in length and between 50-100 microns in width, and do not adhere to melt track boundaries, implying that dendrites did indeed advance via epitaxial growth and were not dominated by the local heat flux in the melt pool. The grains are defined only by dendrite orientation with no visible solute segregation to grain boundaries; the grains were only revealed by using a polarising filter. The orientation of the grains themselves is antiparallel to the bulk heat flux, which is in the negative z direction.

Cross sections of melt tracks are visible depending on the orientation of the dendrites; this varies as a result of the meander scan strategy used. The grain structure is perhaps not as well defined as it is in some reported in literature, Vilaro, Colin et al. (2012) for example, which is attributed to the meander strategy. The depth of the light shaded melt pool areas corresponds to the 20 μm layer thickness and the dark bands are traces of melt pools in different orientations.

Cracks are observed to lie along the grain boundaries, and the morphology implies either DDC or ETSS cracking – this will be discussed further in Chapter 5.

Higher magnification micrographs are displayed in Figure 4.9. From these we note minor levels of interdendritic segregation, which is particularly visible in the horizontal section. In addition, the microstructure appears to be cellular like, although this is better observed in the SEM imaging.

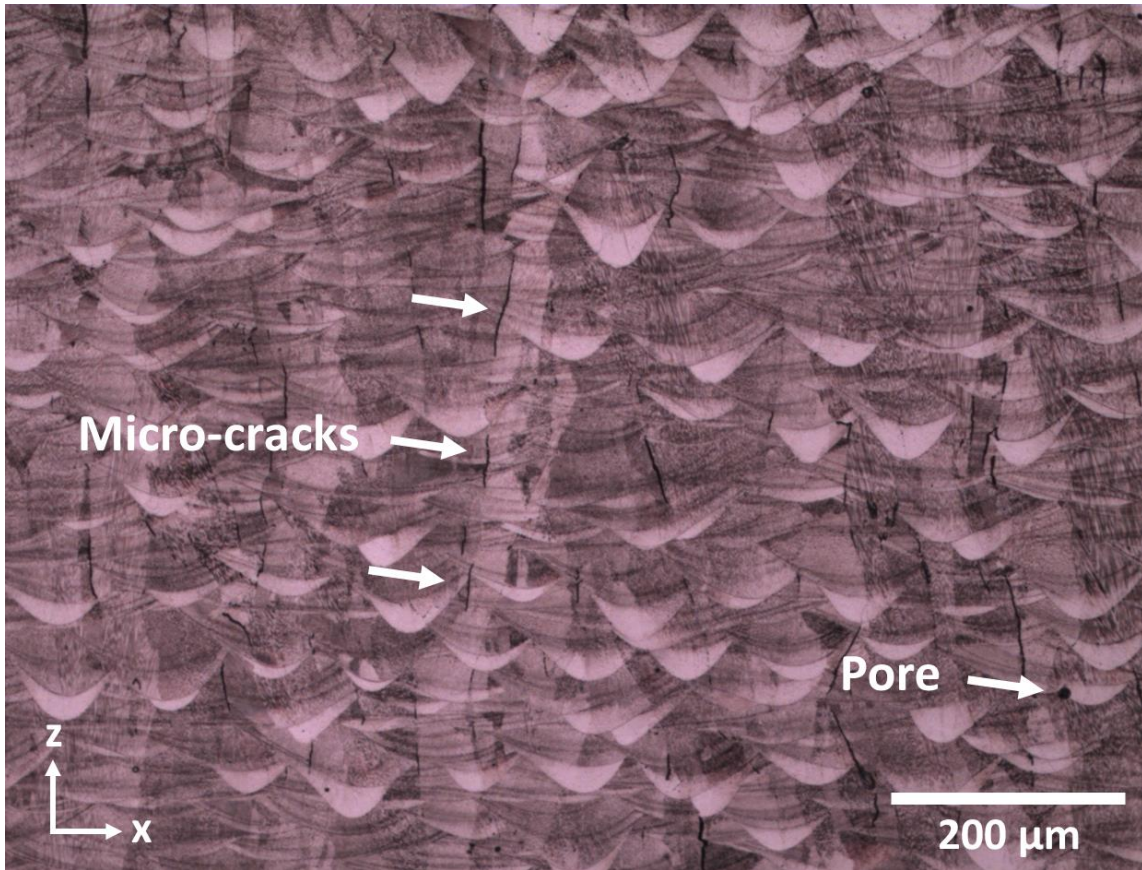


Figure 4.8 – Optical micrograph of etched vertical section of Hastelloy X fabricated with LP of 195W, PD of 53 μm and ET of 115 μs . Sample has a crack density of 34 ± 3.5 cracks per mm^2 . Note the absence of visible boundaries between grains, this is as a result of no segregation of solute to the edges of the grain and thus etching only reveals dendritic structure.

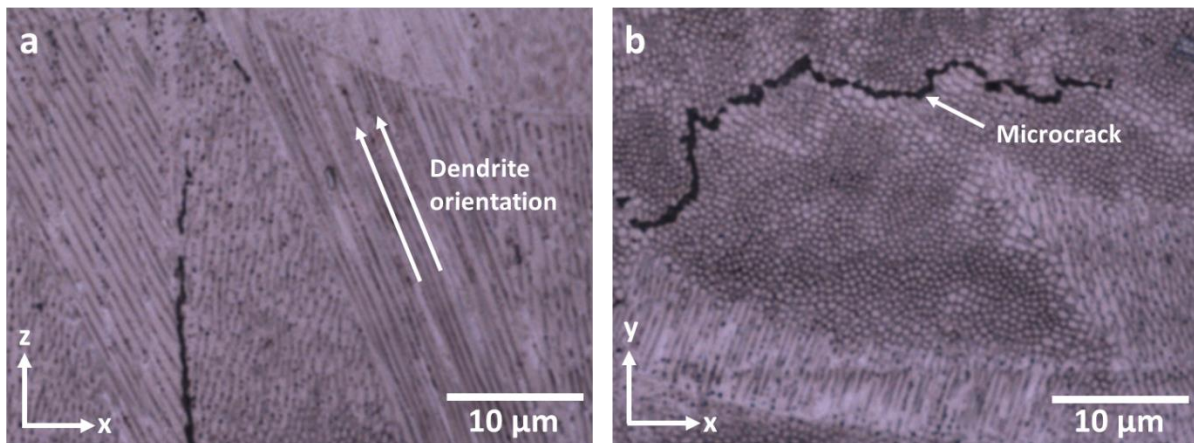


Figure 4.9 - a) Vertical section shows dark interdendritic regions between light coloured dendrites, with micro-crack running between grains regions of different orientated dendrites (grains). b) Horizontal section, orientations which vary from perpendicular to incident line of sight are highlighted by polarisation and appear lighter in colour and deviate from the circular cross section of the cell-dendrites.

More obvious in the SEM micrographs - Figure 4.10 - than in the optical is that the intersecting of melt tracks has caused disruption to the epitaxial grain growth and resulted in the creation of smaller grains interspersed between the primary columnar grains. It is noted that the smaller grains increase in number with build height, as the influence of the heat flux reduces and competitive growth becomes more dominant.

The lighter colour regions which mimic the melt traces are remnants of previous melt pool traces, highlighted by the variations in solute concentration. In the initial stages of the interface front acceleration, the interface velocity is sufficiently low to allow low level solute diffusion, hence why the base of the melt pools (melt traces) become visible with etching. If an established melt trace is heated or partially remelted by an adjacent or subsequent melt track, this allows for diffusion within the solid, thus distributing the concentration across a greater area.

High magnification SEM micrographs initially imply that the crystal structure is cellular or cellular-dendritic with a distinct absence of secondary arms, see top corner of Figure 4.10. However from Figure 4.11 the crystals are arguably closer to dendritic than cellular given the presence of dendrite trunk edge features which are potentially the initial stages of secondary arm growth; although they are not present on every dendrite-cell. The microstructure is therefore closer to cellular than first predicted, although it is consistent with observations from literature. Using high magnification micrographs, primary DAS λ_1 were measured at $1.05 \pm 0.1 \mu\text{m}$, which is slightly less than predicted. Using the Davies relationship, Equation 4.6, a cooling rate of $3 \times 10^5 \text{ K/s}$ may be derived which is consistent with the value predicted and is in agreement with a $V_s \leq 1 \text{ m/s}$, providing thermal gradients did not vary significantly from 10^5 K/m .

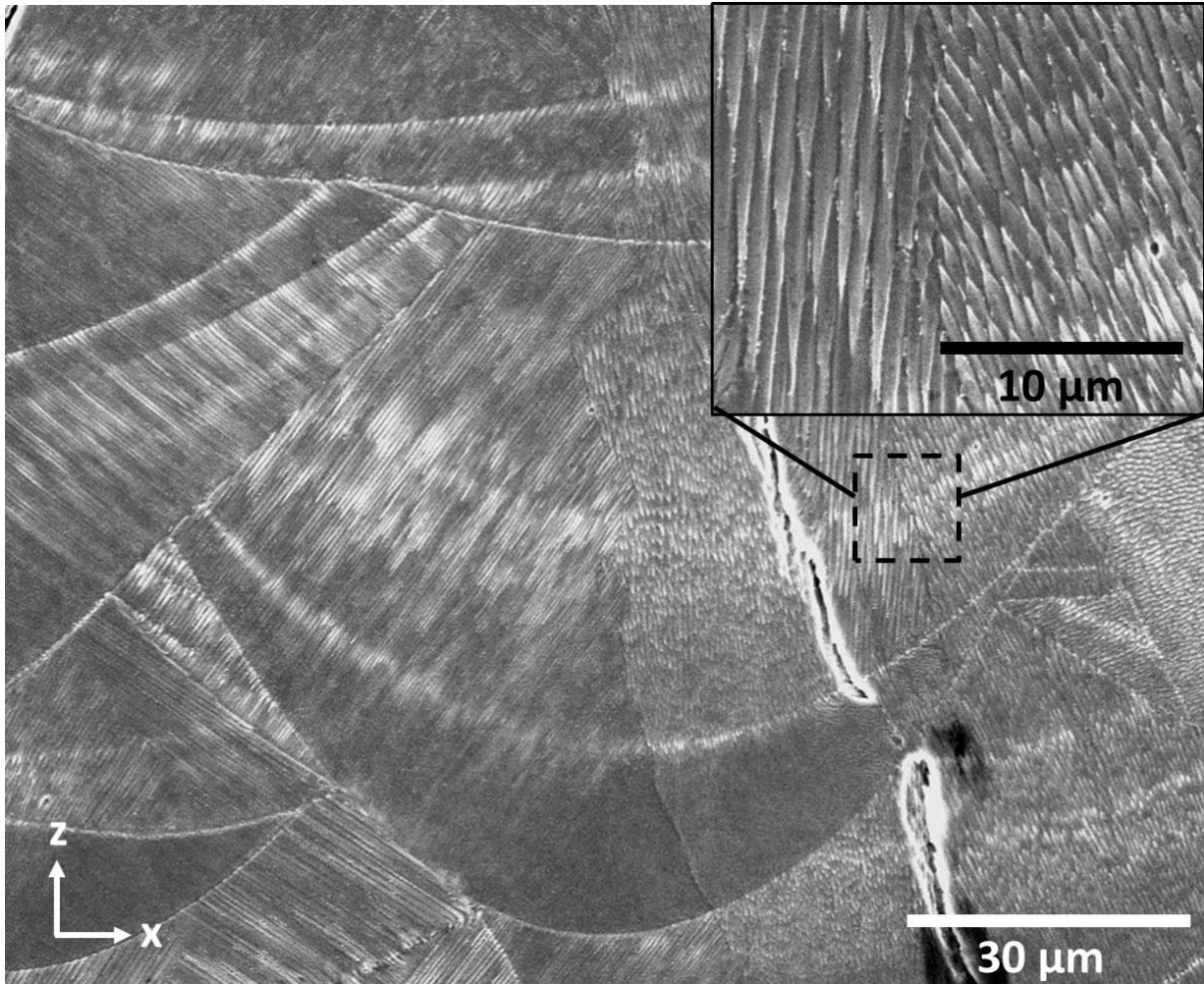


Figure 4.10 - SE mode SEM micrographs. Primary grain boundaries are visible running up the centre of the melt trace, a second less visible boundary is magnified in the secondary image. Note that the visible apexes on the crystals are not a physical feature and are in fact a result of the crystal orientation intersecting the observational plane.

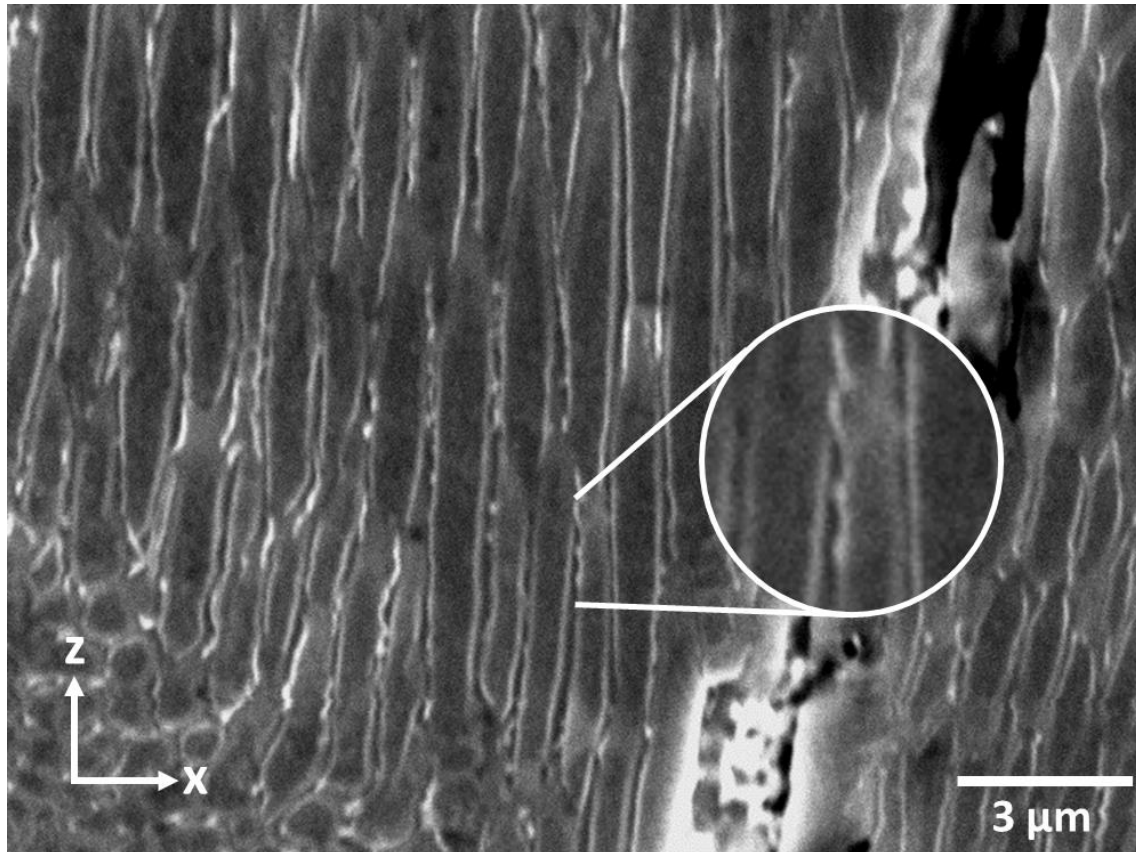


Figure 4.11 - High magnification SE mode SEM micrograph showing dendrite wall features which may be interpreted as secondary arm nubs - magnified in white circle. Light edging implies minor solute diffusion to interdendritic region.

Another key observation is the absence of secondary phase precipitates. Although strengthening phases such as γ' or γ'' were not expected, it was possible that small MC carbides may have time to form. In order for precipitation of secondary phases to occur, there has to be sufficient concentration of diffused solute atoms in the interdendritic region. This requires additional consideration of *solid state* diffusion, as opposed to that at the solid-liquid interface.

If solute diffusion in the solid state can occur from the point at which solidification is complete T_m to $0.5T_m$, the diffusion temperature range is therefore $\Delta T_{dif} = 0.5T_m$ which for the example alloy Hastelloy X is 814 K (Inc. 1997). Given a typical onset of melting of $\sim 1300^\circ\text{C}$ or 1600 K for nickel superalloys (Donachie and Donachie 2002), the following

calculations are applicable to the nickel superalloys as a whole, and not specific to Hastelloy X.

With a cooling rate $\dot{T} = 3 \times 10^5$ K/s, the time window for diffusion $t_{\text{dif}} = 2.2 \times 10^{-3}$ s. The steady state diffusion distance, that is distance from the primary dendrites to the centre of the interdendritic region, $\delta_{\text{precipitate}} = \lambda_1/2 \cong 0.5 \times 10^{-6}$ m. The distance travelled by a solute atom in a time t_{dif} is given by $X = (D_s \cdot t_{\text{dif}})^{1/2}$.

For this scenario, tungsten and tantalum are chosen as a potential MC/precipitate forming solute elements. The solid state diffusion coefficient of tungsten at 1400K is $D_{s[\text{W}]} = 1.1 \times 10^{-15}$ m²/s and tantalum $D_{s[\text{Ta}]} = 9.3 \times 10^{-15}$ m²/s (Karunaratne, Carter et al. 2000) which give an upper and lower limit. This gives an $X(\text{W}) = 1.5 \times 10^{-9}$ m and $X(\text{Ta}) = 4.5 \times 10^{-9}$ m.

The solute atoms will therefore only travel up to 1/100 of $\delta_{\text{precipitate}}$ before temperatures inhibit atomic movement and diffusion ceases. This implies that the required magnitude of solute diffusion for precipitation to occur, and thereby precipitation itself, would be inhibited by the solidification conditions. Observations from recent studies support this (Vilaro, Colin et al. 2012, Wang, Guan et al. 2012).

4.2.2 Microsegregation of minor elements

In Section 4.1.2 it was proposed that the chemical segregation of minor elements should not, based on an analysis the prevalent solidification conditions, be a significant factor contributing to the crack susceptibility of Hastelloy X in SLM. To explore this further, EDS line scans were conducted across crack interfaces on 3 separate samples, two examples of which are displayed in Figure 4.12. Inspection of the line scans indicates variation of alloying elements across the scan length; however, no one element is seen to significantly

increase towards the crack edge, as would be expected if segregation to the grain boundary had occurred. Of particular interest is that Si, one of the minor elements highlighted by Tomus (Tomus, Jarvis et al. 2013), does not show any sign of concentration at the crack edge, nor do any of the primary matrix elements (Ni, Cr and Fe) deplete. The only significant variation is over the crack itself, where all matrix elements dip as expected.

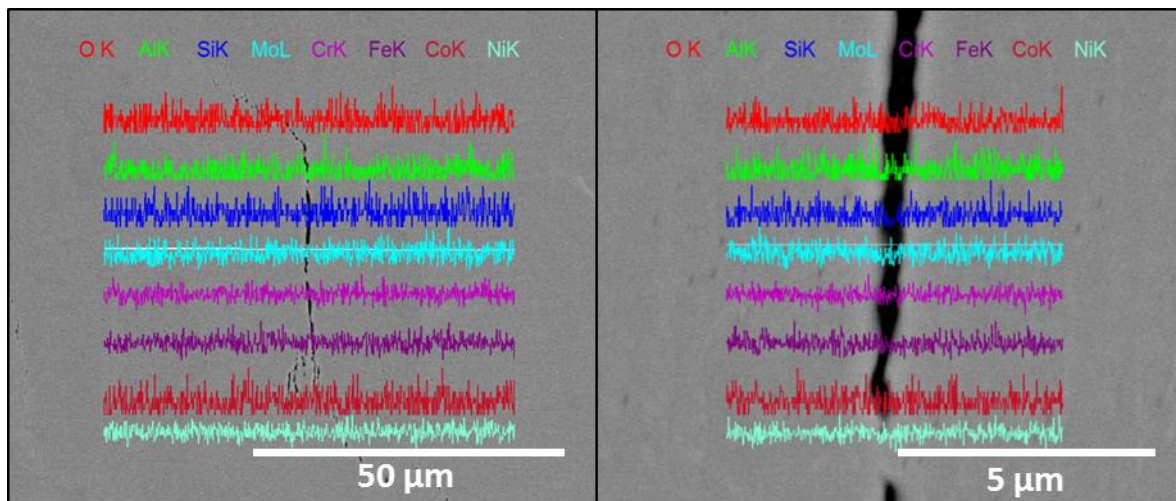


Figure 4.12 - Two EDS line scans of a crack at medium (left) and high (right) magnification.

4.3 Sub-micron precipitate analysis

In Figure 4.10, in the top image, small white specks are observed around the interdendritic regions, likewise in Figure 4.11. In order to establish what the features were, time was acquired on the FEI Inspect F Field Emission Gun (FEG) SEM. The Inspect F has higher magnification capabilities than the Camscan S2, and is effectively able to resolve features of length scales down to 10 nm making it ideal for sub-micron feature analysis. In addition to higher resolutions, the Inspect F also has an EDAX module enabling chemical analysis by EDS.

Before conducting chemical analysis, an ultra-high magnification (120,000 x) image was taken of a dendrite and interdendritic region, Figure 4.13. It observed that the features are clearly part of the microstructure, and their morphology suggests they are secondary phase, although some appear to be extensions of the dendrite trunk. The majority are irregular, discontinuous and globular in morphology, implying either MC carbides or sigma phase (Donachie and Donachie 2002). The continuous wave like structure (bottom left) is similar in appearance to that of the potential secondary arms observed in Figure 4.11, however in this image it is, in parts, separate from the dendrite trunk. From a lower magnification image, Figure 4.14, the continuous features are observed to be attached to some dendrites and of a similar colour to the edges of the dendrites. It is proposed that these irregular continuous features are most likely remnants of the higher solute concentration matrix phase formed from local diffusion to the interdendritic regions, which has been all but eroded by the etchant.

The electron backscatter detector was then used in place of the secondary electron detector (standard imaging) as it highlights any differences in chemical composition. The electron back scatter is stronger from elements of a high atomic number compared to those with a low atomic number, and therefore a region with a higher concentration of heavy elements will appear brighter. This would enable an initial indication as to whether the features were secondary or primary phase.

Figure 4.15, shows the back scatter micrograph of dendrites in the horizontal section. It is observed that there are particulates situated in the interdendritic regions, whose bright appearance implies a different composition to the dendrites. However, it is also observed that they range in relative contrast, implying the composition of the precipitates is not

consistent across the sample. Figure 4.15 also demonstrates the cellular structure of the crystals, with no hint of secondary dendrite arms.

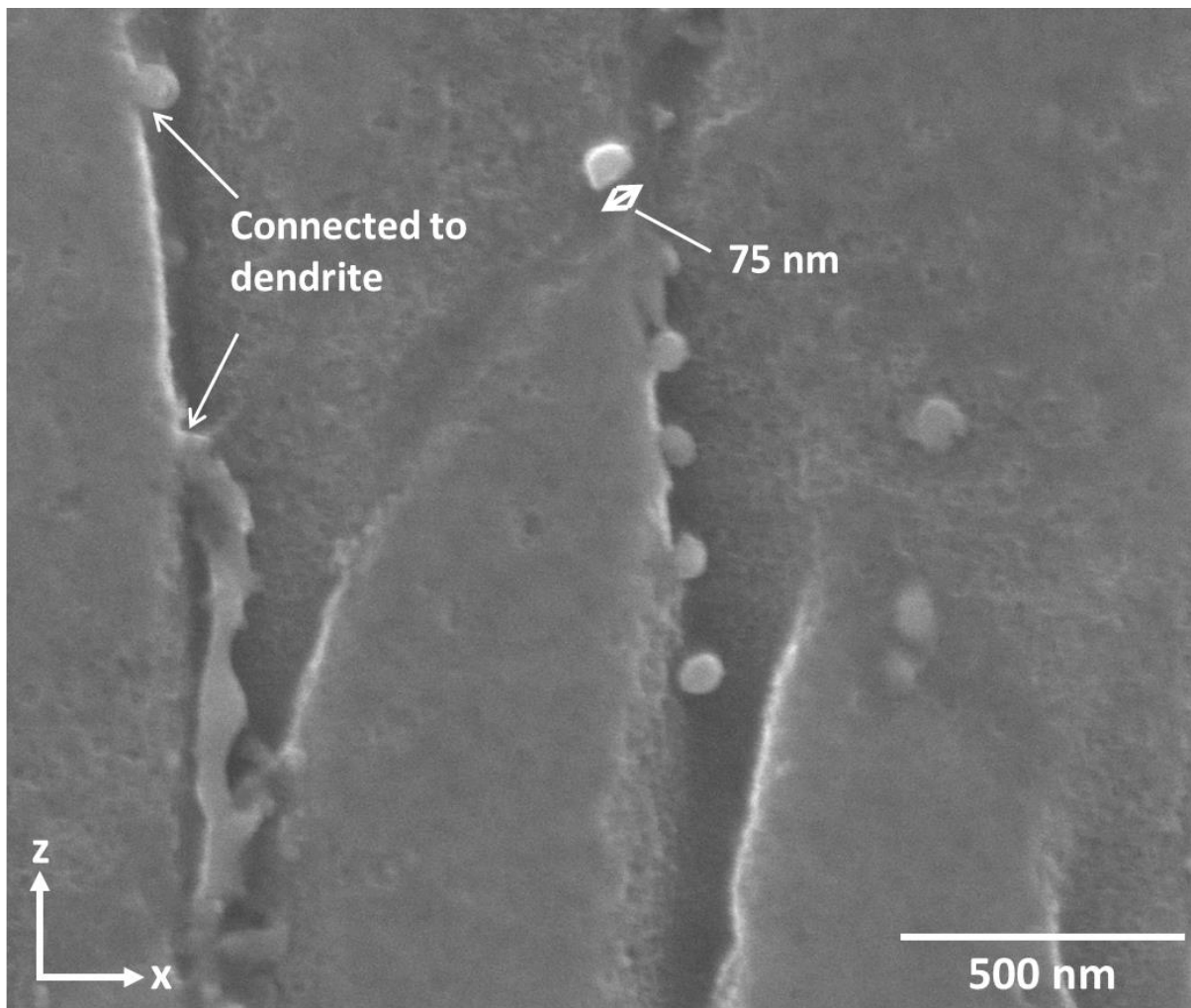


Figure 4.13 - Ultra high magnification SE mode SEM micrograph showing potential secondary phases. Globular particles are of the order of 50-100 nm in size.

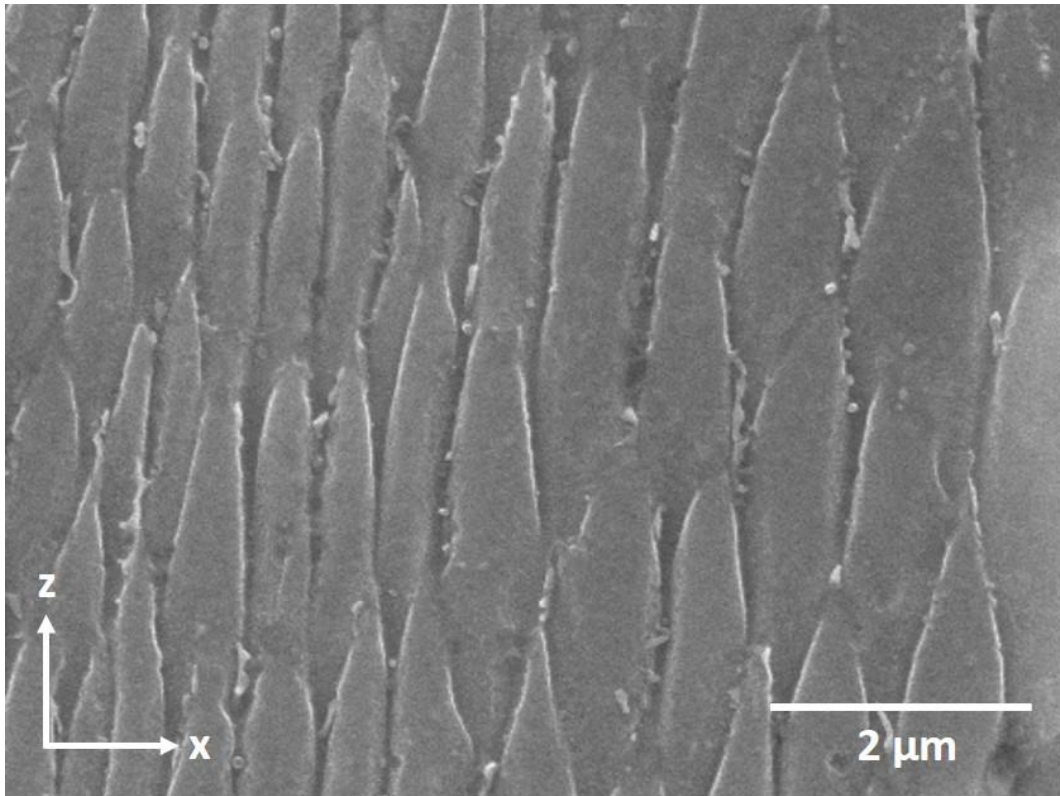


Figure 4.14 - High magnification SE mode SEM micrograph showing dendrite edge features

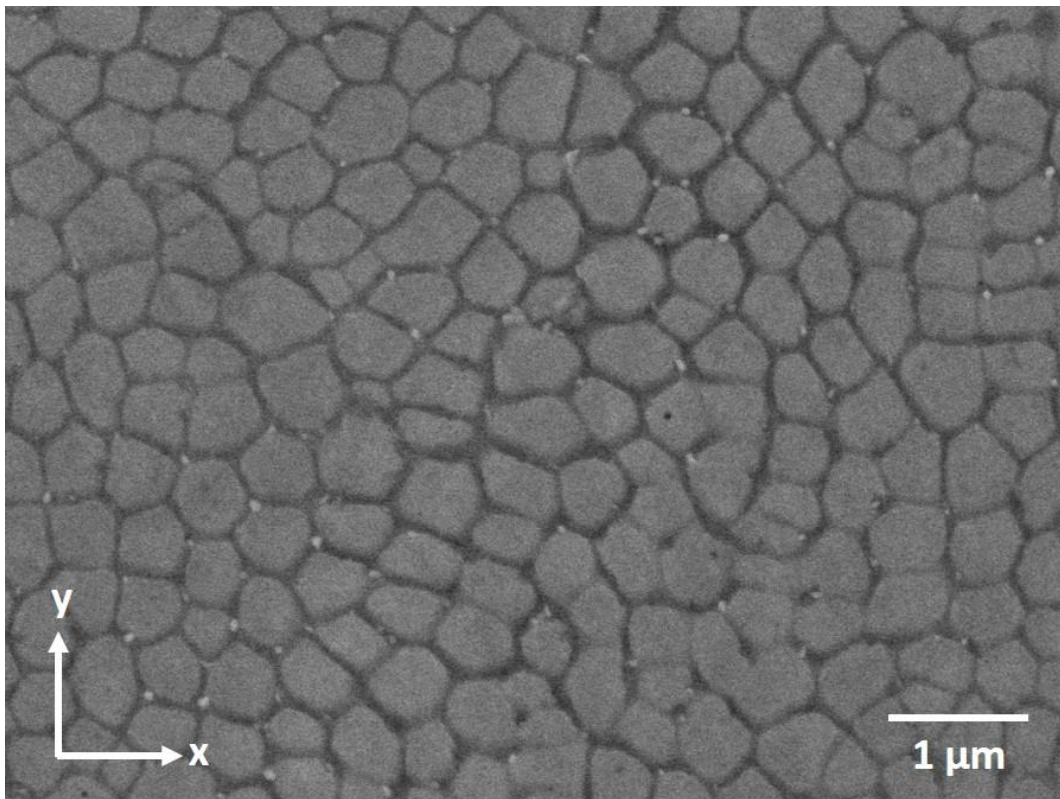


Figure 4.15 - Electron back scatter SEM micrograph showing cell-dendrite primary trunks with precipitates (brighter contrast) in inter-dendritic regions

Figure 4.16 is a higher magnification image of Figure 4.15, used for EDS point scanning. Given the findings of Vilaro, Colin et al. (2012), it was expected that the features may be submicron MC carbides. For Hastelloy X, the most likely composition would be MoC. The EDS spectrum for both precipitate and dendrite is displayed in Figure 4.17. It shows a very weak, near non present, peak for carbon for the precipitate, and a low peak in the dendrite. Other than carbon, all other elements were detected at very similar levels for both precipitate and dendrite. Mo is arguably lower in dendrite, however.

The same analysis was conducted on a vertical section, Figure 4.18 and Figure 4.19. This time the resolution is higher as the material had been more severely etched. From this observation plane, one observes that the precipitates are oblong globular, there is also no presence of the wave like features observed in standard imaging. The spectra for the vertical section are near identical between the precipitate and the dendrite, with no carbon detected in either.

The colour contrast between the precipitates and dendrites implies a difference in composition, however the precipitates are likely too small to be distinguished from the background material using EDS. A smaller electron beam spot size would be required to reduce the electron beam interaction volume, allowing for particle and background volume to be better distinguished. Unfortunately, the spot size could not be reduced further on the Inspect F. Transmission Electron Microscopy (TEM) would likely provide a solution, however the time commitments for TEM meant that this could not be performed in the remaining project time.

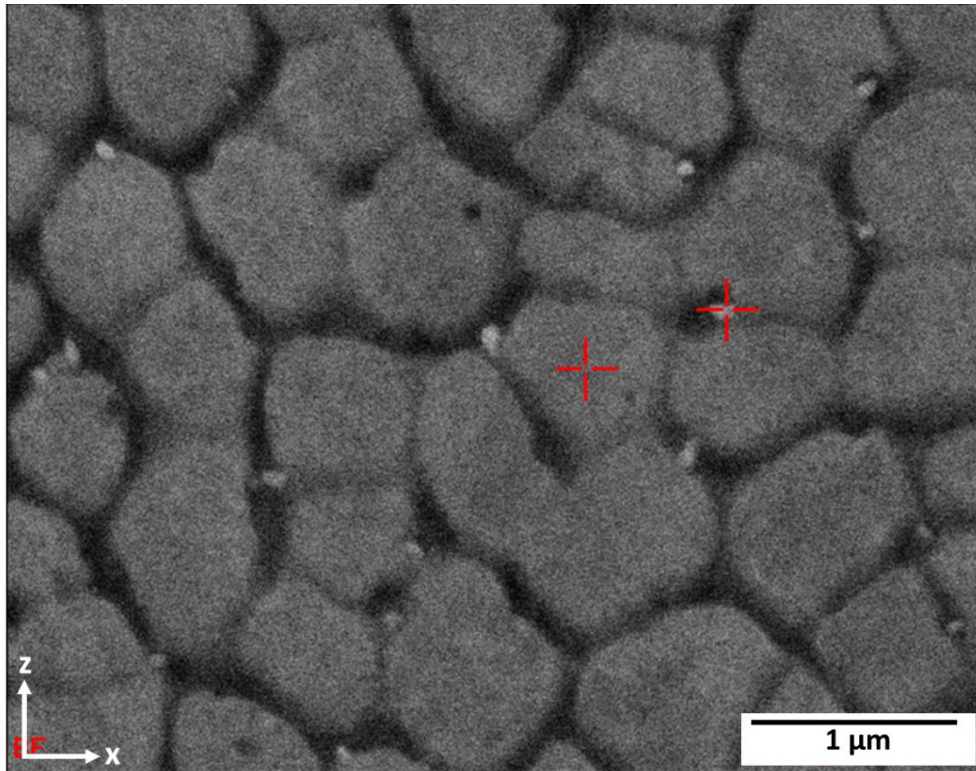


Figure 4.16 - Electron back scattered micrograph of cross sectioned microstructure - indicating positions of EDS point scans (red crosses)

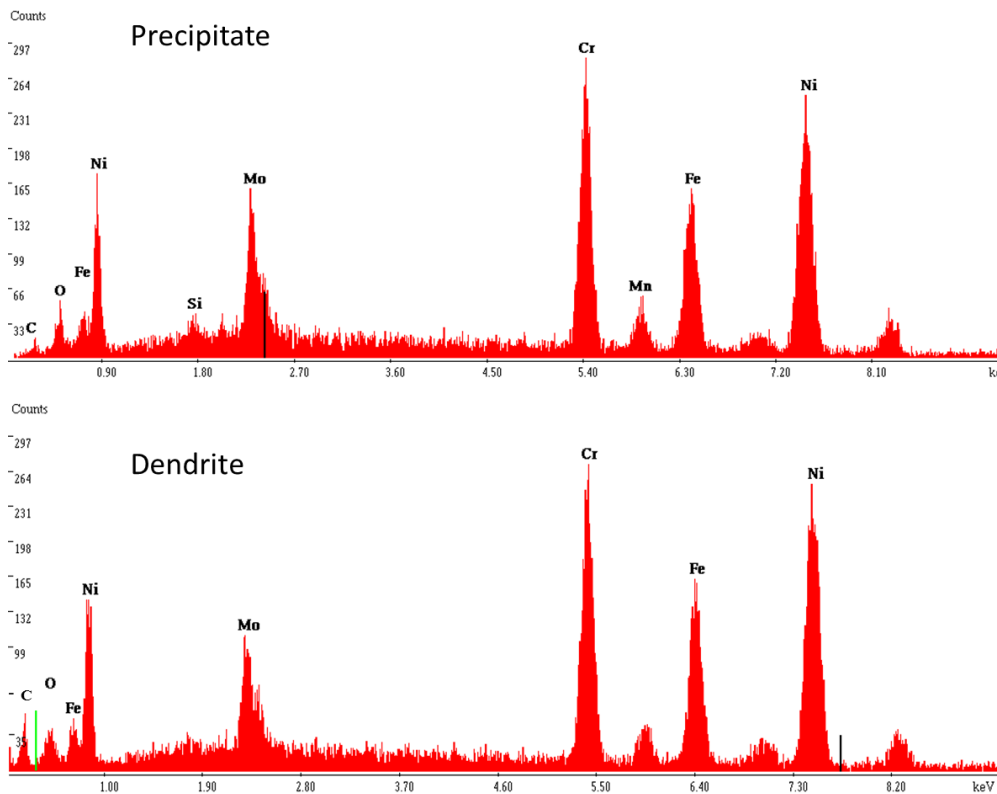


Figure 4.17 - EDS point spectra for precipitate and dendrite in cross section

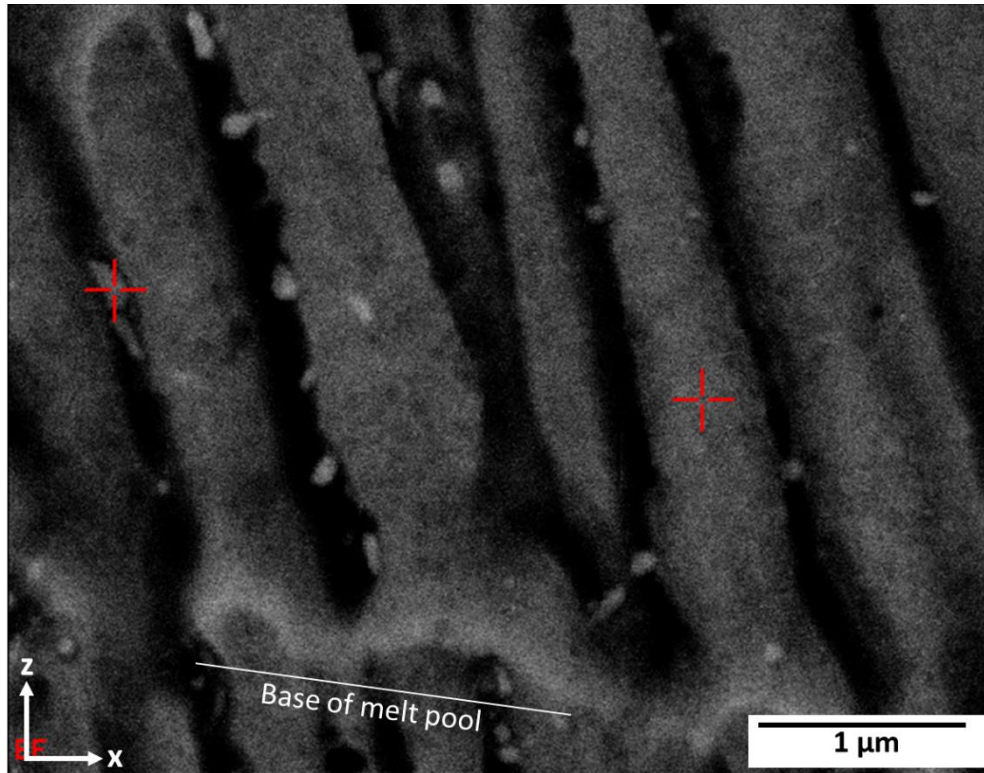


Figure 4.18 - Back scattered micrograph of vertical sectioned microstructure - indicating positions of EDS point scans (red crosses) and base of melt pool trace

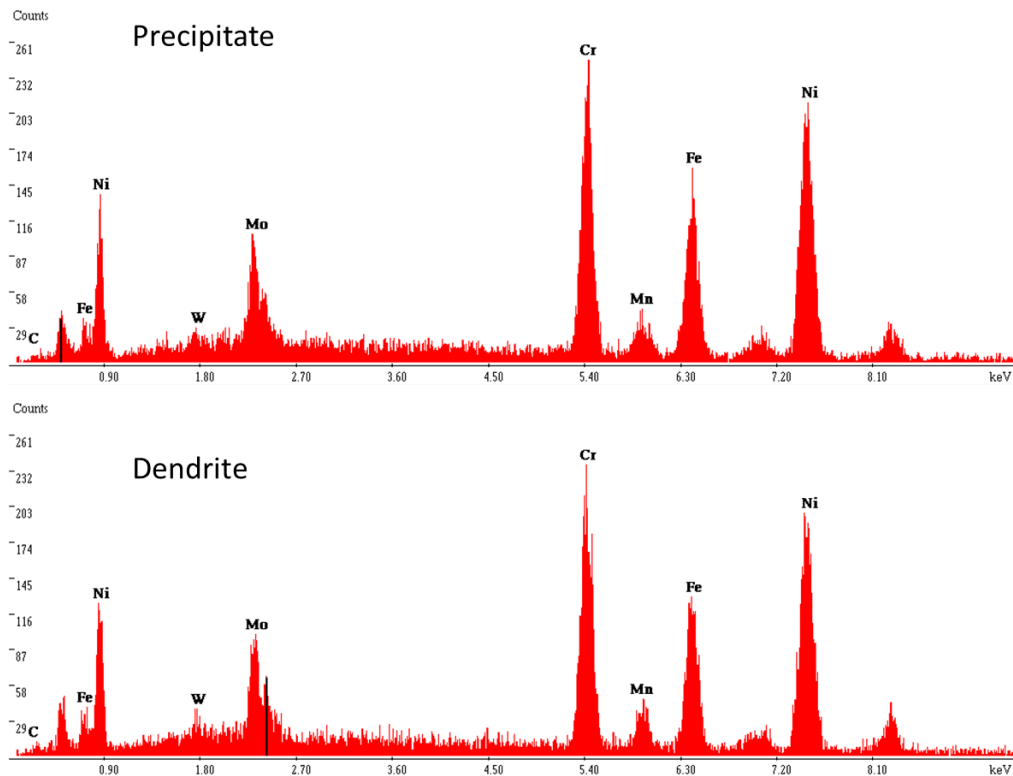


Figure 4.19 - EDS point spectra for precipitate and dendrite in vertical section

That the spectra are easily lost within that of the background implies the precipitates are of a similar composition, differing instead by crystal structure. Sigma phase therefore provides one likely candidate as it can have the following formula: FeCr, FeCrMo, CrFeMoNi and CrNiMo. Ni, Cr, Fe and Mo are the four most abundant elements in Hastelloy X. Sigma phase is tetragonal in crystal structure, appears as irregular globules which are often elongated, and forms after extended exposure at temperatures between 540 and 980°C (Donachie and Donachie 2002). With the exception of the extended exposure, the characteristics of sigma phase fit with the observed precipitates. However, the bright contrast of the precipitates also suggests (at least some) of the precipitates are of significantly higher average atomic mass than the dendrites, in which case MC (Mo) would also fit with observations.

An explanation for how the precipitates are allowed to form is that of recalescence driven by the reheating/remelting from successive laser passes and melt layers. The release of latent heat from an adjacent melt pool increases the material temperature to critical range for precipitation. The small size of the precipitates implies that the time frame in which they precipitate is very short, which ties in with SLM conditions.

It is difficult to assess whether the nano-precipitates affect the material response, or as processed mechanical properties of the material, as no comparable investigations are reported in literature. Sigma phase is known to be detrimental to the ductility of nickel superalloys, however this is when it is present as significantly larger precipitates at the grain boundary (Donachie and Donachie 2002). Although Vilaro, Colin et al. (2012) reported the presence of similarly nano-scale carbides in the interdendritic regions, they did not propose any potential influence on material response or properties. Comparisons of tensile properties between SLM as deposited nickel superalloys and wrought

equivalents (particularly for solution strengthened alloys) suggest that if there is an influence of nano-precipitates, it is beneficial rather than detrimental. It is thus concluded at this point that nano-precipitates are allowed to form within the interdendritic region, despite rapid solidification conditions, as a consequence of the reheating patterns inherent with SLM. The influence of these nano-precipitates, although not quantified, is deemed to be insignificant at this time.

Note, these precipitates are considered separate to the γ'' -bct Ni_3Nb phase precipitates reported in SLM processed Inconel 718 by (Amato, Gaytan et al. 2012), which were significantly larger and coherent within the cell-dendrite structure. As will be discussed in Chapter 8, the larger coherent precipitates may have an influence on material response, however this is likely to be confined to γ'' strengthened alloy systems only.

4.4 Chapter summary

Consideration and application of rapid solidification theory, and a comparison to observations from this investigation and published work, resulted in the establishment of SLM as a rapid solidification process.

Solidification conditions were modelled for single laser spots. Using the properties of Hastelloy X it was calculated that the solidification rate, V_s would be of the order of 0.5 m/s. This was in agreement with the continuous wave model, in which V_s was approximated to be between 0.1-1 m/s.

Aziz's solute redistribution theory was applied using the proposed solidification rates, from which it was implied that significant solute trapping would occur, resulting in a near solid solution.

Characterisation of the microstructures of SLM processed Hastelloy X revealed it to be consistent with that found in literature. Cooling rates determined from primary dendrite arm spacings agreed with those proposed from rapid solidification theory and the calculated solidification rate of <1 m/s.

Although localised micro-segregation was apparent from the presence of interdendritic regions and melt pool traces, the material was observed to be in single phase, and no grain boundary segregation was observed.

5 Cracking mechanism and crack susceptibility defined

The findings in Chapter 4 now allow conclusions to be drawn on the type of cracking present in SLM processed nickel superalloys and the method which may be used to reduce and eliminate them.

In this chapter, established theory is applied to the SLM case and a method for the reduction of crack susceptibility in nickel superalloys is proposed. The hypothesis is then tested experimentally and validated.

5.1 Mechanism for process induced micro-cracking in SLM

In Chapter 4 it was established that the microstructure of an SLM processed nickel superalloy will not vary greatly from that of large columnar grains comprised of fine dendrite-cells with interdendritic limited microsegregation and an absence of significant secondary phases or grain boundary segregation. This implied that any cracking mechanism in which segregation of solute atoms had to occur, was very unlikely to be active in SLM processing. Therefore, of the mechanisms discussed in Section 2.7, solidification cracking is considered unlikely and liquation cracking is to be disregarded. This decision is supported by observational evidence from micrographs of cracks and crack surfaces. In Figure 5.1 it is seen that the cracks have a distinct jagged morphology with evidence of rupture or fracture, as opposed to separation – which would be supportive of solidification or liquation cracking. Micro-cracks are observed to propagate along the grain boundaries only, see Figure 5.2. If solidification cracking was active, it would be expected to observe some smaller interdendritic cracks or cracks running along the base of the melt pool where the limited segregation is noted to occur. When these

observations are combined with those of the EDS line scans in Figure 4.12, it all but eliminates solidification cracking and a cracking mechanism.

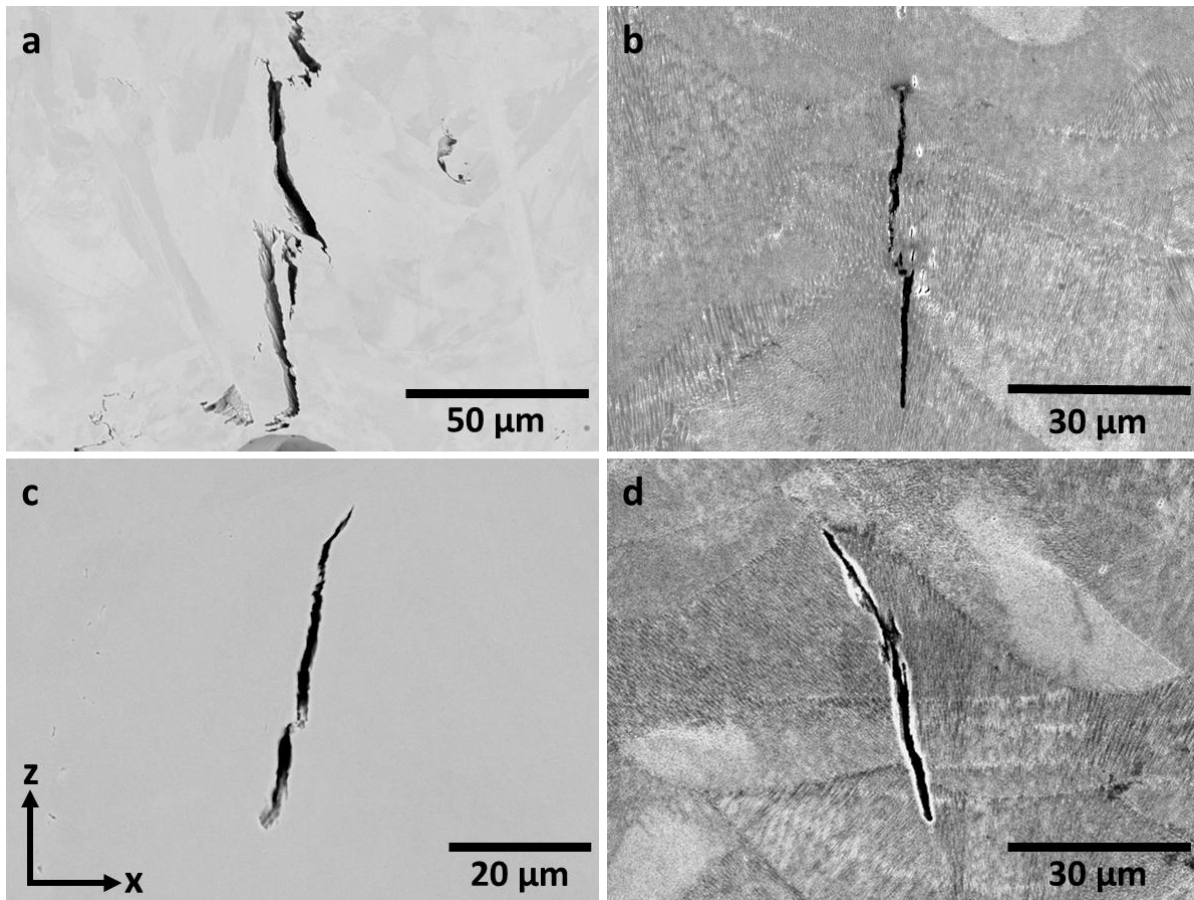


Figure 5.1 – Crack observed with SEM for a range of process parameters, axis in (c) applies to all images. a) is from the initial density trial, a large crack is observed with significant solid state fracturing clear in the centre. b) an etched sample from the LP vs Ap Vel trial, majority of micro-cracks follow this appearance, still appears to be fracture driven rather than separation – likewise with (c). d) less jagged in appearance, although feature central to length of the crack is fracture-like.

The two remaining possible cracking mechanisms are DDC and ETSS. At lower magnifications DDC and ETSS cracks appear very similar, one could even argue that DDC is a type of ETSS. The primary mechanism attributed to DDC in welding of nickel alloys is the formation of micron scale carbides along the grain boundary. High magnification SEM micrographs should allow for the observation of the carbides (of the order of 1µm in size) either along grain boundaries or crack surfaces, see Figure 5.3.

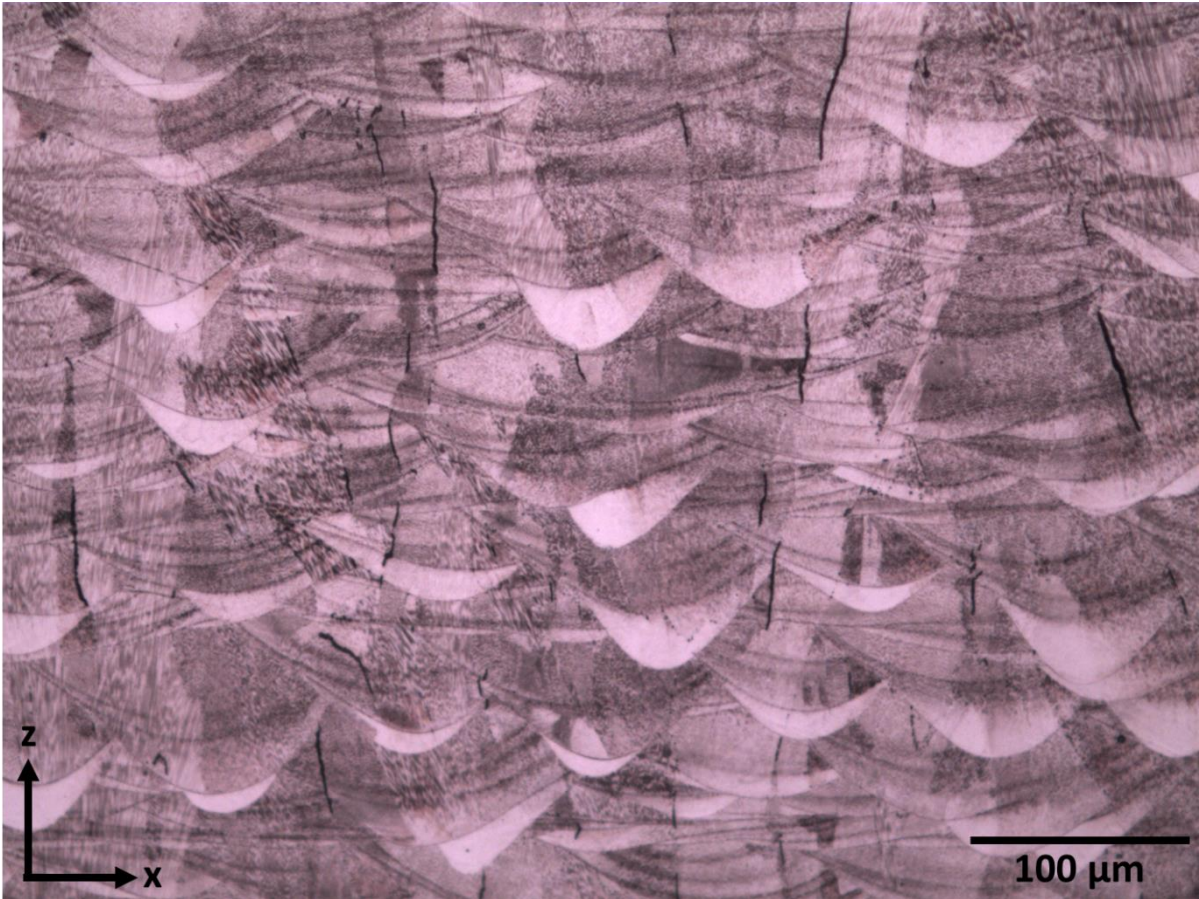


Figure 5.2 - Higher magnification micrograph of sample in Figure 4.#. Cracks lie exclusively along grain boundaries and are all of a similar morphology. None are observed to propagate along melt traces.

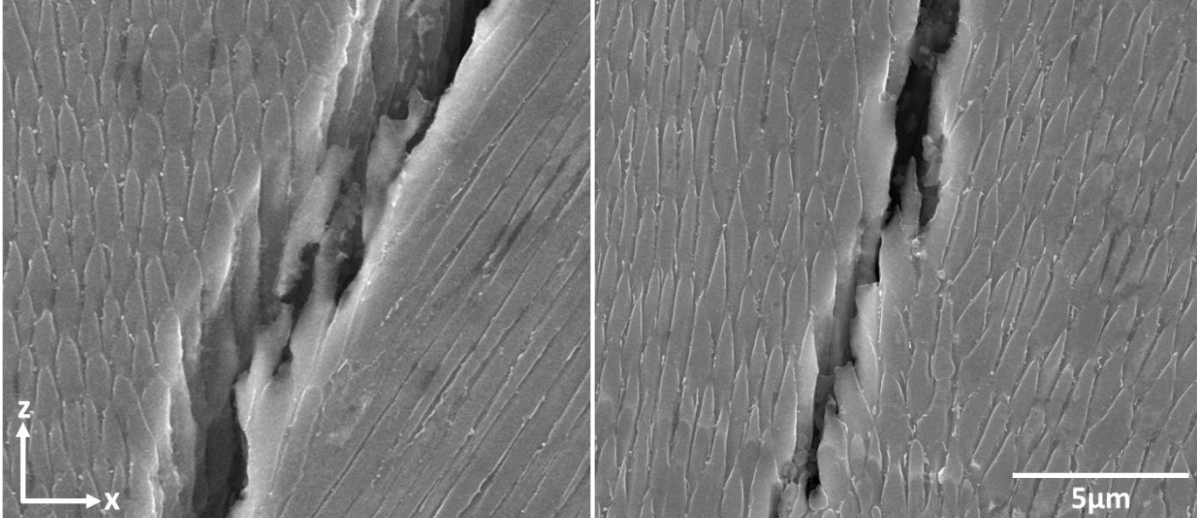


Figure 5.3 - High magnification SEM mode SEM micrographs of microcracks. Fabric of the dendrites is observed to have been disturbed and ruptured, rather than merely separating.

In Figure 5.3, no detectable carbides are observed, instead there is more evidence to suggest rupturing and fracture. If there were carbides, then analysis from Section 4.3 suggests that they would not be detectable.

Stress formation along grain boundaries due to variations in elastic modulus between adjacent grains, is the final mechanism under consideration. Although not specifically validated as a theory, reports detailed in Section 2.4.3 and 2.8.4 provide enough supporting evidence to suggest that it is plausible. One counter argument, however, is that elastic modulus is not very sensitive to composition variation, and hence the majority of nickel superalloys have very similar Young's moduli. Therefore, if the elastic tensor anisotropy was significant in micro-crack formation, it would be expected to effect the majority of nickel superalloys similarly. However, it is noted from literature that compositionally similar alloys, e.g. Hastelloy X and Inconel 718, display markedly different SLM processing crack susceptibilities. Therefore, it is concluded that although elastic tensor anisotropy may be an influencing factor, more likely it is a contributory, rather than the principal, mechanism.

Based on the evidence collected from literature and this investigation, it is therefore concluded that micro-cracking in nickel superalloys is predominantly caused by ETSS mechanism.

5.2 Crack susceptibility defined

ETSS cracking occurs when process induced tensile stress exceeds the local UTS of the material. In SLM, the high thermal gradients inherent with laser surface processing drive the formation of thermal stress through TGM. Logically then, a reduction in the thermal

gradients would reduce the local stress fields and hence reduce crack formation. This can potentially be achieved through optimisation of process parameters, however given that the temperatures required to achieve full melting of nickel superalloys will always exceed 1200 K and in conventional machines the deposited powder is at room temperature, thermal gradients will always remain high. For this reason high thermal stresses are considered an inevitable characteristic of SLM (Tomus, Jarvis et al. 2013), and additional solutions must be explored.

As discussed in Section 2.9, the processability of an alloy can be improved by altering its composition in order to affect the material response. 'SLM Processability' can be defined as:

The ability of a material to be processed with Selective Laser Melting and possess mechanical properties similar or greater than that of the conventionally (wrought/cast) processed equivalent

It was proposed by Deffley (2012) that the SLM processability of an alloy depended largely on two performance indicators, *Thermal Stability* and *Thermal Shock resistance*. *Thermal stability* refers to what extent a material will deform or deflect for a given heat input and geometry. The two material properties associated with this response are thermal conductivity (κ) and co-efficient of thermal expansion (α_{CTE}). The assumption is that 'good thermal stability' refers to minimal deflection, and as such one would wish to maximise κ and minimise α_{CTE} . This can also be described as maximising κ/α_{CTE} .

Thermal shock resistance, or TSR, refers to the material's ability to resist crack formation as a result of a change in temperature for a given heat input and geometry. As described

above, a rupture will occur once the stress exceeds the materials UTS. However, if the material can relieve the stress by elastic deformation then plastic deformation and rupture can be avoided. As such one requires the material to be strong but low in stiffness and, as with thermal stability, a low thermal expansion co-efficient is also desirable. Therefore for a good TSR one must maximise Equation 5.1, where σ_{UTS} is the UTS (preferred over fracture strength when applying TSR to ductile materials), ν is the Poisson ratio and E is Young's modulus. Yield strength is usually chosen over UTS as it is still desirable for the material to not plastically deform, however for fracture UTS is more applicable.

$$TSR = \frac{\sigma_{UTS} \cdot \kappa \cdot (1 - \nu)}{E \cdot \alpha_{CTE}}$$

Equation 5.1

Maximising Equation 5.1 is not as straight forward as initially described however, as there are consequences to altering certain properties. A low stiffness may be desirable for improved TSR; however, this may not be the case for the end use application. This is of particular relevance when considering the application of nickel superalloys, the majority of which are operated under high loading (Donachie and Donachie 2002). Poisson's ratio is difficult to control without also affecting Young's modulus, so is in this instance to be neglected. We therefore look to reduce thermal expansion. However, work on symmetry relationships between alloy properties (Toda-Caraballo, Galindo-Nava et al. 2013) finds that α_{CTE} is inversely related to E . This means that a reduction in α_{CTE} will result in an increase in E , and vice versa. Therefore, the 'good' TSR remit is not achievable through α_{CTE} and E manipulation. It also implies that an attempt to increase thermal

stability may have undesired effects on the elastic modulus and mechanical strength of the alloy.

Thermal stability could be increased by increasing κ . However, in metals thermal conductivity is directly related to electrical conductivity which is driven by the density of free valence electrons. At the surface, the free electrons interact with incident electromagnetic radiation and hinder the coupling of energy of the metal. An increase in thermal conductance means an increase in free electron density and therefore a reduction in the absorption of energy, or absorptivity (Deffley 2012). Given that the process relies on the absorption of energy from a laser source to melt the metal, a reduction in material absorptivity is to be avoided.

It is therefore proposed that rather than the two separate performance indicators, we consider the crack susceptibility of an alloy, χ , which is dependent on the ratio $TSR/\sigma_{th}(T, E, \alpha_{CTE})$, where σ_{th} is the thermal stress and is some function of temperature, T , Young's modulus, E and α_{CTE} . Given the above discussion, this is further reduced to Equation 5.2.

$$\chi = \frac{\sigma_{UTS}}{\sigma_{th}}$$

Equation 5.2

For a material to withstand ETSS cracking, the inequality $\sigma_{UTS} > \sigma_{th}$ must be satisfied. To reiterate, σ_{UTS} is chosen as it is the property which has the least chance of detrimental effect on material performance when increased.

The following sections focus on the control and increase of σ_{UTS} through manipulation of alloy composition. The control of thermal stress is considered in Chapter 7.

5.3 Chapter summary

From the observations and conclusions of Chapter 4, and supported by published literature, it was proposed that the primary cracking mechanism in nickel superalloys during SLM processing, was Elevated Temperature Solid State (ETSS) cracking.

ETSS cracking was defined as occurring when the thermal stress generated by the process exceeds UTS of a material at a given location and temperature. Taking ETSS as the primary mechanism for micro-crack formation, the crack susceptibility of an alloy was defined as the ratio between the tensile strength of the material and the thermal stress generated by the process

6 Tensile strength contribution

6.1 Development of tensile strength model

The yield stress of a metal can be described using the Hall Petch equation.

$$\sigma_{YS} = \sigma_0 + k_d d^{\frac{1}{2}}$$

Equation 6.1

where σ_0 represents the lattice stress, k_d is the locking parameter value and d is the average grain size. It is noted that although UTS is required for the TSR and Crack susceptibility equations, the Hall Petch equation for yield strength represents a more quantifiable relationship than one which accommodates UTS. This is not to say that UTS is now being disregarded, rather than the following assumption is made. The difference in stress $\Delta\sigma$ between material yield (σ_{YS}) and failure (σ_{UTS}) is dependent on the ductility of the material. If it is assumed that ductility does not vary greatly with minor compositional alterations, then $\Delta\sigma$ is fixed and therefore $\Delta\sigma_{YS} \cong \Delta\sigma_{UTS}$.

In Chapter 4 it was concluded that as deposited SLM material will be in a state of saturated solid solution, and only the primary γ matrix phase will be (significantly) present. In this state, i.e. in the absence of secondary strengthening phases, the lattice stress is dominated by the solid solution contribution. The lattice stress in Equation 6.1 can therefore be separated to that of the solid solution contribution, σ_{ss} , and the Peierls stress σ_P .

$$\sigma_{YS} = \sigma_P + \sigma_{ss} + k_d d^{\frac{1}{2}}$$

Equation 6.2

We now consider the comparison of two hypothetical alloys, denoted j and k respectively, with minor compositional variations. In order to assess $\Delta\sigma_{ss}$ processing parameters must be fixed; this then allows the following assumptions to be made. Peierls stress and k_d can be fixed as the alloy composition does not vary significantly enough and thermal conditions are identical; in addition, the contribution of σ_P is minimal. As discussed in Section 2.4 grain structure is controlled by V_s and $|\dot{T}|$ which will not vary under identical processing conditions, therefore d can also be fixed.

The difference in yield strength between alloy j and k , $\sigma_{kYS} - \sigma_{jYS}$, then reduces to $\Delta\sigma_{YS} = \Delta\sigma_{ss}$. It is noted that this relationship holds providing the composition modification does not introduce new phases.

Gypen and Deruyttere (Gypen and Deruyttere 1977) determined a model for multicomponent solid solution strengthening as a function of solute concentration, when the binary Solid Solution Strengthening (SSS) effect of individual solutes is known. The SSS contribution is given by:

$$\sigma_{ss} = \left(\sum_i k_i^{\frac{1}{n}} c_i \right)^n$$

Equation 6.3

where c_i is the concentration of solute (in atomic fraction) i , and k_i is the strengthening constant of solute i . n is taken as $\frac{1}{2}$ to be consistent with the dependence on concentration in Feltham's Trough model (Feltham 1968), as proposed by Roth *et al.* (Roth, Davis *et al.* 1997). The values of k_i are determined empirically by measuring the individual strengthening contribution of the element whilst in a binary alloy. Mishima

(1986) determined the strengthening constants for SSS elements in nickel binary alloys – specific values are presented in Table 6.1.

Alloying Element	Strengthening constant (MPa per At. Fraction)
Al	225
Si	275
Zn	386
Ga	310
Ge	332
In	985
Sn	1225
Sb	960
Ti	775
V	408
Zr	2359
Hf	1401
Nb	1183
Ta	1191
Cr	337
Mo	1015
W	997
Mn	448
Fe	153
Ru	1068
Co	39.4
Rh	520
Cu	86.7
C	1061
Pd	492

Table 6.1 - Strengthening constants for alloying elements of nickel

In the full model, a thermal component is considered but not quantified, rather assimilated into a numerical fit. In this investigation thermal contributions are accounted for in the Peierls stress.

Using Equation 6.2 and Equation 6.3, one could calculate an approximate value for the yield strength of an alloy as a function of elemental composition, providing the relevant values (σ_p , k_i , d , and k_d) were known. However, the simplicity of this model and the nature of the high aspect ratio SLM grain structure would mean absolute values are unlikely to be consistent with those measured experimentally. Instead it is better suited to

predicting the SSS contribution, or for the purposes of alloy composition alternation, the *difference* in lattice stress as a result of minor solute concentration shift.

$$\Delta\sigma_{ss} = \sigma_{ssk} - \sigma_{ssj} = \left(\sum_{ik} k_i^{\frac{1}{n}} c_{ik} \right)^n - \left(\sum_{ij} k_i^{\frac{1}{n}} c_{ij} \right)^n$$

Equation 6.4

with j and k again representing the two alloy compositions. This leads to a powerful relationship. Prediction of change in solid solution contribution is prediction of change in lattice stress, which is in turn prediction in change in yield strength and therefore UTS and ultimately, crack susceptibility. Numerically

$$\Delta\sigma_{ss} = \Delta\sigma_0 = \Delta\sigma_{YS} = \Delta\sigma_{UTS} \propto \Delta\chi$$

Equation 6.5

The relationship in Equation 6.5 allows for the prediction of an increase in UTS as consequence of alteration of the alloy composition. The next step is therefore to use Equation 6.4 to modify the composition of a known high crack susceptibility alloy with the intention of increasing its UTS and reducing its crack susceptibility.

6.2 Application to reduce crack susceptibility

Having identified Hastelloy X as a high crack susceptibility alloy, it was chosen to test the solid solution strengthening–crack susceptibility hypothesis, as described in Section 5.2. Using Equation 6.4, the composition of the Hastelloy X used in the optimisation trials (to

be referred to as Original unmodified Hastelloy X, OHX) would be modified to increase its solid solution contribution. Crucially, the composition would be kept within the Hastelloy X specification range, defined by Haynes International Inc. The modified alloy would then be processed under like for like conditions, and the crack densities would be compared to validate the hypothesis. Tensile properties and thermal expansion coefficients would also be compared to determine the validity of Equation 6.4.

6.2.1 Hastelloy X composition alteration

An independent chemical analysis of OHX powder was undertaken in order to establish the wt% of all detectable elements down to an accuracy of ppm, full details of which are given in Table 6.2.

The relative contribution to the solid solution strength of a solute element, or *potency*, is given by its strengthening parameter k_i , with absolute contribution being the product of k_i with the solutes concentration or atomic fraction (At. Frac). The atomic fraction is the fraction of total atomic weight of the solute with respect to the total atomic weight of the lattice, and is therefore not the same as wt%. If one knows the full composition of an alloy, atomic fraction can be calculated from the wt% values by the following formula.

$$c_i = \frac{\frac{wt\%}{z}}{M}$$

Equation 6.6

where z is the atomic weight of the given element and M is the sum of $(wt\%/z)$ for all of the elements in the alloy

The k_i values from Table 6.2 were used to identify the most potent SSS elements present in the composition of OHX. The three most potent SSS elements were identified as molybdenum, tungsten and carbon. It was decided that because of its association with DDC cracking and affecting alloy ductility in nickel alloys, the concentration of carbon would not be actively increased; it would not be decreased either, because it is still vital for the formation of carbides and required for lattice strengthening.

A modified composition of OHX was therefore proposed, with increases of Mo and W to close to maximum specification values (10 and 1 wt% respectively). Other alterations include a reduction of tramp elements O, N, Cu, Pd and P, which are deemed detrimental to mechanical properties of the alloy in levels down to a few ppm (Donachie and Donachie 2002), and a reduction in Mn which was highlighted by Tomus, Jarvis et al. (2013) as being potentially detrimental crack susceptibility in Hastelloy X. No new additions of potentially advantageous elements were implemented as the aim was to keep the material within specification. The Modified Hastelloy X (MHX) powder was then fabricated by a third party powder mill and supplied by LPW Technology. With the exception of Mo and W, exact wt% values for constituent elements were not requested. It was only requested that tramp elements be reduced as much as feasible and Mn was reduced within specification. All other alterations were only consequential of the intentional additions/reductions.

As with OHX, MHX was subjected to an independent chemical analysis, this was primarily to obtain high accuracy data comparable to that of OHX, but also check that the desired changes to composition had been made. Table 6.2 details the full compositions of the OHX and MHX powder as well as the associated change in atomic fraction and strengthening parameters for each alloying element.

Element	OHX wt%	MHX wt%	Δc_i (At. Frac)	k (MPa At. Fraction^{-1/2})
Ni	47.87±0.28	46.55±0.27	-0.01	-
Cr	21.3±0.19	21.80±0.19	0.007	337
Fe	19.5±0.17	18.59±0.17	0.0004	153
Mo	9.0±0.12	9.40±0.12	0.003	1015
Co	1.04±0.04	1.77±0.05	0.007	39.4
Mn	0.48±0.03	0.22±0.02	-0.003	448
Si	0.32±0.02	0.31±0.02	-0.0002	275
W	0.56±0.03	1.05±0.01	0.0016	997
C	0.057±0.01	0.054±0.01	-0.0001	1061
Pb	$(5 \pm 0.5) \times 10^{-6}$	$(3 \pm 0.3) \times 10^{-5}$	7×10^{-8}	-
O	0.049±0.005	0.025±0.003	-8×10^{-4}	-
Cu	0.45±0.05	0.01±0.001	-0.004	-
N	0.048±0.005	0.009±0.001	-0.002	-
P	0.014±0.001	0.006±0.0006	-1.5×10^{-4}	-
σ_{ss}	309.3 ± 0.29	317.3 ± 0.3	MPa	

Table 6.2– Composition of OHX and MHX with concentrations, elemental strengthening coefficients (k) and resulting σ_{ss} values. Values for k taken from Mishima et al.[32].

Equation 6.3 was used to calculate the solid solution strengthening contribution for OHX and MHX as well as the predicted $\Delta\sigma_{ss}$, all of which are given at the bottom of Table 6.2. The predicted difference in solid solutions strengthening contribution $\Delta\sigma_{ss} = 8.02 \pm 1.2$ MPa. All detectable elements were included in the calculation, providing a strengthening constant existed for them.

6.2.2 Modified Hastelloy X: material response and property comparison

The next step was to process OHX and MHX under identical conditions, then compare crack densities and microstructures. It is noted there was a limited volume of the MHX alloy powder available as it was a special heat. Sample size was therefore reduced to 5x5x5 mm for the alloy comparison trials in order to maximise sample population, as opposed to the 10x10x10 mm cubes used the optimisation trials (Section 3.3.2).

Samples of both OHX and MHX were built for a range of parameter sets, including the optimised set from Section 3.3.2, at the new smaller sample size. Density and crack density analysis was conducted on all samples, as described in Section 3.2. The density of all samples was >99.5%. Figure 6.1 displays the crack densities for MHX and OHX for a range of parameter sets, including the optimised set from Section 3.3.2.

It is observed that the altered sample geometry yielded significantly greater crack densities across the sample range. This is apparent as all of the parameter sets were repeats from the optimisation trials, and therefore direct comparisons between the OHX 10 mm cubes and 5 mm cubes can be made. The increase in cracking is attributed to the significant reduction in volume of the samples which results in a reduction in residual heat (Roberts, Wang et al. 2009), leading to a lower quench temperature and increased thermal gradient (Mercelis and Kruth 2006). As the effect of sample size on crack density was not foreseen, an additional trial was conducted with the aim of quantifying the relationship, see Section 6.3.

For this sample set, MHX yielded significantly lower crack densities in all like for like samples than the standard OHX; with an average reduction of 65% observed in the vertical section and 57% in the horizontal section. The lowest crack density measured for the MHX was 1.6 ± 0.9 cracks per mm^2 , which was an 86% reduction against the equivalent OHX sample (11.6 ± 2.4 cracks per mm^2). Figure 6.1 also demonstrates the uniform reduction in crack density across all energy densities; it shows there was a true reduction in the crack susceptibility of the alloy.

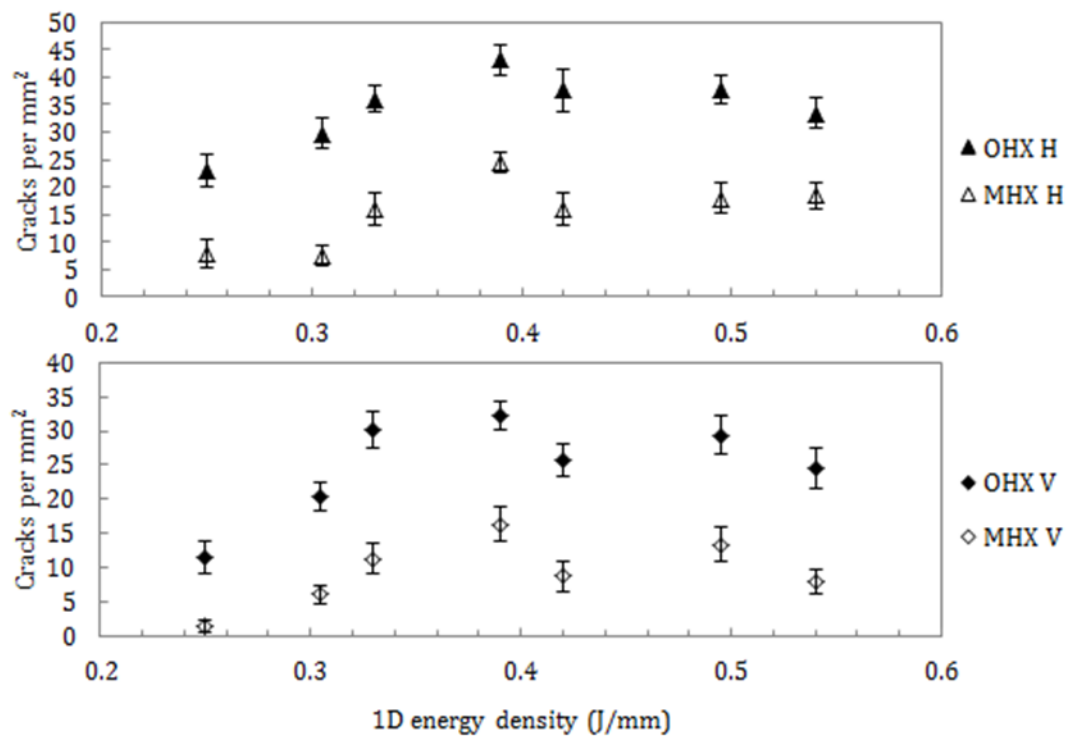


Figure 6.1 - Crack densities of OHX (filled) and MHX (unfilled) measured in vertical (V) build orientation, bottom plot, and horizontal (H) build orientation, top plot.

The reduction in cracking is visually appreciated by comparing micrographs of OHX and MHX samples built with the same parameters. Figure 6.2 shows 4 micrographs, 2 of OHX vs 2 of MHX built with the same two sets of parameters.

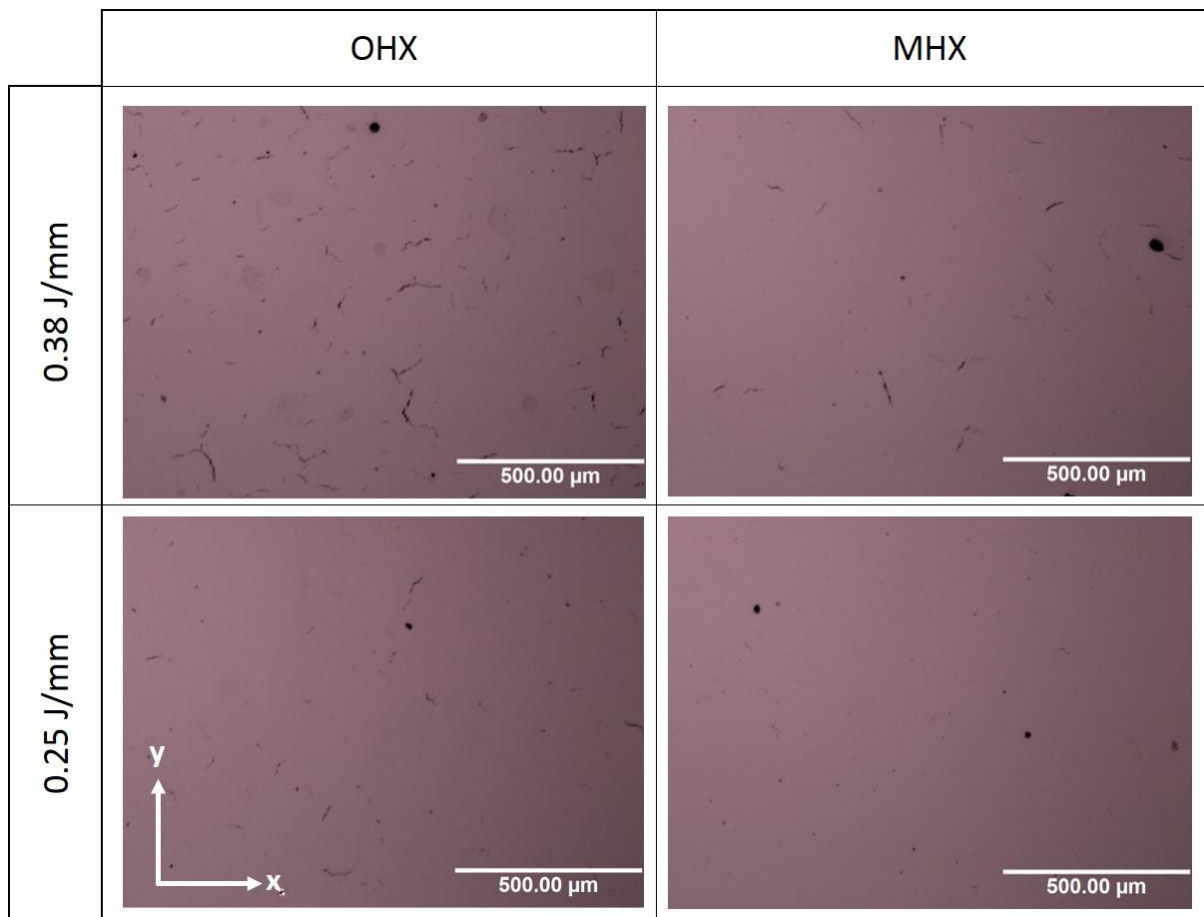


Figure 6.2 - OHX vs MHX. Horizontal sections of OHX and MHX for two sets of processing parameters, demonstrating the reduce micro-cracking in MHX.

In order to confirm the mechanism responsible for the reduction in crack susceptibility and also validate Equation 5.6, OHX and MHX were compared for tensile properties (elongation, yield strength, UTS), Young's modulus, Vickers Hardness and thermal expansion. Tensile testing was carried out at room and elevated temperature (1033 K), see Figure 6.3.

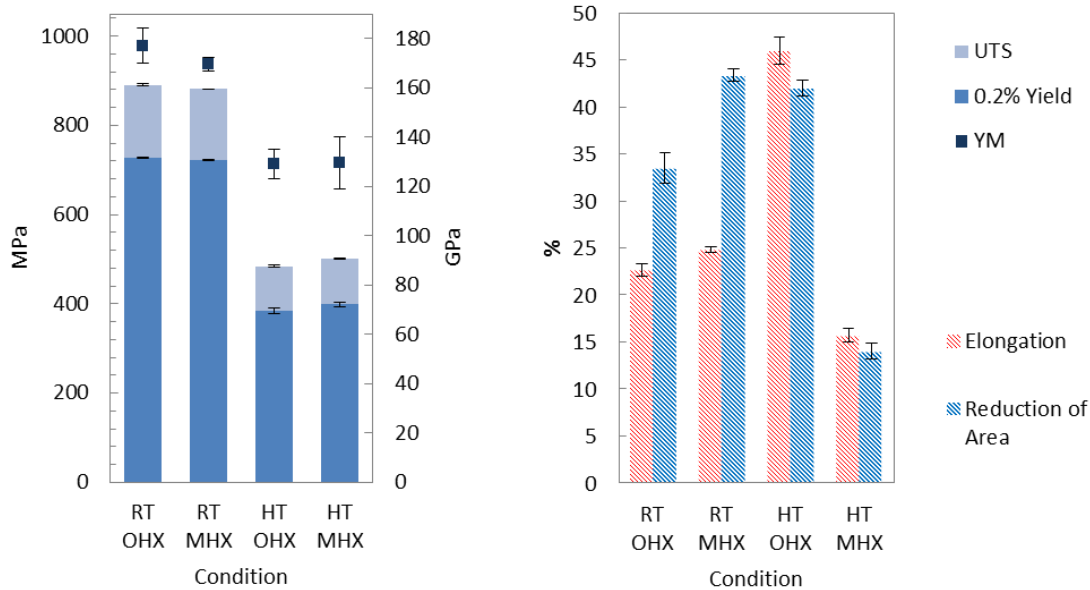


Figure 6.3- Tensile properties comparison for OHX and MHX: RT = Room Temperature, HT = High temperature (1033 K).

There was no discernible increase in the room temperature tensile strength of MHX, however an increase in the elevated temperature UTS was observed. UTS plus standard deviation of OHX was 484.0 ± 4.0 MPa with MHX at 500.3 ± 2.6 MPa. This is attributed to the temperature sensitivity of substitutional SSS of large solute atoms. At elevated temperatures dislocations carry a higher energy state, and the stress required to inhibit their propagation increases. At this point larger substitutional solute atoms, such as Mo and W, become more favourable as they create larger stress fields within the lattice. Their large size also inhibits their diffusion within the solid, making them a more stable barrier at elevated temperatures. This not only explains the elevated tensile results, but also reinforces the argument for increasing the atomic percent of heavy SSS elements in favour of lighter elements such as Fe or Si to maximise TSR.

The elastic modulus of both OHX and MHX are observed to be lower than that of wrought Hastelloy X (as stated on the Haynes International Datasheet), which is 205 GPa. However they are in very close agreement with the values measured by (Etter, Kunze et al. 2015)

for the same material, build orientation, layer rotation (67°) and testing conditions. As described by Etter (and previously in Section 2.8.4), the reduction is attributed to the anisotropy of the elastic tensor in the Hastelloy X single crystal. The SLM process (with 67° rotation) produces a $\langle 001 \rangle$ fibre texture with respect to build direction, thus maintaining anisotropy (although not as strongly as the single crystal) for the bulk material. The typically coarser, and equiaxed grain structures of cast/wrought/annealed material do not possess such anisotropy and thus display more middling (in this case higher) elastic moduli with respect to the maximum of the single crystal.

The reduction in measured elastic moduli is also observed in a number of other published works in which the tensile properties of SLM fabricated nickel superalloys have been investigated. Wang (2011) - Hastelloy X, Wang, Guan et al. (2012) – Inconel 718, Vilaro, Colin et al. (2012) – Nimonic 263, Kanagarajah, Brenne et al. (2013) – Inconel 939, all report elastic moduli in the region of 170-180 GPa, for alloys which have values of 200+GPa in the conventionally manufactured condition.

Average Vickers hardness for OHX and MHX were 277.1 ± 3.9 and 280.9 ± 4.0 Hv0.5 respectively. However, there was great variation across the samples, due to the residual stress present, and any increase in true hardness is lost within the deviation.

Ductility of MHX was marginally higher at room temperature, and was expected due to the reduction of tramp elements, however at elevated temperature a large reduction in ductility is observed. It is proposed that the minor alterations to the composition has resulted in a shift of the critical temperature range for the elevated temperature ductility minimum of the alloy – as discussed in Section 2.7.3 – which is typically around 1033 K (1400F) for nickel-base superalloys (Arkoosh and Fiore 1972).

It is proposed that for OHX the composition is such that the ductility minimum lies below the 1033 K test temperature, and therefore at the test temperature the SSS elements in the matrix are heavily depleted due to extensive carbide formation hence normal ductility resumes. For MHX, the composition is such that the ductility minimum lies close to the test temperature, and hence it displays low ductility.

Inspection of the fracture surface reveals presence of carbides for both alloys, see Figure 6.4 and Figure 6.5. OHX displays a higher concentration of carbides than MHX, indicating more significant carbide precipitation which is consistent with its higher ductility. It is emphasised at this point that this mechanism is not considered as a factor in micro-crack formation, as any local plastic deformation as result of thermally induced stress would not be over a sufficient range. The ductility minimum does pose a concern for operational life of the alloys however, and it is important that the sensitivity of this effect has been highlighted for alloy development.

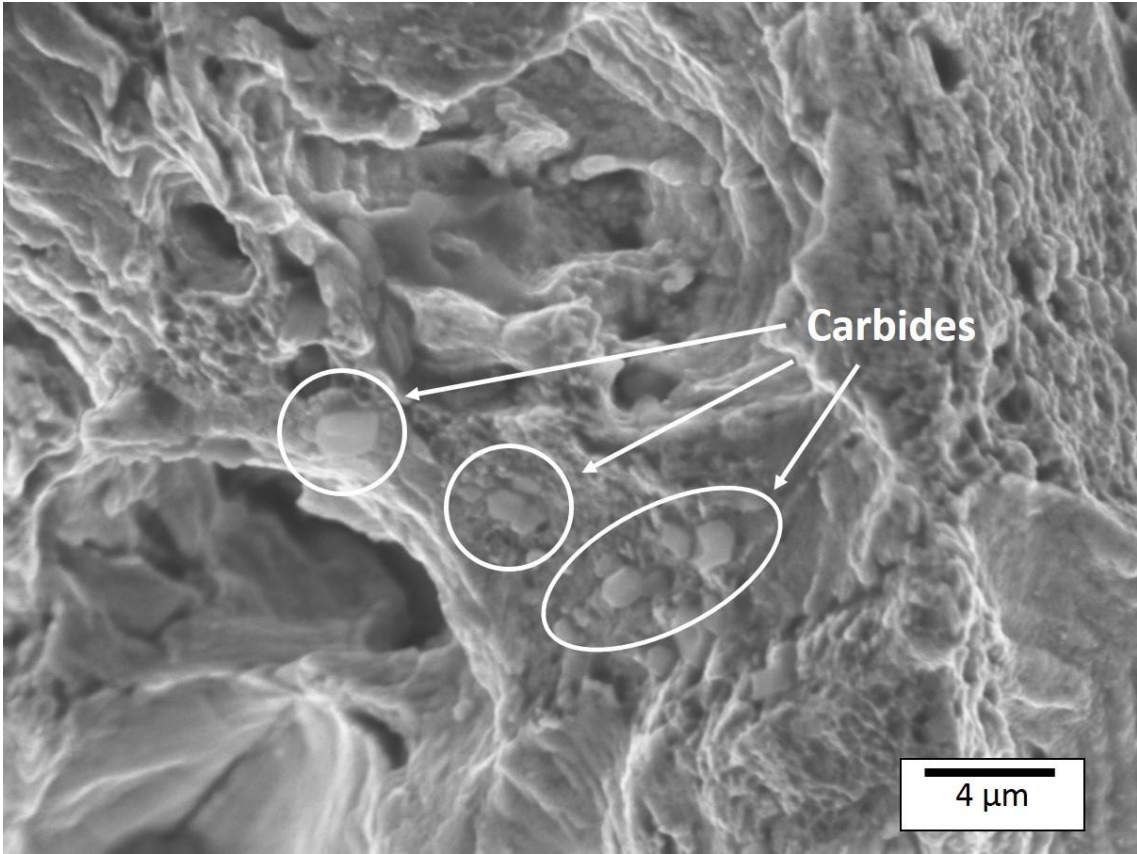


Figure 6.4 - Fracture surface of high temperature tensile bar for OHX, carbides are highlighted by white circles and arrows. Taken in SE mode.

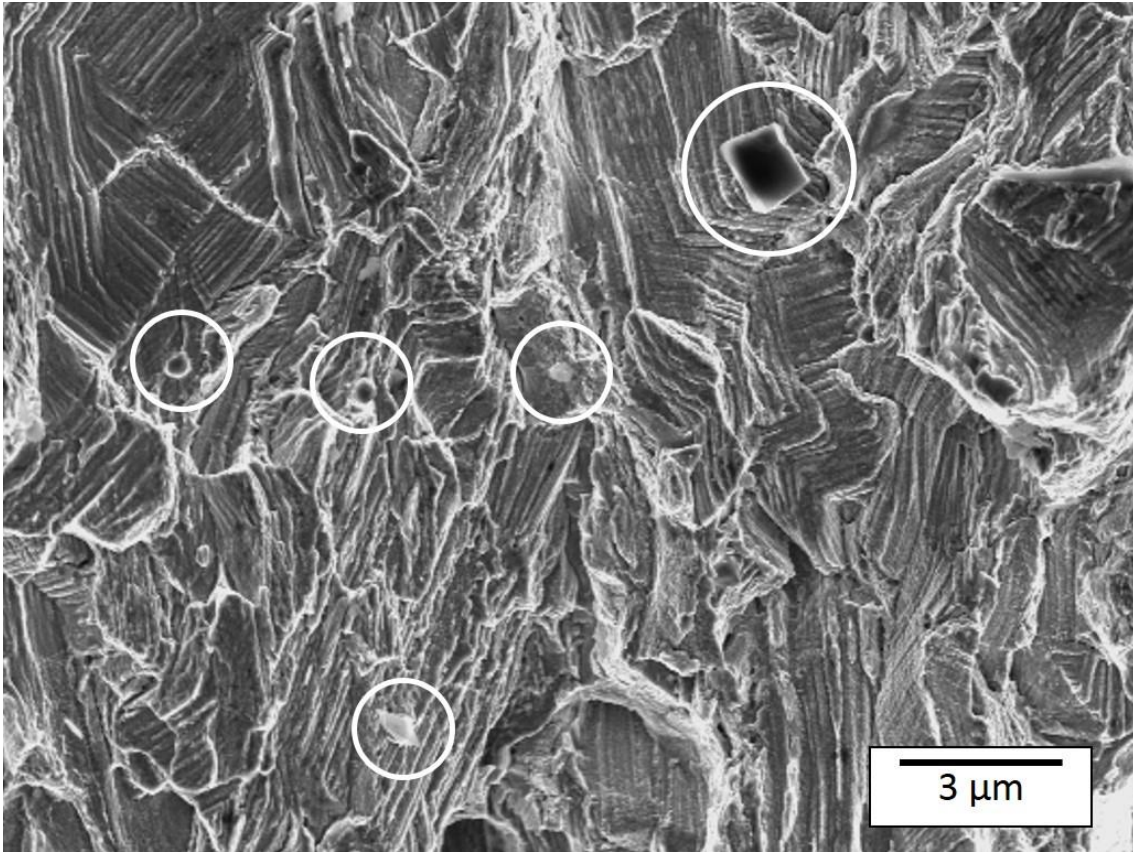


Figure 6.5 - Fracture surface of high temperature tensile bar for MHX white circles highlight precipitated carbides. Both alloys display small carbides which have formed as a consequence of the elevated temperature plastic deformation. Taken in SE mode.

The effect of composition alteration on the thermal expansion of OHX and MHX alloys is displayed in Figure 6.6 and Table 6.3. There is no significant variation between the measured linear expansion and calculated α_{CTE} for the OHX and MHX alloys. This is expected as although molybdenum and tungsten have been reported to reduce α_{CTE} of Ni-base superalloys, particularly in solid solution, a significant reduction ($1 \times 10^{-6} \text{m/K}$) would require increases of the order of 5 wt% (Hull, Hwang et al. 1987). The reduction of α_{CTE} , and hence increased thermal stability, is therefore disregarded as a secondary mechanism responsible for the reduction of cracking in the MHX alloy.

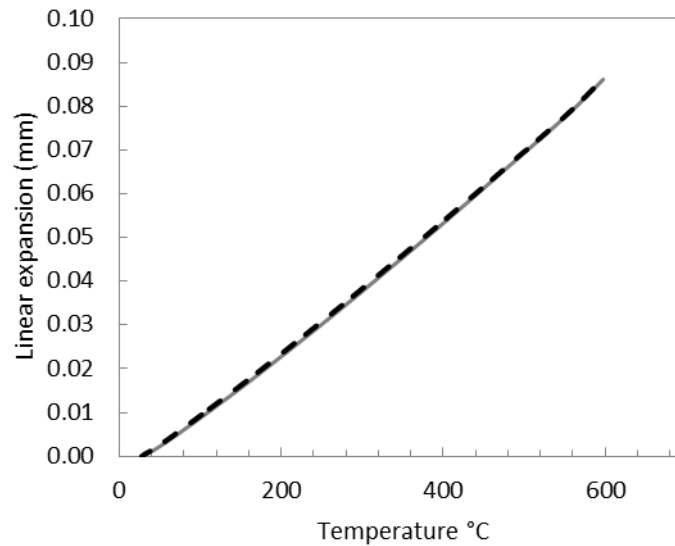


Figure 6.6 - Thermal expansion data for OHX (solid grey line) and MHX (dashed line) plotted as a function of temperature.

Alloy	α_{CTE} ($10^{-6}/K$)		
	303-673 K	303-773 K	303-873 K
OHX	14.34	14.73	15.15
MHX	14.47	14.76	15.17

Table 6.3 - Mean coefficient of thermal expansion for OHX and MHX alloys over full and partial temperature ranges.

For the case of MHX therefore, an increase in solid solution strength has resulted in a significant reduction of crack density (and thus crack susceptibility) over OHX. This result therefore supports the theory of crack susceptibility, based on the assumption that thermal stress contributions, were not significantly different.

6.3 Cracking with geometry, power and energy density

After it was revealed that the smaller 5 mm cubes used in the OHX-MHX comparison trials (Section 6.2) cracked more severely than 10 mm cubes for the same processing parameters, it was deemed necessary to investigate the effect of part geometry/volume on micro-cracking.

6.3.1 Initial findings

Comparing Figure 3.25 to Figure 6.1, we can immediately see that crack density for the same 1D energy densities is significantly lower for the 10 mm OHX samples than for the 5mm OHX samples. Figure 6.7 shows the same data of Figure 6.2 but this time the data has been separated into series of laser power. It is now apparent that the trends observed in the 10 mm samples for laser power and energy density are not repeated in the 5 mm samples.

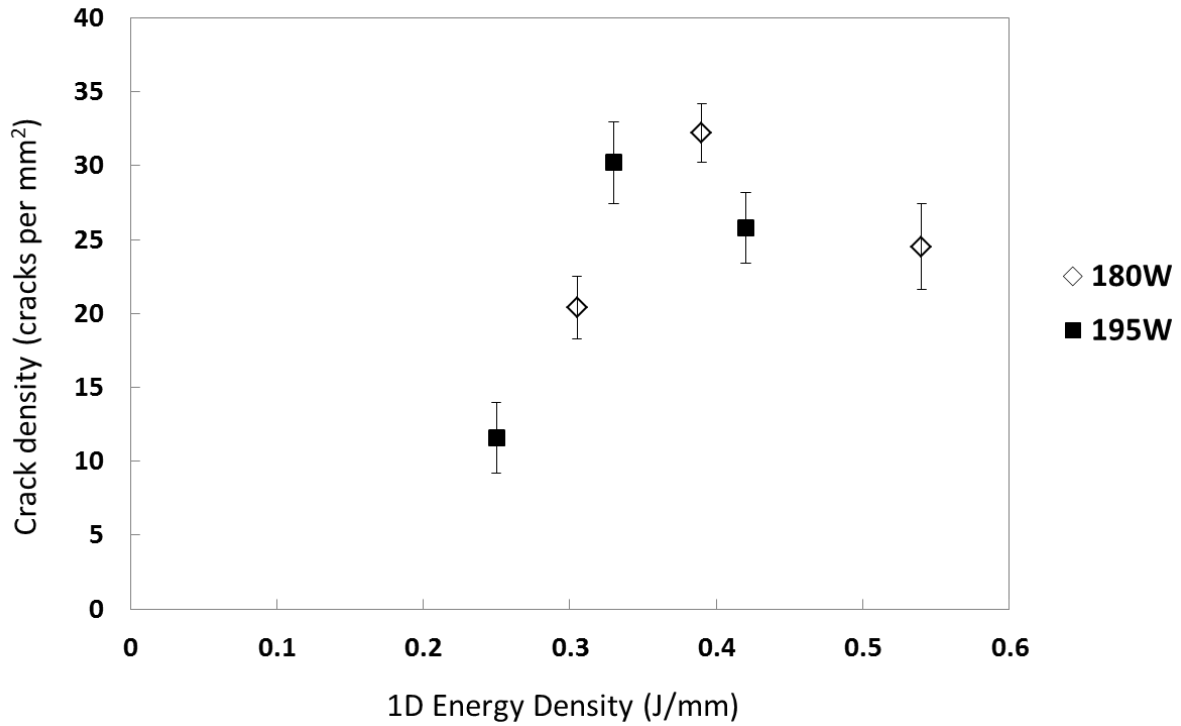


Figure 6.7 - Crack densities of OHX with 1D energy density, separated into series of laser power.

In Figure 6.7 and Figure 6.8 it is seen that in fact 180 W yields higher crack densities on average than 195 W, although the relationship is less well defined for OHX. There is an argument that the relationship is still dependent on energy density, although the drop between the two points closest to 0.4 J/mm would serve to counter this. Clarity is therefore required.

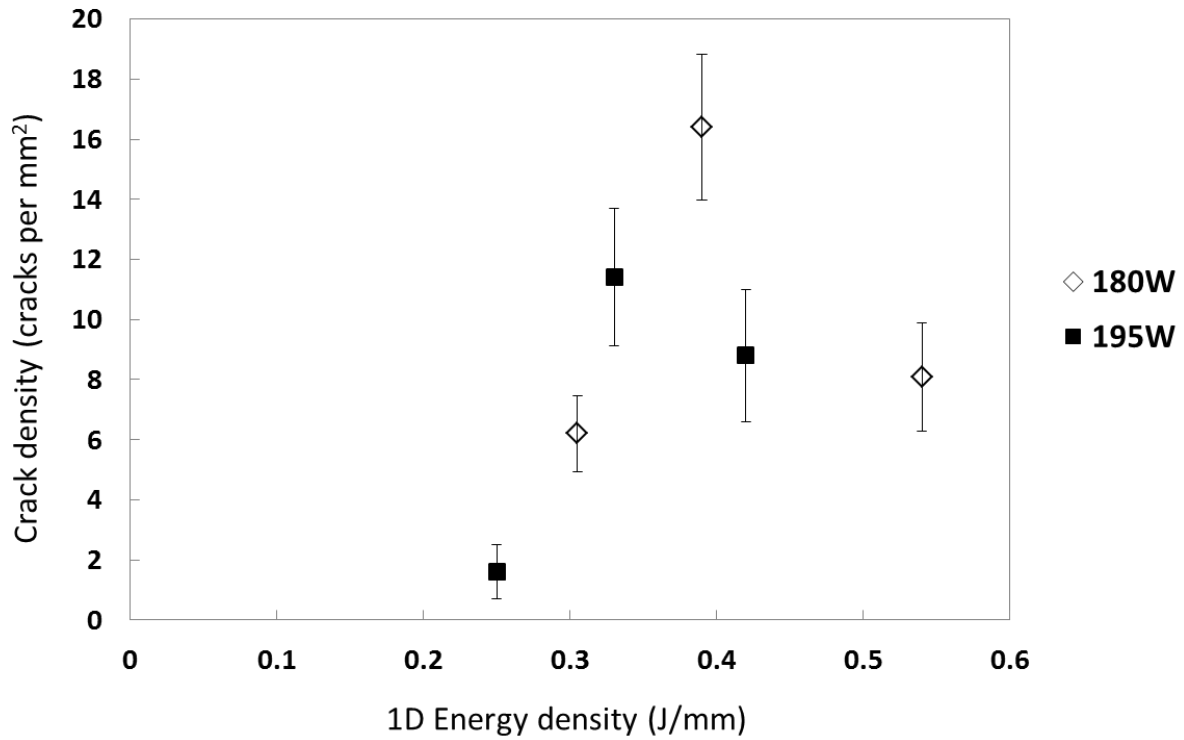


Figure 6.8 - Crack densities of MHX with 1D energy density, separated into series of laser power.

6.3.2 DOE

In order to best determine any relationships, an experiment varying sample size (specifically volume), power and energy density was conducted. Due to the potential inter variable relationships, a high sample volume DOE was deemed most suitable. The DOE consisted of three levels, one for each variable, with four points per variable, totalling 64 samples. The full DOE is detailed in Table 6.4.

Variable				
Sample size (mm)	2.5×2.5×2.5	5×5×5	7.5×7.5×7.5	10×10×10
1D Energy Density (J/mm)	0.2	0.3	0.4	0.5
Laser Power (W)	170	180	190	200

Table 6.4 - DOE values for crack density with volume, power and energy density trial

Note there were not any repeated values, given that this is not a solution based DOE. As one of the proposed mechanisms driving the variation in cracking with volume was residual heat, care was taken in arrange samples on the build plates so that this effect would be minimised. 10 mm and 7.5 mm cubes were built on separate substrates, with 5 mm and 2.5 mm cubes being sufficiently small to allow them to be built on the same substrate. A minimum spacing of 10 mm between each sample was used.

Once built, samples were mounted in groups of laser power. This meant that all four sizes of a power and energy density pair were mounted together. This was purely to aid analysis, given that the primary focus of this investigation is variation with sample volume.

6.3.3 General results

Crack density and porosity were measured for all samples, using the methods detailed previously. Although this investigation was not specifically looking at porosity, it was still necessary to note the porosities of the samples so as to build up a more complete process map.

In order to better identify trends, pivot charts were used to isolate specific fields and plot them against the desired result (either porosity or density). Filters can also be applied so that one can study a specific range or value. The global relationships for the three parameter variables with crack density are plotted in Figure 6.9 and Figure 6.11. It is first noted that there is no value for energy densities of 0.2 J/mm in crack density. This is because the samples had relatively high porosity and had suffered from insufficient fusion. Although some crack measurement was attempted, the extent and type of porosity

nulled any meaningful data. This by no means useless information however, as it demonstrates the sensitivity of the process window – 0.25 J/mm was shown to be sufficient for achieving full density – with 0.05 J/mm being the difference between full density and lack of fusion. This was the case for all sample sizes.

Fortunately, the extensive size of the DOE meant there were still strong relationships observed. Crack density is observed to increase almost linearly with increasing laser power, Figure 6.9, and so too with energy density, Figure 6.10. However, sample volume does not display such a simple relationship, Figure 6.11. The 5x5x5 mm samples displayed the highest crack density, as opposed to the smallest 2.5 mm cubes which were predicted to under the initial hypothesis. In addition, 10 mm cubes display, on average, the second highest crack density which again counters the initial hypothesis. However, the results are in agreement with the initial findings, in that the 5 mm cubes display a high crack density that the 10 mm cubes.

The accompanying density values are also presented. It is interesting to observe that for laser power and energy density, there is negative relationship between the density and the crack density. Thus as one pushes towards higher powers and energy densities, both porosity and cracking increases. This is counter to the relationship observed in the preliminary optimisation trials of Hastelloy X, although that was not as extensive nor were the variables as well defined as in this DOE. One could argue the same is negative relationship is present with the increasing size samples, with the exception of 2.5x2.5x2.5 mm cubes.

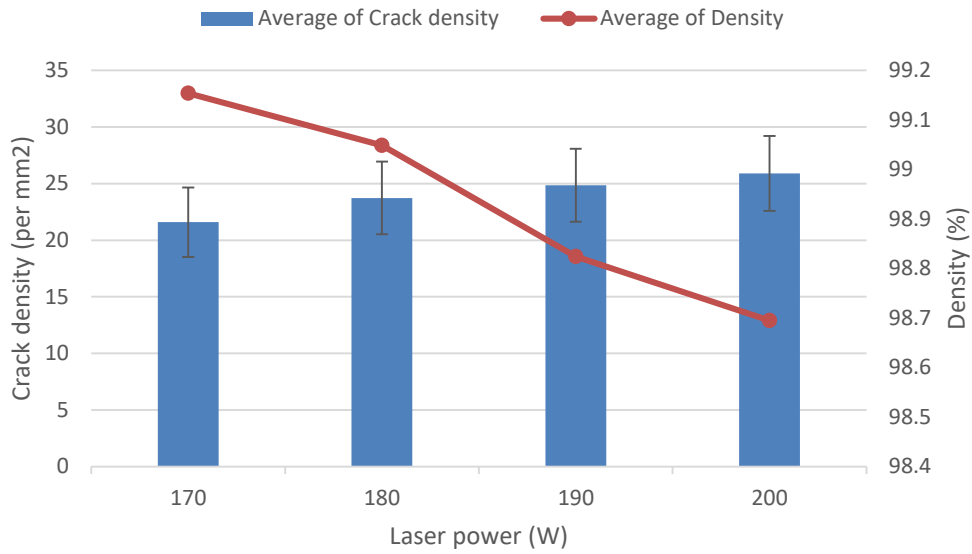


Figure 6.9 - Averaged crack density with density for samples with laser power

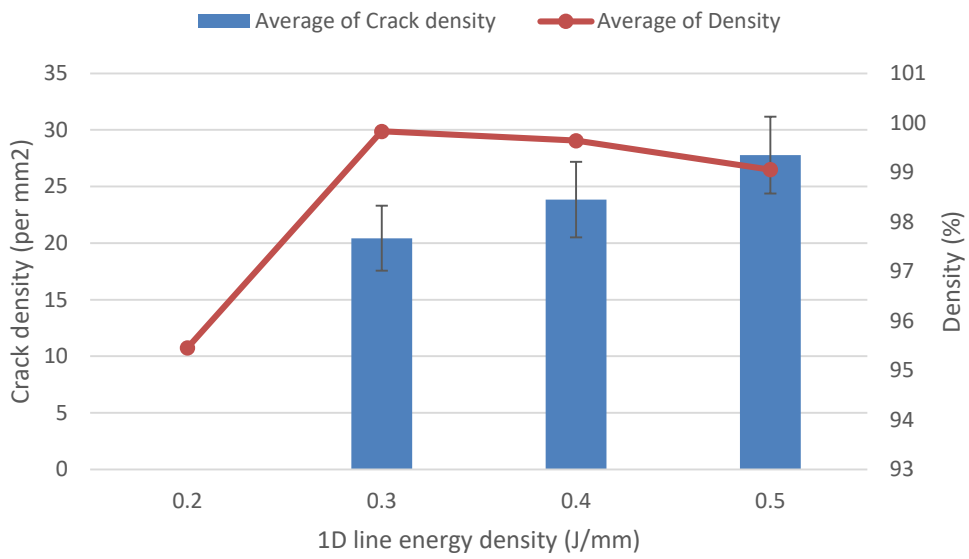


Figure 6.10 - Averaged crack density with density for samples with 1D line energy density

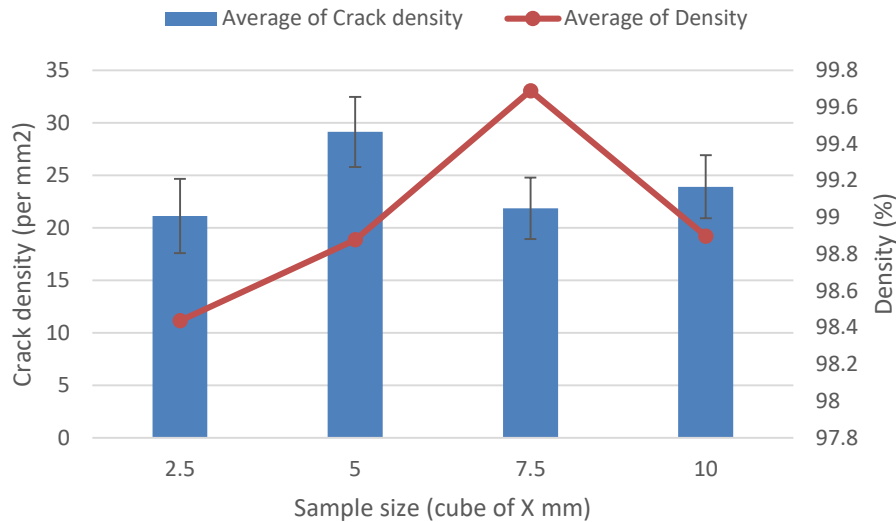


Figure 6.11- Averaged crack density and density with sample volume

6.3.4 Laser power relationship

Although the averaged crack density displays a steady increase with increasing power, study of the individual plots for each sample size reveal a slightly less defined relationship – see Figure 6.13.

Of particular note is the comparably low value for 200W in the 10 mm sample. It is noted that for the 10 mm samples, particularly for those of higher powers, the cracks became increasingly smaller but conversely more densely populated. In addition, the 10 mm samples in general suffered from high porosity, as discussed, which higher power samples exhibiting the more severe porosity. This potentially explains the anomalous result, in what is otherwise a reasonably strong trend.

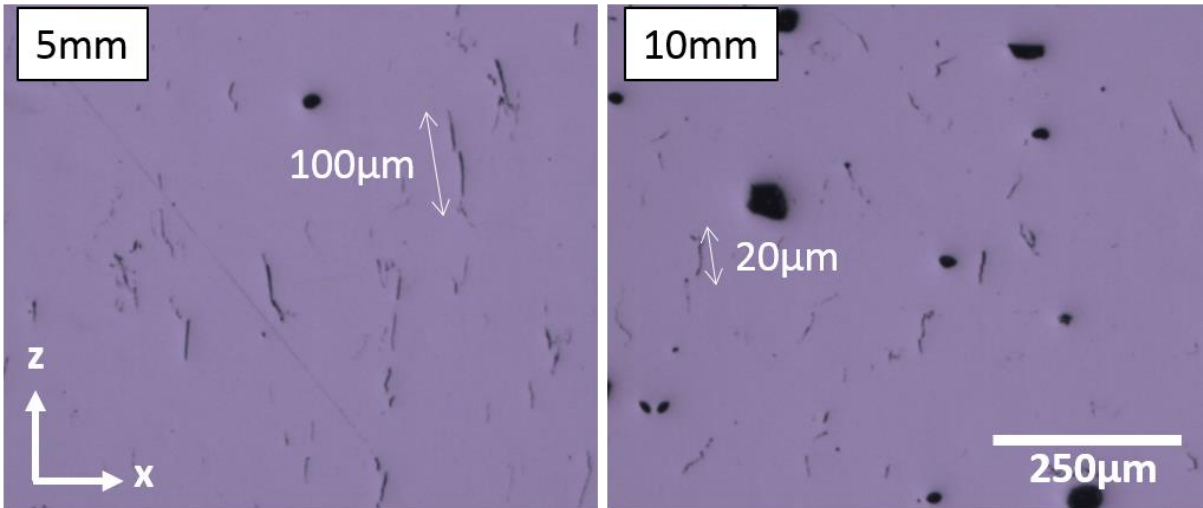


Figure 6.12 - Comparison between crack sizes in 5x5x5mm and 10x10x10mm samples of LP 200W, ED 0.4 J/mm.

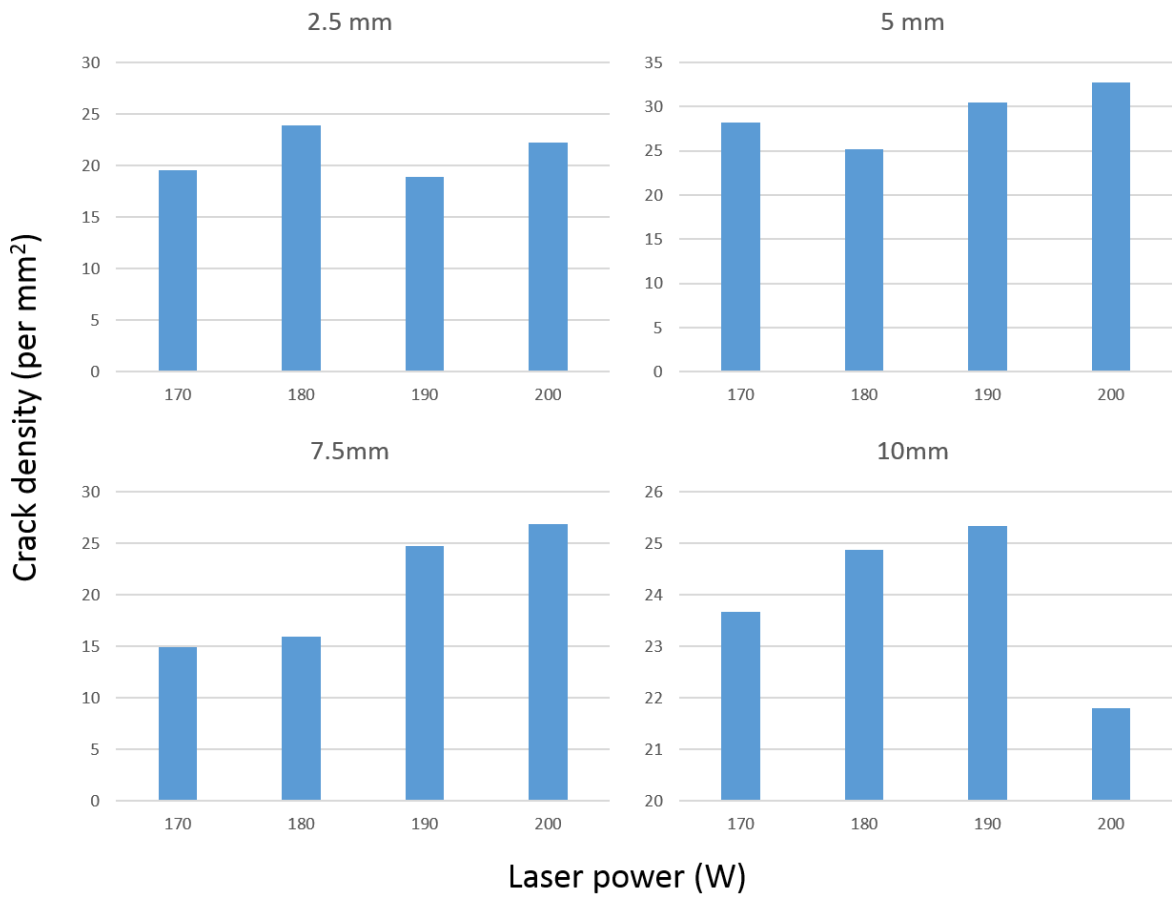


Figure 6.13 - Crack susceptibility with laser power for samples sizes 2.5-10 mm cubes

6.3.5 Energy density relationship

Energy density values are calculated from laser power and exposure time input parameters, and as such energy density is in part a measure of laser power. For each energy density value, there are four power-exposure time pairs, giving a total of 16 exposure time values. By plotting crack density with exposure time instead of 1D line energy density, the influence of laser power is removed, and a truer relationship between cracking and absorbed energy is revealed, see Figure 6.14.

It is observed that although energy density appears to show a linear relationship with crack density, exposure time does not. In fact, there is no discernible relationship between crack density and exposure time, and laser power and sample size clearly have a dominant influence.

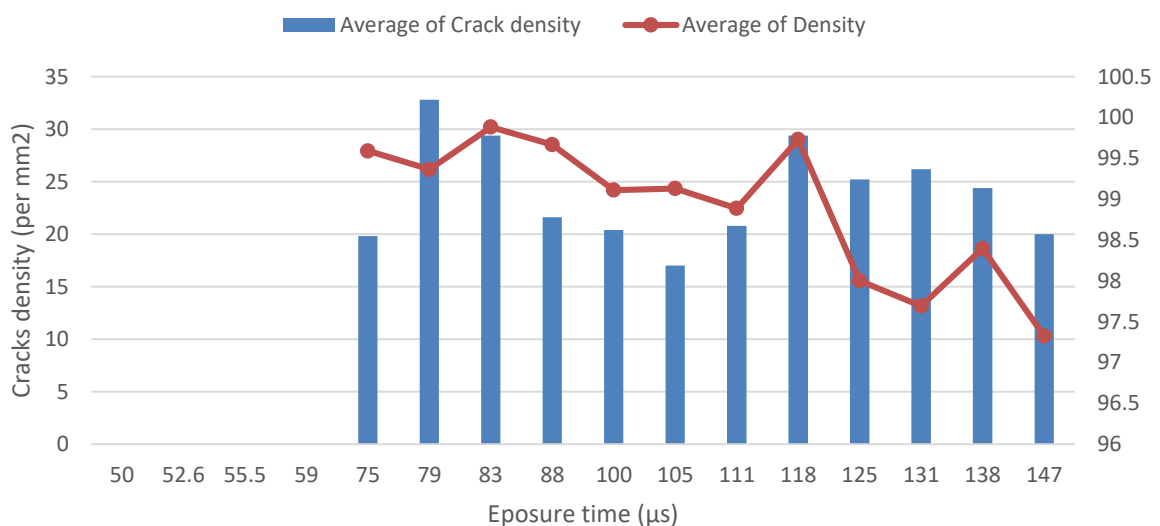


Figure 6.14 - Averaged crack density and density values for set exposure times

6.3.6 Sample size relationship

The initial hypothesis given in Section 6.2, was that smaller volumes would have a higher crack susceptibility due to reduced residual heat and increased cooling rates, therefore greater thermal stress. Instead what is observed implies a more complex relationship. If, like with laser power, the average plot is separated out – Figure 6.15 - it is observed that the relationship is held across all but one of the power sets. One can therefore be confident that this not an anomalous result and that the observed relationship is reliable. In fact, it is the 200W 10 mm sample which again does not conform, and would otherwise give a solid relationship across the full sample range.

10 mm cubes display a higher crack density than 7.5 mm cubes on three out of four occasions

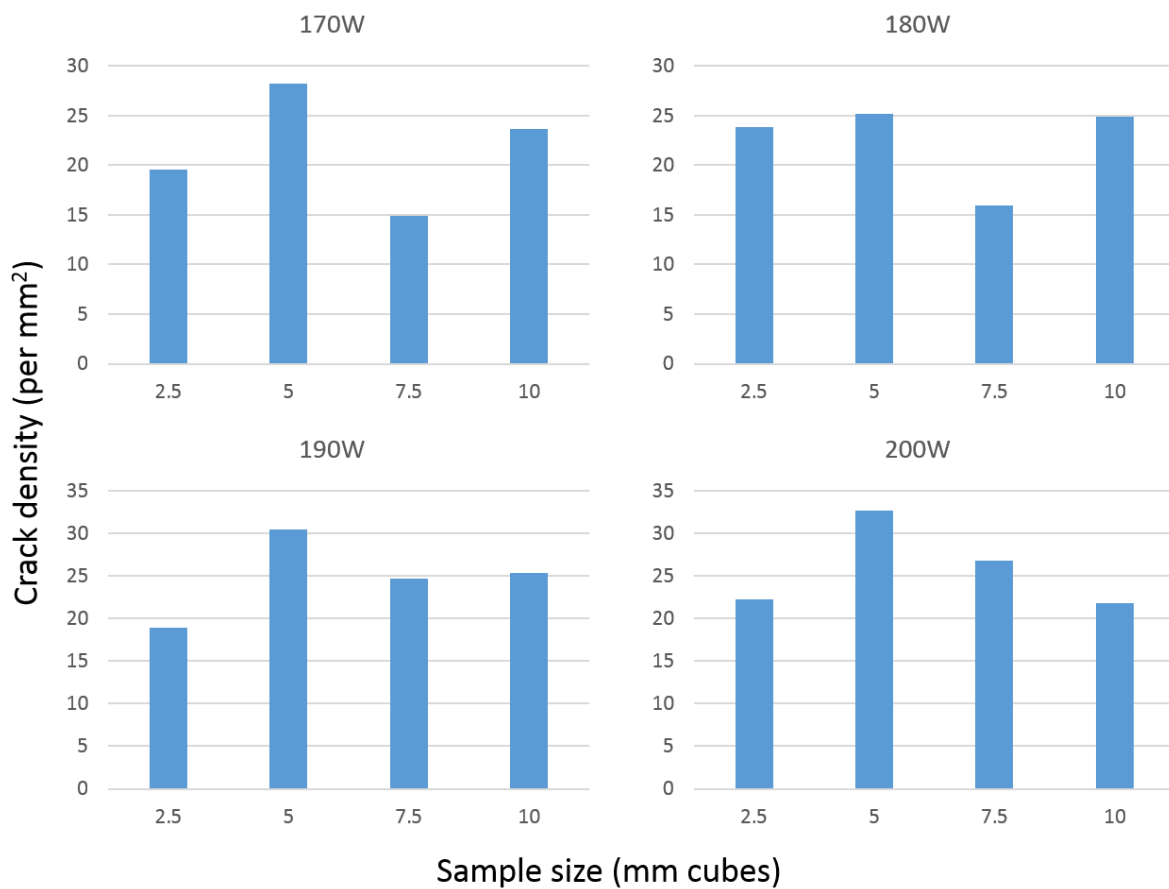


Figure 6.15 - Crack density with sample size and laser power

6.3.7 Applicability to crack susceptibility theory

The observed dominant influence of laser power on crack susceptibility, particularly over absorbed energy, can be used to draw some conclusions on the mechanisms for micro-cracking during SLM processing.

As discussed in Section 5.1, it was hypothesised that ETSS was the mechanism for cracking in SLM processing. Solidification cracking was discounted as it was proposed that the solidification rates were high enough to inhibit the remaining of a liquid film at the grain boundaries, and segregation to grain boundaries was observed to be inhibited – Chapter 4. However, the observations of secondary phase formation in Section 4.1.3 imply that solidification conditions, although clearly still in the region of RS, may also allow for the formation or remaining of a liquid film.

If this were the case, one would expect that an increase in absorbed energy or exposure to the laser would result in an increase in cracking. This is because the material would be held above the freezing temperature for longer. From the results of this investigation however, it was observed that there was no relationship between exposure time and crack density.

Instead, laser power was observed to have a linear relationship with crack density. From the Rosenthal relationship (Rosenthal 1946), for a moving laser source, power is directly proportional to surface temperature of the material. An increase in power therefore results in an increase in thermal gradients. It can therefore be inferred that an increase in thermal gradients, as opposed to absorbed energy results in an increase in processed induced micro cracking. As such, it is unlikely that solidification cracking is the driving

mechanism behind the micro-cracking in SLM, and instead TGM driven ETSS cracking is more applicable.

6.4 Chapter Summary

In this chapter, the tensile strength contribution for the crack susceptibility model was developed and experimentally validated.

By assuming minimal microstructural deviation - when comparing two nickel superalloys processed by SLM under similar conditions- and considering imposed microstructure, a comparative Hall Petch relation for tensile strength was reduced to the difference in solid solution strengthening contributions. The Gypen and Deruyttere (1977) model for solid solution strengthening was implemented, which combined with strengthening parameter data from Mishima (1986) allowed for the calculation of the solid solution contribution of any nickel base superalloy.

Using the developed model, the solid solution contribution of Hastelloy X composition from Chapters 3 and 4 (OHX) was calculated. Knowing the relative solid solution strength potency of the alloy elements – strengthening parameter – a modified version of Hastelloy X, with increase solid solution strength, was designed.

The modified composition, MHX, was processed and directly compared to OHX for micro-cracking. MHX displayed a 65% reduction in crack density over OHX. Tensile testing of the two alloys revealed MHX had superior elevated temperature tensile strength and marginally improved ductility. This result supported the crack susceptibility theory.

Finally, a further investigation into the relationship between laser parameters, part geometry and micro-cracking was conducted. It revealed that laser power had the greatest influence on micro-cracking, with a near linear relationship, however the

relationship for exposure time was less discernible. This further supported that ETSS is the primary cracking mechanism in nickel superalloys.

7 Thermal stress modelling

In this chapter, the thermal stress term of the crack susceptibility equation will be developed. The establishment of lattice strength having a strong influence of crack susceptibility has partly validated the crack susceptibility equation from Chapter 5. However, if those minor changes in composition have a significant impact on one material response, it is likely that it will affect others. The obvious scenario one would want to avoid is one where a compositional alteration that has increased lattice stress by 5%, has resulted in an increase of thermal stress of 10%, thereby increasing crack susceptibility rather than reducing it.

In order to avoid the unintended, the effect of compositional changes on the thermal stress generation must be understood, and then quantified. This will allow for converse simulation of both lattice stress and thermal stress, and therefore a complete simulation for crack susceptibility.

It is important to note at this point that the predicted values for thermal stress do not have to match perfectly with reality. Besides being difficult to validate, it is not the exact value of thermal stress that is actually useable. Instead it is the ratio between the thermal stress and the solid solution strength contribution. Therefore, providing all alloys are assessed using the same method, all can be fairly assessed with respect to one another on the same scale.

7.1 Stress simulation discussion

In Section 2.2.1, models for residual stress by Mercelis and Kruth (2006) and Shiomi, Osakada et al. (2004) were described. Although the residual stress models are in effect modelling the thermal stress build up, they do not describe the in situ thermal stresses experienced by the material during the process. The in situ thermal stress is what is required for the crack susceptibility parameter as it is the direct comparison between the material's UTS and the thermal stress which determines whether the material will crack under processing.

What is required is a method for simulating thermal residual stress as a function of process parameters and alloy composition.

The most comprehensive approach is to model the thermal behaviour of the material as it is being processed and then apply thermal stress simulation to that model. This is of course a heavily involved solution and would take a stand alone project to complete. *This* work would therefore seek an established thermal model, of which there are number published in the public domain for both 2D and 3D cases (Matsumoto, Shiomi et al. 2002, Dai and Shaw 2004, Patil and Yadava 2007, Gusarov and Smurov 2009, Roberts, Wang et al. 2009).

Roberts, Wang et al. (2009) work on three dimensional finite element analysis of temperature fields during laser AM is one of the most comprehensive studies on thermal modelling of SLM to date. One key aspect which elevates it from other work is the simulation of successive layers, this is vital when considering thermal stresses as these can be increased or relieved depending on the magnitude and severity of successive heating.

Lopez (2016) developed the work of Roberts with the intention of then coupling with a microstructure evolution model. As the work of Lopez was conducted along the same project timeline as this work, it allowed for close collaboration between the two. It therefore made sense to use the model developed by Lopez, which was in part verified by the experimental work on Hastelloy X from this work, to simulate temperature fields and consequently thermal stress for nickel superalloys processed by SLM.

ANSYS is an engineering simulation software which is used to both develop models and perform simulations for process and material responses. ANSYS has inbuilt simulation capabilities for thermal stress, which can generate stress field simulations when provided with temperature field data and certain temperature dependant material properties. Lopez's model would be able to provide temperature field data which was both of an appropriate resolution and material dependent. This could then be input into ANSYS's thermal stress simulation module, resulting in a material-process dependant thermal stress field prediction.

Key to an accurate prediction are values for the material's tangential modulus for a range of strains and temperatures; the greater number of values provided, the greater the accuracy. ANSYS uses the tangential modulus to predict the stress strain behaviour of the material. The only way to attain these values is empirically, by performing tensile testing on the material and calculating the tangential modulus at various points along the stress-strain curve. This is of course problematic if the material one is trying to simulate does not exist in physical form; as is the case for theoretical alloy design. In addition, tangential modulus is not a readily available book property, so the use of literature values as a close approximation is also not feasible. Therefore, as desirable as a fully comprehensive simulation would be, the difficulties in acquiring the relevant material data make it an

unviable solution at this point. The thought process for an alternative is detailed in Figure 7.1.

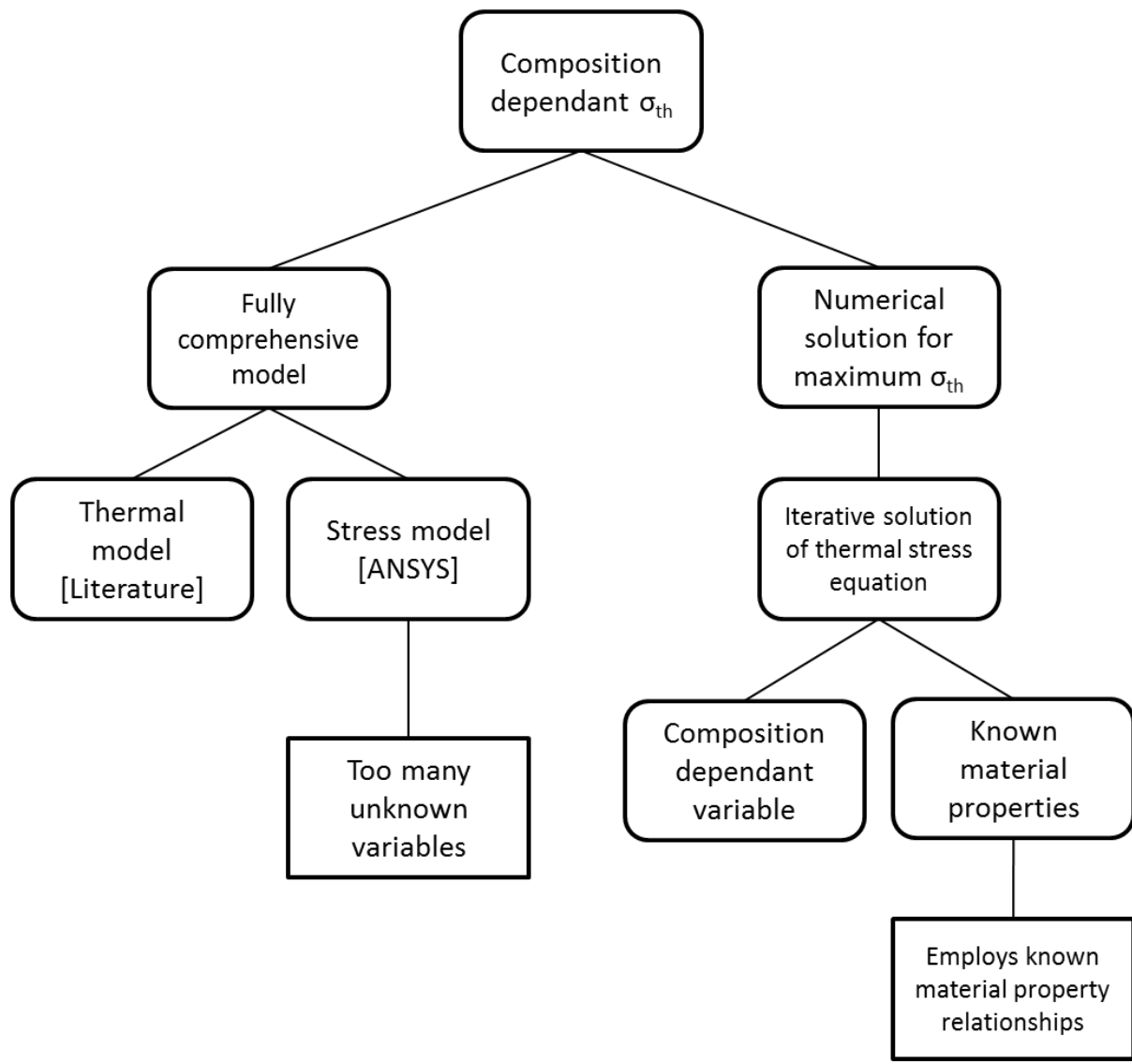


Figure 7.1 - Flowchart representing thought process for determining composition dependent thermal stress

Given that this investigation only seeks to simulate the maximum thermal stress experienced by the material during processing, a full stress field model is not actually required. Instead simpler numerical solutions would be more appropriate, although the solution would still have to be process and material dependent.

A classic relationship for tensile stress generation as a result of a length of material being cooled from a peak temperature is given by Equation 7.1.

$$\sigma_{th} = E\alpha_{CTE}\Delta T$$

Equation 7.1

where ΔT represents the change in temperature as a result of cooling. ΔT can be obtained from Lopez's model, just as was proposed for the ANSYS method. This ensures that the simulation would still be influenced by temperature dependent material properties and the process parameters.

Similar to the ANSYS approach, the calculation of thermal stress generation requires the input of values for certain material properties. Unlike ANSYS though, both elastic modulus and coefficient of thermal expansion are both relatively easy to obtain book values for most alloys. The issue of theoretical alloys still remains however, as Young's modulus is difficult to predict accurately from composition alone. This has the potential to undermine the accuracy of the simulation, particularly for cases where minor modifications for the composition have been made. The following assumptions minimise the impact of the approximation:

As mentioned in Section 5.2, α_{CTE} does not vary greatly with variation in alloy composition. The same is the case for Young's modulus. Therefore, using book values of E and α_{CTE} for the nominal composition of an alloy which is being modified within its specification is a fair approximation.

For novel compositions there are two approaches for Young's modulus. The first is use book values for an establish alloy that has a composition closest to that of the novel alloy. This would result in having to place large variation error on any calculated stress values

to accommodate for the potential difference between assumed and actual Young's modulus. This is not ideal, however given the vast number of nickel superalloys alloys in existence, it is predicted that for the majority of cases a similar alloy will already exist, from which a close approximation can be taken.

The second approach would be to model Young's modulus discretely. Unfortunately, to date, there are no composition-thermal dependant models for Young's modulus, and such an extensive level of modelling is beyond the remit of this investigation.

Fortunately, volumetric thermal expansion can be simulated by the thermodynamics simulation software Thermo-Calc. Coefficient of thermal expansion is taken from linear thermal expansion data; however, the volumetric data can be manipulated to estimate a thermal expansion coefficient. As will be discussed in the following sections, Thermo-Calc will also be used to generate values for the thermal dependent properties required for Lopez's model. Figure 7.2 demonstrates the process steps which will be taken for determining composition dependant thermal stress.

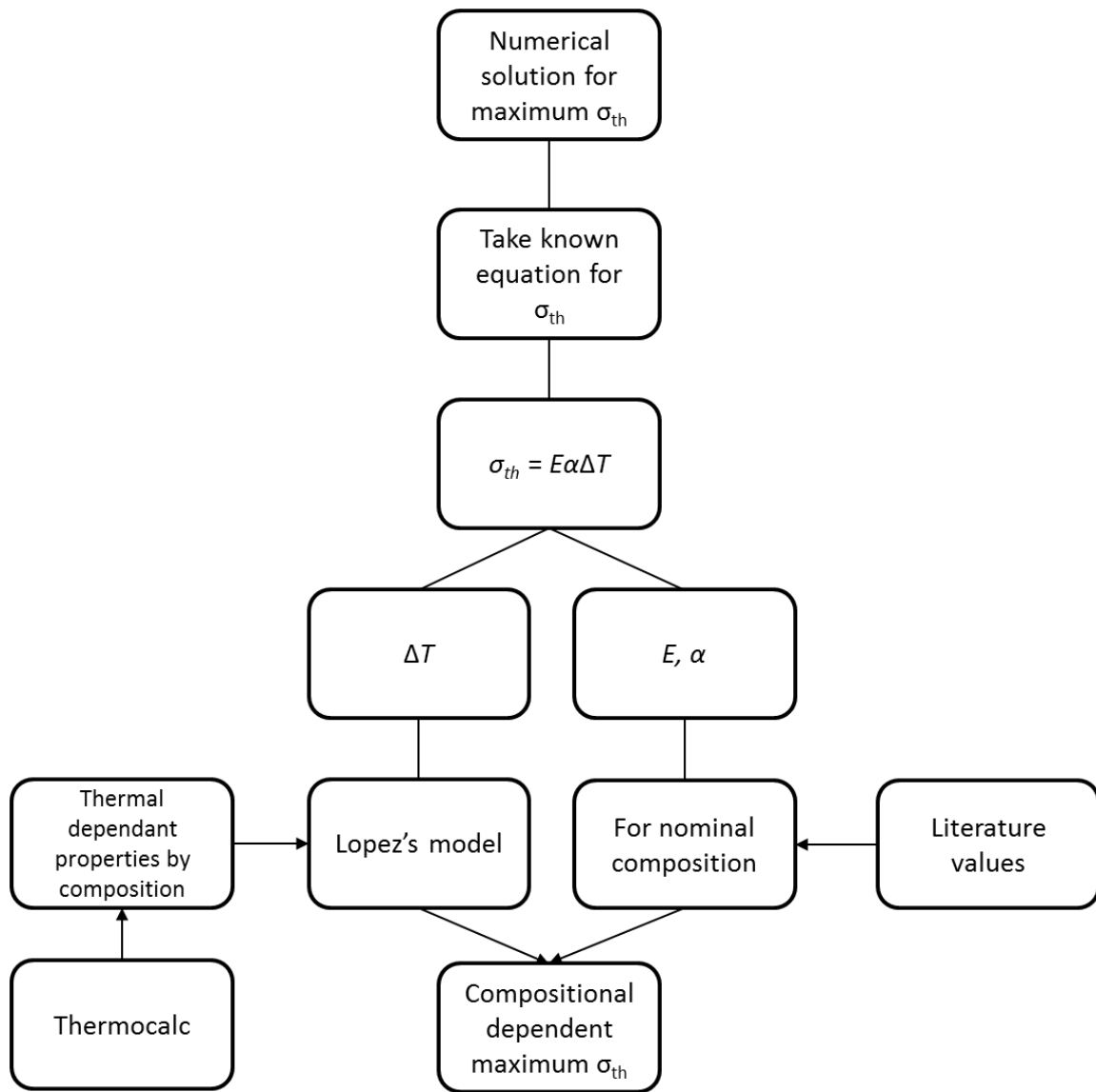


Figure 7.2 - Flowchart representing process steps and inputs for determining composition dependent thermal stress

7.2 Temperature field simulation

The temperature field model is built up from a single spot thermal model, up to a 3D layer by layer thermal model. All iterations were performed using the Finite Element Method (FEM), Computational Fluid Dynamics (CFD) was employed for the initial single spot model, however comparisons with experimental data revealed that the FEM approach was the most reliable. The FEM numerical models were developed using ANSYS

Mechanical and ANSYS Parametric Design Language, which allowed SLM process parameters to be designed in as input variables.

The stages of the model are as follows: Single spot thermal model > Single line thermal model (multiple spot) > Single layer thermal model (multiple lines) in 2D and 3D > Layer by layer thermal model (multiple layers) in 2D and 3D.

Of interest to this investigation is the final stage, which is the multiple layer 3D thermal model. The most obvious reason for this is because the multiple layers are the most representative of the SLM process, and will therefore provide the most reliable temperature profiles. However, there are additional reasons. This investigation requires the prediction of the maximum thermal stress, which is significantly influenced by the ΔT term of Equation 7.1. In order to be confident that the calculated ΔT from the model is the maximum within the HAZ, one needs to be able to simulate the HAZ in its entirety, but also track points within the material that are penetrated successively by the HAZ. There are a number of factors to be considered before deciding on how best to apply the model to the thermal stress situation.

If one considers a line of exposure points on a fresh powder bed, with material and ambient temperature at room temperature. The greatest ΔT experienced by any given point is that of a point located central to the laser beam diameter, on the surface of the powder. However, as liquid state cannot harbour stress, it is actually only the heating and cooling of the material below the point of solidification which results in thermal stress generation. From this one may argue that the maximum ΔT is always $T_m - T_{amb}$, however this relies on the material being allowed to cool to room temperature before another exposure, which is not the case.

The following worked example is considered:

Laser power and exposure time are such that the temperature of the material is brought up to a maximum below its evaporation temperature, for nickel $T_{vap} = 3003$ K. Stress can only form within a solid material, and therefore maximum temperature from which stress can form is $T_m = 1628$ K for Hastelloy X. For the Rensihaw SLM125, the speed at which the optics traverse is quoted as 2.5 m/s. If a point distance of 50 μm is used, the time between each exposure point $t_{idle} = 50 \times 10^{-6} / 2.5 = 20 \mu\text{s}$.

Taking the experimentally determined cooling rate from Chapter 4, $\dot{T} \sim 3 \times 10^5$ K/s, the predicted ΔT between exposure points is $\dot{T} \times t_{idle} = 6$ K.

Of course the material is allowed to cool further as the laser continues to the scan pattern, and in the time taken to begin the subsequent layer. What is needed therefore is a temperature profile for a given point in the material over a period of time encompassing subsequent exposure points, hatch passes and layers.

ANSYS allows for the calculation of temperatures for a given node, point in space, at a given time. If the model is run for multiple layers in 3D, but only the temperature data for a fixed node is recorded, this will provide the required temperature profile. From this profile a series of ΔT values can be extracted thus allowing for the calculation of a stress profile for that node and time frame.

It was mentioned that the FEM model was built around the process parameters of the SLM machine, this allows for simple input of real world machine parameters and therefore a more direct comparison for experimental validation. The model also requires the input of temperature dependent material properties, with values for room

temperature up to and beyond melting temperature. Material density, specific heat capacity, enthalpy and thermal conductivity are all temperature dependent, but in turn also influence transfer and containment of heat within the solid. For example, thermal conductance of nickel increases with increasing temperature, allowing for greater heat transference but also greater heat extraction. The complexities of the behaviour mean that simply using room temperature values for the properties will result in very inaccurate solutions.

7.3 Thermo-Calc: method for obtaining thermal dependent properties

In order to accurately model the temperature fields within the SLM process, the Lopez model requires the input of physical material properties over a temperature range. A full complement of thermophysical properties for a chosen alloy may be difficult to acquire. Fortunately, Hastelloy X is one of a few commercial alloys featured in the K C Mills publication 'Recommended values of thermophysical properties for selected commercial alloys' (Mills 2002). Values in this work have been determined either experimentally or through a mixture of empirical and theoretical based modelling; a further discussion of which will be in Section 7.4.

Although the values in Mills (2002) will allow for an initial determination of the temperature fields, the values for ΔT calculated from those values will only apply to the composition of Hastelloy X used. The remit of *this* investigation – modifications of compositions to affect material response – is dependent on being able to predict changes in material response as function of a modification to the alloy chemistry. As a consequence, simply knowing the thermophysical properties of nominal composition of an alloy is not sufficient.

What is required is a technique which can predict the thermophysical properties, over a range of temperatures, of an alloy of any given composition. Fortunately, this is precisely what the Thermo-Calc 2015b© software is designed for. Thermo-Calc performs thermodynamic calculations based on thermodynamic data from vast material databases. There is a wide range of databases available for many different material types, including a specific nickel superalloy database, TCNI8, which was used for this investigation. The databases are created by means of 'critical assessment and systematic evaluation of experimental and theoretical data', following the CALPHAD technique. Thermo-Calc 2015b therefore provides the best solution for obtaining thermophysical values for modified and novel nickel superalloy compositions.

Of the thermophysical properties required by the Lopez model, enthalpy and heat capacity are direct outputs of Thermo-Calc. Density (in g/cm³) is calculated by taking the reciprocal of volume normalised for mass per gram. Enthalpy and volume are calculated with the equilibrium calculator, and heat capacity with the Scheil solidification calculator, which applies the Scheil-Guliver model for solidification path calculation. Thermal conductivity is not a direct output of the software, however.

Instead the approach taken is similar to that taken by other investigations (Parker, Jenkins et al. 1961, A. Hazotte 1993, Mills 2002). This is to calculate thermal conductivity κ , as a function of temperature, from empirically obtained values of thermal diffusivity α , density ρ and heat capacity c , via the relationship given in Equation 7.2.

$$\alpha = \frac{\kappa}{\rho c}$$

Equation 7.2

In A. Hazotte (1993) thermal diffusivity is measured by means of the 'flash method'. In the flash method, a pulse of energy is applied to the front face of a thin sheet, the resulting energy detected on the rear face is then used to determine the thermal diffusion through the sample. The thermal diffusivities for several nickel base superalloys and intermetallic phases were measured over a 21-1400 °C temperature range. All of the alloys displayed the same behaviour with increasing temperature, with thermal diffusivity increasing linearly up until ~700-800°C at which point diffusivity plateaus for ~200°C before resuming the increase at a lesser rate. Also observed is that although some influence of composition on the diffusivity of the alloys is apparent, the variation between AM3, MC2 and CMSX2, for example, which have markedly different compositions, is minimal. It is therefore assumed that the differences between compositions within the same specification of an alloy will have thermal diffusivities of negligible difference.

Values of density and heat capacity with temperature will be calculated by Thermo-Calc, allowing for a quasi-compositional and thermal dependent thermal conductivity to be calculated.

This is considered an acceptable solution given that the thermal conductivities of nickel superalloys are reported to not vary greatly from a value of 11 W/m/K (Terada, Ohkubo et al. 1997). This is attributed to the high concentrations of the solute elements. The thermal conductivity of nickel monotonically reduces to a constant beyond solute concentration of 20 wt%. Given that typical solute concentration values range between 30 and 50 wt%, it is therefore expected that small changes in individual concentrations will not affect the thermal conductivity significantly.

As mentioned in Section 7.2, Thermo-Calc can simulate temperature dependent volumetric expansion. Thermal expansion can easily be determined using the volume-temperature data set, for any given temperature range.

7.4 Calculation methodology

This section demonstrates the feasibility and validity of the proposed method for prediction of thermal stress as detailed in Figure 7.2. Using the nominal composition of Hastelloy X, for which there are literature values of the key material properties, a series of calculations will be made and compared to empirically obtained values (either book or experimental values from this work). Using Figure 7.2 as the template, thermophysical values will first be simulated on Thermo-Calc, this will then be passed into the Lopez model to produce a temperature profile, which will then be used to calculate values for maximum thermal stress.

The process steps detailed in the following sections are the same as those which will be used to perform the final crack susceptibility predictions in Chapter 8.

The nominal composition from Mills (2002), detailed in Table 7.1, will be used for the validation calculations as it will allow for direct comparison with the empirical data presented in that work.

Element	Ni	Fe	Cr	Mo	Co	W	Si	Mn	C
wt%	47	18.5	22	9	1.5	0.6	0.5	0.5	0.1

Table 7.1 - Nominal composition of Hastelloy X to be used for validation calculations

7.4.1 Thermo-Calc simulation of thermal dependent material properties

Table 7.2 gives the thermophysical values calculated using Thermo-Calc from the composition details in Table 7.1. As stated in Section 7.3, thermal conductivity was calculated using thermal diffusivity values from Mills (2002) and the density and heat capacity values from the Thermo-Calc simulation. This provided a set of thermal conductivity values which were still dependant on the Thermo-Calc simulation and were therefore fair to be considered separate to those given in (Mills 2002)

Temperature (K)	$H_T - H_{293}$ (Jg ⁻¹)	Volume (cm ³)	Density (gcm ⁻³)	Heat capacity (JK ⁻¹ g ⁻¹)	Thermal diffusivity (m ² s ⁻¹)	Thermal conductivity (Wm ⁻¹ K ⁻¹)
301.5	4.34	0.1207	8.287	0.450	2.847	10.61
371.5	13.17	0.1207	8.282	0.484	3.081	12.36
471.5	87.90	0.1213	8.241	0.550	3.406	15.45
571.5	147.26	0.1218	8.214	0.629	3.728	19.27
676.0	322.15	0.1219	8.201	0.519	4.060	17.28
770.0	423.91	0.1223	8.179	0.556	4.365	19.86
870.0	478.49	0.1227	8.147	0.613	4.707	23.52
970.0	536.68	0.1232	8.114	0.700	4.885	27.75
1070.0	599.71	0.1238	8.080	0.841	4.939	33.57
1170.0	668.67	0.1243	8.042	0.768	5.215	32.20
1270.0	746.76	0.1251	7.996	0.610	5.477	26.72
1370.0	824.97	0.1258	7.947	0.646	5.749	29.53
1470.0	891.71	0.1264	7.911	0.689	6.009	32.76
1530.0	933.85	0.1269	7.880	0.715	6.116	34.47
1540.0	941.02	0.1271	7.871	0.720	-	-
1553.4	950.71	0.1272	7.865	0.724	-	-
1560.0	959.94	0.1273	7.855	0.964	-	-
1570.0	970.98	0.1275	7.844	1.086	-	-
1580.0	984.41	0.1277	7.830	1.286	-	-
1590.0	1002.00	0.1281	7.808	1.626	-	-
1600.0	1026.75	0.1286	7.775	2.225	-	-
1610.0	1063.38	0.1295	7.723	3.297	-	-
1630.0	1203.10	0.1332	7.506	8.216	5.917	364.87
1670.0	1251.45	0.1345	7.436	0.712	5.818	30.79
1770.0	1324.23	0.1361	7.345	0.740	5.884	31.98

Table 7.2 - Example thermophysical property values calculated using Thermo-Calc simulation

Note the absence of values for diffusivity, and therefore conductivity, between 1540 K and 1630K. This represents the temperature range for the ‘mushy zone’, in which the material is neither fully solid nor fully liquid, and the flash method cannot be used to determine thermal diffusivity. Values in this temperature range are instead estimated by ANSYS. In the liquid state diffusivity in Mills (2002) are estimated as a flat value, whereas in this investigation the use of Thermo-Calc allows more chemical dependence.

Table 7.3 gives the associated thermophysical values reported in (Mills 2002). For the below values: density is calculated by applying measured thermal expansion to the initial volume and mass of a block of Hastelloy X at room temperature, enthalpy and heat capacity are experimentally determined and thermal conductivity is calculated as done so in this investigation.

Given the expected variations between empirical and simulated values, and progress thermophysical simulation has undoubtedly made in a decade, values for this investigation are in very good agreement with those of (Mills 2002).

The only exception is the value for heat capacity at 1630K. In Mills this is given as the flat rate for liquid phase. However Thermo-Calc is able to simulate heat capacity for both mushy zone and liquid state. Without experimental data, it is difficult to confirm the accuracy of the Thermo-Calc value for this specific case.

Temperature (K)	$H_T - H_{293}$ (Jg ⁻¹)	Density (Kgm ⁻³)	Heat capacity (JK ⁻¹ g ⁻¹)	Thermal conductivity (Wm ⁻¹ K ⁻¹)
298	33.4	8240	0.439	10.3
373	79.7	8221	0.454	11.5
473	128	8193	0.473	13.2
573	178	8162	0.493	15
673	230	8130	0.512	16.9
773	284	8095	0.532	18.8
873	341	8058	0.551	20.9
973	400	8019	0.582	22.8
1073	461	7978	0.604	23.8
1173	525	7934	0.626	25.9
1273	591	7889	0.648	28
1373	659	7841	0.67	30.2
1473	730	7792	0.692	32.4
1533	772	7761	0.71	33.7
1543	779.956	-	-	-
1553	792.648	-	-	-
1563	806.922	-	-	-
1573	823.405	-	-	-
1583	843.04	-	-	-
1593	867.245	-	-	-
1603	898.063	-	-	-
1613	937.932	-	-	-
1628	1112	7240	0.677	29
1673	1146	7363	0.677	29
1773	1214	7280	0.677	29

Table 7.3 - Thermophysical properties from Mills (2002)

The close agreement allows for validation of the process steps used to obtain values using Thermo-Calc. Additionally, because Thermo-Calc 2015b is more advanced than the simulations featuring in Mills, it is assumed that the values given by Thermo-Calc are more reliable, particularly for the mushy zone.

7.4.2 ΔT calculations using Lopez model

The process parameters input into the model are given in Table 7.4. Note the meander strategy was not modelled. This is because for the purposes of microstructure modelling (for which the Lopez model is created for), the meander strategy is an added complexity for validation. Instead a simple raster pattern was modelled. This should not dramatically

affect the temperatures over a few layers, although over the course of a full part would have an effect on the residual stress of the part.

Parameter	Value
Laser Power (W)	180
Exposure time (μs)	100
Point distance (μm)	50
Hatch spacing (μm)	90
Focus Offset (mm)	4
Layer thickness (μm)	20
Strategy	Raster

Table 7.4 - Input process parameters for Lopez model

The model run comprises of 3 layers, each with six hatches (or paths) made up of 4 exposure points. The time between each layer, simulating the recoating of powder, was set at 12 seconds. Figure 7.3 and Figure 7.5 give a visual representation of the temperature field model for the first layer. Although the maximum temperature is reported for each frame, this does not represent the maximum temperature for that exposure point as the frames were not taken at precisely the same instance for each exposure. Using the temperature-colour scale along the base of the images, yellow-green represents the range in which melt/freezing will occur. In spots 11 and 23, the characteristic drop shape of a melt pool expected of a moving laser source is observed. This implies that the point-to-point regime results in similar thermal behaviour to that of a continuous laser source.

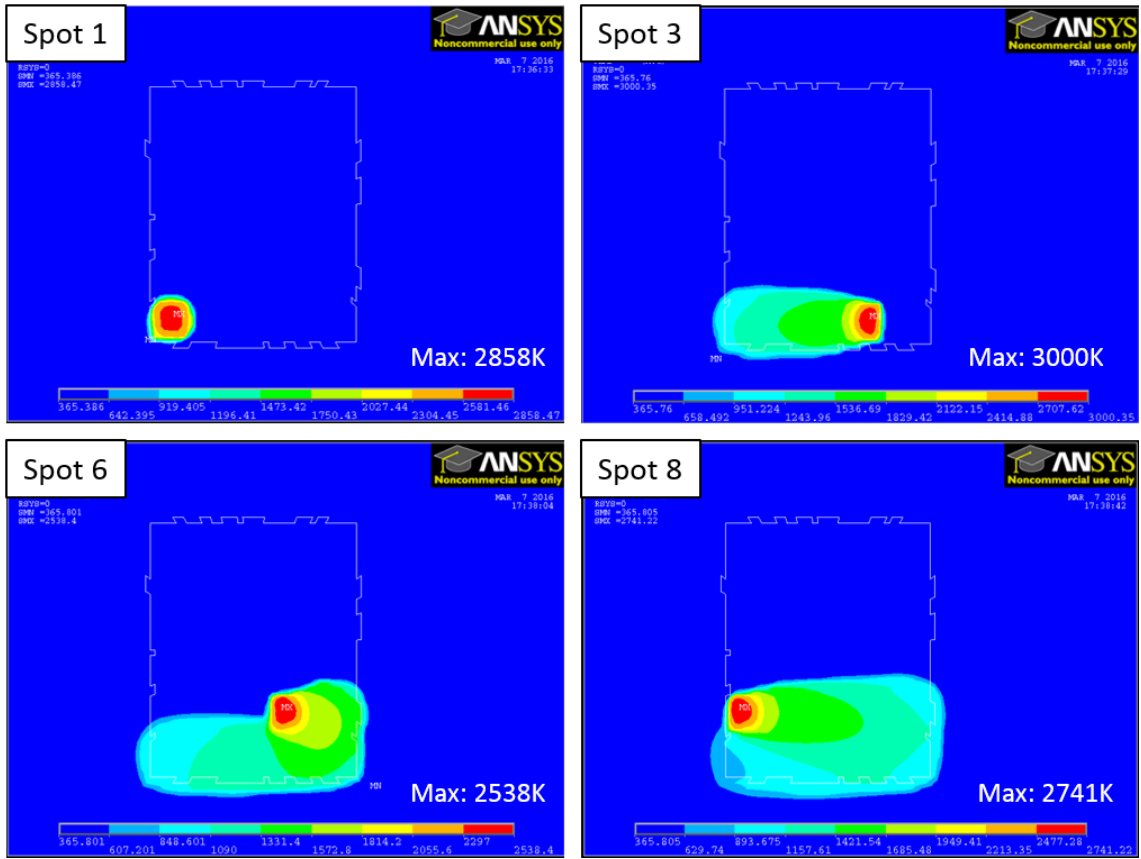


Figure 7.3 - 2D temperature field over time. Spot number indicated in top left corner of each image

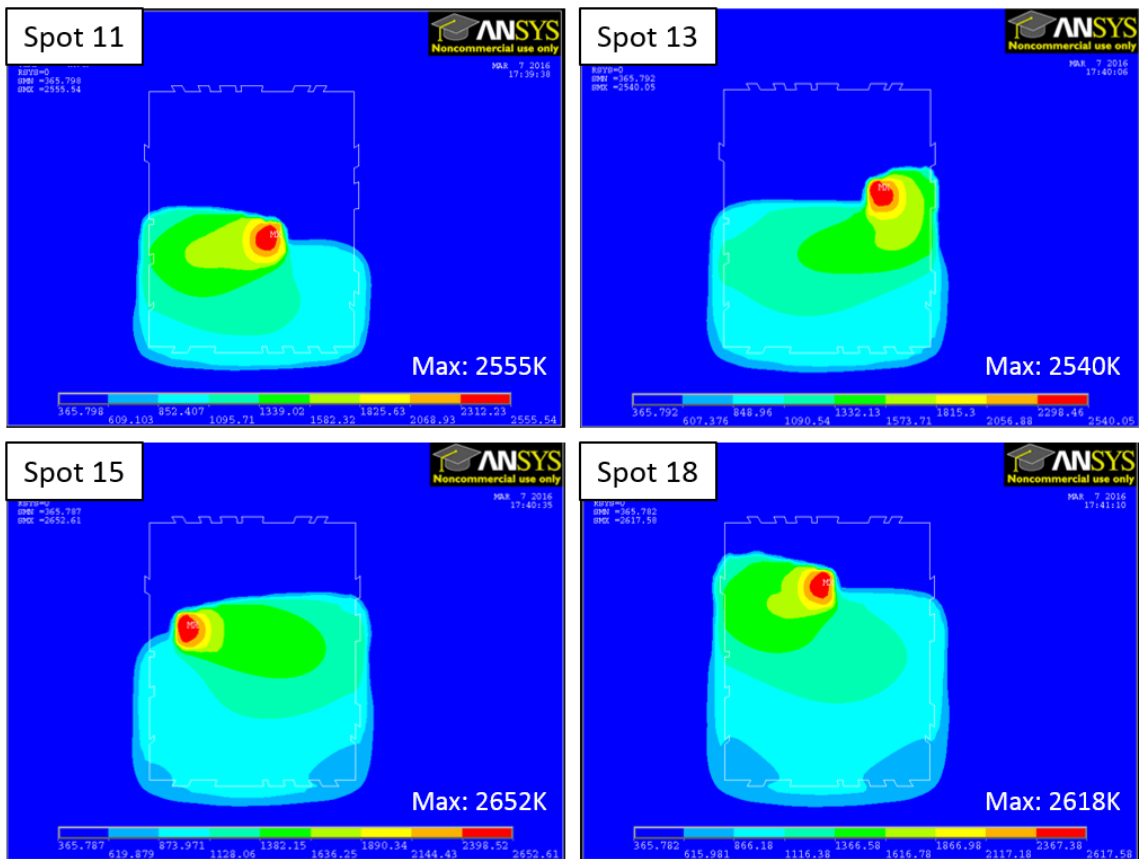


Figure 7.4 - Continuation from Figure 7.3

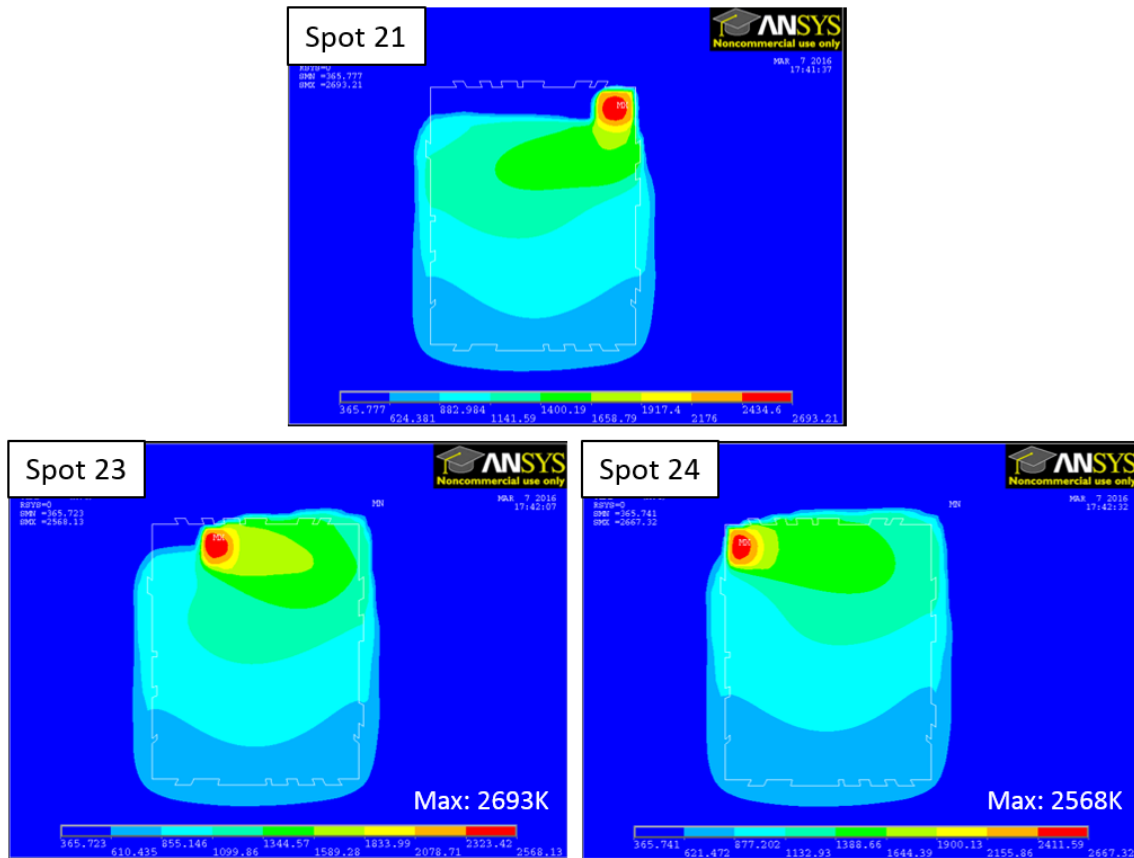


Figure 7.5 - Continuation from Figure 7.4

Quantitative data from ANSYS is obtained by setting predetermined measurement points along the model area. This unfortunately makes it difficult to obtain measurements for the maximum temperatures achieved, as these points cannot be predicted. Figure 7.7 shows temperature-time data for a series of nodes placed along the base of the melt pools in layer 1. In order to help visualise their position in the layer, the exposure points and associated times are represented in Figure 7.6.

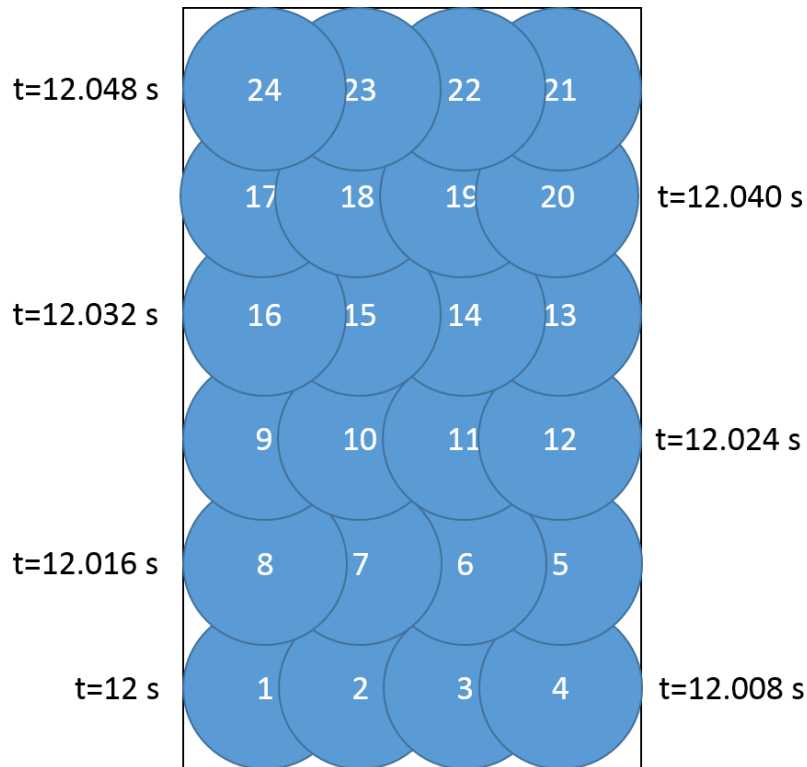


Figure 7.6 - Representation of exposure points (spots), which time after each traverse hatch

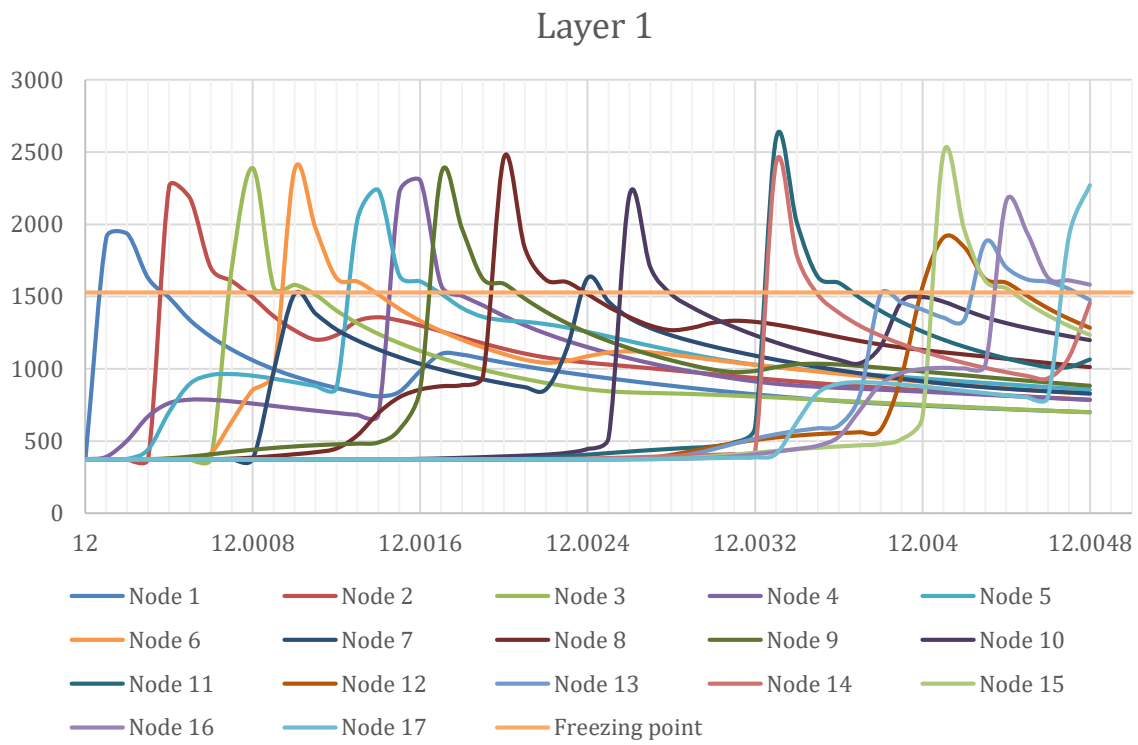


Figure 7.7 - Temperature over time for 18 nodes in layer 1

It is noted that the maximum temperature recorded is for node 11. Based on the time it is suggested this is the node closest to the temperature peak of spot 17, where exposure begins at 12.0032 s, rising to a maximum temperature after 100 μ s (12.0033) before cessation of the laser, and cooling. Although the nodes are not all placed at the same spatial point for each melt pool, the majority display very similar behaviour. The most notable feature is one, typically 200 μ s after temperature peak, at which the cooling is briefly halted. The time interval strongly suggests that the cessation of cooling is as a result of heat conduction from a successive exposure spot. Similar cessations or cooling are observed at later time intervals, and for some nodes, pre-exposure heating from previous exposure points is also evident.

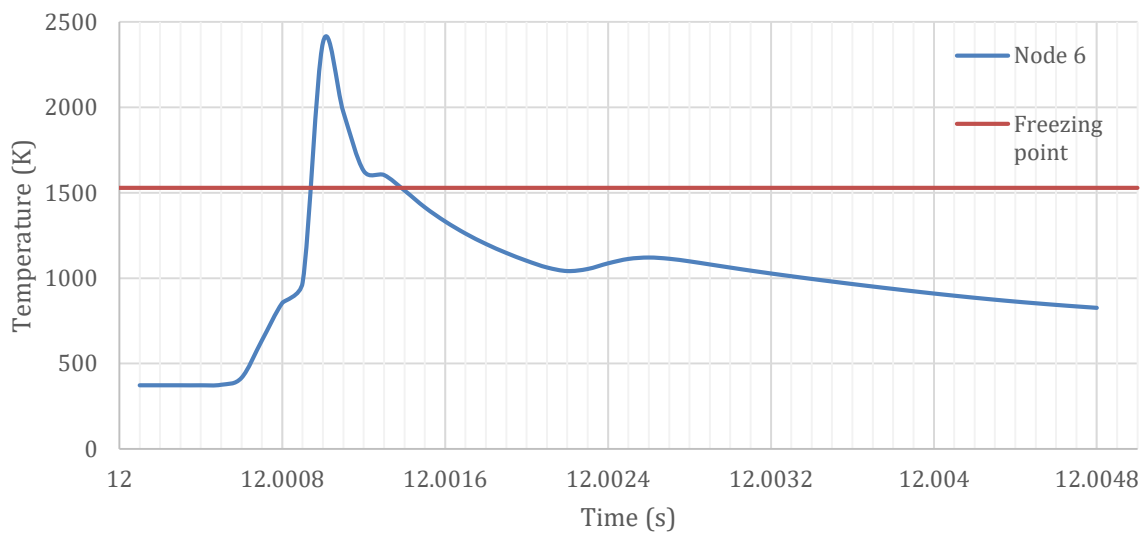


Figure 7.8 shows the isolated temperature profile from node 6, with the freezing point for Hastelloy X added for reference.

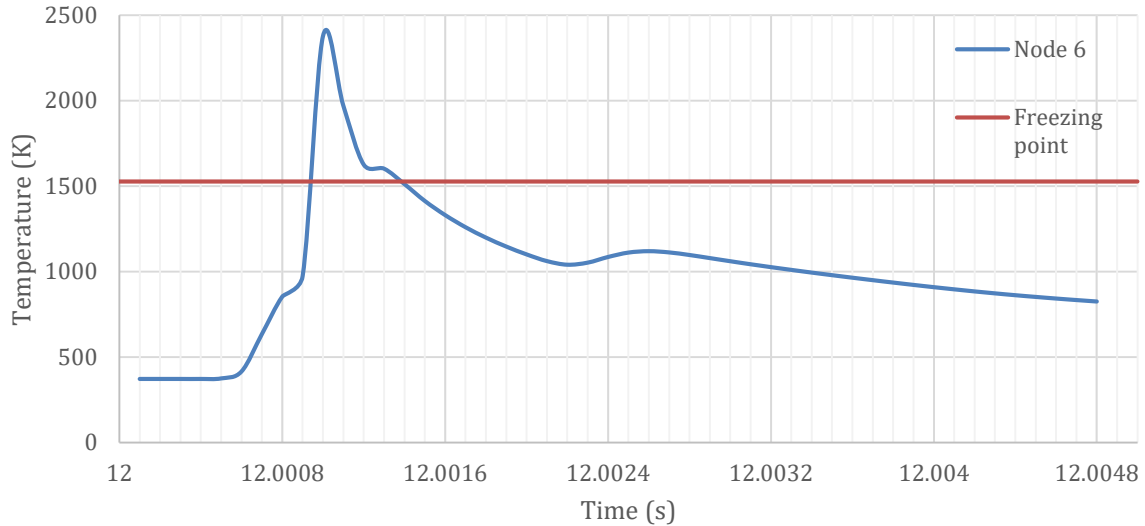


Figure 7.8 - Node 7 for layer 1

The generation of thermal stress can only occur when the material is in a solid state, therefore only the heating/cooling that occurs below freezing point will have an influence on the stress generated. In the case of node 6, the most applicable cooling phase is the one which begins at 12.00026 seconds, as after this point the material is allowed to cool uninterrupted. Although heating will induce expansion and therefore stress, it is the cooling and subsequent contraction which is driving the TGM stress mechanism. Therefore, only the cooling phases will be used to determine ΔT .

Figure 7.9 and Figure 7.10 show the temperature profiles for the same 17 nodes for the remaining two layers.

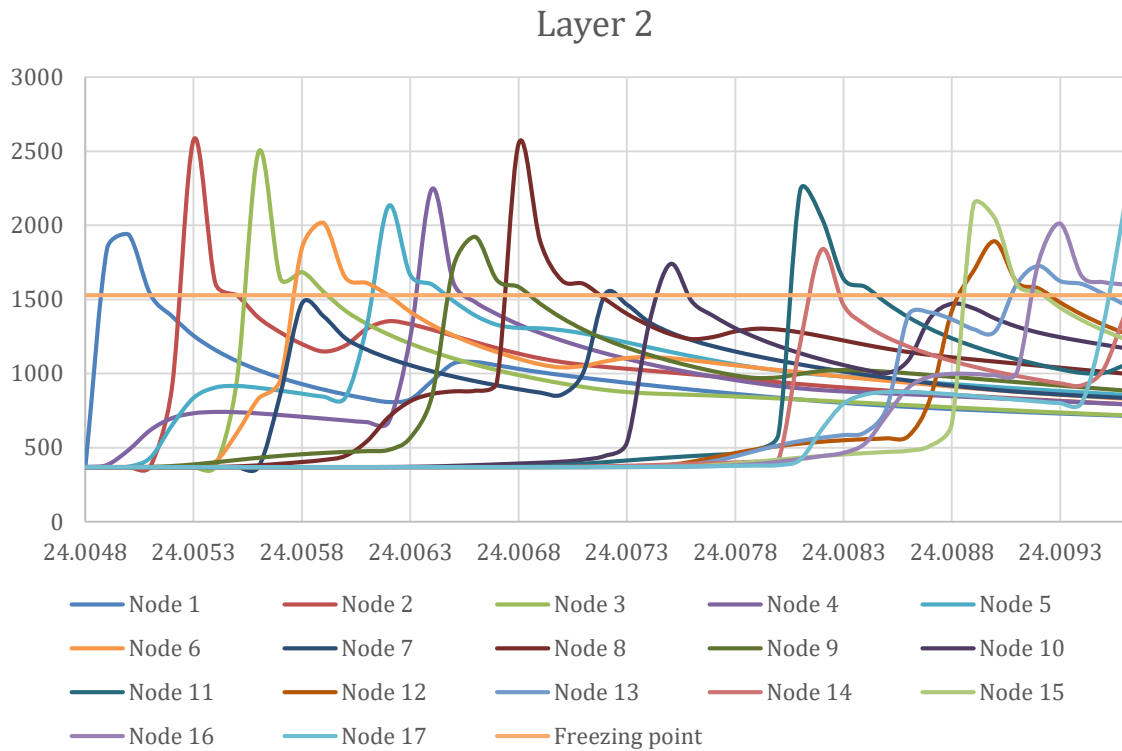


Figure 7.9 - Temperature over time for 18 nodes in layer 2

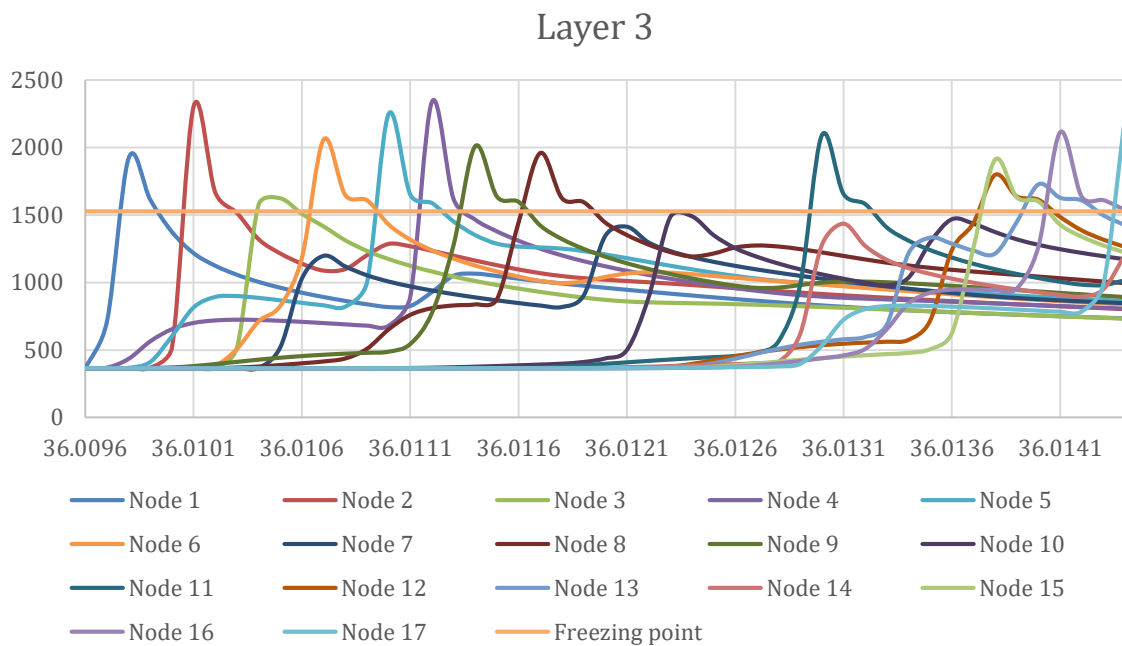


Figure 7.10 - Temperature over time for 18 nodes in layer 3

The key observation is that the majority of nodes measure temperatures above the freezing point. This is expected as the intended meltpool depth is $\sim 100\mu\text{m}$, but the layers

are 20 μm thick. The only node which does not record a temperature beyond T_{freeze} is node 7 in layer three, however it is still significantly heated and cooled. Node 7 is therefore most representative of a point in the solid material which is subjected to extreme temperature variation but is not remelted (resulting in elimination of stress). Two temperature drops are observed for node 7, $\Delta T_1 = 379$ K, and $\Delta T_2 = 1413 - T_{amb}$ K. Unfortunately, the computational time required to simulate a layer cooling in its entirety was too great, and thus the ambient temperature at the end of each layer is not known. This presents a difficult situation, in that clearly ΔT_2 will be greater, but its quantity is unknown, and therefore any value based on it would be as good as arbitrary.

Ultimately, the decision was made *not* to use Lopez's model for ΔT value determination. Although the model offers temperature values with compositional sensitivity, the question of whether this is actually required has been raised. It is argued that any advantage gained by using such a sensitive model, is eliminated by the approximations required to implement its results.

This is not to say that the Lopez model's inclusion in this work is unnecessary. On the contrary, it has provided vital insight into the temperature field evolution of fusion layers in the SLM process and helped to validate proposals of location and occurrence of stress generation in the layer.

As will be discussed further in Chapter 8, crack susceptibility cannot be an absolute value, instead being a quantification of the likelihood of a material cracking during the SLM process. Therefore, providing the same calculation steps are taken, all alloys can be placed on the same scale. This means a fixed ΔT can be used in place of a compositionally sensitive value. Providing the other key values in the thermal stress calculation have compositional sensitivity, it is argued that this will have minimal impact on the validity

of the results. Based on the temperature profiles from the Lopez model, a ΔT value of 500 K has been chosen.

7.4.3 'Apparent' thermal stress calculations

The changes to ΔT discussed in section 7.4.2, mean it is no longer appropriate to calculate a 'maximum' thermal stress. Instead, the values for thermal stress will now be referred to as the 'apparent' thermal stress. This will represent a magnitude of stress generated for a given alloy over the temperature range of 500 K. If anything, this makes alloys more comparable and eliminates uncertainties derived from choosing a 'maximum' thermal stress.

'Apparent' thermal stress values are calculated using Equation 7.1, therefore the key variables are now Young's modulus and coefficient of thermal expansion. Young's modulus values will be taken from literature, and approximated when necessary. Thermal expansion values are calculated from thermal dependent density data output by Thermo-Calc. A coefficient of thermal expansion value is determined for a set temperature range, e.g. 300-400 K. The chosen temperature over which the apparent thermal stress will be calculated is 293-793 K. This range has been determined as the critical range over which ETSS cracking will occur, as it covers the drop from the diffusion limiting $0.5T_{melt}$ down to ambient. Over this range stress will not be able to be relieved through atomic diffusion. Young's modulus values for room temperature will be used, given the difficulty in obtaining elevated temperature values for all alloys.

For example and clarification, the apparent thermal stress σ_{app-th} value of Hastelloy X – using composition from Mills (2002) and values from Table 7.2 – is given below. Linear

coefficient of thermal expansion is calculated from volumetric coefficient of thermal expansion b_{CTE} by simply dividing by 3.

$$E = 200 \text{ GPa}$$

$$\alpha_{CTE [293-793K]} = \frac{V_2 - V_1}{V_1(T_2 - T_1)} / 3 = \frac{0.1243 - 0.1219}{3 \times 0.1219 \times (1170 - 670)} = 13.1 \times 10^{-6} \text{ K}^{-1}$$

$$\sigma_{app-th} = 200 \times 10^9 \times 13.1 \times 10^{-6} \times 500 = 1.31 \times 10^9 \text{ Pa} = 1.31 \text{ GPa}$$

Although absolute values are not of concern, the apparent thermal stress value is certainly of order of magnitude expected given the use of the room temperature E value – elevated temperature values are lower resulting in lower σ_{app-th} value.

The methodology detailed in this Chapter will be used, in conjunction with the solid solutions strengthening contribution methodology from Chapter 6, to determine crack susceptibility values for a range of alloys. The details of this will be discussed in Chapter 8.

7.5 Chapter Summary

The thermal stress contribution for crack susceptibility was considered. Initially, a temperature field model was employed to determine the temperature gradient, and consequently magnitude of thermal stress, for given process parameters and alloy composition. However, it was made apparent that the differences in ΔT between compositions were minimal, and near negligible compared to the influence of elastic modulus – which would often have to be estimated.

It was therefore decided to use the model only to approximate a working ΔT value, applicable for a base alloy set. For the case of nickel superalloys, this would be 500 K, the approximate range between ambient temperature and $0.5T_{melt}$. This was deemed

acceptable as the purpose was to compare nickel alloys for crack susceptibility, thus providing a fixed ΔT actually allows for clear comparison of material response.

The 'apparent' thermal stress for alloys could then be calculated, influenced only by their Young's modulus and thermal expansion, with the chosen ΔT only effecting the final crack susceptibility value.

8 Crack susceptibility model: coupling of solid solution strengthening and thermal stress

In this chapter, the two processes developed for solid solution strengthening and apparent thermal stress predictions are combined, thereby forming a functional method for predicting the crack susceptibility of an alloy from composition alone.

The chapter will primarily focus on validation of calculations from the predictor with experimental data from this investigation and that found in literature. The marked reduction in crack susceptibility of MHX over OHX served as good preliminary validation of the solid solution strengthening hypothesis, but additional effects caused by the composition alterations cannot be entirely ruled out. The following sections detail a series of additional validation investigations with both commercial and in-house fabricated alloy powders.

This will be followed by an in depth discussion of the results from the predictor and what, if any, considerations require attention.

A discussion of how the crack susceptibility predictor can then be reversed into a low crack susceptibility alloy selection model will also be detailed. This represents the ultimate goal of the project.

8.1 Crack susceptibility predictor: Method

Given the complexity of the mechanisms involved in the material response to SLM processing, it would not be sensible to attempt prediction of micro-cracking with a

discrete limit. This also in part due to the use of apparent thermal stress values, rather than absolute maximum values, as initially proposed.

Instead a scale of crack *susceptibility*, ranging from extremely low to extremely high, is more appropriate. A ratio between solid solution strength and the apparent thermal stress will be the basis of a numerical scale along which a material will be placed.

For example, if an alloy has $\sigma_{ss} = 270$ MPa and $\sigma_{app-th} = 1350$ MPa, a simple ratio between the two gives a value of 0.2 and would be considered as having a high crack susceptibility.

The scale with associated crack susceptibility is represented in Figure 8.1.

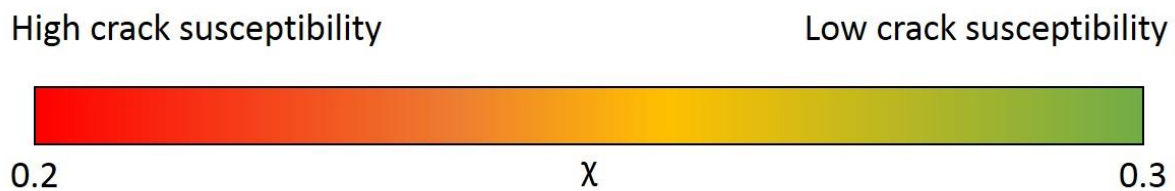


Figure 8.1 - Crack susceptibility scale, numerical value of χ scales inversely with crack susceptibility.

8.1.1 OHX and MHX crack susceptibility comparison

Before discussing the additional validation experiments, the full crack susceptibility values for OHX and MHX are presented and compared to the two alloy's relative material performances in Table 8.1.

Alloy	χ	Experimental observation
OHX	0.253	Moderate cracking
MHX	0.264	Low cracking

Table 8.1 - Crack susceptibility predictions for OHX and MHX

8.2 Validation experiment: Inconel 713 LC

Inconel 713 Low Carbon (LC) is a low carbon content version of Inconel 713, which is a precipitation strengthened nickel-base superalloy typically manufactured by casting. The reduction in carbon was made to reduce the alloys susceptibility to DDC cracking when welding, which was attributed to carbide formation at the grain boundaries.

The primary strengthening phase is γ' Ni₃Al, which is enabled by a high aluminium content. Once solution treated IN713 LC displays impressive elevated temperature properties, details of which are found in Table 8.2.

Temperature (°C)	RT (21)	538
Yield strength (MPa)	740	705
UTS (MPa)	895	895
Elongation (%)	15	11

Table 8.2 - Elevated temperature mechanical properties of Inconel 713 LC taken from (Donachie and Donachie 2002)

It is noted that IN713 LC loses little if no mechanical strength as temperature is increased up to 538 °C but as temperatures exceed 760°C (1400°F) then both yield strength and UTS reduce significantly. Of significance with regards to fracture resistance, is that the elongation values for IN713 LC are relatively low for a nickel superalloy and actually reduce with increasing temperature.

8.2.1 Model predictions

Table 8.3 details the chemical composition of the IN713 LC powder used in this investigation. The composition was then used to calculate a solid solution strengthening contribution $\sigma_{ss} = 269.4$ MPa. This is a significantly lower σ_{ss} compared to either OHX or MHX and hence it is predicted that IN713LC will have a higher crack susceptibility. Apparent thermal stress is calculated at 1281 MPa, using data from CES Edupack 2015.

Element (wt%)	Ni	Cr	Mo	Al	Ti	Ta	C	Zr
Inconel 713LC	bal	12	4.5	6	0.6	4	0.05	0.1

Table 8.3 - Composition used for crack susceptibility predictions of Inconel 713 LC

Care must be taken in using literature values of mechanical properties for predictions of crack susceptibility, as they are associated with the performance of the alloy in a state which is not necessarily similar to that of the as deposited SLM processed material. Precipitation strengthened alloys, like IN713 LC, require post fabrication heat treatments to precipitate out the strengthening phases. In the SLM as deposited state, the alloy is in solid solution only, and strength is near entirely derived from the grain structure and lattice stress.

8.2.2 Experimental and results

Before crack density analysis was conducted, process parameters were optimised for full density. This was achieved with a similar method to that used for Hastelloy X (Section 3.3), using the optimised parameters from the Hastelloy X trials as a guide. Full density was achieved for a range of parameter sets, as with Hastelloy X. These were then dimensionally reduced into eight pairs of LP with 1D energy density, four at 180 W and four at 200 W. The results of the crack density analysis are displayed in Figure 8.2.

The first striking observation is the severity of cracking across all samples, with the minimum crack density value being only slightly lower than the maximum for OHX. Optical micrographs, Figure 8.3, display the severity of the cracking more clearly, showing that the cracks are not only great in number but also in size and propagation. The trends in Figure 8.2 suggest that either lower or higher energy densities than those featured may yield lower crack densities, however beyond these limits density reduces beyond the 99.5% ideal.

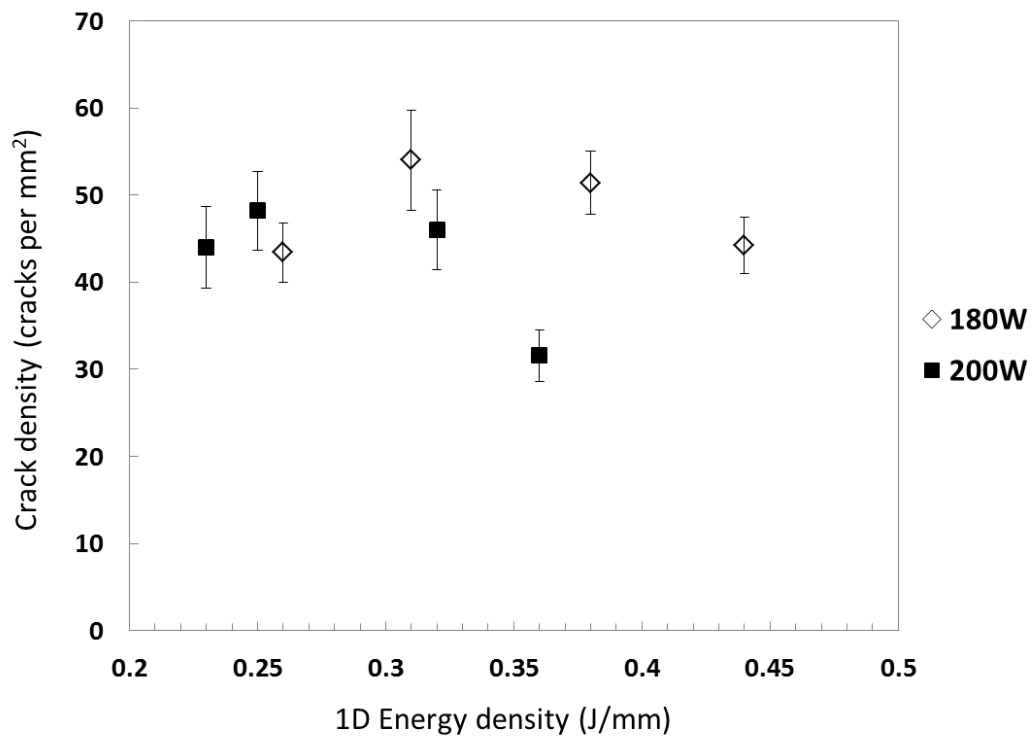


Figure 8.2 - Crack density with 1D line energy density for Inconel 713 LC.

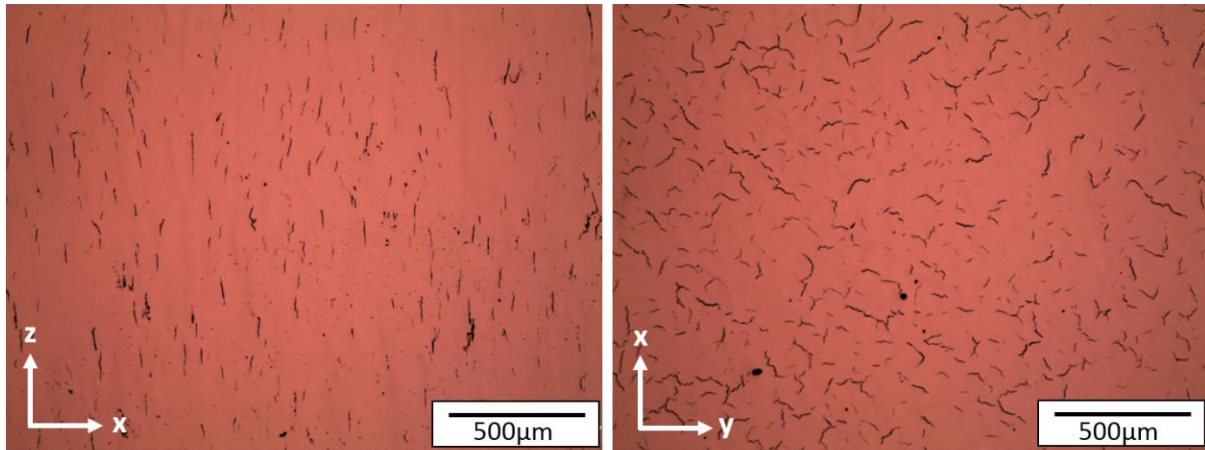


Figure 8.3 Optical micrograph of as processed Inconel 713 vertical (left) and cross (right) section

A combination of low predicted solid solutions strength and high predicted thermal stress generation resulted in a high crack susceptibility rating for Inconel 713LC, which has been strongly supported by the experimental results.

Tensile testing was performed for as processed specimens, the results of which are given in Table 8.4. It is observed that the material displayed very low ductility at room temperature and appears to fracture before yield at elevated temperature. This was technically recorded as a premature fracture, and it was proposed by the testing lab that a layer of unfused particles may have been the cause. However, analysis of the crack surface – see Figure 8.4 and Figure 8.5 - found no evidence of unfused particles or insufficient melting, and it is therefore believed that it was the high density of micro-cracks within the test sample that caused zero yield fracture.

Condition	Yield strength (MPa)	UTS (MPa)	Elongation (%)	Reduction of area (%)	E (GPa)
Room temp (x-y)	710 ± 7.0	836 ± 11.8	3.7 ± 0.5	5.7 ± 1.6	197 ± 10
760°C (x-y)	-	613 ± 10.3	-	-	-

Table 8.4 - Tensile testing data for as processed IN713LC - tensile specimens built in x-y orientation

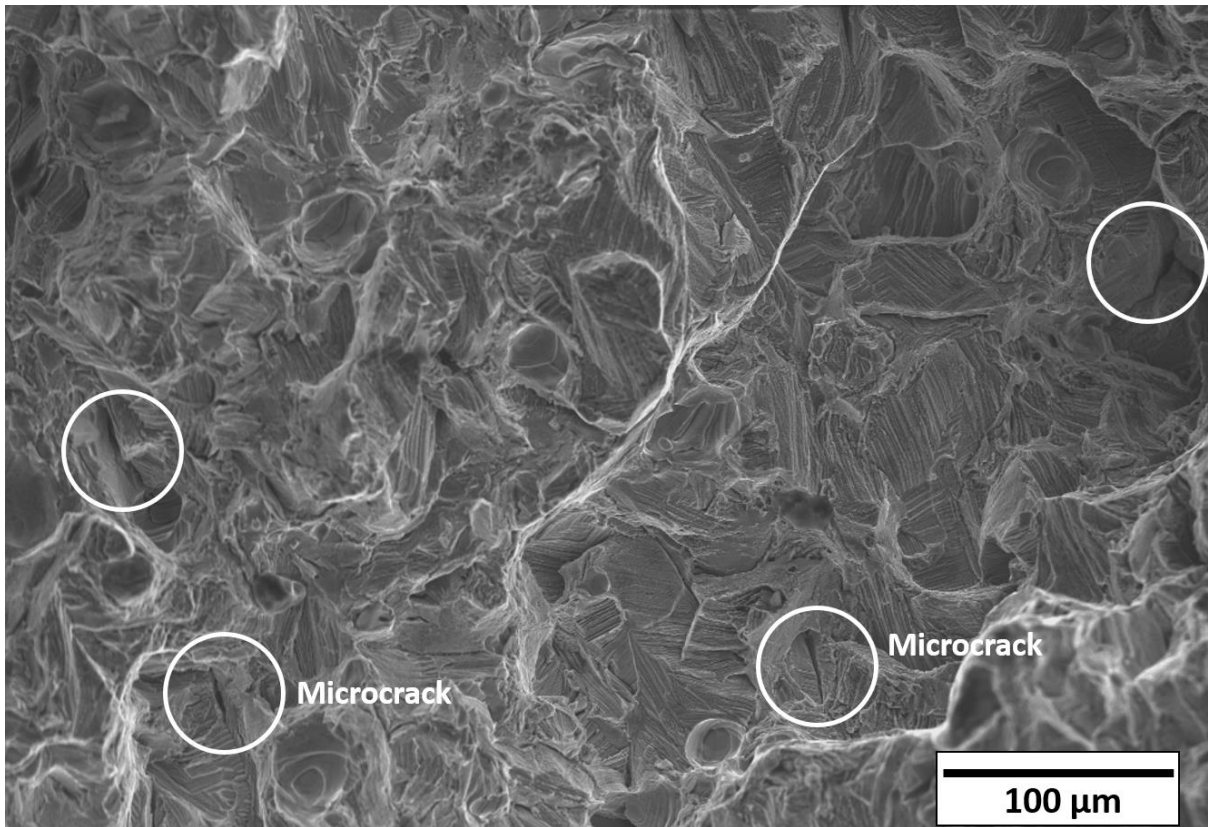


Figure 8.4 – SE mode SEM micrograph of fracture surface of Inconel 713LC as processed tensile specimen tested at room temperature. Micro-cracks are labelled and/or highlighted by white rings.

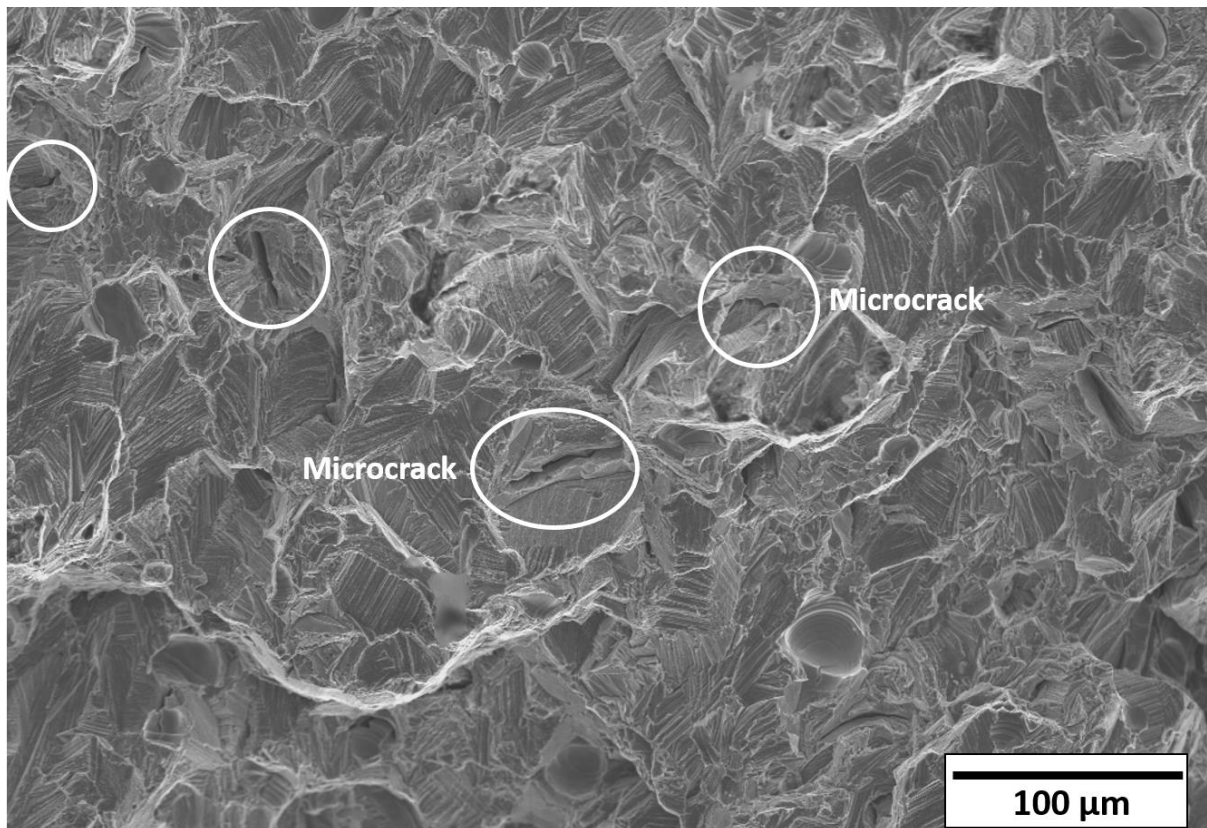


Figure 8.5 – SE mode SEM micrograph of fracture surface of Inconel 713LC as processed tensile specimen tested at 760°C. As expected the fracture surfaces support a brittle fracture, but there is also evidence of pitting implying some amount of deformation had occurred before failure.

Arguably, the tensile testing for this case is not representative of the materials inherent tensile strength, given the high number of crack initiation points already present within the samples. Hardness testing provides an alternative measurement of material mechanical properties; however, it is not an indication of fracture toughness. Testing was performed for $H_v0.5$ with a dwell time of 10 seconds. $H_v0.5$ hardness for Inconel 713 LC was measured as 320.6 ± 23 , which is significantly higher than that for OHX and MHX, however it is in line with the as-cast material (CES Edupack 2015). Consideration of the hardness result and fracture surfaces, lead to the conclusion that the SLM as processed Inconel 713 LC is similar to conventionally manufactured Inconel 713 LC in that it has high tensile strength but low ductility, with a high elastic modulus – ultimately giving it a low fracture toughness.

Mechanical testing aside, Inconel 713 LC clearly suffers from severe process induced micro-cracking which supports the crack susceptibility predictions. However, in this case thermal stress is the more significant factor.

8.3 Validation experiment: Novel alloys

Although the results from the Inconel 713 LC trial provide a level of validation for the crack susceptibility hypothesis, it is accepted that the difference in composition between Hastelloy X and Inconel 713 LC may allow for other compositional dependent effects. In order to gain confidence in the hypothesis, a repeat of the OHX-MHX comparison is required, but with a greater focus on the difference in solid solution contribution. That way, potential additional effects on crack susceptibility, such as increased ductility, can be confidently neglected.

To achieve this, two alloy compositions were designed. Based on the Hastelloy X composition, the only designed difference would be the Mo and W content. Unlike MHX, there would be no intentional reduction of residuals. Also, unlike MHX, the alloys would not be within the specification range of Hastelloy X as the Mo and W contents would be exaggerated in order to better identify the materials response. The two alloys are simply identified as High Solid Solution (SS) and Low SS, and were designed using a solid solution contribution predicting spreadsheet which was developed from Equation 6.3. The designed compositions of High SS and Low SS are detailed in Table 8.5, along with their predicted solid solution contribution values.

Alloy	Ni	Fe	Cr	Mo	W	Co	Mn	Si	C	σ_{ss} (MPa)
High SS	50.35	15	20	10	2	2	0.3	0.3	0.05	322.1
Low SS	50.35	18.5	23	5	0.6	2	0.3	0.3	0.05	263.3

Table 8.5 - Designed alloy compositions with predicted solid solution contribution

The two alloys were then fabricated using arc melting and processed into powder using a ball mill. The powders were then processed by SLM and compared for crack density. Details of the fabrication and processing are given in the following sub sections.

8.3.1 Fabrication: Arc melted casting and ball milling

Unfortunately, due to the high cost of gas atomisation, novel alloy production had to be conducted in house using casting methods available. Arc melt casting is a technique often used when one wants to create small quantities of alloy with minimal oxidation or contamination risk. High currents are passed from a cathode (in this case made from tungsten) into material which is contained with a water cooled copper mould. The arc formed between the tip of the cathode and the material (separated by a distance of ~ 10 mm) as the current passes, gives the process its name. Once the current is suspended, the molten material is rapidly quenched, ensuring the resultant bulk material has minimum segregation. The process is conducted in low oxygen content argon atmosphere to minimise oxidation.

Bulk metals/elements of commercial purity were measured out according to the wt% required, to total a 100 g sample for each alloy. The elemental mix for each alloy was melted and cast as one single ingot, and was flipped and remelted 4 times to ensure homogeneity of the final alloy.

The resulting ingots were approximately 40mm in diameter and 10 mm in depth. The next planned step was to process the bulk alloy into powder by means of attrition using a ball mill. The equipment used in this investigation was a Retsch PM100 Planetary ball mill, with a hardened steel grinding 500 ml jar, which was of sufficient hardness for processing a nickel base superalloy. After consultation with Retsch on the appropriate

grinding medium to be used, 300 10mm diameter hardened steel grinding balls were acquired. The advised size of feed stock was quoted as $<1/3$ of the volume of the grinding balls, which meant the alloy had to be in pieces of no more than 3mm in any dimension.

The ingots could have been successively sectioned; however, this would have resulted in large material loss. Instead the ingots were sectioned into quarters, and then rolled to a thickness of 1 mm. The surfaces were then ground with P1200 silicon carbide grit paper to remove any contamination. The flattened 'discs' were then thin enough to be guillotined into the appropriate size.

Ball milling was attempted on the alloys in the 3mm form, however after considerable time and many attempts, it became clear that the piece size was still too large and attrition would not be achievable. Attrition of the alloys would be difficult regardless of size as the high fracture toughness and good ductility inherent with nickel base alloys mean the material is more susceptible to deformation than fracturing. As such, a high volume of grinding medium is required (300 grinding balls) to induce a grinding regime, as opposed to an impact regime which occurs with freer particle movement. Despite the measures taken, the sample size was still too large.

Case studies by Restch demonstrated fcc Fe alloys could be successfully processed when in foil form. It was decided therefore that the alloys would be melted and recast as ribbon, using the melt spinning technique. This was performed on the custom built melt spinner located in house at the Department of Materials Science and Engineering. Figure 8.6 shows a representation of the melt spinning process. Material is placed within a silica crucible with a 0.5 mm opening at the tip, which is placed within an induction coil. The material is then heated until it is observed to be molten, at which point it is discharged onto a spinning copper wheel, upon which it rapidly solidifies in the form of ribbons.

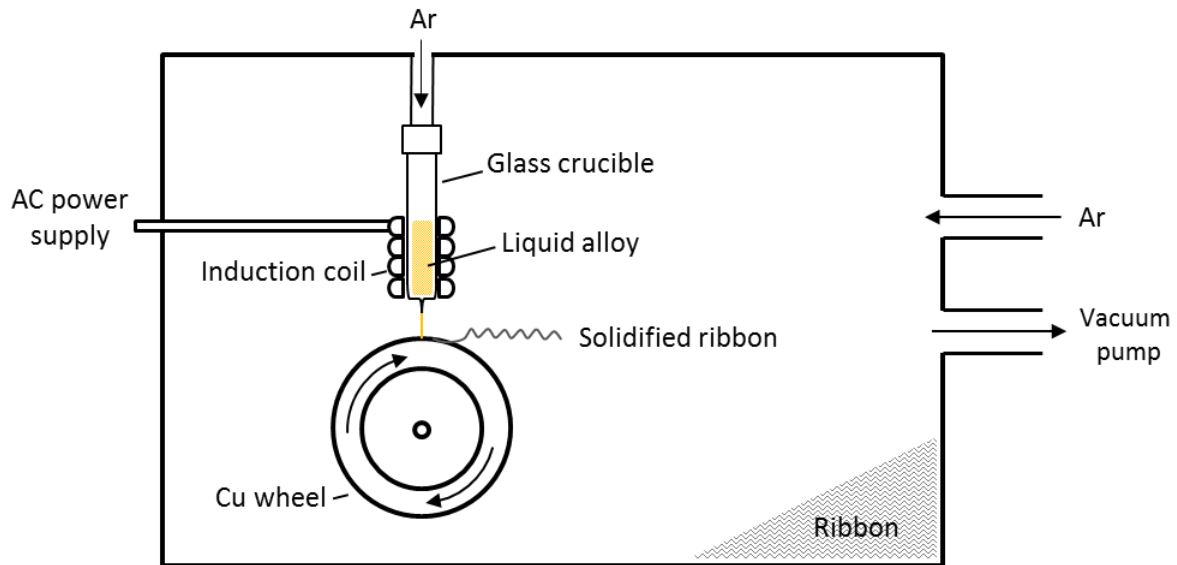


Figure 8.6 - Schematic of melt spinner

Before melting is conducted, the chamber is evacuated down to a pressure of 5×10^{-5} Torr, after which it is flooded with argon to a pressure of 15 psi to provide an inert atmosphere. Melt discharge is achieved by connecting the crucible to a pressurised argon source, which not only acts to force the material out of the crucible, but does so under an inert atmosphere.

A voltage of 700 V was used and the wheel was spun up to 2500 rpm. The crucibles held approximately 25 g of material, therefore each run produced approximately 25 g of ribbon. A total of two runs for each alloy were conducted, giving approximately 50g of ribbon for each alloy.

From the microstructure selection map of rapid solidification (Figure 4.6) it is noted that solidification rates and microstructure regimes of melting spinning and laser processing are very similar. Therefore, the chemical distribution is expected to be close to homogenous and there will be minimal segregation within the ribbons microstructure, and likewise the milled powder.

Once sufficient ribbon had been produced, it was processed with the ball mill. Parameters for most efficient attrition were determined to be 200 RPM for 15 minutes with 10 minute cool down periods between each run. After each run, the full content of the grind jar was emptied into a coarse sieve held over 150 μm sieve and agitated. Particles which passed through the 150 μm sieve was removed and stored, all remaining material was placed back into the grinding jar and the process was repeated. Once all the particles were $<150 \mu\text{m}$ in size, the same process was repeated but with a 53 μm sieve. The ultimate result being powder $< 53\mu\text{m}$ in size. This powder was then of an appropriate size to be processed on the Renishaw SLM125.

Before SLM processing, the powder was analysed for morphology, size and most importantly final chemical composition. The results of characterisation are displayed Table 8.6 and Figure 8.7. Chemical testing was performed by AMG Analytical of AMG Superalloys UK Ltd by Inductively-Coupled Plasma Optical Emission Spectroscopy (ICP-OES) for all elements apart from O, N and H. O, N and H analysis was conducted by Inert Gas Fusion (IGF) at LPW Technology Ltd.

Element	High SS		Low SS	
	Design	Actual	Design	Actual
Ni	50.36	47.28	50.36	48.04
Cr	20.00	19.46	23.00	21.24
Fe	15.00	16.28	18.50	19.42
Mo	10.00	9.34	5.01	5.32
W	2.03	1.78	0.50	0.63
Co	2.00	2.09	2.00	1.92
Si	0.30	0.6	0.30	0.42
Mn	0.30	0.26	0.30	0.36
C	0.05	0.23	0.05	0.21
Al	0	0.22	0	0.14
Ti	0	0.32	0	0.40
B	0	<0.02	0	<0.02
Cu	0	0.08	0	0.04
Nb	0	0.03	0	0.03
P	0	0.006	0	0.008
Sn	0	0.02	0	0.03
Ta	0	0.02	0	<0.02
V	0	0.02	0	0.03
O ^{1,2}	0	2.31	0	2.46
N ¹	0	0.0132	0	0.0166
H ¹	0	0.0124	0	0.0189
Predicted σ_{ss}	322.1	331.3	263.6	285.3

¹Chemical analysis performed by IGF on LECO ONH836

²Values not considered fully accurate as addition pushes total wt% >100

Table 8.6 – Designed and actual composition of the two low SSS and high SSS alloys fabricated by arc melting-ball milling

From Table 8.6 it is observed that although there are some exceptions, in general the designed composition was realised in the final composition of the powder. Of importance for the SSS contribution is that the Mo and W contents of each alloy were close to that of the contents input at the elemental stage (arc melting). It was expected that even with the relatively clean process of arc melting, that there would be some amount of residual contamination picked up. Potential sources of the copper contamination are from either the copper crucibles of the arc melter, or the copper wheel from the melt spinner. However, it is not deemed as a concern as both values are lower than those for the

commercial OHX and MHX alloys (0.45 and 0.01 wt% respectively). Phosphorus is also relatively low, and comparable to OHX and MHX (0.014 and 0.006 wt% respectively).

The apparent additions of Al and Ti are more difficult to explain, particularly as both are of a similar and significant magnitude. The implication is that they were contained within one of the elemental additions, even though all were identified as commercially pure. As noted in Table 8.6 the recorded oxygen content is not recognised as being accurate. Although a high oxygen content was expected, the addition of O, N and H pushes total wt% values for both alloys beyond 100 by nearly 1wt%. ICP-OES is generally accepted as being highly accurate and AMG Analytical are a NASCAP accredited laboratory, therefore it is assumed IGF results are more likely to be inaccurate. For the purposes of discussion, the oxygen content of both alloys will be assumed to be <1%.

The deviation considered most significant to crack susceptibility is the increase of carbon content from the input values of 0.05 wt% up to measured values of 0.2 wt%. This is significantly beyond what was input at the elemental stage, and the limit for most nickel superalloys (0.15 wt%). Beyond 0.15 wt%, the formation of carbides, and with it the susceptibility to DDC cracking, increases (Lippold, Kiser et al. 2011). Although both alloys have the same content of carbon, it has the potential to affect the material response in a way other than through control of solid solution strength. This is unfortunate as this scenario was intended to be avoided by the arc melting process, and time constraints meant that it was not possible to repeat process from elemental stage.

As a consequence of the variations of elemental composition, the predicted SSS contribution also changed. With the high carbon content having the greatest effect, increasing both predicted values by 21.7 MPa and 9.2 MPa for Low SS and High SS

respectively. A significant difference in σ_{ss} still remained however, and therefore its effect on crack susceptibility could still be investigated.

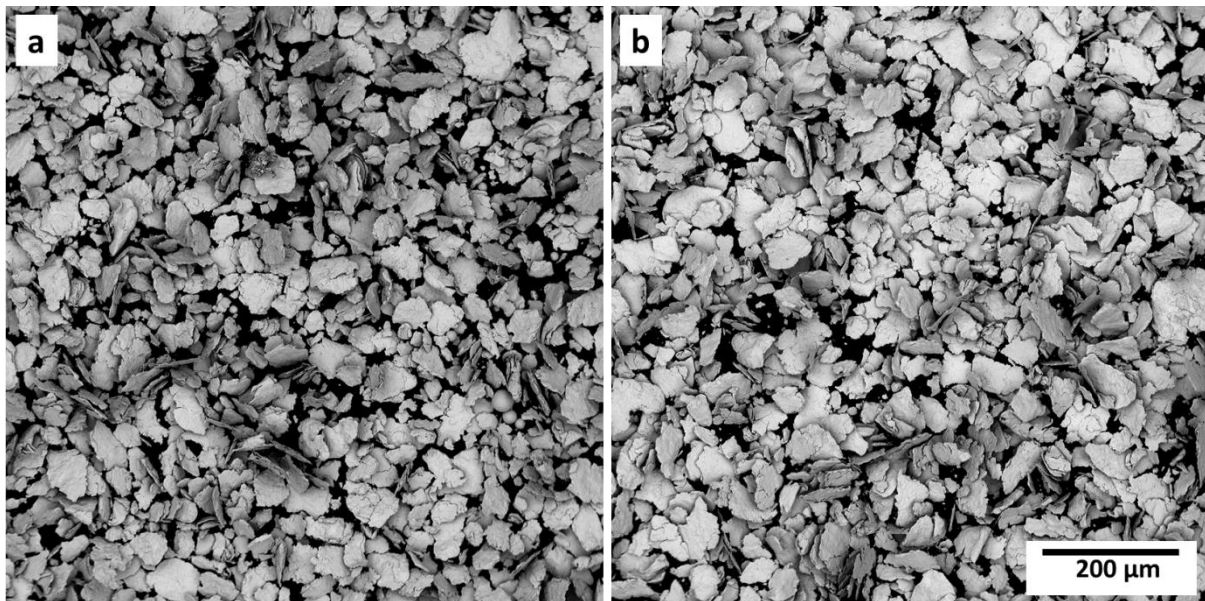


Figure 8.7 – SE mode SEM micrographs of alloys after ball milling. a) Low SS alloy and b) High SS alloy

In order to compare the resultant powder from ball milling to that of conventionally manufactured powder (gas atomisation or plasma spheroidisation), SEM micrographs were taken of the material, see Figure 8.7. It was observed that the powder was in fact in flake form, as opposed to the conventional spherical morphology. The flakes were between 20-75 μm in size, with D50 values of 52 μm and 54 μm for Low SS and High SS respectively. It was perceived the flake would likely have a lower packing fraction than commercial powder, partly because of shape but also because of the observed narrower size distribution. Spheroidisation with the ball mill was not achievable for this material because of the high fracture toughness, and further processing would only have resulted in finer particle size.

8.3.2 Model predictions

Using the σ_{SS} values of the ball milled powder, combined with α_{CTE} values determined by simulation on Thermo-Calc 2015b using the composition of the ball milled powders detailed in Table 8.6, crack susceptibility values were calculated for High SS and Low SS. Table 8.7 details the key values for the calculation.

Alloy	σ_{SS} (MPa)	α_{CTE} (25-100°C)	E (GPa)	σ_{th} (MPa)	χ
High SSS	331	11.0×10^{-6}	170	935	0.35
Low SSS	285	12.2×10^{-6}	170	1037	0.28

Table 8.7 - Key crack susceptibility calculation components of High and Low SS alloys

Young's modulus was chosen to be the same for both alloys, with a value similar to that of MHX. This was the most logical value given the unintentional alloying additions and that the alloys are still closest to Hastelloy X in primary alloying elements. Interestingly High SS is simulated to have a significantly lower thermal expansion as well as the expected superior SSS contribution; the combination of which yields a clear difference in the predicted χ for the two alloys.

8.3.3 SLM processing methodology

Given the small volume of powder created, it was not possible to process the powder by the conventional method on the Renishaw SLM125. Full coating of the standard 125x125mm substrate alone would likely use up the majority of the powder. To navigate this problem, a smaller substrate was designed and fabricated. The design and placement of the small substrate is displayed in Figure 8.8.

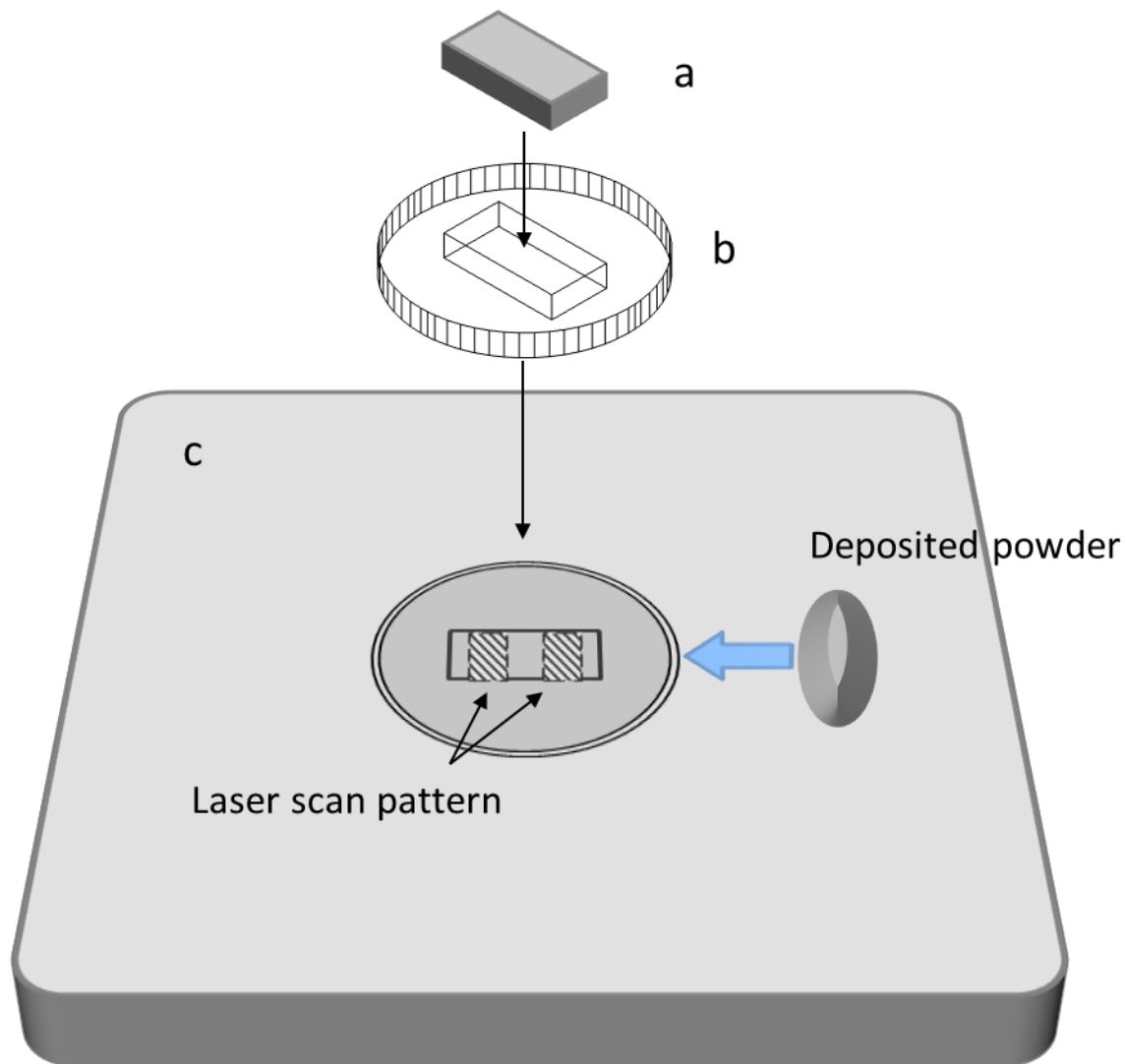


Figure 8.8 - Diagram of modified substrate for novel alloy fabrication

The substrate rig consists of three parts. The first (c) is an aluminium substrate of the standard 125mm dimensions. Within this a circular section of diameter 40 mm and depth 5 mm is cut out. Second (b) is a disk of just under 40 mm in diameter (to allow for easy inert and removal) and 5 mm depth, with a 10×20 mm section cut out of the centre. The final part (a) is that which is actually built upon. This is a 10×20×5 mm steel rectangle that fits into the disk. The small size of the substrate allows for it to be directly mounted for metallurgical analysis without the need for wasteful sectioning. This was necessary as the parts would be built directly onto the substrate, without supports, and the thus the substrates would not be recoverable.

Powder deposition was performed manually. Powder was manually placed in front of the wiper blade, which was allowed to perform the standard layering action. Once the layer had been melted, and the wiper arm and substrate had returned to their start and subsequent positions (respectively), the machine was paused, and a new deposit of powder was placed in front of the wiper arm. In order to maintain the argon atmosphere and minimise the time between layers, manual deposition was performed using the gloves in the machine door. The time between each layer was approximately 4 minutes. This was not considered to affect the thermal history of the part too greatly as the typical time between each layer for conventional building is ~30 seconds, which is enough time to allow the part to cool below the diffusion limiting $0.5T_m$.

To maximise the height of the parts, layer thickness was set at 40 μm . The parts were built as 5x10x1 mm ribbons. The laser scan parameters were LP 180W, ET 125 μs , PD 50 μm and HS 90 μm with an additional part built with the same parameters bar hatch spacing, which was reduced to 60 μm . The reduced hatch spacing was employed in to ensure sufficient overlap, given that 40 micron layers had not be attempted with previous alloys to this point. Due to the unique process setup, MHX was processed in addition to the High SS and Low SS alloys, thereby ensuring a fair comparison between the novel and conventional alloy powders.

8.3.4 Results and discussion

Composite images of the entire cross section of the 90 μm hatch spacing ribbons for all three alloys are shown in Figure 8.9. Note the difference in achieved build height between the ball-milled powder samples and the commercially fabricated MHX powder. This is attributed to the low packing density of the ball mill powder, resulting in layer shrinkage and therefore lower overall build height. This does make direct comparisons between the

MHX powder more difficult, as clearly the material in the ball-milled samples will have been remelted more often per unit height than the MHX powder, resulting in a difference in absorbed energy per unit volume. This will likely affect the cracking within the part but is not of great concern, as the role of MHX was to ensure the thin ribbon method still yielded micro-cracks in conventional material; this role has therefore been fulfilled.

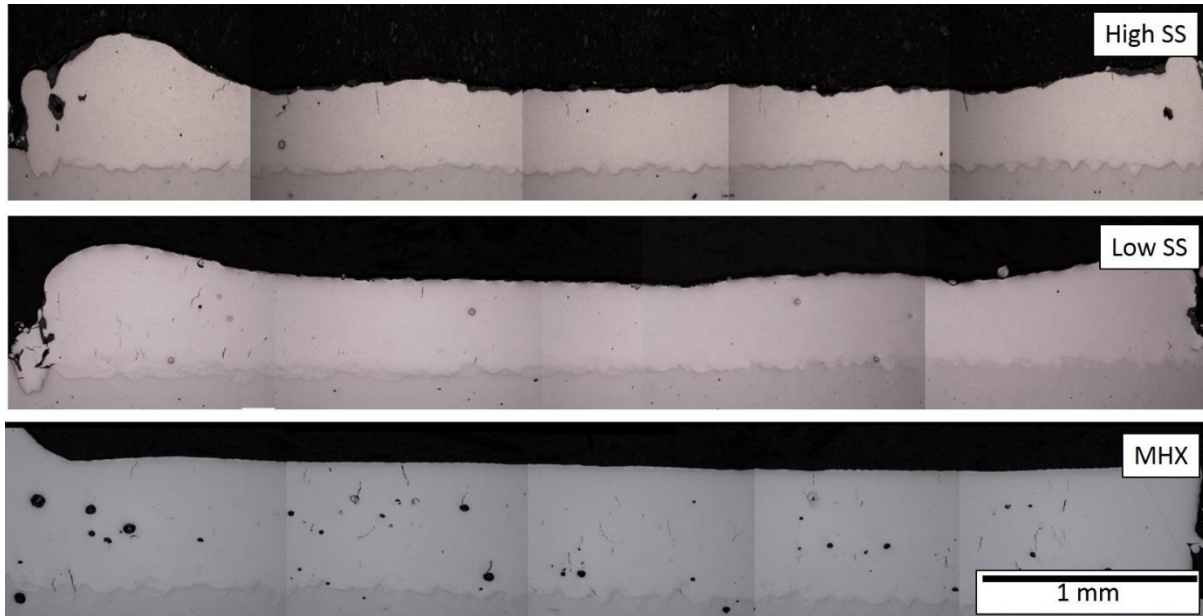


Figure 8.9 - Full cross sections of SLM processed ball milled powders and MHX powder

The density of all three ribbons is above the 99.5% limit for full density, although the full layering in MHX has resulted in a slightly increase porosity. Figure 8.9 is purely for whole part comparison and the resolution is not sufficient for surface analysis; crack density analysis was conducted on the individual micrographs as with previous trials. Crack densities for the three powders are given in Table 8.8, with examples of the individual micrographs in Figure 8.10.

Alloy	Low SS	High SS	MHX
HS 90 μm	21.6 \pm 6.1	7.5 \pm 2.4	20 \pm 1.5
HS 60 μm	8.4 \pm 2.0	3.8 \pm 1.7	15 \pm 2.0

Table 8.8 - Crack density (per mm^2) for the three alloys for both 0.06 and 0.09 μm hatch spacings

Although in the composite images in Figure 8.9 it appears as if the High SS alloy has a higher crack density, it is in fact Low SS alloy that has cracked more severely. This is merely because at full resolution, finer cracks are observable in the low SSS alloy sample, see Figure 8.10. High SS displayed several large cracks across the top of the sample, however the low SS sample had cracks throughout, of varying sizes. It is observed that cracking was more severe in areas adjacent to vertical edges, as observed and noted in Chapter 3. MHX had crack densities comparable to the Low SS alloy, although this likely due to reduced energy absorbed per unit volume.

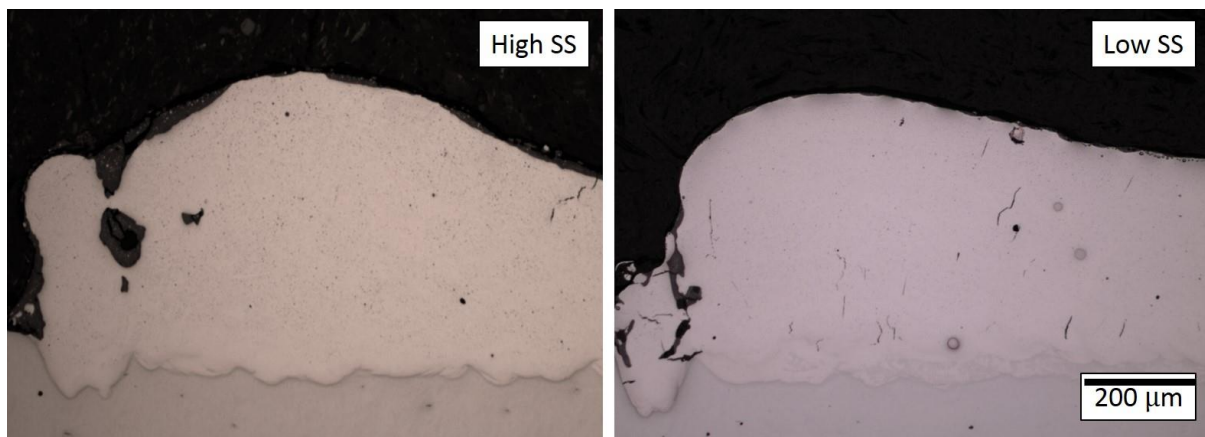


Figure 8.10 - Comparison of micro-cracking between high and low SSS

There is a significant reduction in cracking for the samples built with a 60 μm hatch spacing, for all three alloys, over those built with 90 μm . This is in agreement with the proposed cracking mechanism of ETSS, as the reduced hatch spacing results in greater melt track overlap therefore increased annealing and reduced thermal stress.

In the absence of enough material to build tensile specimens, hardness measurements were made on the polished surfaces of the microstructural analysis samples. Although no quantitative comparison can be made between tensile strength and the predicted solid strength contributions, hardness values are representative of a materials tensile strength. Hardness measurements were performed on an I9 Vickers Hardness system, for HV0.5

with a dwell time of 10 seconds. 10 measurements were taken along the length of cross section of each sample. Table 8.9 displays the hardness results.

Alloy	HV0.5
MHX	254.1 ± 3.17
Low SS	258.3 ± 3.16
High SS	299.1 ± 3.16

Table 8.9 - Hardness values for novel alloys and MHX

The High SS alloy displays a significantly higher hardness than both MHX and the Low SS, both of which are statistically similar. This is particularly interesting when hardness results are compared against the cracking results, where MHX and Low SS also had similar crack densities. All display the same level of variation, supporting that the High SS value is not an anomalous result.

8.3.5 Conclusions

The control sample of MHX, demonstrated the low build height ribbons were still representative of standard SLM processing, although the increased layer thickness (from 20µm to 40µm) had resulted in increased cracking when compared to the trials in Chapter 6.

The arc-melting-ball milling method for novel alloy powder production has shown promise, however there are still aspects which require refinement if it is to be considered in further investigations. The difference in processing between flake and spherical powder has also been observed, indicating that powder morphology may be an additional factor to micro-cracking of material during SLM processing.

The observed relationships between both chemical composition and hatch spacing with crack density are in agreement the primary hypotheses of this work. The designed increase in solid solution strength of the High SS alloy has resulted in a reduction in

cracking against a version of the same alloy base with lower SSS. This result is in agreement with the relationship observed between OHX and MHX in Chapter 6, and together both support the hypothesis of solid solution strengthening being a primary influencing factor for crack susceptibility of nickel base superalloys with SLM processing.

8.4 Crack susceptibility predictor: Discussion and Summary

8.4.1 Additional alloys and validation comparison

Results from the Hastelloy X, Inconel 713LC and novel alloy experimental investigations have all supported the crack susceptibility model, however they represent a limited range of alloys. In order to establish the range of applicability, more validation data from a larger range of alloys is required.

Given that the predictions can only be validated by experimental data, the number of alloys was still limited to those for which publicly accessible SLM processed data exists, i.e. published investigations on the processing of that alloy by SLM. For the majority of cases the composition, microstructure and mechanical properties of the as processed alloys are reported. However, sometimes only nominal compositions are reported (rather than the actual composition of the powder used) and for one alloy the key mechanical property, Young's modulus was not reported. In these cases, literature values for conventionally manufactured material were used. Additionally, the majority of investigations did not report the co-efficient of thermal expansion for the as processed state, however as previously discussed in *this* work, the co-efficient of thermal expansion does not significantly vary for SLM processed compared to conventionally manufactured material; or minor alterations to composition.

In order to assess the impact of using data for conventionally manufactured material, instead of SLM processed material, a second plot was created. On this plot, data for conventionally manufactured material was used in the crack susceptibility model, with the nominal composition stated being used to calculate the SSS contribution.

The two sets of crack susceptibility values were then plotted separately – Figure 8.11 is for SLM as processed data, Figure 8.12 is for book value data.

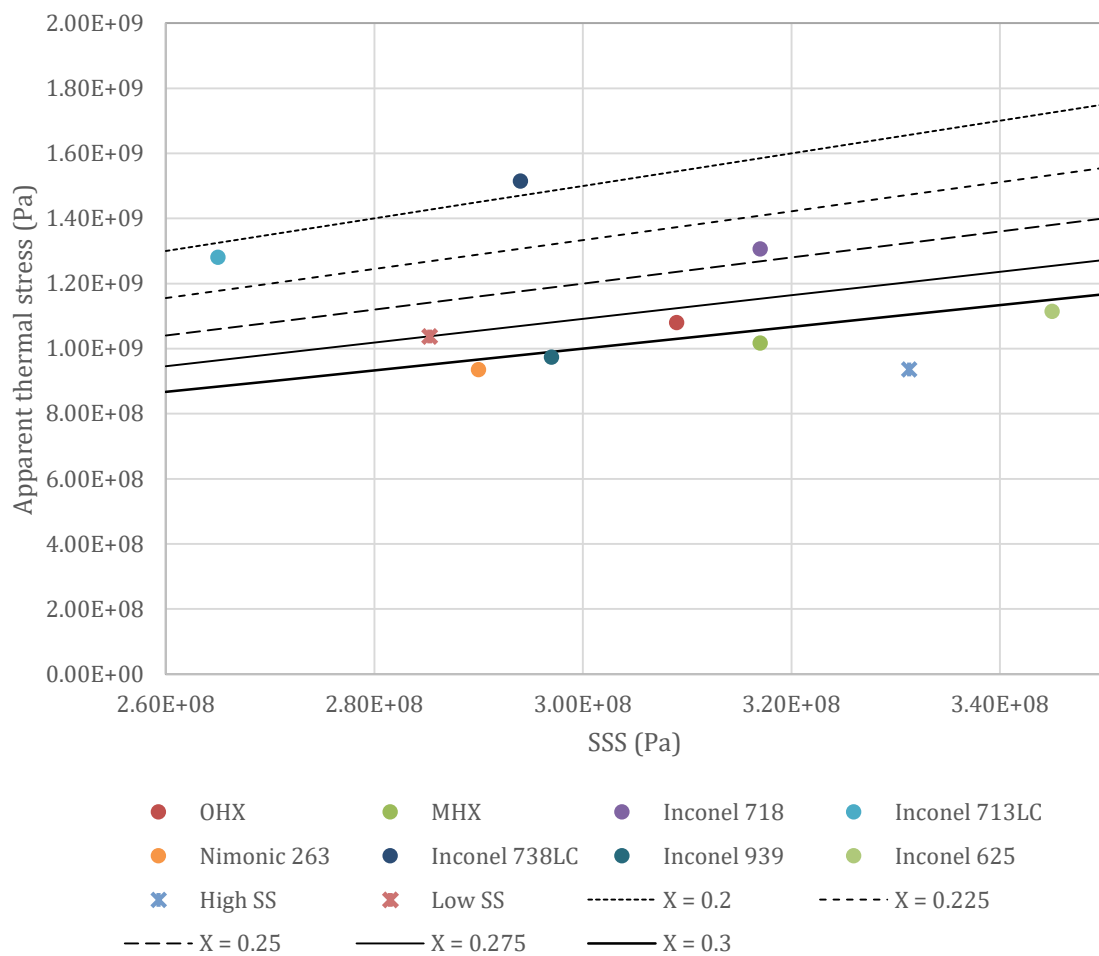


Figure 8.11 - Crack susceptibility of alloys based on SLM as processed properties

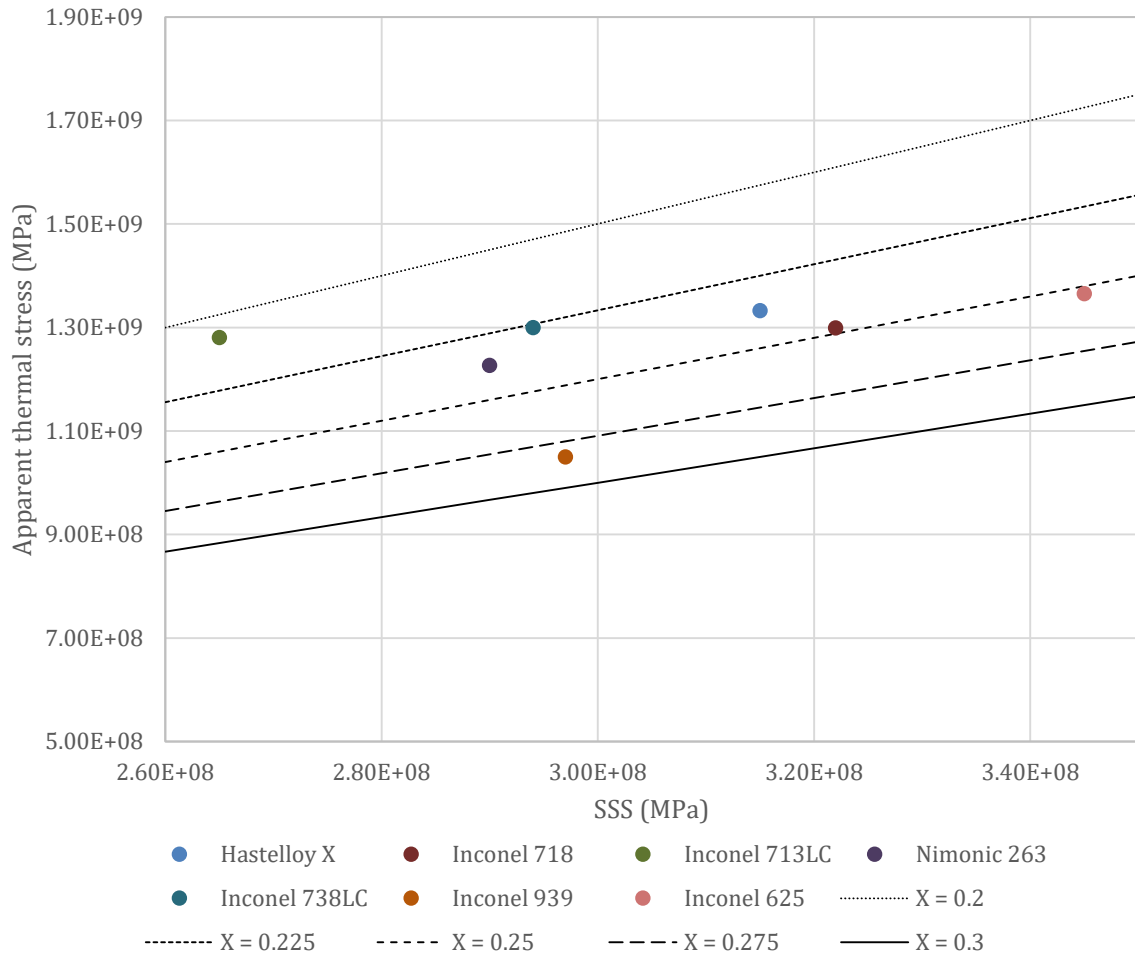


Figure 8.12 - Crack susceptibility of alloys based on conventionally processed properties

Table 8.10 gives the crack susceptibility values of the two sets of data along with the reported process cracking behaviour of that alloy.

Alloy	σ_{ss} (MPa)	σ_{th} – SLM ⁷	χ – SLM	Σ_{app-th} – conv. ⁷	χ – conv.	Observed\reported
Hastelloy X	307	1080 ¹	0.284 ¹	1333	0.236 ²	Medium crack density
OHX	309	1080	0.286	-	-	Medium crack density
MHX	317	1017	0.312	-	-	Low crack density
IN713 LC	265	1281	0.207	1281	0.207 ²	V. high crack density
IN738 LC	294	1515	0.194 ³	1300	0.226 ²	High crack density
IN718	317	1306	0.243 ⁴	1299	0.248 ²	No cracking reported
Nimonic 263	290	935	0.310 ^{5,2}	1227	0.236 ^{2,8}	No cracking reported
IN939	297	974	0.305 ⁶	1050	0.283 ^{2,8}	No cracking reported
IN625	345	1114	0.310	-	-	-
High SS	331	935	0.354 ⁹	-	-	Low crack density
Low SS	285	1037	0.275	-	-	Medium crack density

¹Composition and E from (Wang 2011)

²Properties and/or composition from (Donachie and Donachie 2002)

³Composition and E from (Rickenbacher 2013)

⁴Composition and E from (Wang, Guan et al. 2012)

⁵Composition and E from (Vilaro, Colin et al. 2012)

⁶Composition and E from (Kanagarajah, Brenne et al. 2013) and SLM Solutions IN939 Datasheet

⁷Thermal expansion data taken from CES Edupack 2015

⁸ E taken from CES Edupack 2015

⁹Composition and E from (Amato 2012)

Table 8.10 – Solid solution contribution, apparent thermal stress and crack susceptibility values for alloys with SLM as processed and conventional process ‘book’ properties. With observations from experimental investigations on micro-cracking severity.

Comparing the predictions from Figure 8.11 and Figure 8.12 and the observations stated in Table 8.10, both are in good agreement, with the exception of Inconel 718. Of note is also the relative significance of the apparent thermal stress, an example of which is Inconel 738LC; despite having a similar σ_{ss} to Inconel 939, the high σ_{app-th} value for 738LC gives it the lowest χ value of the group with 939 having among the highest. This ultimately supports the necessity for a thermal stress to be considered in the crack susceptibility predictions.

There is minor discrepancy between the predictions based on SLM properties and those of conventionally manufactured properties. Based on conventionally manufactured properties, the Hastelloy X alloys are predicted as having poorer crack susceptibility than

was observed (with respect to other alloys), however Inconel 713LC and Inconel 738LC predictions are closer to experimental observations (Rickenbacher 2013), compared to the SLM property derived predictions. The High SS and Low SS alloys from the novel alloy validation trials have been included with the SLM processed alloys, but are distinguished by an 'x' style marker. This is to highlight the fact that they were processed in modified manner compared to the other alloys – which must be taken into account when comparing on the plot. This is in part because from observations, the High SS still displayed cracking, but the cracking was less severe than for MHX when processed in the same manner. Taking this into account, its placement on the plot is in agreement with experimental observations, although indirectly.

As a final comparison, solid solution strength of the alloys was plotted against apparent thermal stress, for an elevated temperature of 760°C – see Figure 8.13. Due to an absence of data, values of Young's modulus and coefficient of thermal expansion for Inconel 718, Inconel 713LC, Inconel 939, Inconel 625 and Nimonic 263 were all estimated based on the values for alloys who had comparable properties at room temperature.

It is observed that the relationships are largely the same as those for the room temperature values, however there is one key difference. For room temperature conditions, MHX is predicted has having a marginally higher χ value, however at an elevated temperature the increase is significantly greater. The placement of MHX relative to other alloys has remained the same, rather it is OHX which has seen a comparative reduction. This result is therefore more representative of observations from the experimental section of this work, where MHX displays a 65% reduction in micro-cracking over OHX.

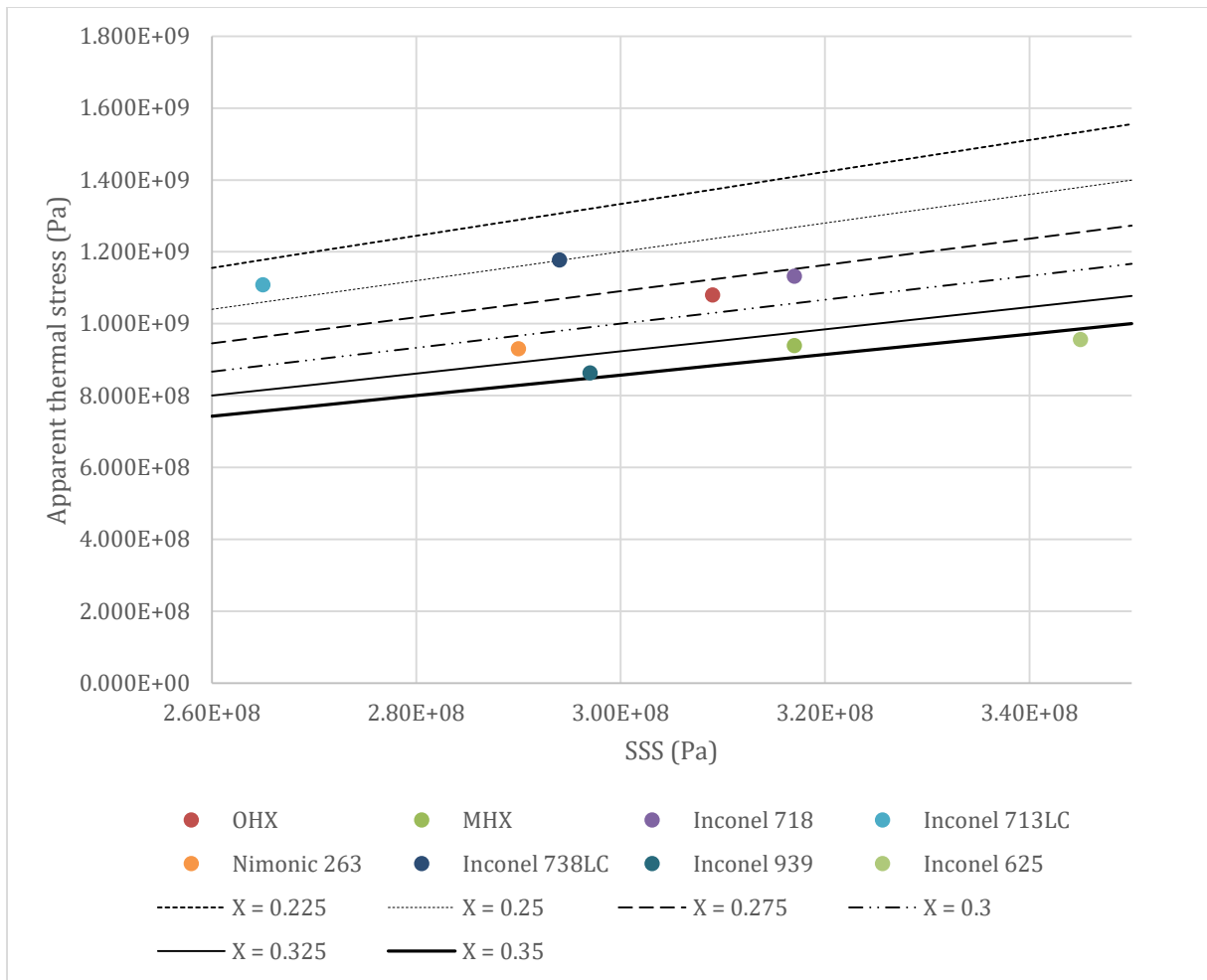


Figure 8.13 - Crack susceptibility of alloys based on SLM as processed properties at elevated temperatures

The SLM property derived predictions were expected to be in closer agreement with experimental observations, because the composition and mechanical properties were taken from the same work and the observations. However, the agreement of conventional manufactured, or book, derived predictions with observations may be considered more important.

The aim of the crack susceptibility predictor is to take composition and properties from an alloy, and be able to predict the crack susceptibility of that alloy before committing time and cost to processing it. It is therefore necessary that the predictor work effectively from nominal data alone.

Conversely, from an alloy design perspective, it is important that the crack susceptibility model is viable for SLM processed material.

8.4.2 Discussion of model effectiveness

It was stated in Chapter 7 that although the Lopez model aided in understanding of the thermal history of selective laser melted material, ultimately it could not be applied affectively for the crack susceptibility model. This is largely because of the strong influence of thermal expansion and Young's modulus in the thermal stress relationship, which render the small changes in a ΔT between two compositions of the same alloy base close to negligible. This was noted when performing the crack susceptibility calculations. When the thermal stress calculation is performed with base units, the Young's modulus has the greatest influence, because it of the highest magnitude. The ΔT value is 3 orders of magnitude less than the thermal expansion coefficient, and 6 less than Young's modulus.

However, when there is a significant difference between compositions, for example different alloy bases, it may prove useful to employ the Lopez model to ascertain the temperature range between the $0.5T_m$ and ambient temperature. For example, the ΔT of aluminium base alloys will be significantly lower than that for nickel, given that the majority have $T_m < 900\text{K}$, meaning $0.5T_m$ in the region of 450K.

As discussed in Section 8.4.1 the crack susceptibility predictor agreed well with experimental observations when using properties for both SLM processed material and conventionally manufactured material, for room temperature. Although there was some minor disparity between the two plots, the most obvious discrepancy was Inconel 718. On both plots Inconel 718 is predicted as have a comparable or higher crack susceptibility

than OHX, yet in published investigations no cracking has been reported (Amato, Gaytan et al. 2012, Wang, Guan et al. 2012).

Inconel 718 has a similar SSS contribution to Hastelloy X, however it has higher Young's modulus in both SLM as-processed and conventionally manufactured states. Wang, Guan et al. (2012) report the as-processed yield strength and UTS of Inconel 718 as 889-907 MPa and 1137-1148 MPa respectively. The as-processed tensile strength of Inconel 718 is therefore significantly greater than that for Hastelloy X - Wang (2011) reports a higher UTS of 936 MPa, than that of this investigation, which is still lower than Inconel 718 - despite the similar SSS contribution. An explanation for this may come from the observations of possible nano-precipitates, reported in Chapter 6. Amato, Gaytan et al. (2012) reports the presence of 50x 250 nm ellipsoidal precipitates of γ'' Ni₃Nb - the strengthening phase in Inconel 718 - coherent with the Ni-Cr matrix and orientated with the [100] crystal structure. The precipitates appear to be 'stacked' in a frequency and spacing which coincides with the succession of melt pools during the epitaxial growth of the crystals. Although Amato admits the XRD chemical evidence is not completely unambiguous, these observations may explain the high mechanical properties of as-processed Inconel 718. The γ'' phase forms between 705-900°C, and importantly can form over time scales of 10s of minutes over the temperature range - see Figure 8.14. It is therefore not unreasonable to expect that the cyclic heating of underlying layers, from the laser interactions above, will be sufficient to allow for the formation and growth of precipitates in regions where (the limited) segregation has occurred, i.e. melt traces. The observation that the precipitates were coherent with matrix, leads to the prediction that they will still act to pin and inhibit the movement of dislocations and improve the tensile strength of the bulk material.

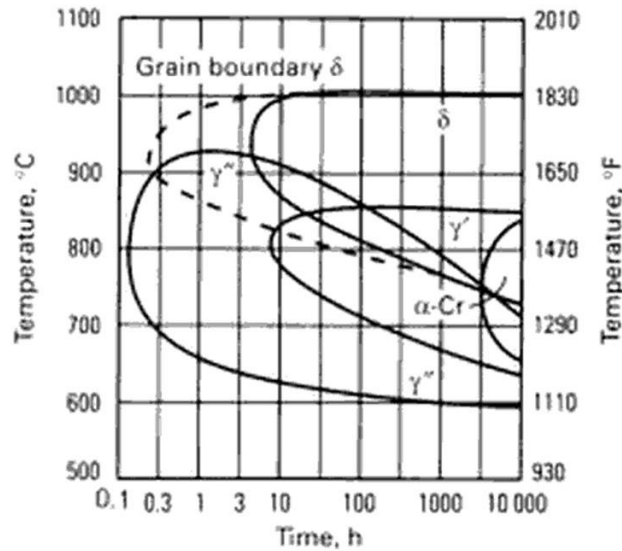


Figure 8.14 - Transformation diagram for γ' and γ'' phases in Inconel 718 - direct from (Davis 1997)

In alloys such as Inconel 713LC or 738LC, the primary strengthening phase is γ' $\text{Ni}_3(\text{Al,Ti})$. From Figure 8.14 it is observed that γ' forms over a narrower temperature range, and critically requires time frames of 10+ hours for transformation. This difference in transformation temperatures and times may explain why precipitates of γ' have not been observed in Inconel 713 or other γ' strengthened alloys, and why they display relatively lower as-processed tensile properties with respect to Inconel 718 (Vilaro, Colin et al. 2012, Kanagarajah, Brenne et al. 2013, Rickenbacher 2013). Hastelloy X does not have any precipitate phases, and although suspected secondary phases were observed, they were significantly smaller than those from (Amato, Gaytan et al. 2012) and located in the interdendritic regions.

The formation of micro-nano precipitates will be strongly influenced by the laser scan parameters used in processing. If laser exposure is extensive, this will allow for the material to be held at higher temperatures for longer, thereby encouraging the precipitation or growth of secondary phases - not least because solute diffusion will also

increase. As with a lot of comparisons between work in literature, care must be taken in drawing conclusions from the few examples that are present.

The reported presence of coherent γ'' precipitates in SLM as-processed Inconel 718 microstructure aligns with the respectively high tensile strength. In turn this could also explain why Inconel 718 does not appear to suffer from process induced micro-cracking, in that the increased strength the as-processed microstructure (compared to if it were purely the γ matrix in solid solution) provides sufficient resistance to thermal stress and the consequential stress-rupture.

The availability of data for elevated temperatures is likely to improve the accuracy of the predictions. It was demonstrated that when the data was available, the model was in better agreement with experimental observations. This is not unexpected, given that it is micro-crack formation likely occurs at elevated temperatures, in the solid material just below the melt layer.

In conclusion, the crack susceptibility predictor is able to predict the likelihood of micro-crack formation during SLM processing, based on composition, thermal expansion and elastic modulus only. The model is most accurate for solid solution or γ' precipitation strengthened nickel alloys, although the anomaly with γ'' strengthened Inconel 718 can be attributed to formation of said precipitates during SLM processing.

Finally, it is noted that alignment of predictions and empirical data is expected to be dependent on the processing conditions, particularly for cases when extreme processing conditions are implemented. The examples from the ball milled material demonstrate that differences in both processing methodology and powder morphology are still significant factors in the formation of micro-cracks during SLM processing.

8.5 Low crack design model

The low crack design model is an inversion of the crack susceptibility predictor. It will enable the design of low crack susceptibility alloys based on the established desirable properties from Section 8.4. Regrettably, time constraints on this investigation meant that this stage of the project could not be fully realised. Fortunately, however, it is to be included as part of a successive project by Harrison. As a result, this section will discuss only the initial plan and considerations of the model.

8.5.1 Model plan

Figure 8.15 demonstrates the model step by means of a flow diagram. The main inputs for the model are alloy base, additional alloying elements (with ranges where applicable) and the desired crack susceptibility value χ . Once a set of elements is chosen, an initial composition is generated using the minimum values of each range, with the remainder added to the nickel content. The solid solution contribution and thermal stress contribution are then calculated from this composition and the ratio between the two is put through a simple 'if' statement. If the ratio is greater than the chosen χ value, the composition is published, if not, the concentration of final element is increased by a chosen increment and the loop is performed again. The number of increments can be altered but is initially set at 10 per element; therefore, the size of each increment is the range divided by 10. The loops continue, cycling through each element until every possible combination has been processed. For an 8 element alloy (Ni + 7 alloying) this would therefore take a maximum of 10^8 calculations. It is proposed that if 10 or more combinations yield a χ greater than the input value, this will initiate a dialogue box ask if

the user wishes to continue. The user can then either choose to continue or alter in the initial elemental ranges.

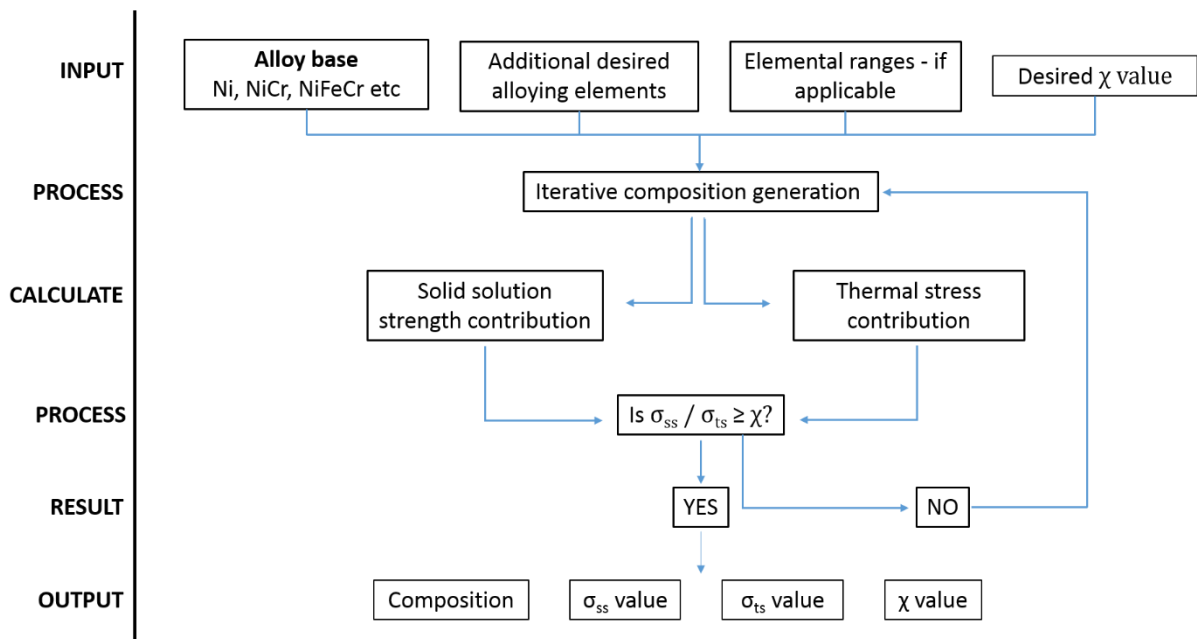


Figure 8.15 - Basic design model flow chart

8.5.2 Input and additional model considerations

Ultimately the purpose of this design model is to produce compositions which do not crack when processed by SLM. However, the operational properties of the alloy are the most important, and therefore allowances have to be made for alloying elements which may not be beneficial to the crack susceptibility rubric, e.g. Co for precipitation modifications. This is extended by allowing the input of limits for certain alloys, based on known beneficial effects, e.g. 10-20% wt Cr content to ensure corrosion resistance.

The choice to input a target χ value is to allow for the inevitable variation of a machine platform's/scan strategy's influence on crack generation. Additionally, the user may have

knowledge that chosen elements will not yield an ultra-low crack susceptibility composition and instead are seeking for a best case composition.

The calculations for the solid solution contribution and thermal stress contribution will rely on additional data libraries. In the case of the solid solution contribution this will simply be the list of strengthening parameter values used in Chapter 6. For the thermal stress contribution it is more complicated, given that a similar (to the Gypen and Deruyttere (1977)) model does not currently exist for Young's modulus. Thermal expansion can be calculated using Thermo-Calc: although not ideal, a macro can be written so that the software performs iterative calculations of varying composition. It may prove more efficient to generate a dataset of lower resolution from which approximate values of thermal expansion can be extracted. However, this would have to be trialled first to be validated.

Ideally the design model would be developed into a dedicated software, which could then accommodate more complex/additional requirements making it more applicable for end users. It is hoped that this will be realised in future projects.

8.6 Chapter Summary

The development of a thermal stress contribution in Chapter 7, allowed for the completion and validation of the crack susceptibility model in full. Although some level of validation had been completed in Chapter 6, for OHX and MHX, further validation was required.

A combination of performing additional experiments on established and novel alloys, and using data and information from published literature, allowed for the creation of several

crack susceptibility graphs, based on properties for SLM processed, conventionally processed, and elevated temperature conditions.

The predicted behaviours of the alloys agreed well with the observations from both this work and those found in literature. It was therefore concluded that the crack susceptibility model was a viable method for determining the susceptibility of a given nickel superalloy to SLM process induced micro-cracking.

9 Further considerations, summary and conclusions

In this final chapter, relevant articles which have been published since the initial considerations of the literature review, and during the latter stages of this investigation, are discussed. Further considerations either prompted by said articles, or results of this investigation form the final discussion of this work.

This is followed by summary of the main findings of the work conducted in this investigation, after which conclusions will be drawn on the individual aspects and investigation as a whole. As summaries were not written at the end of each chapter, they are separated into the respective areas.

9.1 Recent publications and further considerations

9.1.1 Recent publications

Cloots, Uggowitzer et al. (2016) investigated the mechanisms behind cracking of Inconel 738LC processed by SLM using both Gaussian and doughnut profiles. Rickenbacher (2013) had investigated the high temperature mechanical properties of Inconel 738LC processed by SLM, and noted that the alloy suffered from micro-cracking during processing. Cloots et al. cited Harrison, Todd et al. (2015) in the initial discussion, stating that the EDX method used to analyse the grain boundaries of SLM processes nickel for solute segregation, was not of a high enough resolution to be conclusive. Although the author stands by their comments, they concede that higher resolution techniques such as TEM are required to be completely confident of solute redistribution within the microstructure.

Rather than focussing on the lattice strength of the material, Cloots, Uggowitzer et al. (2016) state that the cause of the cracking is by means of thin liquid film remnant in the final stages of solidification i.e. solidification cracking. The qualification for this is by means of a rapid solidification thermophysical simulation of the liquid fraction with temperature – a software not dissimilar to Thermo-Calc used in this investigation. The results of the solidification simulation imply that zirconium diffuses significantly and increases in concentration up to near 28 wt% - with Ni making up the remainder - of the final liquid phase – Figure 9.1. Coupled with the Zr increase, a significant lowering of the solidus temperature of the alloy (in this phase) down to a remarkably low 682°C. The reason for this very low solidus temperature is not explained, and the result is simply accepted. Given that the melting point of Ni is 1455°C and Zr is 1855°C it is impossible that a phase of the two can still be liquid at 700°C, and therefore strange that this was not challenged/ further explained by the authors.

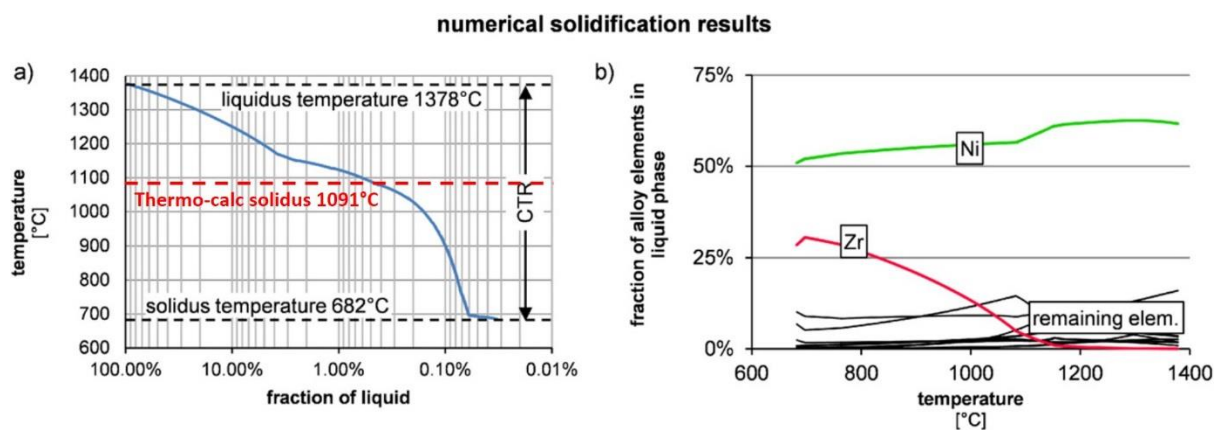


Figure 9.1 - Liquid fraction simulation of Inconel 738LC – modified from (Cloots, Uggowitzer et al. 2016). Red dotted line indicates solids temperature simulated by Thermo-Calc 2015.

For comparison, the exact composition of the Inconel 738LC used in the Cloots investigation was input into Thermo-Calc, and the same Schiell solidification model was performed. Figure 9.2 and Figure 9.4 show the results of the Thermo-Calc simulation. As can be seen in Figure 9.2, the model simulates a solidus temperature of 1091°C and, in

Figure 9.3 and Figure 9.4, a final Zr concentration of 2.6 wt%, all of which is far more in agreement with what would be expected. Additionally, comparing the Thermo-Calc with the simulation in Clouts, we see that both models are in agreement up to a specific point, at which Thermo-Calc simulates the final freezing of the alloy but the model used by Clouts continues on; to what is considered an unrealistically low solidus point.

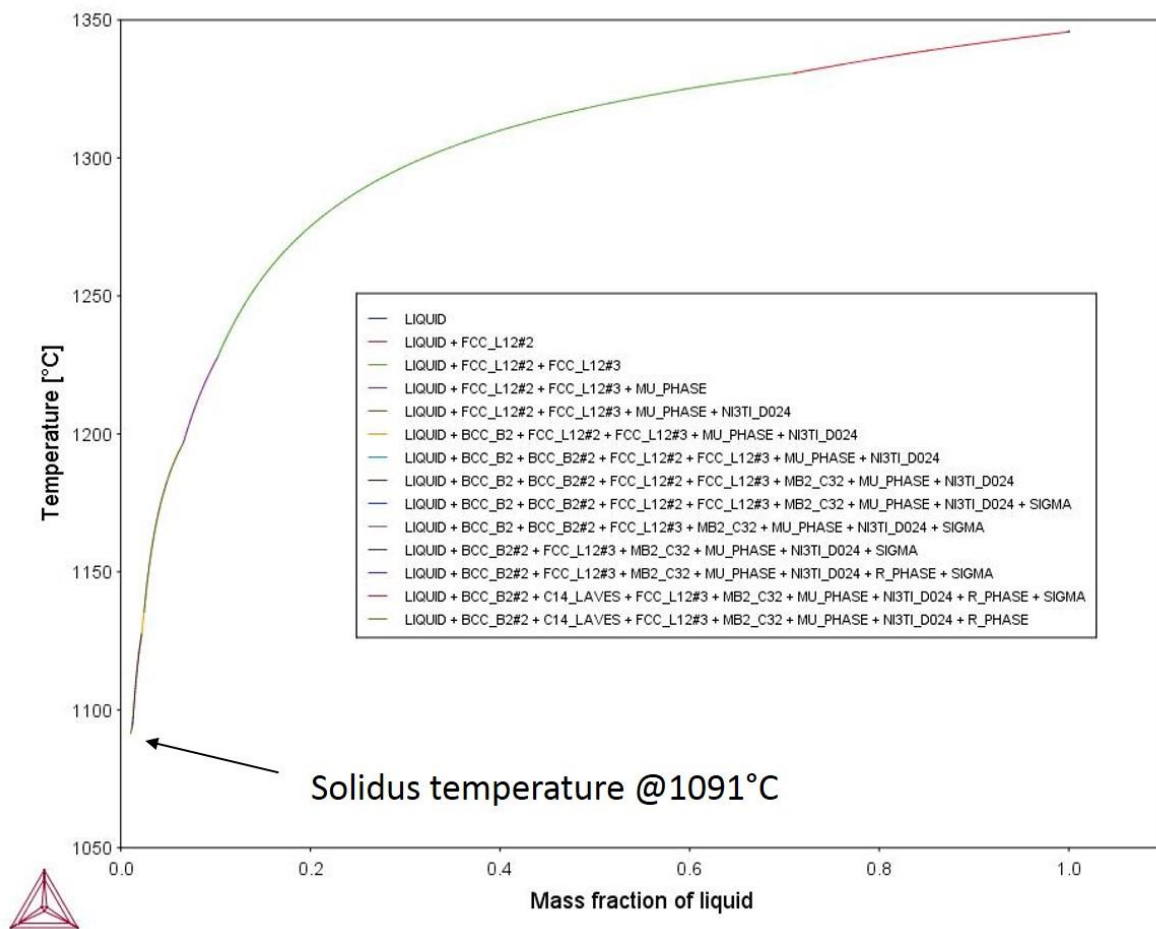


Figure 9.2 - Mass fraction of liquid with temperature for Inconel 738LC as simulated by Thermo-Calc 2015 using Schiel solidification model.

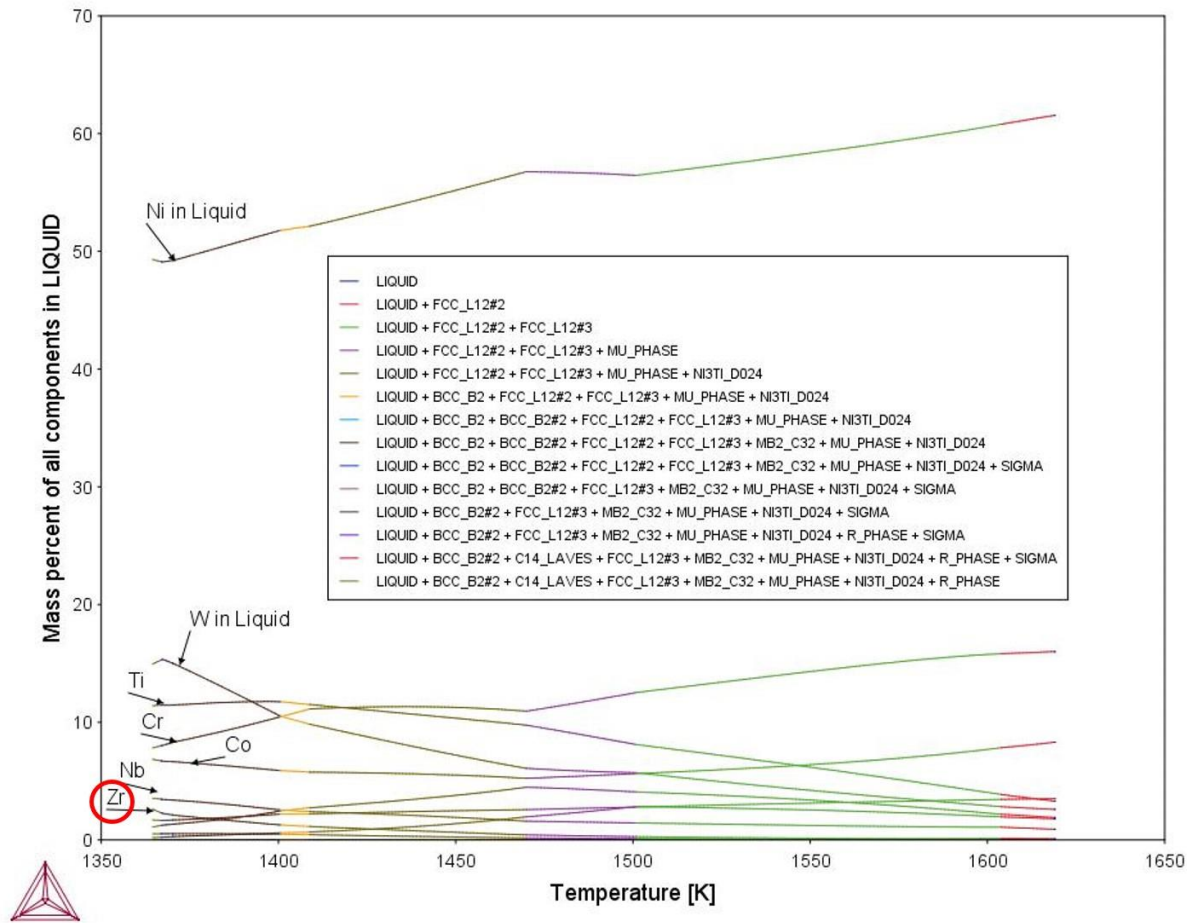


Figure 9.3 - Composition of liquid phase with temperature of Inconel 738LC as simulated by Thermo-Calc 2015 using Schiel solidification model.

Comparing Figure 9.3 to the Figure 9.1b, it is also noted that the Zr content (and all element concentrations) is similar in both simulations up to the crucial temperature – after which point Clouts’ model simulates a huge increase.

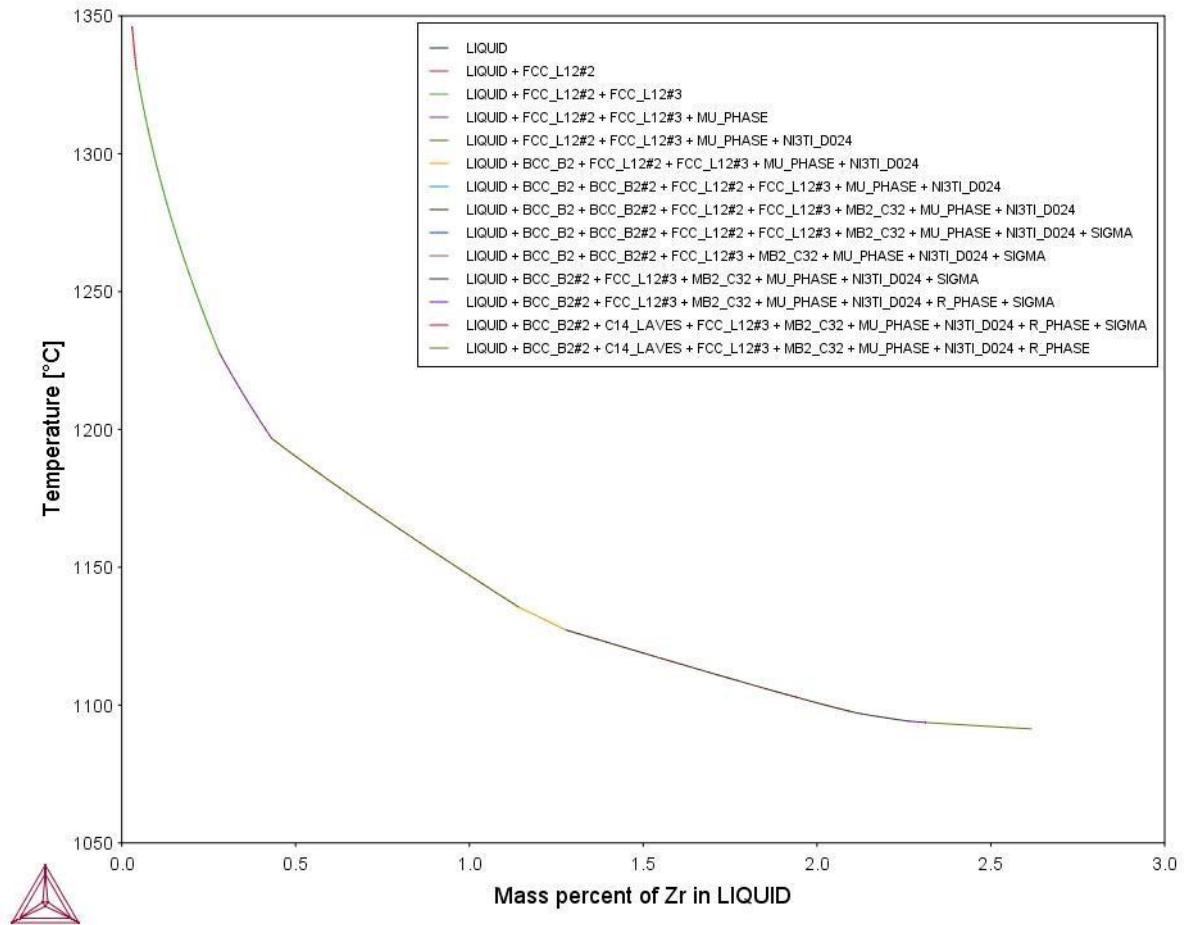


Figure 9.4 - Mass percent of Zr in liquid phase of Inconel 738LC as simulated by Thermo-Calc 2015 using Schiel solidification model

Cloots aims to support the solidification cracking hypothesis by sampling material from a grain boundary and performing Atomic Probe Topography (APT) on the sample – with the intention of observing an increased concentration of Zr.

Reported is an increase in concentration of Zr from 0.04 at% in the bulk alloy to 0.5 wt% - 20x increase. Although certainly a significant increase, this is significantly less than the 28 wt% simulated by the model, and is far more in line with the Thermo-Calc simulation.

A point acknowledged by Harrison et al. is that there was localised segregation interdendritically. Being that the grains of SLM nickel superalloys are only ever visible by

orientation, not brought up by etching, the implication is that there is not observable chemical difference at the grain boundary. Instead, there is a chemical difference interdendritically, which when two grains meet will likely form part of a grain boundary. Therefore, if Cloots had sampled an interdendritic region, they would likely have observed the same chemical composition. Additionally, the grain boundary sampled did not feature a micro-crack. Cloots concluded that the increased Zr at grain boundary supported the solidification cracking theory, however given that the sampled region was not a crack surface there is no guarantee that the two are mutually exclusive.

We must also consider that the grain boundaries are not the regions where the final instances of solidification occur. This would actually be the centre of the melt pool, as the solidification front will travel radially inwards from the edge of the melt pool. This would mean any solidification crack which occurs at this point would be in the centre of the melt pools, or at the very least propagating from the centre of the melt pools. Yet when analysing the micrographs from this investigation and others (Mumtaz, Erasenthiran et al. 2008, Wang 2011, Wang, Wu et al. 2011, Rickenbacher 2013, Tomus, Jarvis et al. 2013, Harrison, Todd et al. 2015) there is no trend to suggest the cracks are propagating from the centre of melt pools. Cloots argues several mechanisms for the formation of the cracks along the grain boundary, with one proposal being that the crack does from in the centre of the melt pool, but then propagates enough so that on the successive layer – despite the material being most remelted – a small crack remains in the solid material and through thermal stress is allowed to propagate and remain. This is possibility, however one would expect to see cracks along the top surface of processed material, which again is not supported well by observations in this investigation.

Finally, there was no detectable Zr content in either OHX or MHX and conversely the composition detailed in Kanagarajah, Brenne et al. (2013) – investigating microstructure of SLM processed Inconel 939 – gave Zr at 0.1 wt% but micro-cracking was not reported. Thus, if Zr content does have an influence on the crack susceptibility of nickel superalloys, the two are not mutually exclusive.

9.1.2 Further considerations

As with many projects, time constraints have inhibited the full completion of objectives has laid out in the beginning of the project. Most notable of which was restrictions of novel alloy validation imposed by equipment failures and delays in the final third of the project. This in turn meant batch scale production of the novel alloy powders could not be performed and as such more comprehensive validation by means of tensile testing and full scale test parts could not be realised.

Ultimately the level of validation that was initially planned was not realised, however this is not to detract from the validation work that was carried out - which still yielded significant results. The following details the further considerations by the author, based on results from the investigation as a whole.

9.1.2.1 Model for predicting elastic modulus

The ability to model the elastic modulus with composition and temperature would have been very beneficial for this project. Elastic modulus carries significant influence on the thermal stress generated during the process, and therefore it would have been ideal if it could have been simulated as proficiently as thermal expansion.

As of writing there still does not exist a model which encompasses both composition and temperature dependence. This therefore represents a good avenue of investigation for future projects, and it is believed by the author that developing this understanding will greatly advance alloy design for laser fusion processes in the future.

9.1.2.2 Influence of minor and residual elements

As discussed in Section 1.6.1, there are a number of investigations which attribute the presence of certain minor and residual elements to the cracking problems of nickel superalloys. Although the evidence is supportive it is not currently conclusive enough.

Certainly it would appear there is no one element, or even mechanism, responsible for micro-cracking in nickel superalloys. In this investigation, solid solution elements have been concluded to reduce the crack susceptibility of Ni-Cr-Fe based alloys. The effect of residual elements was considered, and chemical analysis suggested their influence was negligible. However, it is possible the solidification conditions are such that higher resolution techniques are required to verify the true extent of solute redistribution in SLM processing.

Process parameters, particularly laser scan parameters, are also still significant, and the introduction of 1kW laser and multi-laser systems, and heated platforms by manufacturers will only serve to further complicate investigations. It is proposed that exposing material to higher energy densities may provide the necessary conditions for mechanisms such as liquation and solidification cracking. The variety of SLM systems, hatch strategies and an individual's experience of the process, make it difficult to confidently compare results from published investigations.

Ultimately, no single investigation will be able to encompass and solve the many aspects of SLM processing that are yet to be understood. It is hoped, however, that this investigation has provided a significant step forward in this field.

9.2 Summary of chapters

9.2.1 Review of literature

At the time of writing there was a relatively low number of published investigations on the processing of alloys by Selective Laser Melting (SLM), and only a proportion of these focussed on nickel base superalloys. Fortunately, many of the publications featured microstructural analysis, which allowed for conclusions to be drawn on the possible solidification rates and characteristics of Selective Laser Melting.

In order to demonstrate understanding of solidification mechanisms and characteristics, extensive theory on crystal formation and rapid solidification was reported. This was vital in aiding the hypothesis and ultimate validation of establishment of SLM as a rapid solidification process.

Although there were a number of published investigations into the processing of nickel base superalloys, only a fraction of these reported or investigated process induced micro-cracking. There was not enough information to draw up a sound hypothesis from these reports alone, and therefore more information was sought from processing of nickel superalloys by laser welding.

The key mechanisms behind the formation of residual stress, TGM and shrinkage were also detailed, as these were expected to be significant factors in the formation of micro-cracks.

9.2.2 Experimental methodology and preliminary investigations

Hastelloy X was chosen as the candidate alloy as it was one of the few which had previously been reported in publications as suffering from micro-cracking. Processing was performed on a Renishaw SLM 125, which had a total of 7 controllable processing parameters, all of which were demonstrated to have significant influence on the density and crack density of fabricated material.

Characterisation was performed on both the process and material. Analysis of the beam profile and influence of focus offset on the beam profile revealed that when fully focussed (focus offset = 0 mm) the beam had a very sharp profile. This led to the inclusion of focus offset in optimisation trials, to investigate the effect of energy distribution on porosity and cracking.

Process optimisation was conducted in two stages. Due to the large number of controllable parameters it was first necessary to conduct a screening trial and establish a basic processing window. After this, factorial DOE's were drawn up to investigate the individual influences of each parameter on the density and crack density of the material. After the screening trial, layer thickness was fixed at 20 μ m.

Porosity was found to fall into three primary categories:

- Lack of fusion – insufficient melting/wetting resulting from insufficient energy for a given volume of powder. Often presents as irregular pores with unfused particles, aligned with the layer direction
- Spherical/gaseous – either trapped gas from pores contained within the powder particles or trapped in voids left by sufficient track overlap

- Vapourisation – Large irregular pores void of material, caused by the evaporation and consequential vapour/plasma recoil which ejects material. Results from excessive energy input

It was established that there was a relatively wide window in which full density (>99.5%) could be achieved with Laser Power (LP) and Exposure time (ET) once Point Distance (PD), hatch spacing and focus offset were all fixed/optimised. LP, ET and PD were then dimensionally reduced to give a single parameter of 1D Line Energy density, providing a more fundamental parameter on which to observe relationships.

Crack density was reduced to 3.2 cracks per mm² for a 10 mm cubic sample, however it was not possible to eliminate the cracking. This provided justification for a solution by alloy design.

9.2.3 Establishment of rapid solidification and microstructure

Review of SLM microstructures from published literature implied there was a tight constraint on solidification, evidenced by a consistency of grain structure and size for a number of different alloys. The grain structure is of high aspect ratio columnar grains, orientated with the build direction, which can transcend over a hundred layers. Grains are composed of cell-like dendrites orientated in aligned with the preferential crystal orientation.

From rapid solidification processing theory, laser surface techniques typically produce solidification rates of the order of 0.1-1 m/s, placing them just inside RSP. If this was the case, it would imply that solute distribution (segregation) would be minimal leading to a solid solution rather than multi-phase material.

Solidification conditions, including cooling rate and thermal gradients were modelled for single laser spots. Using material properties of Hastelloy X and known melt pool geometries, it was calculated that solidification rate for a single melt pool would be of the order of 0.5 m/s.

Aziz's solute redistribution theory was applied using the proposed solidification rates; from which it was implied that significant solute trapping would occur resulting in a near solid solution.

To validate the theory, samples from the optimisation trials were reanalysed with higher resolution techniques. The microstructure was observed to be consistent with that of published literature. Primary dendrite arm spacings were used to calculate cooling rates, which agreed with those proposed from rapid solidification theory and solidification rate ≤ 1 m/s. Etching of melt traces and interdendritic regions implied localised segregation in those regions, however grain boundaries were only defined by the orientation of cells.

EDS line scans were performed across crack regions to determine if significant segregation had occurred, however no variation in solute concentration around the crack interface was detected. This provided support that the mechanism behind micro cracking, in Hastelloy X at least, is not solidification cracking or liquation cracking.

High magnification SEM imaging revealed the presence of nano-scale globular precipitates. The small particle size made it difficult to analyse the chemical composition of the precipitates, although from morphology and indirect evidence it was concluded they were most likely MC carbides or sigma phase.

9.2.4 Micro-cracking mechanism

The conclusions from Chapter 4 allowed for theory of cracking mechanism to be proposed for nickel superalloys processed by SLM.

Observations from the experimental work, along with information from literature on SLM processed and welded nickel superalloys lead to the proposal of Elevated Temperature Solid State cracking as the primary mechanism. ETSS is defined as occurring when the thermal stress exceeds the ultimate tensile strength of the material at a given location and temperature, resulting in failure by rupture or fracture. It occurs only when the material is in solid state.

Using the key response indicators of Thermal Stability and Thermal Shock Resistance (TSR), along with understanding of TGM, an equation for determining the crack susceptibility of an alloy was defined. Taking ETSS as the primary mechanism for micro-crack formation, the crack susceptibility of an alloy was defined as the ratio between the tensile strength of the material and the thermal stress generated by the process.

In order to predict a material's crack susceptibility, both tensile strength and thermal stress components would need to be simulated – so that they then may be controlled through alloy design.

9.2.5 Tensile strength contribution

Using the Hall-Petch relationship it was concluded that, given the constrained solidification conditions, only the lattice strength (composed of Peierls stress and solid solution contribution) of the material would be significant when comparing alloys of different compositions.

Solid solution strengthening (or hardening) theory can be used to calculate the solid solution contribution of an alloy based on alloying composition alone – providing the necessary empirically determined values exist; which for nickel they do.

Therefore, it was proposed that the crack susceptibility of an alloy could in fact be determined not by tensile strength, but by solid solution contribution – as it had previously been established that SLM processed material would be a near solid solution.

The hypothesis was tested by means of experimental validation. A modified version of the Hastelloy X composition used in the preliminary investigations was designed with increased solid solution strength and reduced residual limits – named MHX. It was then processed in direct comparison to the original Hastelloy X – named OHX – and the crack densities, along with material properties were compared. Critically, MHX was still within the Hastelloy® X specification and modifications would be considered minor in magnitude.

MHX displayed an average reduction in cracking of 65% over OHX. Tensile testing revealed that MHX displayed superior tensile strength at elevated temperatures and marginally improved ductility and hardness.

Although not fully explored at this point, the effect of thermal expansion on thermal stress – and therefore crack susceptibility – could not be ruled out. However, both MHX and OHX displayed near identical coefficients of thermal expansion.

For the case of MHX therefore, an increase in solid solution strength had resulted in a significant reduction of crack density (and thus crack susceptibility) over OHX. This result therefore supports the theory of crack susceptibility based on the assumption that thermal stress contributions were not significantly different

Finally, as a result of observations from the MHX-OHX comparison trials, some experimental work was conducted to investigate the effect of geometry, specifically component volume on the micro-cracking of material.

Although a relationship was observed between cracking and cube volume, it was not linear or proportional. However, it was observed there was a dominant influence of laser power on the cracking of the material. Specifically, increasing power lead to increased crack density, whereas as there was no defined relationship for exposure time (absorbed energy per unit area). This result implies solidification cracking is not the primary mechanism for micro-cracking, as one would expect a relationship between exposure time and cracking if this were the case. Conversely, it supports ETSS as increased power results in increased surface temperatures and increased thermal gradients. This drives the TGM for thermal stress generation and hence increased cracking by ETSS.

9.2.6 Thermal stress simulation

The second part of the crack susceptibility model is the simulation or calculation of thermal stress experienced by the alloy as a consequence of SLM processing.

It was established that complete 3-dimensional simulation of thermal stress for real-world processing was beyond the resources of this investigation, however if one or more of the influencing components of thermal stress could be simulated, this would be beneficial.

The three primary components of residual generation are the expansion of the material due to a change in temperature, the material's resistance to the expansion – it's stiffness – and the change in temperature i.e. co-efficient of thermal expansion, elastic (Young's) modulus and ΔT . In order to predict crack susceptibility a method was required by which

thermal stress could be predicted based on chemical composition and fixed processing parameters alone.

Presently, a model or method of simulating Young's modulus with chemical composition is not in existence – and again this would be beyond the resources of this investigation. Therefore, Young's modulus would have to be taken from closest known compositions if the alloy was not in existence. However, for predicting of known alloys, the Young's modulus of the annealed state would be sufficient.

Thermophysical calculation software can be used to calculate coefficient of thermal expansion, however it is not affected significantly by grain structure and therefore values can also be taken from literature for known alloys.

It was initially proposed that the ΔT values be taken from a 3-dimensional temperature field model. With the model, one could simulate the temperature field with time, as laser spots were successively melted in lines, then hatches and ultimately layers. Although the results were initially promising, it became evident that extracting a usable ΔT value was not possible – due to the random nature in which the model 'measured' points. In addition, it was realised that subtle differences in a ΔT value between two similar alloys would be insignificant compared to the differences of E or α_{CTE} which carried much larger magnitudes.

It was therefore decided to use the model only to approximate a working ΔT value, applicable for a base alloy set. For the case of nickel superalloys, this would be 500 K, the approximate range between ambient temperature and $0.5T_{melt}$. This was deemed acceptable as the purpose was to compare nickel alloys for crack susceptibility, thus providing a fixed ΔT actually allows for clear comparison of material response.

The 'apparent' thermal stress for alloys could then be calculated, influenced only by their Young's modulus and thermal expansion, with the chosen ΔT only effecting the final crack susceptibility value.

9.2.7 Crack susceptibility predictor

OHX and MHX had provided the first levels of validation for crack susceptibility theory, however more validation was required, on both commercially available and novel alloys, to better support the findings.

In order to test the solid solution influence in crack susceptibility, two alloys were designed with identical base alloying elements but markedly different predicted solid solutions strengths. Based on the Hastelloy® X compositions, a High SSS and Low SSS alloy were designed. High SSS had significant increases in Mo and W content, whereas Low SSS had significant reductions, compared to the standard Hastelloy® X composition.

The two alloys were fabricated using a novel process, by which the alloys were first cast by vacuum arc melting, then rolled and sectioned, before being processed into ribbons by melt spinning. Finally, the ribbon was processed into a powder by means of ball milling. Chemical testing revealed a significant increase in oxygen content, most likely from milling process, although both powders had similar levels.

Due to the small volumes of powder produced, a custom rig was created to fit inside the standard Renishaw SLM 125. This allowed for processing of $5 \times 10 \times 1$ mm ribbons of material, which could be mounted and analysed for microstructure and hardness.

High SSS displayed lower cracking than Low SSS, which had similar crack density to MHX when processed in the same manner. Despite the seemingly high oxygen content, the

powders behaved similarly to the commercial material, and therefore the result was deemed reliable.

The final stage was to use the crack susceptibility predictor method to predict the crack susceptibility of commercial alloys, and compare the results to those reported in investigations in which said alloys were processed by SLM.

When using properties and compositions reported in the published investigations, the predicted crack susceptibilities had good agreement to observations, the primary reason being that the Young's modulus values were appropriate for the SLM as processed state. When using data from 'book' values, there was still majority agreement, however some alloys have markedly different properties depending on microstructural states, which was reflected in the comparison.

Inconel® 718 proved to be only a true anomaly, as it is reported to process without cracks, but has a similar χ to OHX. A possible explanation for the anomaly is that in an as processed state, SLM processed Inconel® 718 contains coherent sub-micron precipitates of its primary strengthening phase, γ'' . The volume fraction is significant enough that it could influence the tensile strength of the material, which is reflected in the very high as processed mechanical properties (compared to the similar composition of Hastelloy® X).

9.3 Conclusions

- The microstructure of SLM is unique to the process, in that epitaxial growth produces large high aspect ratio grains, comprised of fine cell-dendrites, orientated parallel to the build direction. The cell-dendrites grow epitaxially, with the majority growing from the vertically orientated cells that remain at the base of the melt pool after the successive layer. As the upper melt pool solidifies, the

dendrite growth continues from the underlying dendrites and the grain is continued. Strong heat flux imposed by the large substrate (which acts as a heat sink) ensures close alignment to the z axis of the cell-dendrites and therefore grains.

- The high solidification interface velocities and cooling rates inhibit the formation of secondary dendrite arms and significant secondary phase formation. As a result, although there is interdendritic microsegregation, the bulk material can be regarded as saturated solid solution with chemical variation only over length scales of microns.
- Successive melting and extension of heat affected zone – recalescence - results in the formation of nano-precipitates in the interdendritic regions. EDX analysis of the precipitates implied composition was that of sigma phase, but electron back scatter images imply higher density phases such as MoC. It is accepted high resolution techniques would be required for confirmation.
- Microstructural analysis as well as implementation of RSP theory and solute redistribution theory was used to establish Selective laser melting as a rapid solidification process.
- The primary cracking mechanism in SLM processed nickel superalloys is believed to be elevated temperature solid state (ETSS) cracking. This is supported by the establishment of RSP, as well as fracture analysis and relationships between crack density and laser power.
- The crack susceptibility of a nickel superalloy is defined as the ratio between the solid solution strengthening contribution and apparent thermal stress: $\chi = \frac{\sigma_{SS}}{\sigma_{app-th}}$

- Minor increases in solid solutions strengthening elements in a known high crack susceptibility alloy, resulted in average reductions of crack density of 65%. Thereby supporting solid solution strength as a key factor in the crack susceptibility of a nickel superalloy.
- A thermal stress contribution has to be included in the crack susceptibility model, however it is not required to be fully simulated. Apparent thermal stress values based on a fixed ΔT and composition dependant α_{CTE} and E are sufficient.
- Ball milling of novel alloy ribbon is a potential method for novel alloy powder production, however more refinement is required to ensure production of clean alloys.
- The crack susceptibility predictor was demonstrated as being applicable and reliable for the majority of nickel superalloys.
- The understanding is now in place to allow for the creation of a design tool to aid the development of nickel superalloys optimised for selective laser melting
- However, as more investigations are conducted, additional information will need to be included in the crack susceptibility model to improve accuracy and applicability across the full range of nickel and other alloys.

10 References

- A. Hazotte, B. P., P. Archambault (1993). "High temperature thermal diffusivity of nickel-based superalloys and intermetallic compounds." Journal de Physique IV **3**(C7): C7-351-C357-354.
- Ahmad, N. A., A. A. Wheeler, W. J. Boettinger and G. B. McFadden (1998). "Solute trapping and solute drag in a phase-field model of rapid solidification." Physical Review E **58**(3): 3436-3450.
- Amato, K. (2012). "Comparison of Microstructures and Properties for a Ni-Base Superalloy (Alloy 625) Fabricated by Electron Beam Melting." Journal of Materials Science Research **1**(2).
- Amato, K. N., S. M. Gaytan, L. E. Murr, E. Martinez, P. W. Shindo, J. Hernandez, S. Collins and F. Medina (2012). "Microstructures and mechanical behavior of Inconel 718 fabricated by selective laser melting." Acta Materialia **60**(5): 2229-2239.
- Arkoosh, M. A. and N. F. Fiore (1972). "Elevated temperature ductility minimum in Hastelloy alloy X." Metallurgical Transactions **3**(8): 2235-2240.
- Arnold, C. B., M. J. Aziz, M. Schwarz and D. M. Herlach (1999). "Parameter-free test of alloy dendrite-growth theory." Physical Review B **59**(1): 334-343.
- Ashby, M. F., H. Shercliff and D. Cebon (2007). Materials: Engineering, Science, Processing and Design, Elsevier Science.
- Aziz, M., J. Tsao, M. Thompson, P. Peercy and C. White (1986). "Solute Trapping: Comparison of Theory with Experiment." Physical Review Letters **56**(23): 2489-2492.
- Aziz, M. J. (1982). "Model for solute redistribution during rapid solidification." Journal of Applied Physics **53**(2): 1158-1168.
- Aziz, M. J. (1988). "Proceedings of the Sixth International Conference on Rapidly Quenched Metals Non-equilibrium interface kinetics during rapid solidification: Theory and experiment." Materials Science and Engineering **98**: 369-372.
- Baeri, P., G. Foti, J. M. Poate, S. U. Campisano and A. G. Cullis (1981). "Orientation and velocity dependence of solute trapping in Si." Applied Physics Letters **38**(10): 800-802.
- Baker, J. C. and J. W. Gahn (1969). "Solute trapping by rapid solidification." Acta Metallurgica **17**(5): 575-578.
- Bass, M. (2012). Laser materials processing, Elsevier.

Bauer, T., K. Dawson, A. B. Spierings and K. Wegener (2013). "Microstructure and mechanical characterisation of SLM processed Haynes® 230®." J. Chem. Inf. Model **53**: 1689-1699.

Boettinger, W. J., S. R. Coriell and R. F. Sekerka (1984). "Solidification Microstructure: 30 Years after Constitutional Supercooling Mechanisms of microsegregation-free solidification." Materials Science and Engineering **65**(1): 27-36.

Böllinghaus, T., H. Herold, C. E. Cross and J. Lippold (2008). Hot Cracking Phenomena in Welds II, Springer-Verlag Berlin Heidelberg.

Carrard, M., M. Gremaud, M. Zimmermann and W. Kurz (1992). "About the banded structure in rapidly solidified dendritic and eutectic alloys." Acta Metallurgica et Materialia **40**(5): 983-996.

Carter, L. N., K. Essa and M. M. Attallah (2015). "Optimisation of selective laser melting for a high temperature Ni-superalloy." Rapid Prototyping Journal **21**(4): 423-432.

Carter, L. N., C. Martin, P. J. Withers and M. M. Attallah (2014). "The influence of the laser scan strategy on grain structure and cracking behaviour in SLM powder-bed fabricated nickel superalloy." Journal of Alloys and Compounds **615**: 338-347.

Chlebus, E., B. Kuźnicka, T. Kurzynowski and B. Dybała (2011). "Microstructure and mechanical behaviour of Ti–6Al–7Nb alloy produced by selective laser melting." Materials Characterization **62**(5): 488-495.

Cloots, M., P. J. Uggowitzer and K. Wegener (2016). "Investigations on the microstructure and crack formation of IN738LC samples processed by selective laser melting using Gaussian and doughnut profiles." Materials & Design **89**: 770-784.

Collins, M. and J. Lippold (2003). "An investigation of ductility dip cracking in nickel-based filler materials-Part I." Welding Journal **82**(10): 288.

Dai, K. and L. Shaw (2004). "Thermal and mechanical finite element modeling of laser forming from metal and ceramic powders." Acta Materialia **52**(1): 69-80.

Davies, H. A., N. Shohoji and D. H. Warrington (1980). The Structure of Rapidly Quenched Nickel-based Superalloy Ribbons Produced by Melt Spinning. International Conference on Rapid Solidification Processing.

Davis, J. R. (1997). ASM Speciality Handbook: Heat Resistant Materials, ASM International.

Deffley, R. J. (2012). Development of processing strategies for the additive layer manufacture of aerospace components in Inconel 718. Department of Materials Science and Engineering, University of Sheffield. **Ph.D.**

Divya, V. D., R. Muñoz-Moreno, O. M. D. M. Messé, J. S. Barnard, S. Baker, T. Illston and H. J. Stone (2016). "Microstructure of selective laser melted CM247LC nickel-based superalloy and its evolution through heat treatment." Materials Characterization **114**: 62-74.

Donachie, M. J. and S. J. Donachie (2002). Superalloys : a technical guide. Materials Park, OH, ASM International.

Etter, T., K. Kunze, F. Geiger and H. Meidani (2015). "Reduction in mechanical anisotropy through high temperature heat treatment of Hastelloy X processed by Selective Laser Melting (SLM)." IOP Conference Series: Materials Science and Engineering **82**(1): 012097.

Feltham, P. (1968). "Solid solution hardening of metal crystals." Journal of Physics D: Applied Physics **1**(3): 303.

Fulcher, B. A., D. K. Leigh and T. J. Watt (2014). "COMPARISON OF ALSI10MG AND AL 6061 PROCESSED THROUGH DMLS."

Gedeon, M. (2010). Solid Solution Hardening and Strength. Technical Tidbits. Brush Wellman Inc.

Gessinger, G. H. (1984). Powder metallurgy of superalloys. London, Butterworths.

Gibson, I., D. W. Rosen and B. Stucker (2010). Additive manufacturing technologies: rapid prototyping to direct digital manufacturing, Springer.

Gremaud, M., M. Carrard and W. Kurz (1990). "The microstructure of rapidly solidified Al•Fe alloys subjected to laser surface treatment." Acta Metallurgica et Materialia **38**(12): 2587-2599.

Gu, D., Y.-C. Hagedorn, W. Meiners, G. Meng, R. J. S. Batista, K. Wissenbach and R. Poprawe (2012). "Densification behavior, microstructure evolution, and wear performance of selective laser melting processed commercially pure titanium." Acta Materialia **60**(9): 3849-3860.

Gu, D. and W. Meiners (2010). "Microstructure characteristics and formation mechanisms of in situ WC cemented carbide based hardmetals prepared by Selective Laser Melting." Materials Science and Engineering: A **527**(29-30): 7585-7592.

Gusarov, A. V. and I. Smurov (2009). "Two-dimensional numerical modelling of radiation transfer in powder beds at selective laser melting." Applied Surface Science **255**(10): 5595-5599.

Gusarov, A. V., I. Yadroitsev, P. Bertrand and I. Smurov (2007). "Heat transfer modelling and stability analysis of selective laser melting." Applied Surface Science **254**(4): 975-979.

Gusarov, A. V., I. Yadroitsev, P. Bertrand and I. Smurov (2009). "Model of Radiation and Heat Transfer in Laser-Powder Interaction Zone at Selective Laser Melting." Journal of Heat Transfer **131**(7): 072101-072101.

Gypen, L. A. and A. Deruyttere (1977). "Multi-component solid solution hardening." Journal of Materials Science **12**(5): 1034-1038.

Gypen, L. A. and A. Deruyttere (1977). "Multi-component solid solution hardening." Journal of Materials Science **12**(5): 1028-1033.

Harrison, N. J., I. Todd and K. Mumtaz (2015). "Reduction of micro-cracking in nickel superalloys processed by Selective Laser Melting: A fundamental alloy design approach." Acta Materialia **94**(0): 59-68.

Howie, D. (2014). Big sister: High-powered Trent XWB-97. the magazine Rolls Royce: 12-15.

Hull, F. C., S. K. Hwang, J. M. Wells and R. I. Jaffee (1987). "Effect of Composition on Thermal Expansion of Alloys Used in Power Generation." J. Materials Engineering **9**(1): 81-92.

Hussein, A., L. Hao, C. Yan and R. Everson (2013). "Finite element simulation of the temperature and stress fields in single layers built without-support in selective laser melting." Materials & Design **52**: 638-647.

Inc., H. I. (1997). "Haynes International Inc. - Hastelloy® X Alloy Datasheet." from <http://www.haynesintl.com/pdf/h3009.pdf>.

Jena, A. K. and M. C. Chaturvedi (1984). "The role of alloying elements in the design of nickel-base superalloys." Journal of Materials Science **19**(10): 3121-3139.

Kamath, C., B. El-dasher, G. F. Gallegos, W. E. King and A. Sisto (2014). "Density of additively-manufactured, 316L SS parts using laser powder-bed fusion at powers up to 400 W." The International Journal of Advanced Manufacturing Technology.

Kanagarajah, P., F. Brenne, T. Niendorf and H. J. Maier (2013). "Inconel 939 processed by selective laser melting: Effect of microstructure and temperature on the mechanical properties under static and cyclic loading." Materials Science and Engineering: A **588**: 188-195.

Karunaratne, M. S. A., P. Carter and R. C. Reed (2000). "Interdiffusion in the face-centred cubic phase of the Ni-Re, Ni-Ta and Ni-W systems between 900 and 1300°C." Materials Science and Engineering: A **281**(1-2): 229-233.

Kempen, K., E. Yasa, L. Thijs, J. P. Kruth and J. Van Humbeeck (2011). "Microstructure and mechanical properties of Selective Laser Melted 18Ni-300 steel." Physics Procedia **12**: 255-263.

Kruth, J. P., L. Froyen, J. Van Vaerenbergh, P. Mercelis, M. Rombouts and B. Lauwers (2004). "Selective laser melting of iron-based powder." Journal of Materials Processing Technology **149**(1-3): 616-622.

Kruth, J. P., G. Levy, F. Klocke and T. H. C. Childs (2007). "Consolidation phenomena in laser and powder-bed based layered manufacturing." CIRP Annals - Manufacturing Technology **56**(2): 730-759.

Kurz, W. and D. J. Fisher (1998). Fundamentals of solidification. Switzerland, Trans Tech Publications.

Kurz, W. and R. Trivedi (1994). "Rapid solidification processing and microstructure formation." Materials Science and Engineering: A **179-180, Part 1**(0): 46-51.

Li, S., Q.-W. Hu, X.-Y. Zeng and S.-Q. Ji (2005). "Effect of carbon content on the microstructure and the cracking susceptibility of Fe-based laser-clad layer." Applied Surface Science **240**(1-4): 63-70.

Limmaneevichitr, C. and S. Kou (2000). "Visualization of Marangoni convection in simulated weld pools." WELDING JOURNAL-NEW YORK **79**(5): 126-s.

Lippold, J. C., S. D. Kiser and J. N. DuPont (2011). Welding Metallurgy and Weldability of Nickel-Base Alloys, Wiley.

Matsumoto, M., M. Shiomi, K. Osakada and F. Abe (2002). "Finite element analysis of single layer forming on metallic powder bed in rapid prototyping by selective laser processing." International Journal of Machine Tools and Manufacture **42**(1): 61-67.

McLean, M. (1983). Directionally solidified materials for high temperature service. London, The Metals Society.

Mercelis, P. and J.-P. Kruth (2006). "Residual stresses in selective laser sintering and selective laser melting." Rapid Prototyping Journal **12**(5): 254-265.

Mills, K. C. (2002). Ni - Hastelloy-X. Recommended Values of Thermophysical Properties for Selected Commercial Alloys. K. C. Mills, Woodhead Publishing: 175-180.

Mishima, Y., Ochiai, S., Hamao, N., Yodogawa, M., Suzuki, T. (1986). "Solid Solution Hardening of Nickel -Role of Transition Metal and B-subgroup Solutes." Transactions of the Japan Institute of Metals **27**(9): 656-664.

Moat, R. J. (2009). Microstructural and residual stress characterisation of laser deposited nickel-base superalloy test structures, University of Manchester. **PhD**.

Moat, R. J., A. J. Pinkerton, L. Li, P. J. Withers and M. Preuss (2011). "Residual stresses in laser direct metal deposited Waspaloy." Materials Science and Engineering: A **528**(6): 2288-2298.

Morgan, R., C. J. Sutcliffe and W. O'Neill (2004). "Density analysis of direct metal laser re-melted 316L stainless steel cubic primitives." Journal of Materials Science **39**(4): 1195-1205.

Mumtaz, K. (2008). Selective Laser Melting of Inconel 625 using Pulse Shaping. Mechanical and Manufacturing Engineering, Loughborough University. **PhD**.

Mumtaz, K. A., P. Erasenthiran and N. Hopkinson (2008). "High density selective laser melting of Waspaloy®." Journal of Materials Processing Technology **195**(1-3): 77-87.

Newey, C. and G. Weaver (2013). Materials Principles and Practice: Electronic Materials Manufacturing with Materials Structural Materials, Elsevier Science.

Norman, N. C. (1998). Chemistry of arsenic, antimony and bismuth. London, Blackie Academic & Professional.

P. J. Withers, H. K. D. H. B. (2001). "Residual Stress Part 1 - Measurement techniques." Materials Science and Technology **17**: 355-365.

Parker, W. J., R. J. Jenkins, C. P. Butler and G. L. Abbott (1961). "Flash Method of Determining Thermal Diffusivity, Heat Capacity, and Thermal Conductivity." Journal of Applied Physics **32**(9): 1679-1684.

Parthasarathy, J., B. Starly, S. Raman and A. Christensen (2010). "Mechanical evaluation of porous titanium (Ti6Al4V) structures with electron beam melting (EBM)." Journal of the Mechanical Behavior of Biomedical Materials **3**(3): 249-259.

Patil, R. B. and V. Yadava (2007). "Finite element analysis of temperature distribution in single metallic powder layer during metal laser sintering." International Journal of Machine Tools and Manufacture **47**(7-8): 1069-1080.

Rancourt, D. G. and M. Z. Dang (1996). "Relation between anomalous magnetovolume behavior and magnetic frustration in Invar alloys." Physical Review B **54**(17): 12225-12231.

Reed, R. C. (2006). The superalloys : fundamentals and applications. Cambridge, Cambridge University Press.

Rickenbacher, L. (2013). "High temperature material properties of IN738LC processed by selective laser melting (SLM) technology." Rapid Prototyping Journal **19**(4): 282-290.

Roberts, I. A., C. J. Wang, R. Esterlein, M. Stanford and D. J. Mynors (2009). "A three-dimensional finite element analysis of the temperature field during laser melting of metal powders in additive

layer manufacturing." International Journal of Machine Tools and Manufacture **49**(12-13): 916-923.

Rosenthal, D. (1946). "The Theory of Moving Sources of Heat and Its Application to Metal Treatments." Transactions of the ASME **68**: 849-866.

Roth, H. A., C. L. Davis and R. C. Thomson (1997). "Modeling solid solution strengthening in nickel alloys." Metallurgical and Materials Transactions A **28**(6): 1329-1335.

Roy, R., D. K. Agrawal and H. A. McKinstry (1989). "Very Low Thermal Expansion Coefficient Materials." Annual Review of Materials Science **19**(1): 59-81.

Savage, W. F. and B. M. Krantz (1966). "An Investigation of Hot Cracking in Hastelloy X." Welding Journal **45**.

Savage, W. F. and B. M. Krantz (1971). Microsegregation in Autogenous Hastelloy X Welds, Defense Technical Information Center.

Savitha, U., H. Gokhale, G. J. Reddy, A. Venkataramana, A. A. Gokhale and M. Sundararaman (2012). "Effect of Process Parameters on Porosity in Laser Deposited IN625 Alloy." Transactions of the Indian Institute of Metals **65**(6): 765-770.

Shiomi, M., K. Osakada, K. Nakamura, T. Yamashita and F. Abe (2004). "Residual Stress within Metallic Model Made by Selective Laser Melting Process." CIRP Annals - Manufacturing Technology **53**(1): 195-198.

Swartz, D. (2016). Head and optics innovations key to laser cutting growth. The Fabricator.

Terada, Y., K. Ohkubo, T. Mohri and T. Suzuki (1997). "Thermal conductivity in nickel solid solutions." Journal of Applied Physics **81**(5): 2263.

Thijs, L., F. Verhaeghe, T. Craeghs, J. V. Humbeeck and J.-P. Kruth (2010). "A study of the microstructural evolution during selective laser melting of Ti-6Al-4V." Acta Materialia **58**(9): 3303-3312.

Tilley, R. J. D. (2013). Understanding Solids: The Science of Materials, Wiley.

Toda-Caraballo, I., E. I. Galindo-Nava and P. E. J. Rivera-Díaz-del-Castillo (2013). "Unravelling the materials genome: Symmetry relationships in alloy properties." Journal of Alloys and Compounds **566**: 217-228.

Tomus, D., T. Jarvis, X. Wu, J. Mei, P. Rometsch, E. Herny, J. F. Rideau and S. Vaillant (2013). "Controlling the Microstructure of Hastelloy-X Components Manufactured by Selective Laser Melting." Physics Procedia **41**: 816-820.

Vandenbroucke, B. and J.-P. Kruth (2007). "Selective laser melting of biocompatible metals for rapid manufacturing of medical parts." Rapid Prototyping Journal **13**(4): 196-203.

Vilaro, T., C. Colin, J. D. Bartout, L. Nazé and M. Sennour (2012). "Microstructural and mechanical approaches of the selective laser melting process applied to a nickel-base superalloy." Materials Science and Engineering: A **534**: 446-451.

Wang, F. (2011). "Mechanical property study on rapid additive layer manufacture Hastelloy® X alloy by selective laser melting technology." The International Journal of Advanced Manufacturing Technology **58**(5-8): 545-551.

Wang, F., X. H. Wu and D. Clark (2011). "On direct laser deposited Hastelloy X: dimension, surface finish, microstructure and mechanical properties." Materials Science and Technology **27**(1): 344-356.

Wang, W. Z., H. U. Hong, I. S. Kim, B. G. Choi, H. W. Jeong, M. Y. Kim and C. Y. Jo (2009). "Influence of γ' and grain boundary carbide on tensile fracture behaviors of Nimonic 263." Materials Science and Engineering: A **523**(1-2): 242-245.

Wang, Z., K. Guan, M. Gao, X. Li, X. Chen and X. Zeng (2012). "The microstructure and mechanical properties of deposited-IN718 by selective laser melting." Journal of Alloys and Compounds **513**: 518-523.

Yilbas, B. S., C. Karatas, A. F. M. Arif and B. J. Abdul Aleem (2011). "Laser control melting of alumina surfaces and thermal stress analysis." Optics & Laser Technology **43**(4): 858-865.

Young, G., T. Capobianco, M. Penik, B. Morris and J. McGee (2008). "The mechanism of ductility dip cracking in nickel-chromium alloys." WELDING JOURNAL-NEW YORK- **87**(2): 31.

Yu, J., M. Rombouts and G. Maes (2013). "Cracking behavior and mechanical properties of austenitic stainless steel parts produced by laser metal deposition." Materials & Design **45**: 228-235.

Zhong, M., H. Sun, W. Liu, X. Zhu and J. He (2005). "Boundary liquation and interface cracking characterization in laser deposition of Inconel 738 on directionally solidified Ni-based superalloy." Scripta Materialia **53**(2): 159-164.

Zimmermann, M., M. Carrard and W. Kurz (1989). "Rapid solidification of Al-Cu eutectic alloy by laser remelting." Acta Metallurgica **37**(12): 3305-3313.